CHARACTERIZATION OF A CRYOGENIC CENTRIFUGAL COMPRESSOR TRAIN FOR RELIABLE WIDE-RANGE OPERATION OF HELIUM SUB-ATMOSPHERIC SYSTEMS

By

Jonathon Winslow Howard

A DISSERTATION

Submitted to
Michigan State University
in partial fulfillment of the requirements
for the degree of

Mechanical Engineering – Doctor of Philosophy

2024

ABSTRACT

Operation of helium cryogenic systems below the normal boiling point of helium (approximately 4.2 K) has become a common need for modern high-energy particle accelerators. Nominal cooling near 2 K (or a corresponding saturation pressure of approximately 30 mbar) is often required by superconducting radio-frequency niobium resonators (also known as SRF cavities) to achieve the performance targets of the particle accelerator. To establish this cooling temperature, the cryogenic vessel (or cryostat) containing the SRF cavities is operated at the sub-atmospheric saturation pressure by continuously evacuating the vapor from the liquid helium bath. Multi-stage cryogenic centrifugal compressors ('*cold-compressors*') have been proven to be an efficient, reliable, and cost-effective method to achieve sub-atmospheric cryogenic operating conditions for large-scale systems. These compressors re-pressurize the sub-atmospheric cryogenic helium to just above atmospheric conditions before injecting the flow back into the main helium refrigerator. Although multi-stage cryogenic centrifugal compressor technology has been implemented in large-scale cryogenic systems since the 1980's, theoretical understanding of their operation (steady-state and transient) is inadequate to provide a general characterization of the compressor and establish stable wide-range performance. The focus of this dissertation is two-fold regarding multi-stage centrifugal compressors as used for sub-atmospheric helium cryogenic systems. First, to develop a reliable performance prediction model for a multi-stage cryogenic centrifugal compressor train, validated with measurements from an actual operating system. Capabilities of the model include steady-state performance estimation and prediction of operational envelops that ensure stable and wide-range steady-state operation. Second, to develop and validate a process model of the entire sub-atmospheric system (*e.g.* FRIB) and establish a simple methodology to obtain a reliable thermodynamic path for the transient ('*pump-down*') process of reducing the helium bath pressure from above 1 bar to the operational steady-state conditions near 30 mbar. The effectiveness of the developed methodology is demonstrated by comparing the estimated and measured process parameters from the sub-atmospheric system studied (*i.e.* FRIB). The developed model and methodology are intended to benefit the design and operation (both steady-state and transient) of multi-stage cryogenic centrifugal compressor trains used in large-scale cryogenic helium refrigeration systems.

For my family,
whose patience and encouragement gave me the confidence to succeed.

ACKNOWLEDGEMENTS

There are numerous people that I need to acknowledge, without whom this dissertation and my graduate education would have been unachievable. Firstly, my Lord and Savior, Jesus Christ, who has blessed me beyond measure. Through Jesus, I am rejuvenated with the energy and perseverance to accomplish all things, “for I can do everything through Christ, who gives me strength.” Indeed, all things stem from Jesus, as “Salvation is not a reward for the good things we have done, so none of us can boast about it. For we are God’s masterpiece. He has created us anew in Christ Jesus, so we can do the good things he planned for us long ago.”

Next, I would like to extend gratitude to my academic advisor, Dr. Abraham Engeda, whose proactive interaction with the Facility for Rare Isotope Beams (FRIB) provided the opportunity for graduate students like myself to explore the exciting field of cryogenics. Dr. Engeda was eager for continuous discussion of my research topic, and provided insightful and valuable advice for both career and research aspirations. He has had a tremendous impact on the trajectory of my academic and professional career, for which I will forever be grateful for.

I would also like to thank the remainder of my guidance committee, Dr. Andre Benard, Dr. Nusair Hasan, Dr. Peter Knudsen, Dr. Wei Liao, and Dr. Norbert Mueller, for their willingness to participate and provide suggestions on the direction of my research. Their expertise and wide range of research experience formed a well-rounded group that helped to elevate my graduate research.

Research in the area of cryogenic would not have been possible without the excellent guidance and mentorship available to me through the FRIB cryogenics group. Specifically, I would like to thank Peter Knudsen, Nusair Hasan, and Rao Ganni for their mentorship and dedication to the education of future cryogenic engineers. A special thanks is also necessary for Mathew Wright, who was always willing to answer all of my (numerous) questions and take me out into the field to get hands-on experience and provide beneficial visual explanations. Opportunities for research at FRIB were provided through Fabio Casagrande (Cryogenic Department Manager, FRIB), Thomas Glasmacher (Laboratory Director, FRIB), and funding

through the Accelerator Science and Engineering Traineeship (ASET) program, all of whom I am indebted to and will forever be thankful for their role in my education.

Graduate school would not have been bearable without some of my classmates and friends that I have made along the way. Duncan Kroll, Scott Anthony, Tasha Williams, and Austin Grake made the FRIB environment a wonderful place for learning, teamwork, and comradery. Members of the mechanical engineering turbomachinery group are also greatly appreciated for their assistance and collaboration, including Javad Hosseinpour, Casey Palanca, Jinbo Chen, Mekuannint Mesfin and Ahmed Helmy. Finally, I would not have made it without my best of friends Archana Lamsal and Bibek Poudel, whose friendship provided much needed stability and encouragement during my first few years of graduate school.

Lastly, I would to thank my family for their constant belief in my ability to make it through to the completion of my Ph.D. My lovely wife, Kaitlyn, whose patience, constant love and words of reassurance always meant the most during times of struggle. My sister and brother-in-law, Courtney and David, and my little nephew, Ezra, whom visiting and talking to always produced calmness and energized me for new challenges ahead. My parents, Timothy and Julie, whose love and support throughout my entire life has always made be believe in myself and elevated my self-confidence so that anything seemed possible. You have all been instrumental in achieving this milestone, and I could not have done it without you.

This material is based upon work supported by the U.S. Department of Energy Office of Science under Cooperative Agreement DE-SC0000661, the State of Michigan and Michigan State University. Michigan State University designs and establishes FRIB as a DOE Office of Science National User Facility in support of the mission of the Office of Nuclear Physics.

TABLE OF CONTENTS

CHAPTER 1 : INTRODUCTION

1.1 Background

Cryogenics is defined as processes or techniques which operate at extremely low temperatures, with a delineation proposed as temperatures below -150 degrees Celsius, or 123 Kelvin, by Scott [1]. A common application of cryogenics involves refrigeration cycles which require the absorption of heat under cryogenic conditions, *i.e.* temperatures below 123 K. Refrigeration systems generally require an operating fluid which will retain its fluidity (*i.e.* does not solidify) throughout the thermodynamic process cycle. Due to this, cryogenic refrigeration systems are required to use noble gases or reactive nonmetals with melting points well below target refrigeration temperatures. Examples of cryogenic fluids and their respective normal boiling and melting points are shown in *Figure 1.1*. An exception in refrigerants for cryogenic applications is helium, which is the only molecule that is known to exist as a liquid when approaching the temperature limit of absolute zero (*i.e.* does not have a normal melting point).

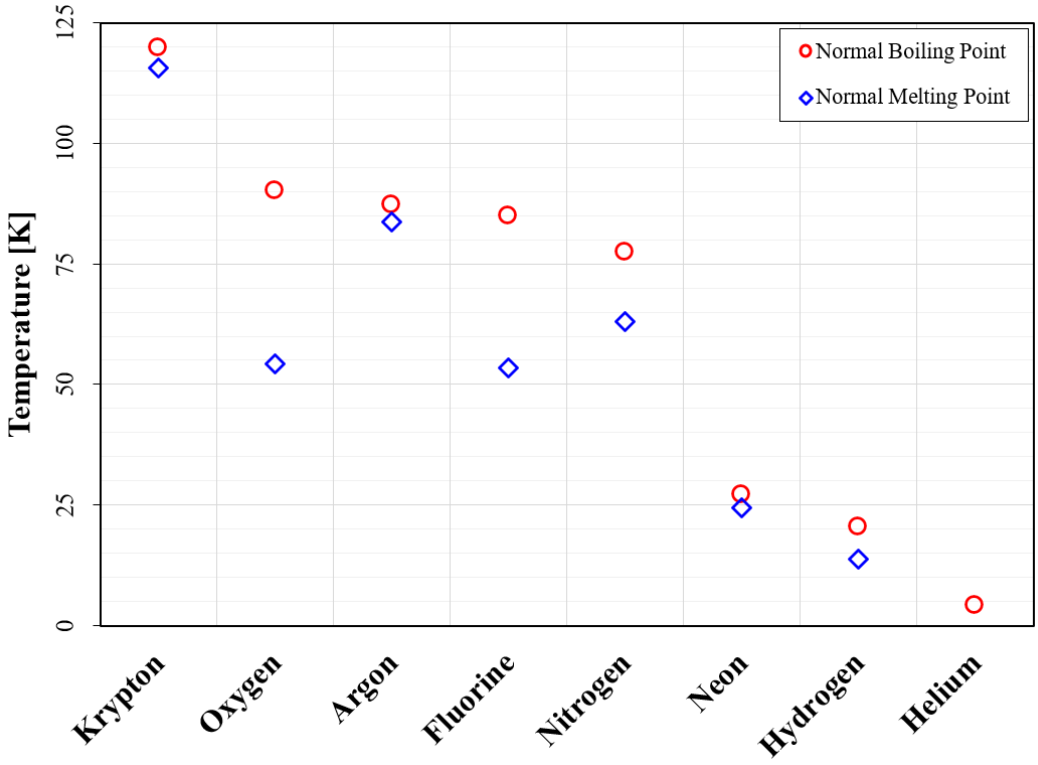

Figure 1.1: *Normal boiling point and normal melting point for various cryogenic fluids*

From *Figure 1.1*, it is observed that the only viable refrigerant for temperatures below 15 K is helium, which has a normal boiling point of approximately 4.2 K. In conjunction with helium's low temperature NBP, helium exhibits superfluid properties below a temperature of 2.1768 K (saturation pressure of 50.42 mbar). Below this temperature (known as the '*lambda point'* on the saturation curve), helium transitions from helium-I to helium-II, a quantum fluid with superfluid properties. The phase diagram for helium is provided in *Figure 1.2*, distinguishing the '*lambda line*' location and the transition from normal helium (*i.e.* helium-I) to helium-II. Properties of a quantum fluid include zero viscosity and high thermal conductivity. Near the '*lambda line'*, helium-II only contains a small fraction of the quantum-condensed state, but as the fluid gets colder this fraction increases, so that by temperatures of approximately 1 K nearly all the helium-II exhibits quantum fluid properties. Due to high thermal conductivity, a superfluid helium bath will evaporate directly from the fluid surface rather than boiling in a traditional manner within the bulk fluid, creating an advantageous environment for heat transfer from submerged components that are sensitive to external disturbances (*i.e.* boiling fluid bubbles).

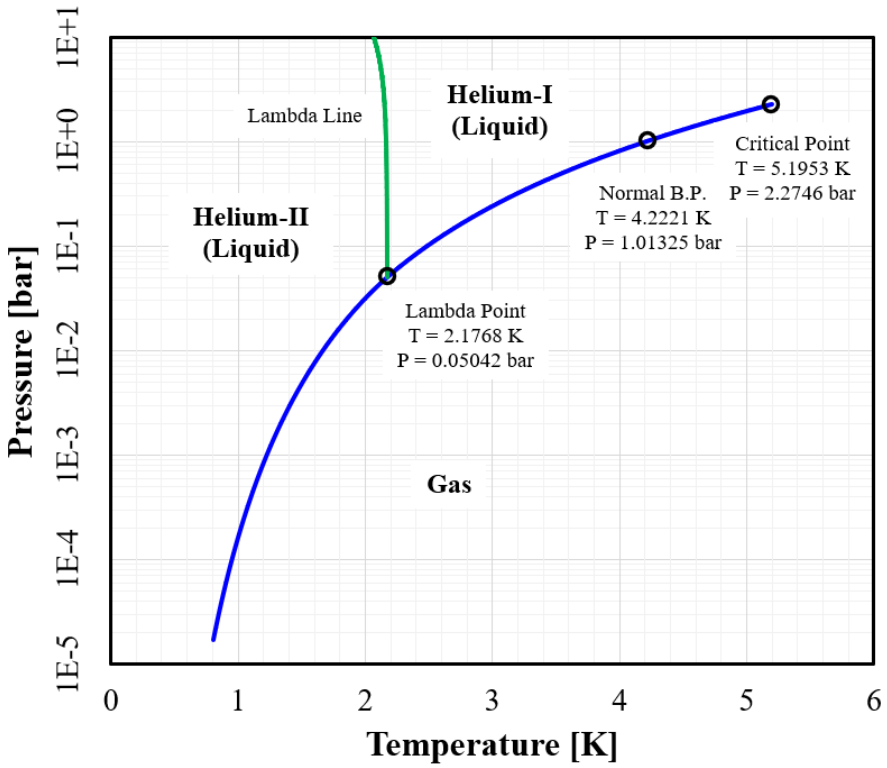

Figure 1.2: *Relationship between helium process pressure and saturation temperature*

Components that are constructed with superconducting materials often require cryogenic temperatures to retain their superconducting properties. Applications of low-temperature superconducting materials include superconducting magnetics and superconducting radio-frequency devices. Common materials used for low-temperature superconductivity include pure niobium (Nb) and niobium-titanium (Nb-Ti) alloys, which are both considered type-II superconducting materials.

Superconducting magnetics are used in magnetic resonance imaging (MRI), nuclear magnetic resonance (NMR) spectroscopy, high-energy particle accelerators, and tokamaks. MRI machines are a non-invasive medical imaging technology, which produce images using superconducting magnets submerged within cryogenic helium baths. *Figure 1.3* shows a simplified schematic of an MRI machine operating with a cryocooler to liquefy helium inside a *cryostat*, submerging the superconducting magnetic coils [2].

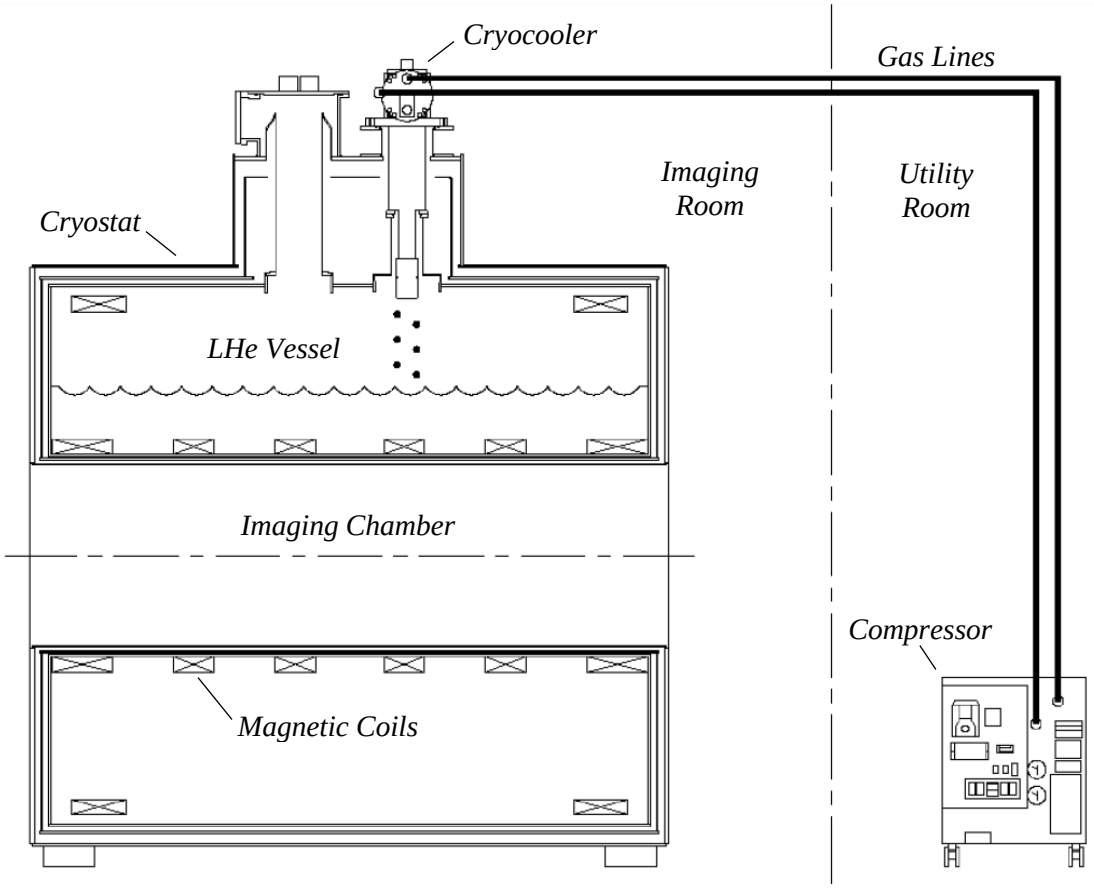

Figure 1.3: *Example cryogenic system for magnetic resonance imaging (MRI), adapted from [2]*

Modern high-energy particle accelerators require both superconducting magnets and superconducting radio-frequency (SRF) cavities, which are used for particle acceleration, guidance of the high-energy particles, and particle beam tuning. These devices are cooled using cryogenic helium at temperatures of 4.5 K or below, creating a significant margin between the critical temperature of the superconductor and the operational temperature. Examples of superconducting magnetics and superconducting radio frequency cavities used in particle acceleration systems are provided in *Figure 1.4* and *Figure 1.5*, respectively.

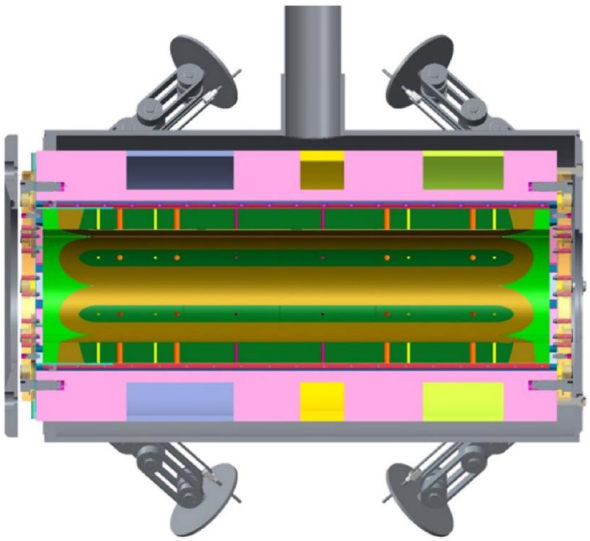

Figure 1.4: *Example of superconducting magnetic used in particle accelerator facilities [3]*

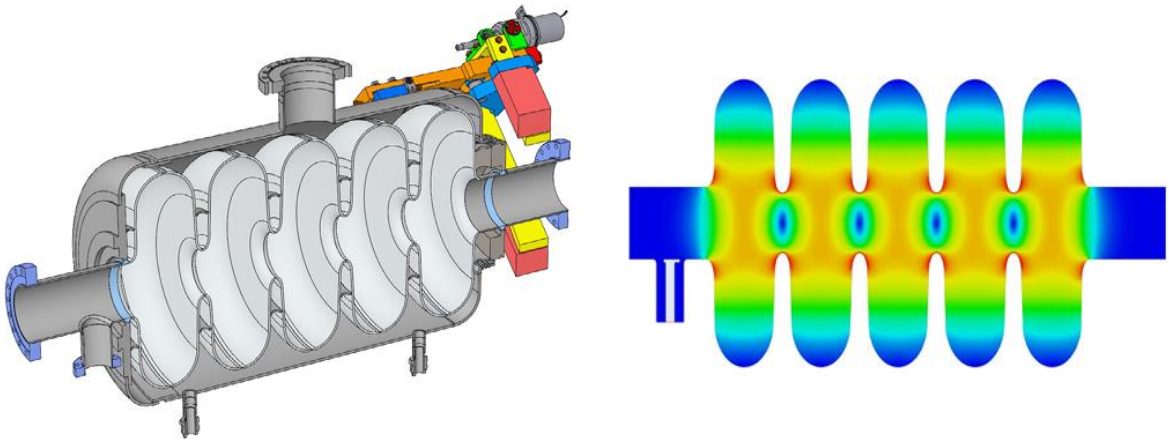

Figure 1.5: *Example of superconducting radio frequency cavity used in particle accelerator facilities [4]*

Superconducting materials exhibit ultra-low electrical resistivity in SRF cavities, which enables high quality factors (non-dimensional characterization of a resonators oscillatory underdamping, *i.e.* energy retention during oscillation). This means that the radio frequency cavities have a lower rate of energy dissipation when constructed using superconducting materials. To obtain ultra-high qualities factors, it requires further reduction of the helium bath temperature in which the SRF cavity is submerged. Radio frequency power dissipation is dependent on operational conditions, following a logarithmic relationship with respect to temperature. *Figure 1.6* shows the relationship between the residual SRF resistance and the inverse of the operational temperature, establishing that the minimum resistance can be achieved between 2 K and 1.25 K for varying material properties. Therefore, it is often advantageous to operate modern SRF cavities below helium's NBP, typically at sub-atmospheric pressures corresponding to temperatures between 1.8 to 2.1 K.

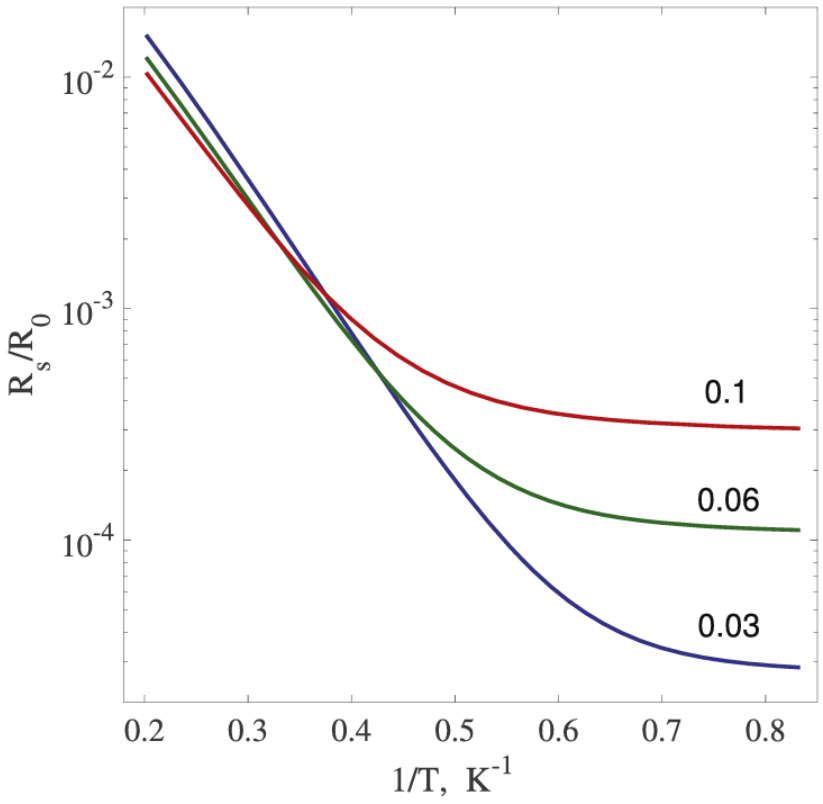

Figure 1.6: *Residual resistance of SRF cavities with different material properties [5]*

Quantum computing and low-temperature detectors require operational temperatures well below those needed for devices utilizing superconducting materials. The temperature requirement for these applications can be as low as the milli-kelvin (mK) range. A type of helium cryogenic refrigerator that can achieve this requirement is a dilution refrigerator, which exploits the mixture behavior of the He-3 isotope and the normal (He-4) isotope to produce target refrigeration temperatures. An example of the geometrical configuration of a dilution refrigerator is provided in *Figure 1.7.* A dilution refrigerator may also employ a 2 K helium cryogenic sub-system which is operated in support of the main dilution refrigeration unit, *i.e.* the pulse tube cryocooler in the example geometry.

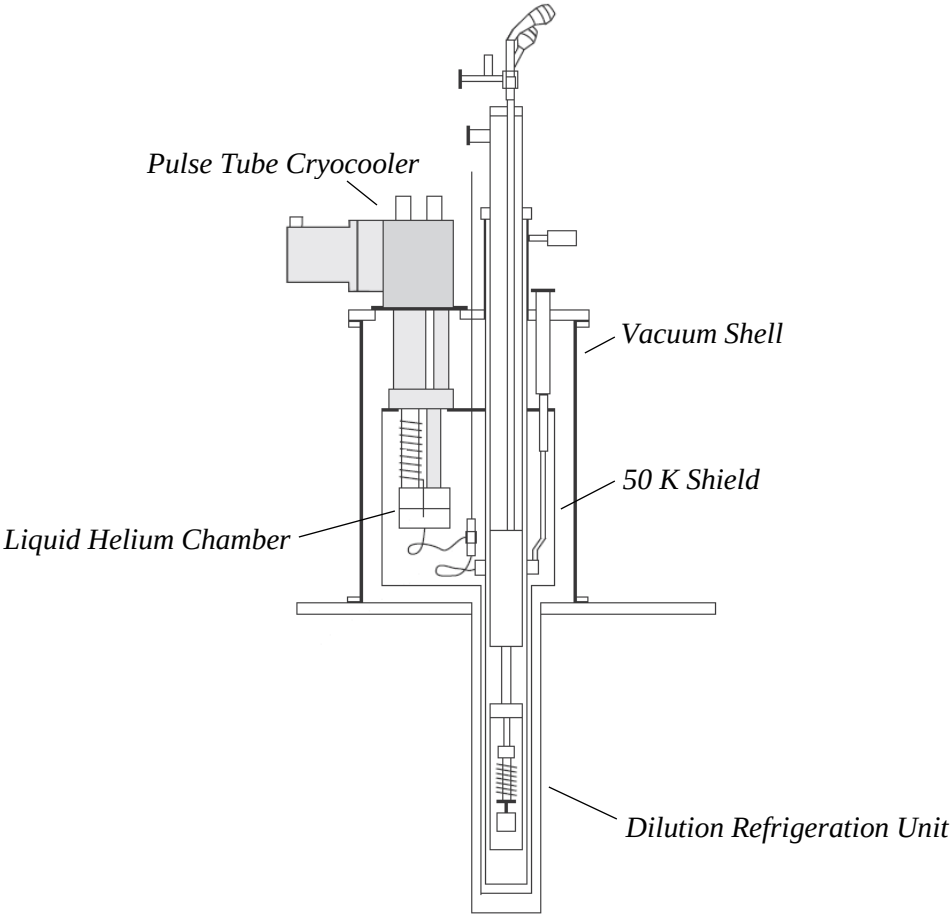

Figure 1.7: *Dilution refrigerator example geometry for ultra-low temperature applications [6]*

The discussed examples all showcase the requirement for helium cryogenic 2 K cooling technology. Two types of helium refrigeration systems are commonly employed to achieve refrigeration capabilities at temperatures below the NBP of helium. These include '*cryocoolers*' for small refrigeration capacities, and '*helium refrigerators'* for medium to large refrigeration loads.

Cryocoolers are smaller refrigeration units that can operate over a large range of cryogenic temperatures. There are numerous thermodynamic cycles which are utilized in these refrigeration systems, such as the Stirling and Gifford-McMahon cycles [7]. Typical refrigeration system types used for various refrigeration loads and load temperatures are shown in *Figure 1.8*. While each type of refrigeration cycle can be theoretically scaled for refrigeration capacities, cryocoolers with present day technology have limited cooling capacities compared to the turbo-Brayton / Claude cycle refrigeration systems. Recent developments have enabled cryocooler operation for load temperatures below 2 K, but these cryocoolers still remain limited in refrigeration power and overall efficiencies. An advantage for using cryocoolers is their reduced footprint, allowing these refrigerators to be extremely compact and portable.

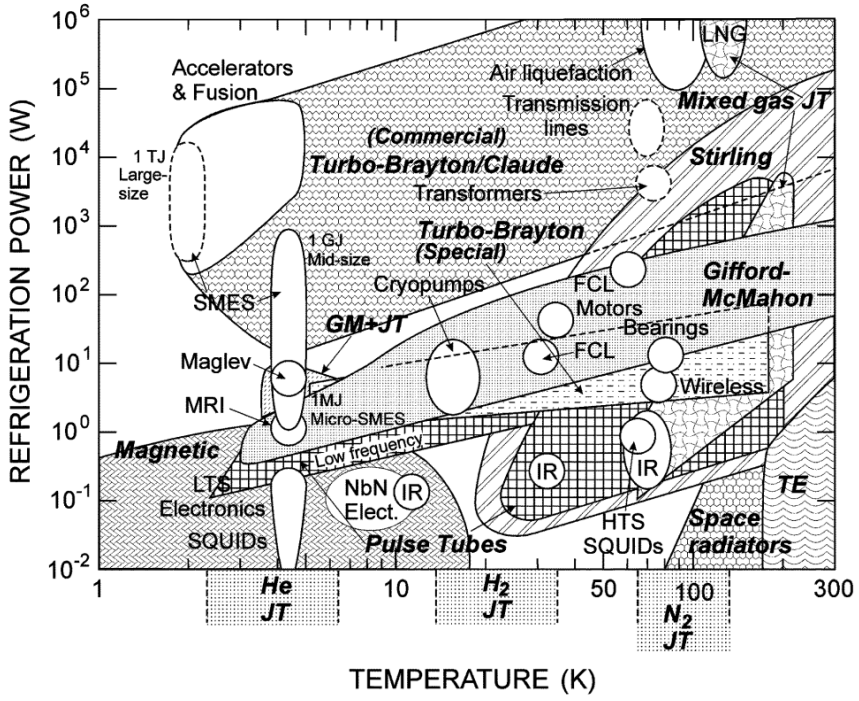

Figure 1.8: *Refrigeration load capabilities and temperature ranges for varying refrigerator types [8]*

Helium refrigerators can support medium to large scale refrigeration loads at or below temperatures of 2 K. The term '*helium refrigerator'* in this context refers to a turbo-Brayton Claude or Collins-type helium cryogenic system that can support both refrigeration and liquefaction loads and has considerably larger loading capabilities than a cryocooler. The portion of the helium refrigeration system that produces the sub-atmospheric conditions (to achieve temperatures below the fluid NBP) is the main research focus of this dissertation, and therefore supplementary details will be provided for helium refrigeration systems. Sub-atmospheric cryogenic systems require the output of a 4.5 K helium refrigerator which supplies the availability for the 2 K load. A basic understanding of the main aspects of a 4.5 K helium refrigerator is vital to the overall understanding of a sub-atmospheric system, as the supply and return of the sub-atmospheric system interacts directly with the 4.5 K system.

Generally, a 4.5 K helium refrigerator consists of two or more staged reverse-modified Brayton cycles (temperature levels) for expansion stages and a Joule-Thomson (JT) process to handle the 2-phase fluid produced at the cold end of the cycle. An ideal reverse Brayton process is a thermodynamic cycle defined as isentropic compression, isobaric heat rejection, isentropic expansion, and isobaric heat addition. The modification of this process involves isothermal compression replacing the isentropic compression. The Joule-Thomson process is defined as isothermal compression, isobaric heat rejection, isenthalpic expansion, and isobaric heat addition. Schematics for both processes are shown in *Figure 1.9*.

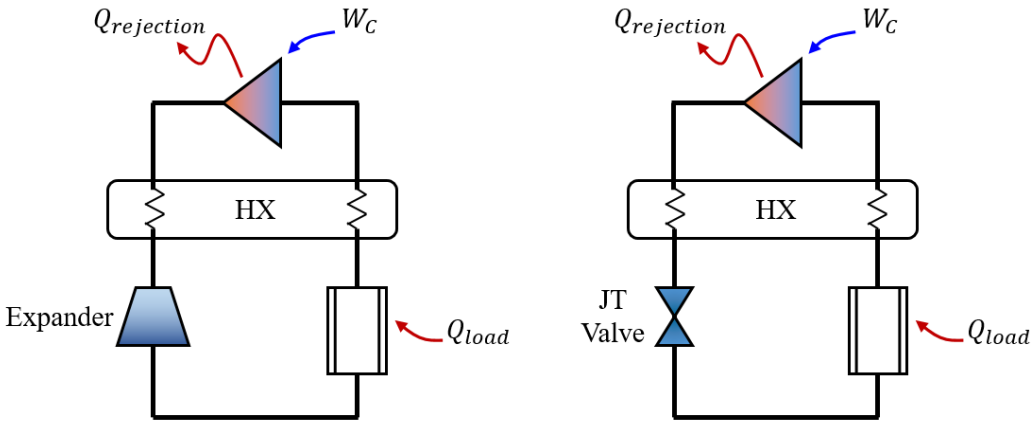

Figure 1.9: *Reverse-modified Brayton (left) and Joule-Thomson (right) process schematics*

4.5 K helium refrigeration systems combine these two processes in various ways to optimize the refrigerator and main compressor system for a required refrigeration load. The simplest combination is referred to as a Claude process, consisting of a single reverse-modified Brayton stage and a Joule-Thomson stage. Adding an additional reverse-modified Brayton stage, the refrigerator becomes a cycle known as a Collin's type helium liquefier. Schematics for these cycles are shown below in *Figure 1.10*. Advanced helium refrigeration cycles are developed using a similar methodology, but detailed description of these cycles and the nuances behind more advanced cycle selection are beyond the scope of this introduction.

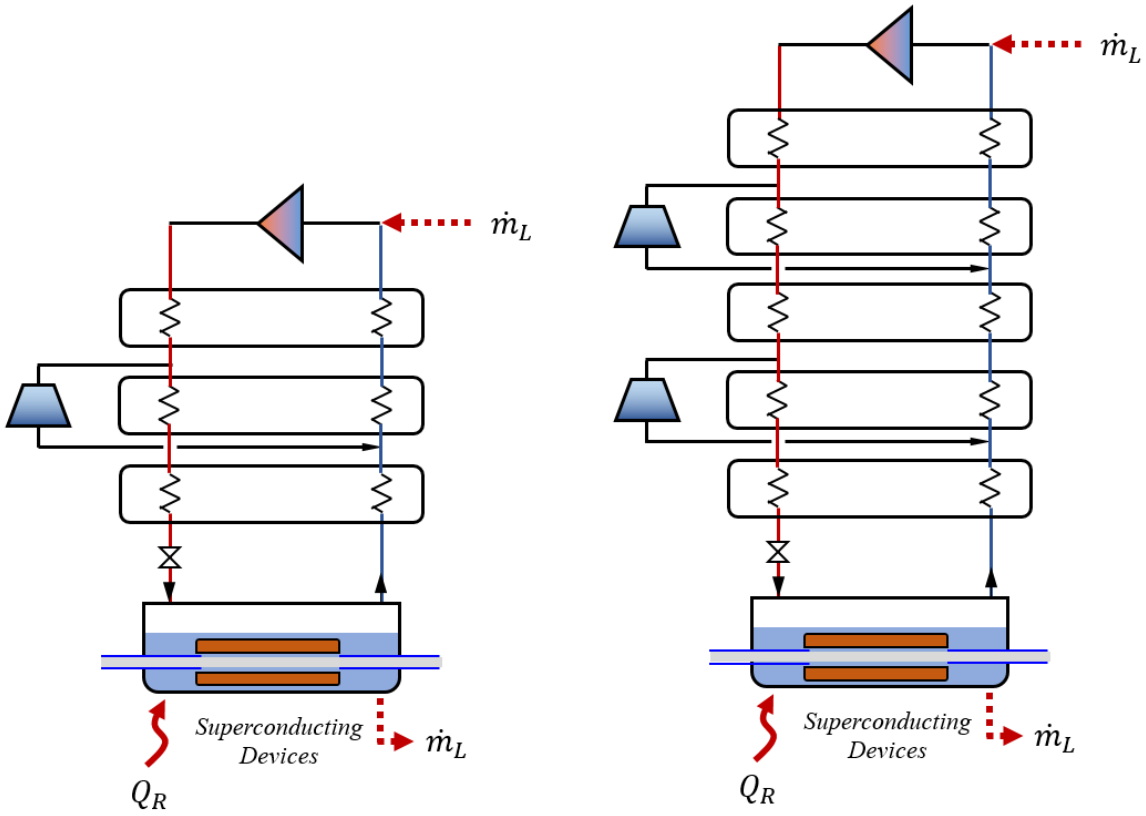

Figure 1.10: *Claude (left) and Collin's (right) helium refrigerator process diagrams*

Helium refrigeration systems contain many components that are critical to reliable operation of the cryogenic plant. A brief description of selected operational components will be provided, focusing mainly on components that are required for large-scale helium refrigeration systems.

Compression

The thermodynamic availability necessary for the required load is provided by the main compressor system. Oil-flooded rotary-screw compressors are a common choice for helium cryogenic systems due to their high reliability and compactness. Oil is injected into the compression process and provides the benefits of improved sealing, lubrication of the rotating elements/components, and heat removal from the compression process, which is considerably higher for helium as compared to normal refrigerants due to helium's high specific heat ratio. The oil injected must be removed before entering the cold box or risk damage to turbines, serious performance degradation of heat exchangers, blockage in components, and damage or destruction of load components.

Expansion

Extraction of work from the high-pressure process fluid provides cooling to the process stream supplied to the load. Typically, this is accomplished in modern refrigerators using centrifugal turbo-expanders due to their high efficiency and reliability. Such turbines are small in diameter, usually on the order of 10 millimeters, but operate at large rotational speeds in the range of 1000's of hertz. Power extracted from the turbo-expander must be recovered or dissipated to enable steady-state operation. For helium systems, a dissipative braking system is normally used, with the shaft of the turbine directly coupled to a turbo-compressor wheel which compresses a working fluid (*i.e.* helium) within a closed-system braking loop. The brake loop is comprised of the turbo-compressor, brake (or *throttling*) valve, and a heat exchanger to reject heat to the environment (cooling-water is commonly used). Depending on the whether it is designed as a fixed or variable brake, the power output is modulated with either the rotational speed or the brake valve, with the latter being significantly more efficient.

The final expansion stage of helium cryogenic systems is generally isenthalpic, expanding the high-pressure stream through a Joule-Thomson (*throttling*) valve. This expansion stage will cause the helium to '*flash*' into the 2-phase region, resulting in liquid helium. Although the ratio of helium's saturated liquid to

vapor densities at positive pressures is considerably smaller than other cryogenic fluids and two-phase helium expanders have been successfully used, this is generally avoided due to the erratic thrust and radial loading on the turbine bearings.

Heat Exchangers

Efficient heat transfer between the high-pressure supply stream and low pressure return stream is essential to efficient cryogenic plant operation. Brazed aluminum plate-fin heat exchangers are typically used in medium to larger scale cryogenic cold boxes. These heat exchangers are compact and have a large number of parallel flow paths. Important design considerations for these heat exchangers include the effect of longitudinal conduction (along the length of the heat exchanger), process stream layering sequence, and header-distributor-core pressure drop ratios to ensure proper flow distribution. Generally, around 100 NTU's are required to span from 300 K to 4.5 K for an efficient cycle design. Depending on the type of load, the effect of an overall more unbalanced or more balance stream capacity rate through the heat exchangers must be accounted for in the design process.

Liquid Storage

For process fluid (refrigerant) inventory management, a liquid helium storage vessel, usually referred to as a *dewar*, may be used. These storage vessels are vacuum insulated and are designed to limit heat in-leak and minimize the boil-off produced. Stored liquid in the phase-separator and *dewar* should be kept above a minimum level necessary for adept load and helium management.

Cryogenic helium refrigeration systems generally operate by removing heat from energized components submerged in liquid helium. The liquid helium bath is confined within a *cryostat* as a saturated liquid and is boiled off when absorbing heat energy from the load. Helium saturation properties provide a pressure constraint on the target load temperature, which can be observed in *Figure 1.2* as the logarithm of pressure relationship to the inverse of temperature. As the temperature requirement of the load is reduced, a reduction in pressure is necessary to reach the saturation condition corresponding to the load temperature.

Pressure reduction is accomplished through evacuation of vapor from the saturated liquid helium paths. The extraction of the vapor and subsequent re-injection at a higher pressure requires a compression process.

Re-pressurization of the vapor leaving the sub-atmospheric load requires a compression system which can develop large pressure ratios of 30 to 70, depending on the temperature requirement of the load (*i.e.* 2.1 K to 1.8 K). The discharge from the sub-atmospheric compression system is re-injected into the 4.5 K helium refrigerator at an appropriate temperature level or into the main compression system. Direct re-injection into the 4.5 K cold-box is essential for recovering the maximum amount of the remaining refrigeration capacity available in the returning stream, and this availability is wasted when re-injected into the main compressor system. The integrated system for 2 K operation of a helium cryogenic refrigerator involves coupling between several major systems, which include; the main compression system, 4.5 K refrigerator (4 K cold-box), distribution system, 4.5 K to 2 K heat exchanger, load (*cryostat*), and cryogenic sub-atmospheric compression system. A generalized schematic is shown in *Figure 1.11* [9].

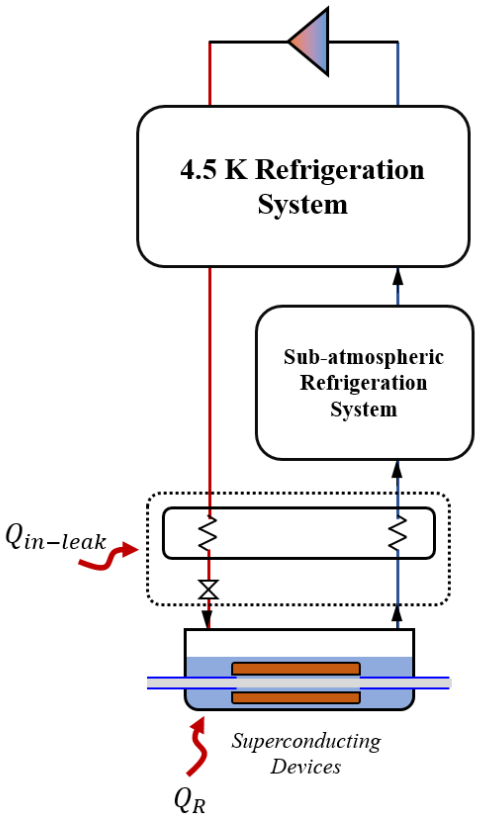

Figure 1.11: *Generalized sub-atmospheric helium cryogenic system*

Transportation of the cryogenic helium to the refrigeration load is accomplished through distribution systems. Helium cryogenic distribution systems are typically composed of single or multiple vacuum insulated process lines that traverse between the 4.5 K refrigeration system, the load, and the sub-atmospheric cold box (re-compression system). These transfer-lines require an integrated thermal-hydraulic and mechanical design effort that is often quite complex, requiring considerable attention during the design and fabrication stages. To ensure reasonable overall system efficiency, the distribution sub-system contains a heat exchanger that sub-cools the 4.5 K liquid helium supply, recovering the refrigeration from the sub-atmospheric load. In modern systems, the location of the heat exchanger may be integrated into the load(s) to ensure that the sub-atmospheric return heat in-leak is absorbed at approximately 4 K, rather than 2 K. After sub-cooling the 4.5 K supply, there is a JT expansion valve at the load where the two-phase helium is produced, creating liquid to absorb heat from the submerged superconducting device(s) resulting in helium phase change. The JT valve(s) reduce the pressure of the primary supply down to the saturation pressure corresponding to the load temperature requirement. *Figure 1.12* shows several layout options for the 2 K distribution sub-system [10], where the dashed line indicates a substantially long section of transfer line piping. Optimized configuration of this sub-system is described in detail by Knudsen [10].

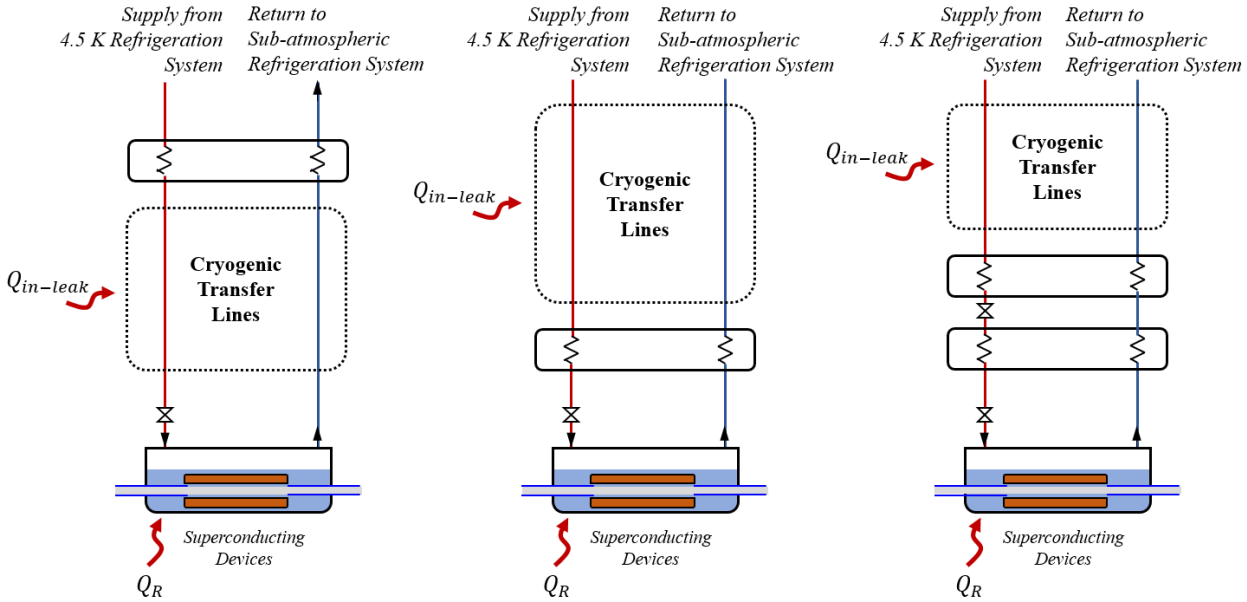

Figure 1.12: *Several Joule-Thomson expansion stage layouts*

The sub-atmospheric compression system is responsible for re-pressurizing the sub-atmospheric vapor returning from the 2 K load before injection into the main 4.5 K refrigerator. Re-compression can be accomplished using cryogenic centrifugal (*cold*) compressors, warm vacuum compressors, or a combination of these two. The former has been referred to as full *cold-compression*, the middle is known as *warm-compression*, and the latter is usually referred to as *mixed-compression*. Simplified schematics of these system basic configuration are shown in *Figure 1.13* through *Figure 1.15*. Due to sub-atmospheric operation, special design measures must be taken to address air in-leak risks, such as the implementation of a guard vacuum systems or positive pressure helium guards at connection joints and relief valves.

Cold-compression systems can support high pressure ratios (30 to 70) and require multiple centrifugal-type compressors operating in series due to single-stage pressure ratio limitations. These cryogenic centrifugal compressors are efficient, with isentropic efficiencies of approximately 75 percent or greater [11]. However, due to the Mach tip speed number and drive motor limitations, cryogenic centrifugal compression stages for helium are generally restricted to a pressure ratio of approximately three, even for colder stages. The turn-down ratio for full *cold-compression* systems can reach values of nearly 2:1 at operational conditions, but turn-down energy savings can only be realized if the coupled 4.5 K refrigeration system can also operate efficiently over the desired range [12]. Transient operation (*pump-down*) of the full *cold-compression* systems is more complex than systems using partial compression, which can be attributed to the change in inlet density and increased pressure ratio along the '*pump-down*' path that the *cold-compressors* must handle [12]. The cold-compressors must also maintain adequate margin along the surge and choke limits of the cold-compressor during '*pump-down*', while ensuring the ability of the 4.5 K system to support these transient flow parameters.

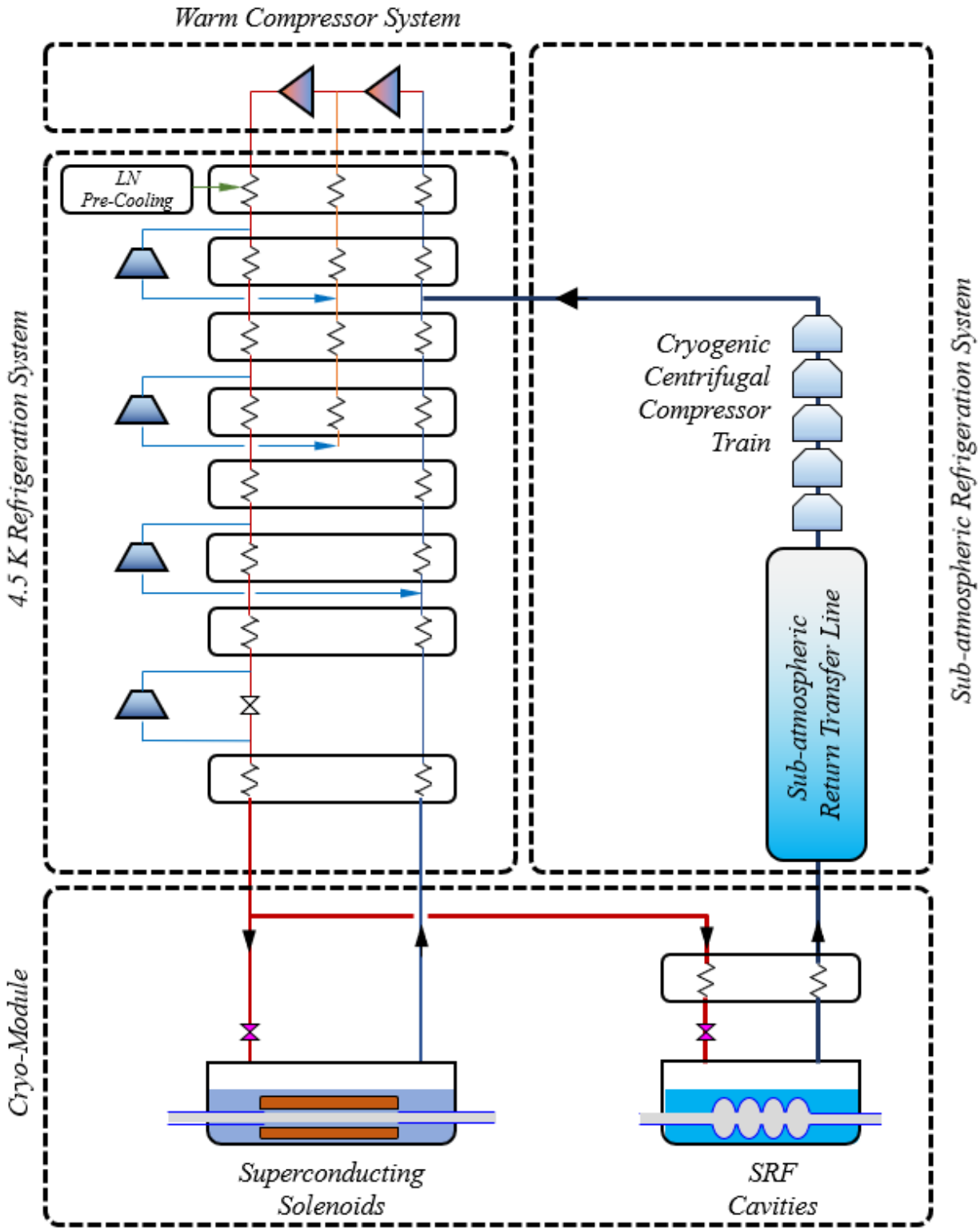

Figure 1.13: *Sample schematic for full cryogenic centrifugal compressor 2 K sub-atmospheric system.*

Note the actual number of cryogenic centrifugal compressors will vary based on the design.

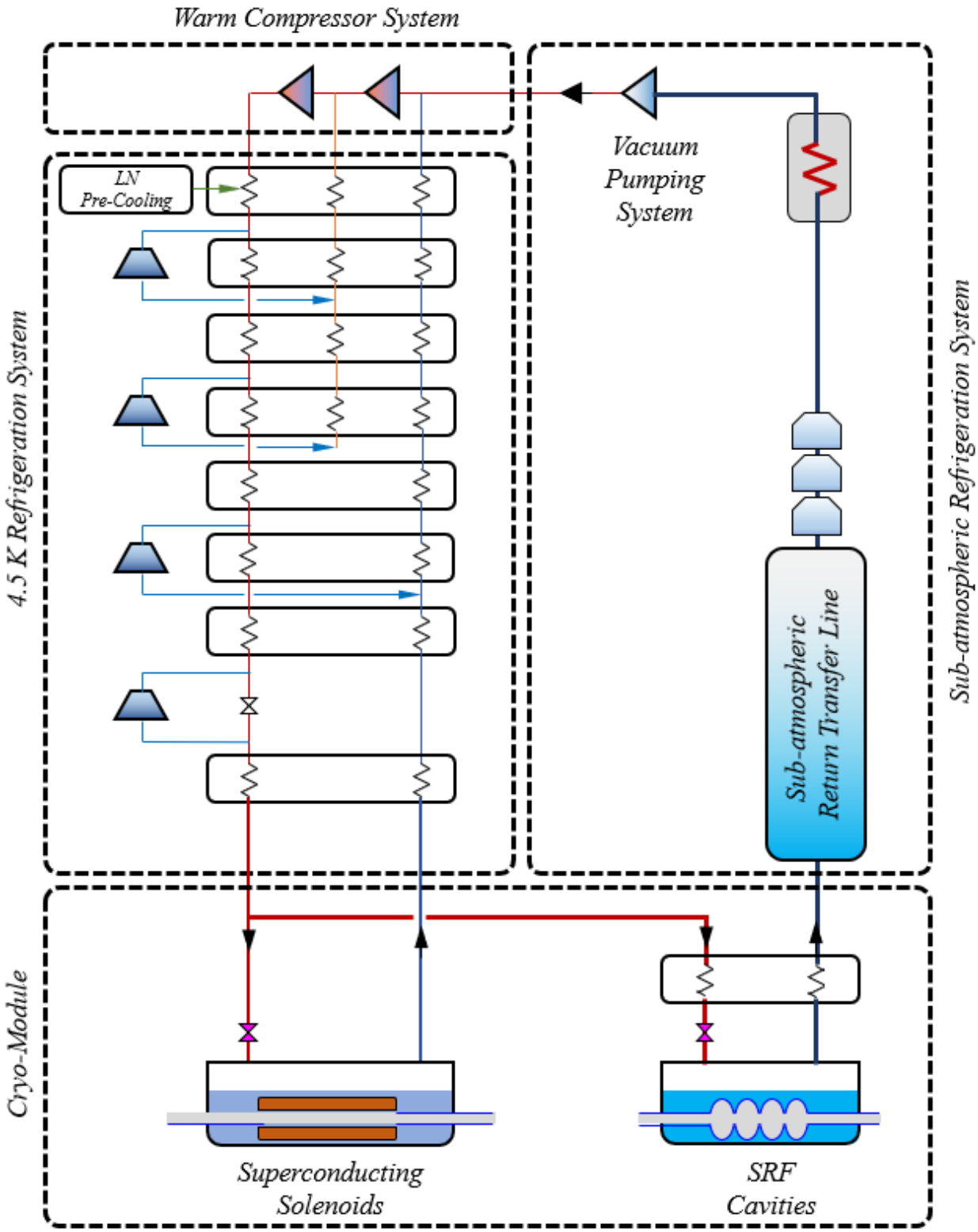

Figure 1.14: *Sample schematic for mixed compression 2 K sub-atmospheric system. Note the actual number of cryogenic centrifugal compressors will vary based on the design.*

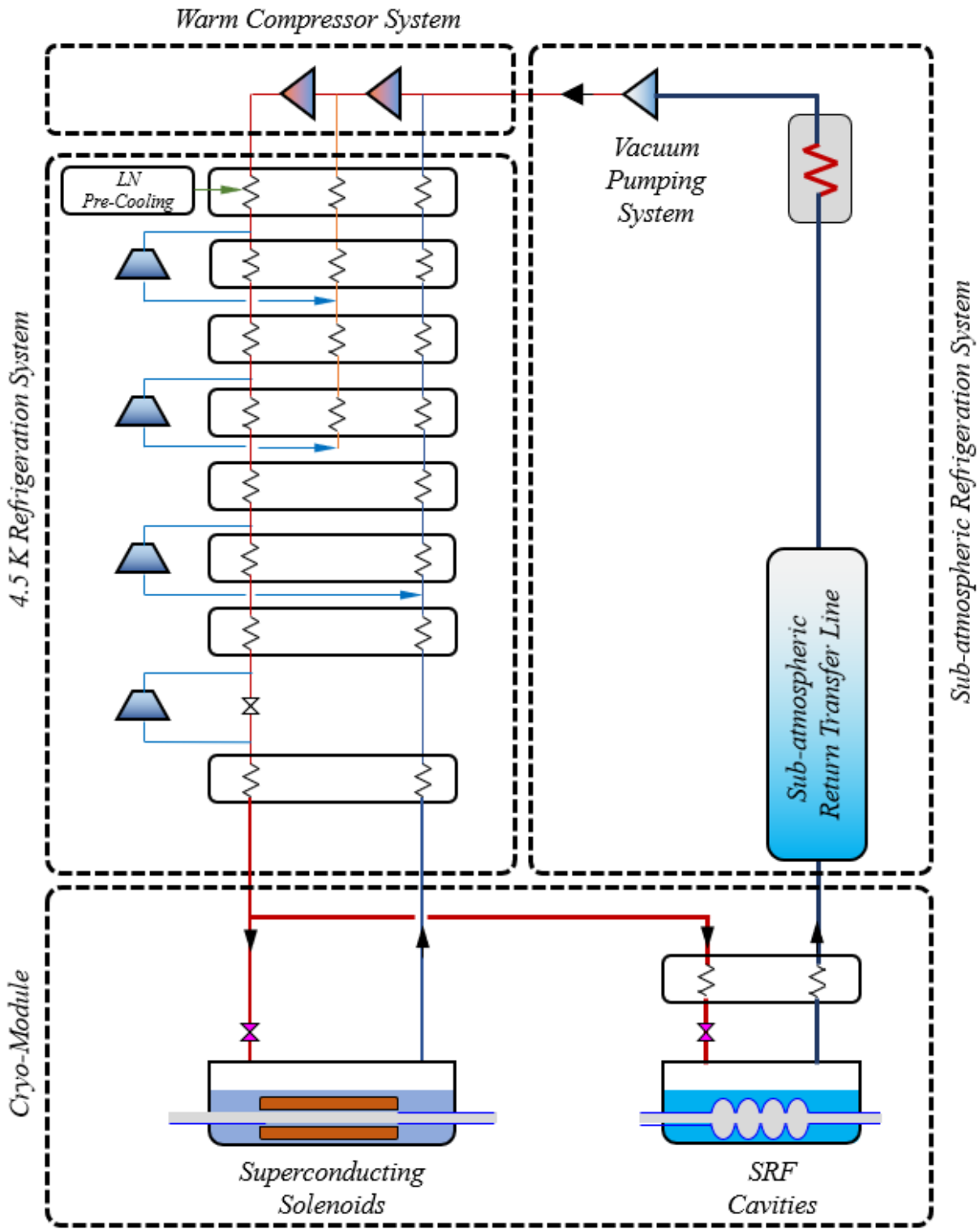

Figure 1.15: *Sample schematic for warm vacuum compression 2 K sub-atmospheric system.*

Warm compression can utilize centrifugal compressors, roots blowers, rotary-vane pumps, liquid-ring pumps, or lubricated/non-lubricated (dry) screw compressors to achieve the required pressure ratio, but operate solely on room temperature fluid (helium). *Warm-compression* systems that operate using roots blowers, rotary-vane pumps or screw compressors are stable throughout a wide range of operating conditions, increasing operational margin when pumping-down the system. Re-compression at ambient temperatures has undesired consequences, including low efficiency, high capital cost, increased equipment footprint and higher risk of air in-leak contamination from non-hermetic compressors. The former is easily understood considering the low density of the sub-atmospheric helium at ambient conditions resulting in significantly increased volumetric flow requirements. The systems usually perform with lower efficiency (compared to systems using cryogenic centrifugal compressors), as typically implemented for small loads, given economic and facility space constraints. Additionally, if oil is injected during the warm vacuum compression process, an oil removal system is needed. Recovering the refrigeration of the sub-atmospheric stream requires the use of larger heat exchangers that involve complex designs (to achieve the heat transfer with low pressure drop) and increased capital cost. Transfer lines for these systems are significantly larger to reduce the pressure drop. Re-compression at ambient temperatures increases the risk for air in-leak into the process line, due to the higher number of components (*e.g.* valves, relief vales, *etc.*) operating under sub-atmospheric conditions.

Mixed-compression systems operate using both cryogenic centrifugal compressors and warm vacuum compressors to re-compress the sub-atmospheric helium. *Mixed-compression* can provide a higher turn-down ratio and may be appropriate for small to medium 2 K system capacities. These systems are less operationally challenging to bring the system from the normal boiling point to the operating sub-atmospheric pressure, since using warm vacuum compressors reduces the pressure ratio that is handled by the cold-compressors. Drawbacks of *mixed-compression* approach stem from the same issues previously mentioned for warm vacuum compression.

Advancement in sub-atmospheric technology over the last several decades has been driven by the increased interest in superconducting radio-frequency (*SRF*) cavities, which are generally required to operate at temperatures below the normal boiling point of helium. Early sub-atmospheric systems relied on vacuum compression systems that operated at room temperature to obtain the low temperatures required for the SRF cavities. Several refrigerators with a load of approximately 300 W at 1.8 K were designed using this approach in the late 1960's, including projects at Stanford, Karlsruhe, and CERN [13-17]. The sub-atmospheric helium flow returning from the bath was warmed to near ambient temperatures using counter-flow heat exchangers (coupled to the 4.5 K refrigerator), causing the flow to become less dense and thereby increasing the volumetric flow rate for a given process mass flow. The design of highly effective heat exchangers required for efficient operation of this application is challenging, and large piping is necessary to minimize pressure drop and the size of the vacuum compressors [18, 19]. However, many modern small-capacity sub-atmospheric systems still use vacuum compressors that operate at room temperature to compress the helium back partially or fully to atmospheric conditions.

To reduce the footprint of small to medium capacity sub-atmospheric refrigeration systems, partial compression of the sub-atmospheric return flow from the refrigeration system loads (*i.e.* from SRF cavities and superconducting magnets) using single or multi-stage cryogenic centrifugal compressors has been implemented [18]. However, this does not substantially reduce the size of the refrigeration system heat exchangers handling most of the duty or reduce the risk of air in-leak issues associated with warm vacuum compressors. For large capacity sub-atmospheric refrigeration systems, the most practical approach to improve the overall system efficiency and minimize the equipment footprint, including both the refrigerator cold box size and the rotating machinery, is to use multi-stage cryogenic centrifugal compressors to fully recompress the sub-atmospheric helium returning from the load [20]. That is, to recompress the helium back to a positive pressure (1 bar, or thereabout) before being reinjected and processed by the 4.5 K refrigerator cold box. This approach minimizes the risk of air in-leak, and results in the best overall system efficiency and lowest capital investment for large systems if properly designed and integrated [12, 20-22].

The benefit of full *cold-compression* of the sub-atmospheric helium may not be explicitly obvious. On one hand, less power and much smaller equipment size can be easily visualized since the helium density is orders of magnitude lower, and the flow can be efficiently compressed using relatively small and high-speed turbomachinery. However, this process is not thermodynamically ideal for an isothermal refrigeration process, and the (*adiabatic*) heat of compression, even if it were isentropic (*i.e.* reversible), must be processed by the refrigerator cold box and ultimately the main refrigerator compression system, requiring additional power input as compared to an ideal isobaric refrigeration process. The design of full *cold-compression* (*i.e.* higher efficiency, smaller footprint, and lower capital cost) becomes challenging for low capacity systems due to reduced volumetric flow rates. Therefore, many modern small to medium scale systems are designed utilizing other methodologies than strictly full *cold-compression*.

Refrigeration plants that have adopted the full *cold-compression* approach include CEBAF at Jefferson National Lab [23], the Spallation Neutron Source [24], the 12 GeV upgrade at Jefferson Lab [25], FRIB at MSU [26], European X-Ray Free Electron Laster (XFEL) [27], and LCLS-II at SLAC [28]. Tore Supra is usually considered in the community to be the precursor to CEBAF, providing evidence that a full *cold-compression* of the sub-atmospheric helium using multi-stage cryogenic centrifugal compressor system may be a viable option [18]. However, Tore Supra did not implement full *cold-compression*, but rather used a *mixed-compression* system.

1.2 Helium Cryogenics: Design Challenges

Extremely low temperatures required for the liquefaction of helium require complex system and thus limit the maximum efficiency attainable by the cryogenic system. The Carnot efficiency clearly displays the difficulties of operation at low temperatures. In terms of the (theoretical) minimum possible inverse coefficient of performance (*COP*), approximately 70 W of input power at 4.2 K and 150 W at 2 K is required for every Watt of cooling at the respective load temperatures, as compared to a home refrigerator of 0.25 W of input power at 265 K. A large and efficient 4.5 K helium cryogenic refrigerator should be capable of an inverse COP of around 250 W/W (for the present state of the art), and a large and efficient

2.0 K helium refrigerator should be capable of an inverse *COP* of around 750 W/W (for the present state of the art). The inverse *COP's* can be much higher, and will tend to increase as the refrigerator capacity decreases [20]. Numerous system design challenges in cryogenic refrigeration stem from the objective of minimizing system losses which contribute to higher inverse *COP's*. Large helium cryogenic systems produce equivalent 4.5 K refrigeration in the multi-kW range, and therefore minor improvements in the system Carnot efficiency can yield significant reduction in electrical power input (*i.e.* operational cost).

Thermodynamic processes have natural limitations, and therefore some amount of efficiency loss is unavoidable (even more so for low temperature cryogenic systems). Heat transfer, such as heat exchange between the supply and return streams, produce losses due to the inherent irreversibility caused by finite temperature differences between the two streams. Designing these heat exchangers to provide highly effective heat transfer can reduce the associated losses, but due to the fundamental nature of heat transfer these losses cannot be fully eliminated. Undesired energy input to the system, such as heat in-leak through modes of conduction, convection, and radiation are minimized through various system designs. Vacuum insulation, low thermal conductivity component support spacers, and thermal shielding are common methods of minimizing heat in-leak into the cryogenic process fluid.

Thermal strain on process piping and components produce another challenge in cryogenic system design. At low temperatures required for accelerator operation, most materials have significantly different mechanical and thermal properties than at standard atmospheric conditions. Piping flexibility is an important design consideration to address the contraction of piping and other components when the cryogenic system is cooled down to operational temperatures. Expansion joints, flex-hoses, *U-bends*, and other piping flexibility design measures are necessary to ensure the components are within the allowable stress limits during extreme temperature variations encountered during operation.

The main warm compressors, while producing the thermodynamic availability for the refrigeration process and load, are also the single largest producer of irreversibility in cryogenic systems. Typically, the warm compressor losses account for at least half of the input power required and comprise of about two-

thirds of the exergetic losses in the overall system. Oil-flooded rotary-screw compressors can presently achieve isothermal efficiencies in the range of 55 – 65 percent at their optimal pressure ratio (which is usually around 2.5 to 3.5) [29].

Centrifugal turbo-expanders utilized in work extraction (resulting in cooling) can achieve isentropic efficiencies of approximately 85 percent [30]. Efficiencies of the turbo-expanders are generally optimized by the turbomachinery designer around a single operational point. However, the system may not operate at the design point due to differences between the design and as-built condition, changes in the load components designs, safety margins assigned, actual operations, and during transients (such as '*pump-down*' from atmospheric pressure down to the sub-atmospheric load temperature). In addition, the turbo-expander brake design has a significant influence on the efficiency of the expander. A variable brake design allows the turbine to operate at an optimal speed, whereas a fixed brake has less control to operate at optimal speed under varying process conditions, resulting in lower turbine efficiency and therefore lower system efficiency.

Cryogenic centrifugal compressor research and development has improved the overall efficiency of the centrifugal compressors utilized in the sub-atmospheric compression, increasing the isentropic efficiency from 55 percent at Tore Supra to nearly 75 percent at LHC [31]. As with turbo-expanders, although centrifugal compressors are typically designed around a single operating point, the system may not operate at the design point and will seldom operate at a single point. Turn-down of the centrifugal compressor mass flow rate is another aspect of cost savings, although this may not be fully appreciated when focused solely on the sub-atmospheric system. A gram per second reduction in mass flow processed by the sub-atmospheric system can result in a 15 – 20 kW reduction of input power at the main compressor. Therefore, while the centrifugal compressor train may not be locally operating at their peak efficiency, the overall cryogenic system operational cost savings from turning down the sub-atmospheric flow (liquefaction load) can significantly outweigh the energy cost savings of lower compressor efficiency.

For full *cold-compression*, the current areas of research interest include optimized control with minimal complexity of multi-stage cryogenic centrifugal compressors during steady-state operation and during the transient '*pump-down*' process from the normal boiling point to the sub-atmospheric load temperature (nominally, 2 K). Research interest is mainly driven by the desire for a wider range of efficient and stable operation of larger 2 K systems. This dissertation focuses both aspects of cryogenic centrifugal compressor control, including stable steady-state operation and the transient '*pump-down*' process.

1.3 Motivation

Presently, manufactures of cryogenic centrifugal compressors used for large-scale helium sub-atmospheric systems do not have the option or capabilities for full-scale experimental compressor testing. The systems which operate using cryogenic centrifugal compressors have substantial capital costs and are not economically feasible to construct for cryogenic centrifugal compressor testing. Therefore, manufacturers rely on numerical analysis rather than experimental evaluation of the compressor performance. FRIB provides a unique opportunity for experimental testing of cryogenic centrifugal compressors due to availability and accessibility of a large-scale helium cryogenic system, and the implementation of a centrifugal compressor train for the sub-atmospheric cryogenic system.

Stable, wide range steady-state operation of the multi-stage cryogenic centrifugal compressor train greatly influences the reliability of the sub-atmospheric system. The time scale associated with variance in the refrigeration load and the propagation of the variability towards to compressor train require that the centrifugal compressors operate with an appreciable margin between stable and unstable regions. Adjustment in compressor speeds is necessary to maintain a steady-state LINAC pressure, but variation in suction conditions due to cryostat controls (*e.g.* non-linearities and dead-bands in liquid level control valve and level sensor) may require speed corrections which breach the unstable region of the compressor performance map. Therefore, it is essential to develop and validate a model which can accurately estimate stable operational regions of the individual centrifugal compressors, allowing for the selection of a steady-

state region that minimizes the possibility of compressor instability when perturbations are encountered from the LINAC return flow.

As previously mentioned, a challenge for low temperature cryogenic refrigeration systems is the fundamental requirement of high inverse coefficient of performance (*COP*), or high input power. For temperatures near 2 K, a state-of-the-art large-scale cryogenic system may be able to achieve an inverse *COP* of 750 W/W, requiring 750 W of input power for every 1 W of cooling available at 2 K. When full capacity of the refrigerator is not being utilized, there are significant input power savings which can be achieved from "*turning down*" the cryogenic refrigeration system, *i.e.* reducing the cooling load. Limitations of the sub-atmospheric system contribute to the lower limit of turn-down capacity and is mostly due to the stable operating regions available for the installed centrifugal compressor geometries. Reduction in the mass flow rate processed through the sub-atmospheric system (and therefore reduction in the load) causes the centrifugal compressors to operate closer to their surge (unstable) regions. To minimize the input power requirements, centrifugal compressor modeling can be applied to estimate operational regions at reduced mass flow rates which still satisfy the reliability and stability margins throughout the multi-stage centrifugal compressor train.

If the cryogenic centrifugal compressor train approaches the unstable region of operation, there are safety precautions which will turn off, or '*trip*', operation of the compressor train to protect against possible component damage. Unplanned '*trips*' reduce the available time for accelerator user testing, and therefore it is imperative that the sub-atmospheric system resumes operation through a quick and reliable transition of the LINAC from positive pressure to 2 K steady-state sub-atmospheric pressure. The transient process of reducing this pressure is dependent on the installed system, and the '*pump-down'* time and stability is coupled to the required liquid helium levels and total system volume. Since the integration of centrifugal compressor technology into helium sub-atmospheric systems, the '*pump-down*' process has been developed mainly through empirical observations, *i.e.* trial and error techniques. While this approach has produced reliable '*pump-down*' paths, it does not provide a theoretical understanding of the process or insight into

the thermodynamic behavior of the system to make improvements or to develop a different reliable process path. Development and application of models which can estimate centrifugal compressor train stability during the transient '*pump-down*' process and the total time required for the '*pump-down*' is invaluable for minimizing '*down*' time and maximizing the reliability and stability of the transient process.

1.4 Scope

The following are the research goals of this dissertation:

1. Develop a reliable performance prediction model for a multi-stage cryogenic centrifugal compressor train and validate with measurements from an actual operating system.
2. Characterize the performance of the FRIB *cold-compressors* in a manner that allows reliable prediction of their performance using the one-dimensional centrifugal compressor model. This will require 'fitting' the model to actual test data.
3. Use the validated model to predict the operational envelope at a given (variable) operating point, *i.e.* estimate the compressor stability limits, or range between unstable stall and surge regions.
4. Using the 'fitted' and validated model, establish a dependable '*pump-down*' path for the transient process of reducing the helium bath pressure from above 1 bar to operational steady-state conditions near 30 mbar (2 K).
5. Applicability of the developed methodologies to the operation of any large-capacity helium refrigerator using full *cold-compression* sub-atmospheric system, being based on applied theory with a bare minimum of empirical relationships specific to a specific helium refrigerator.

REFERENCES

[1] R.B. Scott, U.S.A.E. Commission, Cryogenic engineering, D. Van Nostrand, 1959.

[2] T.C. Cosmus, M. Parizh, Advances in Whole-body MRI Magnets, IEEE Transactions on applied superconductivity, 21(3) (2010) 2104-2109.

[3] H. Pan, D. Arbelaez, H. Felice, A.R. Hafalia, T. Lipton, S. Myers, G. Machicoane, M. Omelayenko, S. Prestemon, E. Pozdeyev, Mechanical Study of a Superconducting 28-GHz Ion Source Magnet for FRIB, IEEE Transactions on Applied Superconductivity, 29(5) (2019) 1-6.

[4] P. Ostroumov, C. Contreras, A. Plastun, J. Rathke, T. Schultheiss, A. Taylor, J. Wei, M. Xu, T. Xu, Q. Zhao, Elliptical Superconducting RF Cavities for FRIB Energy Upgrade, Nuclear Instruments and Methods in Physics Research Section A: Accelerators, Spectrometers, Detectors and Associated Equipment, 888 (2018) 53-63.

[5] A. Gurevich, Theory of RF Superconductivity for Resonant Cavities, Superconductor Science and Technology, 30(3) (2017) 034004.

[6] K. Uhlig, Dry Dilution Refrigerator with 4-He 1-K Loop, Cryogenics, 66 (2015) 6-12.

[7] R. Radebaugh, Cryocoolers: The State of the Art and Recent Developments, Journal of Physics: Condensed Matter, 21(16) (2009) 164219.

[8] R. Radebaugh, Refrigeration for superconductors, Proceedings of the IEEE, 92(10) (2004) 1719-1734.

[9] V. Ganni, P. Knudsen, Helium Refrigeration Considerations for Cryomodule Design, AIP Conference Proceedings, 1573(1) (2014) 1814-1821.

[10] P.N. Knudsen, Testing and Analysis of an Exergetically Efficient 4 K to 2 K Helium Heat Exchanger, Old Dominion University, 2016.

[11] A. Bézaguet, P. Lebrun, L. Tavian, Performance Assessment of Industrial Prototype Cryogenic Helium Compressors for the Large Hadron Collider, (1998).

[12] P. Knudsen, V. Ganni, F. Casagrande, A. Fila, N. Hasan, M. Wright, G. Vargas, N. Joseph, Design, Fabrication, Commissioning and Testing of FRIB 2 K Cold Compressor System, in: IOP Conference Series: Materials Science and Engineering, IOP Publishing, 2020, pp. 012092.

[13] S.C. Collins, R.W. Stuart, M.H. Streeter, Closed-Cycle Refrigeration at 1.85°K, Review of Scientific Instruments, 38(11) (1967) 1654-1657.

[14] A. Sellmaier, R. Glatthaar, E. Kliem, Helium Refrigerator With Capacity of 300 W at 1.8 K, in: pp 310-14 of Proceedings of the Third International Cryogenic Engineering Conference. Guildford, Eng. Iliffe Science and Tech. Publications Ltd.(1970). Linde AG, Munich, 1970.

[15] W. Baldus, Helium-II Refrigerator for 300 W at 1.8°K, in: K.D. Timmerhaus (Ed.) Advances in Cryogenic Engineering: Proceeding of the 1970 Cryogenic Engineering Conference The University of Colorado Boulder, Colorado June 17–17, 1970, Springer US, Boston, MA, 1971, pp. 163-170.

[16] W. Daus, R. Ewald, A Refrigeration Plant With 300 W Capacity at 1.8 K, Cryogenics, 15(10) (1975) 591-598.

[17] A. Steel, S. Bruzzi, M. Clarke, A 300 W 1.8 K Refrigerator and Distribution System for the CERN Superconducting RF Particle Separator, in: Proceedings of the sixth international cryogenic engineering conference, Grenoble, 11-14 May 1976, 1976.

[18] T. Peterson, Status: Large-scale Subatmospheric Cryogenic Systems, in: Proceedings of the 1989 IEEE Particle Accelerator Conference,.'Accelerator Science and Technology, IEEE, 1989, pp. 1769-1773.

[19] P. Knudsen, V. Ganni, Process Study of Nominal 2 K Refrigeration Recovery, AIP Conference Proceedings, 985(1) (2008) 846-858.

[20] P. Knudsen, V. Ganni, Process Options for Nominal 2-K Helium Refrigeration System Designs, AIP Conference Proceedings, 1434(1) (2012) 800-813.

[21] D. Hatfield, F. Casagrande, I. Campisi, P. Gurd, M. Howell, D. Stout, H. Strong, D. Arenius, J. Creel, K. Dixon, V. Ganni, P. Knudsen, SNS Cryogenic Systems Commissioning, in: AIP Conference Proceedings, American Institute of Physics, 2006, pp. 1436-1443.

[22] P. Knudsen, V. Ganni, K. Dixon, R. Norton, J. Creel, Commissioning and Operational Results of Helium Refrigeration System at JLab for the 12GeV Upgrade, in: IOP Conference Series: Materials Science and Engineering, IOP Publishing, 2015, pp. 012125.

[23] W. Chronis, D. Arenius, D. Kashy, M. Keesee, C. Rode, The CEBAF Cryogenic System, in: Proceedings of the 1989 IEEE Particle Accelerator Conference,.'Accelerator Science and Technology, IEEE, 1989, pp. 592-594.

[24] D. Arenius, W. Chronis, J. Creel, K. Dixon, V. Ganni, P. Knudsen, Cryogenic System for the Spallation Neutron Source, AIP Conference Proceedings, 710(1) (2004) 200-207.

[25] D. Arenius, J. Creel, K. Dixon, V. Ganni, P. Knudsen, A. Sidi-Yekhlef, M. Wright, An Overview of the Planned Jefferson Lab 12GeV Helium Refrigerator Upgrade, AIP Conference Proceedings, 985(1) (2008) 588-593.

[26] F. Casagrande, V. Ganni, P. Knudsen, S. Jones, A. Sidi-Yekhlef, H. Tatsumoto, C. Nguyen, A. Fila, G. Vargas, C. Dudley, FRIB Cryogenic System Status, in: IOP Conference Series: Materials Science and Engineering, IOP Publishing, 2017, pp. 012102.

[27] Y. Bozhko, K. Escherich, K. Jensch, B. Petersen, T. Schnautz, D. Sellmann, Commissioning and First Cooldown of XFEL Linac, in: IOP Conference Series: Materials Science and Engineering, IOP Publishing, 2017, pp. 012100.

[28] R. Bhattacharya, D. Arenius, C. Kaufmann, N. Laverdure, C. Scanlon, J. Hogan, M. Bevins, Commissioning Plan for LCLS II 2 K Cold Box, in: IOP Conference Series: Materials Science and Engineering, IOP Publishing, 2020, pp. 012121.

[29] P. Knudsen, V. Ganni, K. Dixon, R. Norton, J. Creel, Performance Testing of Jefferson Lab 12 GeV Helium Screw Compressors, in: IOP Conference Series: Materials Science and Engineering, IOP Publishing, 2015, pp. 012072.

[30] P. Knudsen, V. Ganni, N. Hasan, M. Wright, F. Casagrande, G. Vargas, N. Joseph, FRIB Helium Refrigeration System Commissioning and Performance Test Results, in: IOP Conference Series: Materials Science and Engineering, IOP Publishing, 2020, pp. 012090.

[31] L. Tavian, Large Cryogenics Systems at 1.8 K, 2000.

CHAPTER 2 : REVIEW OF RELATED WORKS

Centrifugal compressors are ubiquitous in modern society, with a wide range of applications that an individual is likely to encounter on a consistent basis. This section focuses on centrifugal compressor technology used in industrial applications, with an emphasis in large-scale sub-atmospheric cryogenic systems. An overview is given for common industries that employ centrifugal compressors, and the basic components required for centrifugal compressor operation. Numerical modeling for design and performance prediction purposes is discussed, with supplementary information provided for common open-literature correlations developed and implemented to improve accuracy of centrifugal compressor performance modeling. Lastly, centrifugal compressors applications for helium cryogenic systems are presented, including examples of operating systems using this technology, such as the sub-atmospheric system commissioned at the Facility for Rare Isotope Beams (FRIB).

2.1 Centrifugal Compressors in Industrial Applications

Turbomachines are defined as rotating machinery which manipulate the state of a working fluid through the addition or subtraction of energy from the fluid stream. In contrast to positive displacement machines, turbomachines continuously interact with the process fluid stream and are capable of significant energy fluxes with moderately small component footprints. These machines have become commonplace since their introduction to industrial applications, spanning nearly every industrial sector and being integrated into many complex systems with wide ranges of size and speed requirements.

Investigation into the application of radial flow centrifugal compressors appeared as early as the 18th century, but it would not be until the early to mid-20th century that research and development increased sufficiently to establish normal operation of industrial centrifugal compressors. A detailed description of the historical development of centrifugal compressor technology is provided by Engeda [1]. Accompanying compressor research and development, numerous literature resources have been published which establish and discuss foundational equations for turbomachinery design and performance characterization.

Characterized by large single-stage pressure ratio capabilities and wide operational ranges, radial flow centrifugal compressors provide solutions for a broad range of applications. Considerable variance in centrifugal compressor geometry and rotational speed further improves their applicability across different industrial fields, with impeller diameters ranging from 10 mm to 2000 mm and operational tip-speeds of 100 m/s to 700 m/s [2]. A list of common centrifugal compressor applications are provided by Casey and Robinson [2]:

- Transportation (private and commercial)
- Power generation and energy storage
- HVAC, refrigeration and heat pumps
- Air compression and vacuum systems
- Industrial wastewater treatments
- Oil, gas and chemical industries
- Medical field

Centrifugal compressors are composed of four main components; the compressor inlet (*eye*), impeller wheel, diffuser (*i.e.* vaneless or vaned), and volute (single or multi-channel). A simplified schematic showing each of these components is provided in *Figure 2.1*. The impeller wheel is the major component where energy is transferred to the fluid in the form of fluid angular momentum imposed by the impeller blade. Momentum is then converted to static pressure gain through the remaining down-stream components, *i.e.* the diffuser and volute. Other components which may be present in the compressor assembly include inlet guide vanes, and an exit diffuser (*exit cone*) at the volute outlet.

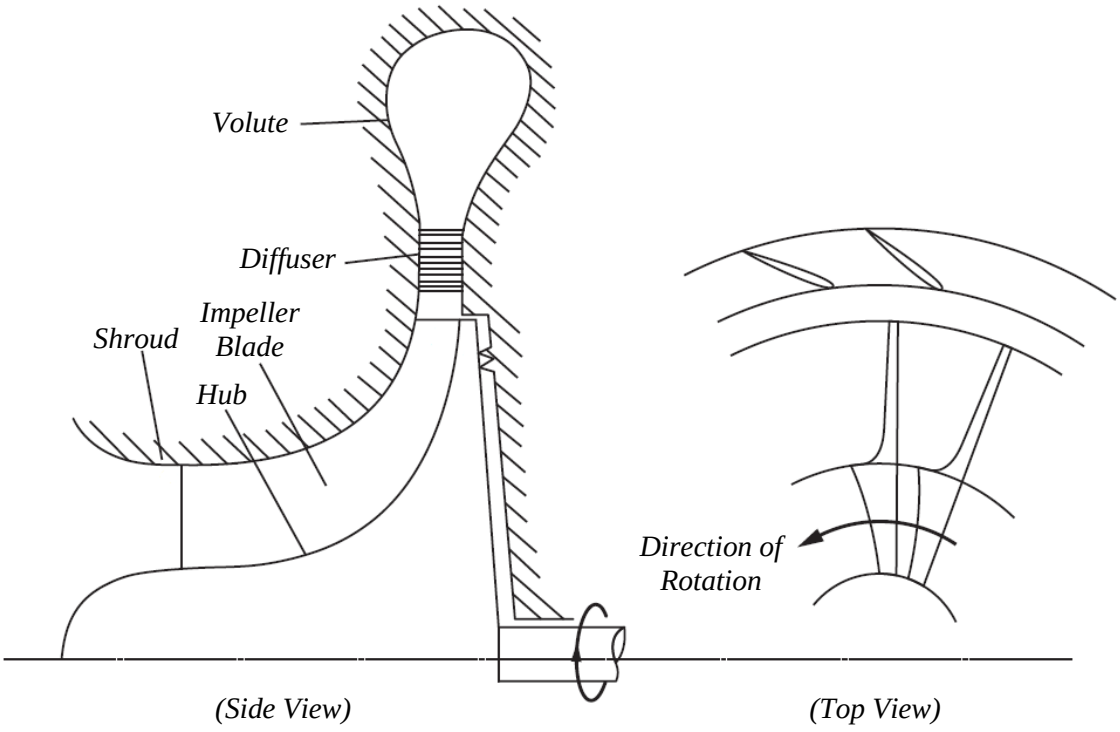

Figure 2.1: *Centrifugal compressor simplified schematic, adapted from [3]*

Centrifugal compressor impellers can take different forms depending on the operating conditions and application of the compressor. There are several distinguishing factors that are used to describe the impeller type; open or closed impeller, inclusion of splitter blades, and the total flow area width (*i.e.* two or three-dimensional blade geometries). An open or closed impeller type corresponds to whether the shroud (or *casing*) is directly fixed to the impeller blades or if there is a clearance gap present between the blade and casing. Open impellers can operate at higher rotational speed due to reduced stress on the impeller blade, increasing the maximum pressure ratio achievable, but observe a reduction in efficiency due to flow leakage through the clearance gap. Inclusion of splitter blades for a compressor design improves compressor performance while maintaining flow stability and efficiency. Splitter blades are shortened blades that often have a similar or equivalent design as the main blades, with axial lengths of approximately 50 percent of the main blades. Drawbacks of splitter blades stem from increased design and manufacturing complexity. Lastly, the flow width requirement through the impeller distinguishes between a two or three dimensional blade geometry. Flow width is characterized through a non-dimensional parameter defined as the flow

coefficient, which is a function of the mass flow rate, impeller diameter and impeller rotational speed. Depending on the value of the flow coefficient, impeller geometries can vary between fully three dimensional impeller wheels, or impeller wheels which are flat and two-dimensional. Geometrical effects of increasing flow coefficient can be observed in *Figure 2.2*.

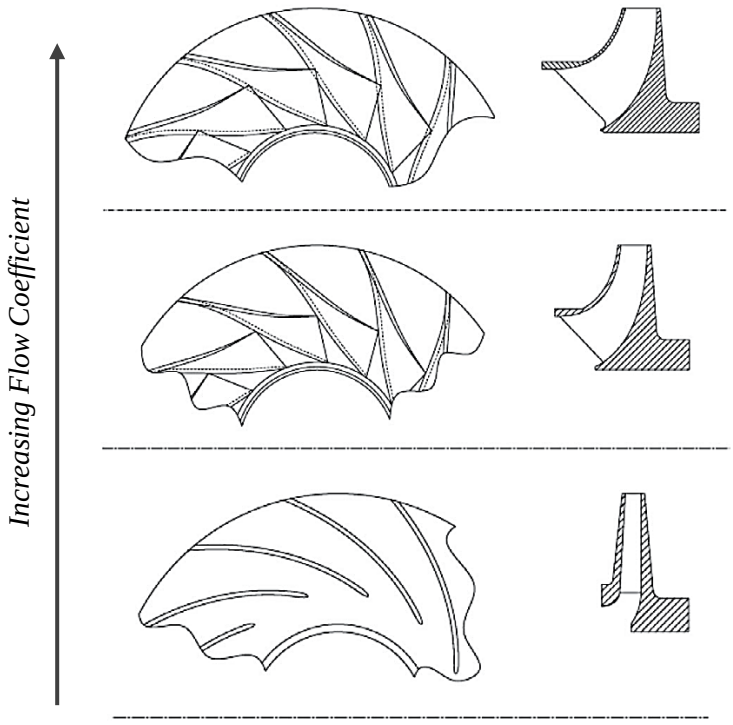

Figure 2.2: *Effect of flow coefficient on centrifugal compressor impeller geometry, adapted from [2]*

2.2 Modeling of Centrifugal Compressors

Centrifugal compressor operation involves complicated three-dimensional fluid motion that is inherently difficult to fully capture through thermodynamic analysis. Therefore, there are a variety of common modeling techniques which range from simplified mean-line numerical analysis and complex three-dimensional analysis utilizing computational fluid dynamics (*CFD*). While there is variance in accuracy between different modeling techniques, each technique can provide important information during initial design and post-design performance prediction of centrifugal compressors. Comparison of model characteristics between low complexity mean-line modeling and high-complexity three-dimensional CFD

modeling is provided in *Table 2.1*. From *Table 2.1*, it is evident that the selection of a model requires weighing advantages and disadvantages of the modeling technique. In practice, models ranging from relatively high to relatively low complexity each have important applications in centrifugal compressor design and performance estimation.

Table 2.1: *Comparison between mean-line and three-dimensional CFD model characteristics*

Characteristics	***Mean-line Model***	***Three-Dimensional CFD***
Geometric Input Requirements	Limited	Complete
Computational Time	Low	Moderate to High
Accuracy	Moderate	High
Flow Characterization	Mean Flow	Complete
Governing Equations	Theoretical/Empirical	Theoretical

During the design phase of a centrifugal compressor, it is beneficial to begin the process with a simpler mean-line impeller design model that can provide a rough estimate for component geometries and associated performance characteristics. Although there can be slight inaccuracies when predicting compressor performance through mean-line modeling, the computational complexity is considerably lower than more advanced methods. Using optimization techniques in conjunction with the mean-line model, regions which contain optimal component geometries can be quickly identified. The proposed geometry can then be loaded into three-dimensional CFD models which can give more accurate estimations of performance and further optimize the selected design. An important aspect of this design strategy is that CFD models can optimize within a poor design region, so it is critically important to explore a wide range of design geometry options with mean-line modeling prior to implementation of CFD analysis.

Performance prediction modeling also provides important information for installed centrifugal compressor operation, *i.e.* post-design compressor analysis. Estimations of performance characteristics are often established at design conditions or other pre-specified conditions by the compressor manufacturer.

Therefore, when process conditions require variation from the compressor design state, it is beneficial to characterize the compressor with predictive modeling to estimate performance (*i.e.* pressure ratio, efficiency, stability, *etc.*). Depending on the known geometrical information, accuracy required, and computational time available, either mean-line and three-dimensional CFD modeling can be employed to calculate off-design conditions.

Applications of mean-line modeling for both design and post-design analysis involves coupling between theoretical and empirically based governing equations, while three-dimensional CFD is grounded on a theoretical basis. Empirically based governing equations within the mean-line model are present in two significant performance calculations, estimation of the slip factor and efficiency (enthalpy) losses. Numerous empirical correlations have been developed to calculate these parameters, which are based on experimental measurements taken from specific impeller types, sizes and applications.

Impeller flow velocity slip is defined as the deviation of the outlet relative flow angle from the outlet blade angle. *Figure 2.3* establishes the outlet velocity triangle definition for a centrifugal compressor, where the impeller flow slip can be clearly visualized. When the outlet flow is '*perfectly guided'*, there is no deviation between the outlet flow angle and the outlet blade angle. From the principle of angular momentum, as the flow slip increases, the maximum amount of energy that can be transferred to the fluid from the impeller blade is decreased. Therefore, performance gains can be achieved through the minimization of the flow slip (*i.e.* reduction of relative flow angle deviation from the outlet impeller blade angle).

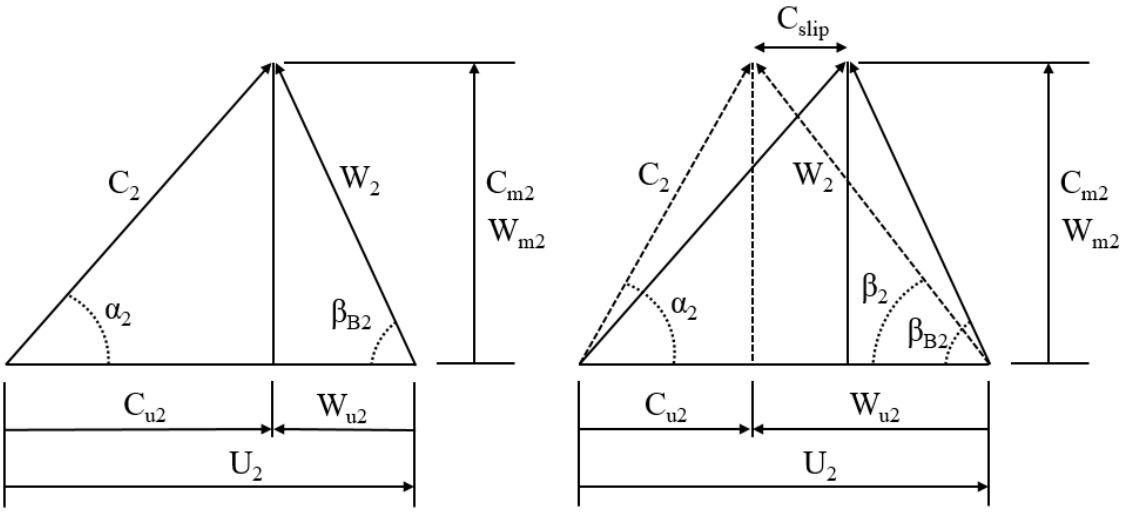

(Perfectly Guided Flow) *(Observed Flow)*

Figure 2.3: *Outlet velocity triangle diagram for a centrifugal compressor*

Flow phenomena that produce the deviation between the outlet impeller blade angle and the fluid stream flow angle is not captured through mean-line analysis. Assuming that the flow is perfectly guided results in over-prediction of the pressure ratio, requiring empirical correlations to be developed to estimate flow slip and correct for the associated performance degradation. A comprehensive investigation into centrifugal compressor slip model development and application can be found in [4]. Early development of slip model correlations focused solely on the effects of impeller geometry on flow slip, and neglected the effects of flow conditions [5-7]. Further investigation provided evidence that flow slip is inherently variable over the compressor's operating range, which lead to the development of slip correlations that incorporated flow conditions and/or impeller rotational speed [8-13]. While these correlations can provide excellent slip factor estimations over large operational ranges, they are generally adjusted through empirical constants to *tune* the correlation for specific compressor geometries and applications.

Centrifugal compressor loss correlations are imposed within the mean-line model to estimate energy dissipation that reduces compressor performance. Energy dissipation due to the loss mechanisms fall into two distinct categories; internal and external losses. Internal losses reduce total pressure gains due to entropy generation during the compression process, while external losses are parasitic losses which

consume shaft work prior to being available for fluid total pressure gains. Common energy dissipation mechanisms associated with these categories are listed below, along with supplementary discussion of available open-literature empirical loss correlations established for each type. Losses considered are listed in alphabetical order, with *a*, *b*, *c*, *d*, *e*, and *g* defined as internal losses, and *f*, *h* and *i* defined as external losses.

a. Blade loading
b. Choking
c. Clearance
d. Disk Friction
e. Incidence
f. Leakage
g. Mixing
h. Recirculation
i. *Skin Friction*

Blade loading losses are associated with phenomena within the flow boundary layer, *i.e.* the velocity gradients within the boundary layer, flow separation at the blade surface, and secondary flows. Correlations provided in open-literature are established by Aungier [14] and Coppage *et al.* [15]. Aungier's correlation is based on calculation of the average blade velocity difference, which is a function of the blade work input, impeller tip diameter, rotational speed, blade length and total number of blades. The average blade velocity difference is then adjusted through an empirical constant to obtain the enthalpy loss. Coppage *et al.* approach the estimation of blade loading losses through application of a *diffusion factor*, which has been observed to govern boundary layer growth (and therefore blade loading) along the blade length. The diffusion factor is defined as a function of the relative velocity ratio between the impeller outlet and inlet, and is derived for use in centrifugal compressor applications. The square of this diffusion factor in conjunction with an empirical constant is expressed to calculate blade loading enthalpy losses.

Choking losses account for the increased boundary layer, frictional, and flow separation losses associated with the flow Mach number approaching unity, or chocking conditions, at the impeller throat. This loss was established by Aungier [14] to capture the rapid decline in compressor performance when approaching choked operational conditions. Choking enthalpy loss is calculated through multiplication of the inlet relative flow velocity and an algebraic function of the contracted throat area and the sonic flow throat area. The contracted flow area accounts for aerodynamic blockage in the throat, and is computed

from the contraction ratio. Sonic flow throat area is defined as the area which would produce sonic flow velocity (*i.e.* Mach number of unity) under the present process conditions.

Clearance losses are associated with process flow leakage between the impeller blades and the compressor casing, exiting the high-pressure side and leaking over the blade edge to the low-pressure side. Correlations available for clearance losses in open-literature are provided by Aungier [14], Jansen [16], Krylov and Spunde [17], and Rodgers [18]. Aungier utilizes the mass flow rate fraction between clearance leakage and process mass flow rates and the pressure difference across the clearance gap to estimate the enthalpy losses. Clearance mass flow and average pressure difference through the gap of open impellers are calculated using supplementary equations provided by Aungier. Jansen's correlation is developed through pressure difference across the clearance gap using blade loading assumptions, and loss factors associated with the sudden contraction and sudden expansion processes. The application of this correlation depends on known values of the clearance gap distance between the impeller blades and the compressor shroud. Krylov and Spunde developed their clearance loss correlation based on geometrical properties of the impeller wheel. Both the ratio of the clearance gap to the outlet impeller blade height and the ratio between the inlet and outlet tip radii are utilized in their correlation, multiplied by the square of the impeller tip speed and combined with empirical constants. Likewise, Rodgers' correlation is developed from geometrical parameters but disregards the ratio between the impeller tip radii. The leading empirical constant is adjusted for this correlation, multiplied by the square of the impeller tip speed.

Disk friction losses are a result of the viscous fluid frictional forces between the rotating machinery wall and machine enclosure (casing) wall. Aungier [14], Boyce [19], Daily and Nece [20], and Shepherd [21] provide correlations in open-literature to estimate the losses due to disk friction. Correlations developed by each author involve the usage of a friction factor to estimate pressure losses as a function of the Reynolds number. Aungier recommends using the disk friction correlation developed by Daily and Nece, with a correction factor for the calculation of leakage flow. Boyce's correlation is a function of the head coefficient and several parameter ratios; the inlet shroud to hub ratio, the inlet to outlet impeller tip

ratio, inlet to outlet density ratio, and outlet relative velocity to tip speed ratio. The Daily and Nece correlation is calculated using the mass flux through the outlet, an average density through the impeller, and the cube of the impeller tip speed. Likewise, Shepherd's correlation uses the mass flux through the impeller, but uses the outlet density and a differing correlation for the Reynold's number calculation. Although the correlations all utilize a friction factor calculation, the friction factor empirical calculations deviate between the different correlations.

Incidence losses account for the flow adjustment at the inlet of the impeller due to the difference between the incoming relative flow angle and the inlet blade angle. Boundary layer growth and separation occurs at the leading edge of the impeller blade due to mismatch between the relative flow angle of attack and the blade angle, generating losses within the fluid stream. Open-literation correlations associated with incidence loss are developed by Aungier [14], Conrad et al. [22], Galvas [23], Gravdahl and Egeland [24], and Stanitz [25]. Aungier modeled the incidence loss using the difference between the predicted relative velocity at the inlet and the relative velocity associated with a perfectly guided flow. The proposed equation is then applied at the hub, shroud and mean surfaces and combined by taking a weighted average of the three calculations. Conrad *et al.* predict the incidence loss through the examination of the kinetic energy associated with the change in relative velocity between the impeller inlet location and slightly downstream of the inlet (described as the beginning of the *wake-zone* in the impeller). The energy loss is assumed to be proportional to the relative kinetic energy reduction, and is adjusted through the use of an empirical constant. Galvas proposes a similar correlation, calculating the enthalpy loss as a function of the relative velocity kinetic energy. For this correlation, the loss from incidence is calculated from the deviation between an optimum incidence angle and the actual incidence angle, and the lost relative kinetic energy is found by multiplying the mean relative velocity by a trigonometric function of this difference. The overall enthalpy loss is then calculated using the lost relative kinetic energy and adjusted using the constant pressure specific heat of the process fluid. Gravdahl and Egeland provide a correlation which follows the methodology of Aungier, where the relative kinetic energy difference between perfectly guided flow and

actual flow is determined. Using velocity triangle relationships at the inlet, the proposed correlation is a function of the inlet *RMS* blade speed, flow area, mass flow rate, and the inlet *RMS* blade angle. Stanitz's correlation is nearly equivalent to the correlation proposed by Galvas, with the sole deviation being the absence of the enthalpy loss adjustment through the application of the process fluid specific heat.

Leakage loss is associated with fluid escaping through the compressor seals from high-pressure regions to low-pressure regions. This loss is similar to clearance losses, but the leakage does not flow back into the impeller region. Clearance loss correlations developed by Aungier [14] and Jansen [16] were manipulated to allow for enthalpy loss estimations of seal leakage.

Mixing losses capture the entropy generation caused by the jet-wake flow interaction at the impeller outlet. There is an obvserved boundary between two different flow regions at the impeller outlet, namely the jet and wake flows, and these flow regions collapse and mix near the impeller outlet region. Correlations for mixing losses are proposed by Aungier [14] and Johnston and Dean [26]. Aungier's correlation involves computation of the difference between the maximum relative kinetic energy along the impeller profile and the outlet free stream fluid relative kinetic energy. Calculation of the free stream fluid relative velocity associated with the relative kinetic energy is dependent on whether flow separation is assumed to occur within the blade passage, which is established based on a diffusion factor defined by Aungier. Johnston and Dean calculate the mixing loss using the outlet kinetic energy, wake flow fraction, and the fraction between the (downstream) diffuser outlet and inlet heights. The wake flow fraction is defined as the area fraction between the wake and jet flows through the impeller outlet area, which must be calculated or estimated.

Recirculation losses are caused by the backflow of the process flow from the diffusor section back into the impeller outlet region. Recirculation becomes more prevalent as the flow angle at the exit of the impeller is increased, and this is evident through the correlations associated with this loss mechanism. Open-literature correlations available for estimating recirculation loss were developed by Aungier [14] , Coppage *et al.* [15], Jansen [16], and Oh *et al.* [27]. Aungier's developed correlation involves the equivalent diffusion ratio through the impeller, the ratio between the tangential and meridional relative flow at the

outlet, and the outlet flow angle. The function of these parameters are multiplied by the square of the impeller tip speed to calculate the enthalpy losses. Coppage *et al.* describe the potential for recirculation being directly coupled to the diffuser boundary layer that would need to develop and produce flow separation, enabling back flow into the impeller outlet. Through this assumption, the developed expression includes multiplication of the diffusion factor (as described by Coppage *et al.*), the tangent of the impeller outlet flow angle, and an empirical constant. Jansen presents a correlation as a modified form of the Coppage *et al.* loss equation, where the empirical constant is adjusted and a square root is applied to the tangent of the impeller outlet flow angle.

Skin friction losses are generated due to the interaction between the process flow and the impeller blade walls, which in continuum flow require a non-slip, or zero velocity, boundary condition. Correlations for this loss mechanism are provided in open-literature through Aungier [14], Coppage *et al.* [15], Galvas [23], and Jansen [16]. Developments by authors all estimate the skin friction losses using the average relative velocity through the impeller, the length of the impeller blade, and the mean hydraulic diameter of the blade flow passage. The function containing these parameters is multiplied by an empirical constant and an estimated friction factor to calculate the total enthalpy losses due to skin friction. Although each the correlations are similar in form, individual differences arise due to varying definitions of the mean length along the flow path, the mean relative velocity, and mean hydraulic diameter of the impeller flow passage.

Attempts have been made to choose an optimum set of loss models for centrifugal compressor performance prediction [27-33], but complete flow characterization is not feasible using mean-line modeling. Therefore, deviation is inherently present between mean-line performance prediction and experimental results, and optimization can simply minimize the calculated error between predicted performance and obtained measurements. Optimal sets of loss correlations are available in open literature, but these correlation sets should be used cautiously as they are often optimized for specific applications. When experimental data is unavailable, application of a mean-line model to predict compressor performance requires loss correlation optimization through experimental measurements gathered from a

compressor with similar geometry and process application. Empirical loss correlations can be chosen that minimize deviation from the data, and therefore can be considered reasonable for the performance analysis of a similar compressor. The accuracy of the empirical loss correlations strongly depends on the compressor type, size and application, and analysis is strongly recommended to establish an optimum sets of loss correlations when modeling centrifugal compressor performance.

2.3 Centrifugal Compressors in Cryogenic Applications

Centrifugal compressors are utilized in two different types of cryogenic helium applications, cryogenic circulators and 2 K cryogenic compression systems. Cryogenic circulators are generally single-stage centrifugal compression systems used to establish a minor pressure head which promotes fluid circulation. 2 K cryogenic compression systems employ centrifugal compressors in a multi-staged configuration, operating in series to reduce helium bath pressure and subsequently reach superfluid helium temperatures. As discussed in Chapter 1, sub-atmospheric 2 K systems can achieve target operational pressures using three different methodologies, *i.e. warm-compression, mixed-compression,* and *cold-compression*. *Cold-compression* systems solely use cryogenic centrifugal compressors to reach outlet pressures exceeding atmospheric conditions, while *mixed-compression* involves coupling between cryogenic centrifugal compressors and warm vacuum pumps (compressors).

Cryogenic circulators are generally limited to use in fusion reactors and for supercritical helium systems. The JT-60SA Super Advanced Tokamak uses cryogenic circulators to promote cryogenic fluid circulation through superconducting magnets and associated support structures [34]. Likewise, ITER has designed and commissioned cryogenic circulators for supercritical helium distribution for superconducting magnets, the toroidal field, and cryo-pumps [35]. These centrifugal compressors operate at suction pressures of approximately 5 bar, and produce a low pressure head of 0.5 to 1.5 bar. Although the gained pressure across these devices are somewhat insignificant, they promote cooling mass flow rates in the range of hundreds of grams per second.

Before the introduction of centrifugal compressors in 2 K helium cryogenic systems, the helium bath pressure reduction was achieved through the use of warm vacuum pumps. These vacuum pumps were inherently large due to the process volumetric flow rate of helium at ambient temperatures, requiring a significant equipment footprint within the main cryogenic refrigerator facility. Introduction of centrifugal compressors for 2 K operation removed reliance on warm vacuum compressors, reduced the geometrical size of other process components (heat exchangers, transfer line piping, *etc.*), and limited the risk of contamination due to sub-atmospheric operation.

A number of systems that use centrifugal compressor technology for 2 K helium cryogenic systems opted to combine the centrifugal compressors with warm vacuum compressors to achieve the total pressure ratio requirements (*i.e. mixed-compression* systems). Tore Supra is considered by many in the helium cryogenic community as the first operational 2 K sub-atmospheric system which employed cryogenic centrifugal compressors. This proof-of-concept system coupled two cryogenic centrifugal compressors operating in series with two warm vacuum pumps (oil ring pumps) to achieve design capacity requirements of 300W at 1.75 K and a maximum mass flow capacity of 40 grams per second [36]. The Large Hadron Collider at CERN also incorporated a *mixed-compression* system, achieving a refrigeration capacity of 2400W at 1.8 K and a maximum flow capacity of 126 grams per second [37-39]. Drawbacks of *mixed-compression* systems at higher mass flow requirements have shifted larger capacity systems towards the use of *cold-compression* systems, but *mixed-compression* is still utilized within smaller scale systems, such as the cryomodule test facility at Fermilab [40].

The Continuous Electron Beam Accelerator Facility (*CEBAF*) at Jefferson National Lab was the first large-scale sub-atmospheric system to adopt a *cold-compression* sub-atmospheric 2 K system [41-43]. This system used a multi-staged cryogenic centrifugal compressor train to fully compress the return helium vapor to above atmospheric conditions, allowing for re-injection of the process flow back into the main 4.5 K refrigeration system. Successful operation of this system lead to the development and application of *cold-compression* systems at other large-scale facilities which require 2 K sub-atmospheric operation. *Table 2.2*

provides information regarding large-scale 2 K sub-atmospheric systems that have been commissioned and operated solely using cryogenic centrifugal compressor systems (*i.e. cold-compression*).

Table 2.2: *Characteristics of large-scale cold-compression 2 K sub-atmospheric systems in operation*

Facility	**Commissioning Year**	**Maximum Design Flow** [g/s]	**Operating Pressure** [mbar]	**Design Pressure Ratio** [--]	**Reference**
CEBAF	1994	237	31	39	[41, 42]
CEBAF (2)	1999	250	39	31	[43]
SNS	2004	125	41	27	[44]
FRIB	2018	180	29	41	[45]
CEBAF (3)	2021	250	39	31	[46]
SLAC	2022	230	31	39	[47]

Considerations for shaft bearings and drives utilized for cryogenic centrifugal compressor systems has been reviewed to determine the optimal component selection for helium refrigerator applications. Quack [48] provides a matrix of possible bearing and drive selections, and comes to the conclusion that magnetic bearings with direct motor drives is the most feasible combination for cryogenic centrifugal compressors. The facilities previously discussed which employ cryogenic centrifugal compressor systems operate using active magnetic bearings (*AMB*) with direct motor drives. An example schematic of the cryogenic centrifugal compressor bearing and motor drive is shown in *Figure 2.4*. The direct motor drives were previously cryogenically cooled using liquid nitrogen [43], but most modern systems provide cooling for the motor drive through the use of cooling water [45]. These compressor systems require an electronic supply system for the direct motor drive and AMB, and mechanical touchdown bearings are installed to protect against possible signal or power loss from the electronic supply system.

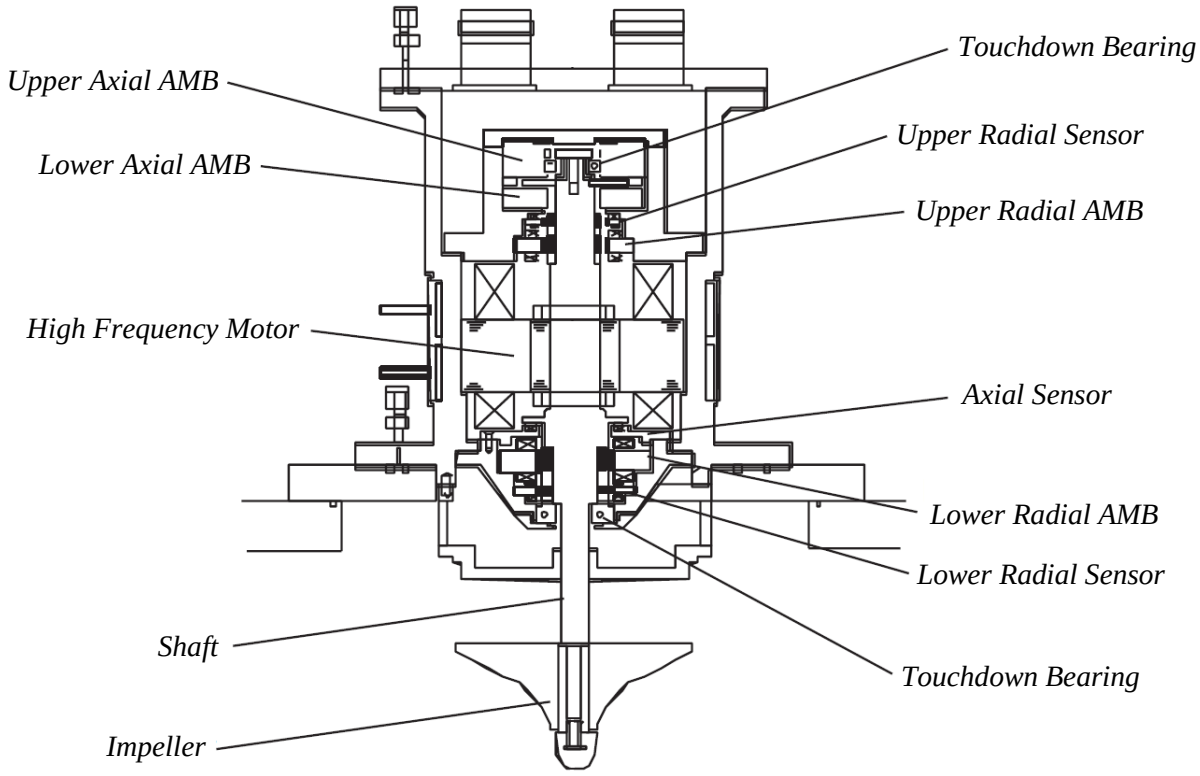

Figure 2.4: *Example schematic of a cryogenic centrifugal compressor system operating with an active magnetic bearing and direct motor drive, adapted from [49]*

2.4 FRIB Sub-atmospheric Refrigeration System

Operation of the linear accelerator (*LINAC*) at the Facility for Rare Isotope Beams (FRIB) requires temperatures of approximately 2 Kelvin (K) to support superconducting radio frequency (*SRF*) cavities. These SRF cavities are submerged in liquid helium within cryogenic housings, or *cryomodules*, which are installed along three LINAC segments (designated *LS1*, *LS2* and *LS3*). To achieve liquid helium saturation conditions corresponding to the necessary process temperature, a 2 K sub-atmospheric cold box was designed, fabricated and commissioned by the FRIB cryogenic staff. Preliminary analysis and process studies were conducted to fully specify the requirements of the sub-atmospheric system, which led to a process configuration operating with five cryogenic centrifugal compressors (*i.e. cold-compressors* or *CCs*) in series. Successful pressure reduction (*pump-down*) of the LINAC using the installed sub-atmospheric

system was achieved in December of 2018, demonstrating the capabilities of LINAC operation at process conditions of 2 K (*i.e.* saturation conditions at pressures of approximately 30 mbar).

As discussed in chapter 1, there are historically three types of compression system configurations used to achieve sub-atmospheric conditions in helium cryogenic systems, *i.e. warm-compression*, *mixed-compression* and *cold-compression*. The FRIB sub-atmospheric system employs a *cold-compression* system, defined as the capability of the cryogenic centrifugal compressor train to pressurize the returning helium vapor to positive pressure above atmospheric conditions. Suction conditions of the centrifugal compressor train range from 3.5 to 4.5 K at approximately 29 mbar. The compressor train pressurizes the helium up to 1.2 bar (with discharge temperatures of around 30 K) prior to injection back into the main 4.5 K cryogenic refrigeration system. Compressors are operated using 5-axis active magnetic bearings (AMB), which are coupled with touchdown mechanical bearings to protect the compressors in the case of AMB failure. The compressor motors are mounted externally on the sub-atmospheric cold-box, and can be removed from the compressor casing without interfering with the cold-box insulating vacuum. These motors are water cooled (*i.e.* do not require cryogenic cooling), and have guard vacuum intercepts to prevent air in-leak into the sub-atmospheric process.

Specifications for the FRIB sub-atmospheric system developed by the cryogenic staff is provided in *Table 2.3*. The process design requirements are given for three distinct operation conditions, namely the maximum, nominal, and minimum mass flow rates and corresponding suction conditions through the centrifugal compressor train. This system was designed such that any combination of the three FRIB LINAC segments can be connected, and therefore mass flow capacity can be distributed between each of the LINAC segments requiring operation at 2 K.

Table 2.3: *Process design requirements established for the FRIB sub-atmospheric system*

	CC Train	**CC1 Suction**		**CC5 Discharge**	
Capacity	*Mass Flow Rate*	*Temperature*	*Pressure*	*Temperature*	*Pressure*
	[g/s]	*[K]*	*[mbar]*	*[K]*	*[bar]*
Maximum	180	3.9	≤ 28	< 30	1.20
Nominal	120	4.2	29	< 30	1.20
Minimum	110	4.3	29	< 30	1.20

Construction of the LINAC segments were staggered to streamline the installation and commissioning process of the accelerator system. Once the first LINAC segment was installed and connected to the sub-atmospheric system, commissioning of the sub-atmospheric system was enabled through the adequate suction volume provided from *LS1*. Successful pump-down occurred on the third attempt in December of 2018, with supplementary commissioning occurring in January and February of 2019 to characterize system operation and verify process design requirements. Although the pump-down path during commissioning was established empirically, the FRIB sub-atmospheric cryogenic system has been operated with high reliability since commissioning was completed.

Commissioning and testing showed that the operation of the cryogenic centrifugal compressors was stable, and the system has a considerable operating range. The turn-down of the 2 K sub-atmospheric system was found to be nearly 2 to 1, meaning that the mass flow rate can be reduced to approximately 50 percent of the maximum achievable mass flow rate. Turn-down capabilities of the FRIB 2 K system is provided in *Figure 2.5*, and includes demonstration of operation under variable suction pressure conditions. Corresponding pressure ratios over the volumetric flow range considered during testing is shown in *Figure 2.6*.

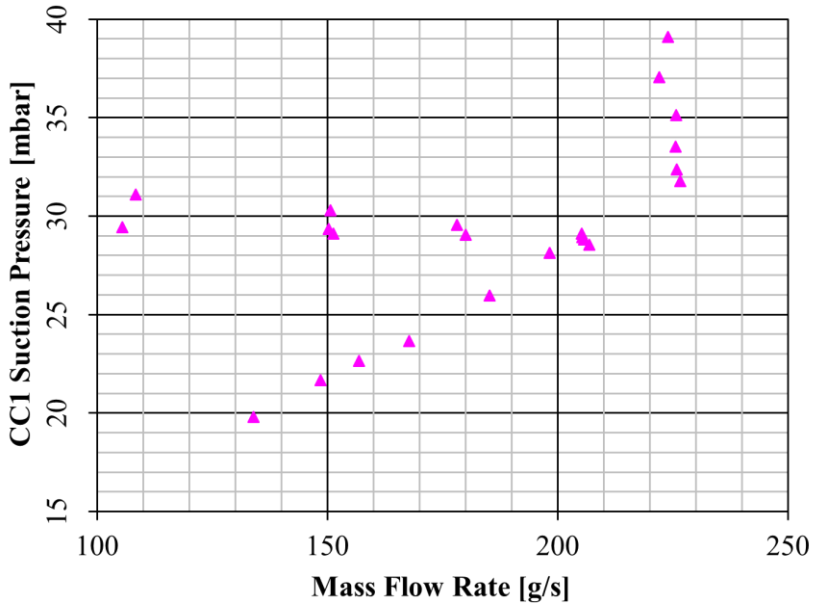

Figure 2.5: *FRIB CC train mass flow rate versus CC1 suction pressure [45]*

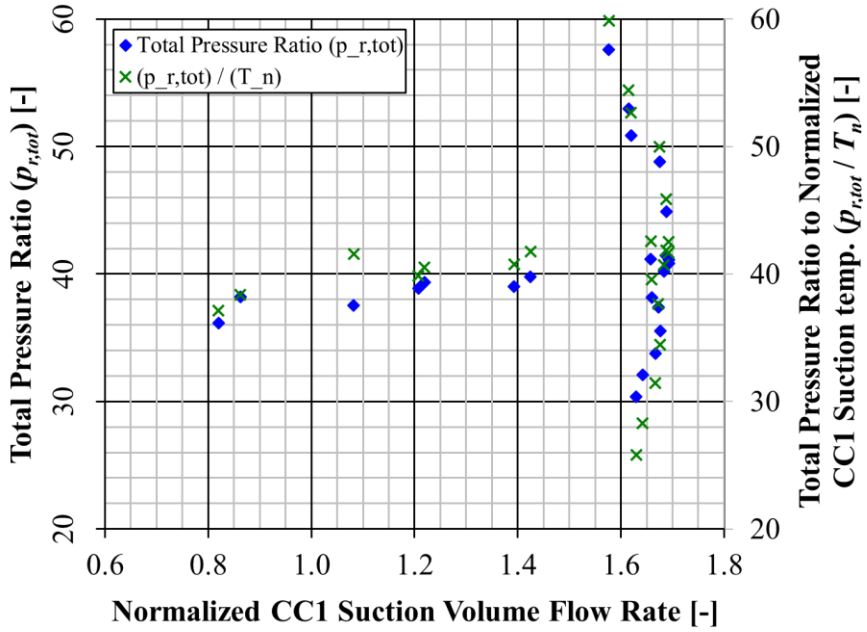

Figure 2.6: *FRIB CC1 normalized volumetric flow rate versus total pressure ratio [45]*

REFERENCES

[1] A. Engeda, From the Crystal Palace to the Pump Room, Mechanical Engineering, 121(02) (1999) 50-53.

[2] M. Casey, C. Robinson, Radial Flow Turbocompressors, Cambridge University Press, 2021.

[3] S.L. Dixon, C. Hall, Fluid Mechanics and Thermodynamics of Turbomachinery, Butterworth-Heinemann, 2013.

[4] H.M. Harrison, F. Lou, N.L. Key, Investigation of Slip Models for High-Speed Centrifugal Compressors, Journal of Propulsion and Power, 37(1) (2021) 3-12.

[5] A. Stodola, Steam and Gas Turbines, McGraw-Hill, 1927.

[6] J. Stanitz, Some Theoretical Aerodynamic Investigations of Impellers in Radial- and Mixed-flow Centrifugal Compressors, Transactions of the American Society of Mechanical Engineers, 74(4) (1952) 473-497.

[7] F. Wiesner, A Review of Slip Factors for Centrifugal Impellers, (1967).

[8] A. Whitfield, Slip Factor of a Centrifugal Compressor and its Variation with Flow Rate, Proceedings of the Institution of Mechanical Engineers, 188(1) (1974) 415-421.

[9] K. Paeng, M.K. Chung, A New Slip Factor for Centrifugal Impellers, Proceedings of the Institution of Mechanical Engineers, Part A: Journal of Power and Energy, 215(5) (2001) 645-649.

[10] T.W. von Backström, A Unified Correlation for Slip Factor in Centrifugal Impellers, (2006).

[11] A.S. Del Greco, F.R. Biagi, G. Sassanelli, V. Michelassi, A New Slip Factor Correlation for Centrifugal Impellers in a Wide Range of Flow Coefficients and Peripheral Mach Numbers, in: Turbo Expo: Power for Land, Sea, and Air, 2007, pp. 977-986.

[12] X. Qiu, D. Japikse, J. Zhao, M.R. Anderson, Analysis and Validation of a Unified Slip Factor Model for Impellers at Design and Off-design Conditions, (2011).

[13] H.M. Harrison, N.L. Key, A New Approach to Modeling Slip and Work Input for Centrifugal Compressors, Journal of Engineering for Gas Turbines and Power, 143(2) (2021) 021013.

[14] R.H. Aungier, Mean Streamline Aerodynamic Performance Analysis of Centrifugal Compressors, (1995).

[15] J. Coppage, F. Dallenbach, H. Eichenberger, G. Hlavaka, E. Knoernschild, N. Van Lee, Study of Supersonic Radial Compressors for Refrigeration and Pressurization Systems, Wright Air Development Center, 1956.

[16] W. Jansen, A Method for Calculating the Flow in a Centrifugal Impeller when Entropy Gradients are Present, Inst. Mech. Eng. Internal Aerodynamics, (1970).

[17] E. Krylov, Y.A. Spunde, About the Influence of the Clearance Between the Working Blades and Housing of a Radial Turbine on its Exponent, Physics, Engineering, 9 (1967).

[18] C. Rodgers, A Cycle Analysis Technique for Small Gas Turbines, in: Proceedings of the Institution of Mechanical Engineers, Conference Proceedings, SAGE Publications Sage UK: London, England, 1968, pp. 37-49.

[19] M.P. Boyce, New Developments in Compressor Aerodynamics, in: Proceedings of the 1st Turbomachinery Symposium, Texas A&M University. Gas Turbine Laboratories, 1972.

[20] J.W. Daily, R.E. Nece, Chamber Dimension Effects on Induced Flow and Frictional Resistance of Enclosed Rotating Disks, (1960).

[21] D.G. Shepherd, Principles of Turbomachinery, Macmillan, 1956.

[22] O. Conrad, K. Raif, M. Wessels, The Calculation of Performance Maps for Centrifugal Compressors with Vane-island Diffusers, Performance prediction of centrifugal pumps and compressors, (1979) 135-147.

[23] M.R. Galvas, Fortran Program for Predicting Off-design Performance of Centrifugal Compressors, 1973.

[24] J.T. Gravdahl, O. Egeland, Centrifugal Compressor Surge and Speed Control, IEEE Transactions on control systems technology, 7(5) (1999) 567-579.

[25] J.D. Stanitz, Effect of Blade-thickness Taper on Axial-velocity Distribution at the Leading Edge of an Entrance Rotor-blade Row with Axial Inlet, and the Influence of this Distribution on Alignment of the Rotor Blade for Zero Angle of Attack, 1953.

[26] J. Johnston, R. Dean Jr, Losses in Vaneless Diffusers of Centrifugal Compressors and Pumps: Analysis, Experiment, and Design, (1966).

[27] H.W. Oh, E.S. Yoon, M. Chung, An Optimum Set of Loss Models for Performance Prediction of Centrifugal Compressors, Proceedings of the Institution of Mechanical Engineers, Part A: Journal of Power and Energy, 211(4) (1997) 331-338.

[28] P.-Y. Li, C.-W. Gu, Y. Song, A New Optimization Method for Centrifugal Compressors Based on 1D Calculations and Analyses, Energies, 8(5) (2015) 4317-4334.

[29] E.I.G. Velásquez, Determination of a Suitable Set of Loss Models for Centrifugal Compressor Performance Prediction, Chinese Journal of Aeronautics, 30(5) (2017) 1644-1650.

[30] C. Zhang, X. Dong, X. Liu, Z. Sun, S. Wu, Q. Gao, C. Tan, A Method to Select Loss Correlations for Centrifugal Compressor Performance Prediction, Aerospace Science and Technology, 93 (2019) 105335.

[31] L. Bourabia, C.B. Abed, M. Cerdoun, S. Khalfallah, M. Deligant, S. Khelladi, T. Chettibi, Aerodynamic Preliminary Design Optimization of a Centrifugal Compressor Turbocharger Based on One-dimensional Mean-line Model, Engineering Computations, 38(9) (2021) 3438-3469.

[32] P. Kovář, A. Tater, P. Mačák, T. Vampola, Searching for the Most Suitable Loss Model Set for Subsonic Centrifugal Compressors Using an Improved Method for Off-design Performance Prediction, Energies, 14(24) (2021) 8545.

[33] X. Yang, Y. Liu, G. Zhao, Modification and Validation of 1D Loss Models for the Off-Design Performance Prediction of Centrifugal Compressors with Splitter Blades, Machines, 11(1) (2023) 118.

[34] C. Hoa, F. Bonne, P. Roussel, V. Lamaison, S. Girard, P. Fejoz, R. Goncalves, J. Vallet, J. Legrand, Y. Fabre, Performance of the JT-60SA Cryogenic System Under Pulsed Heat Loads During Acceptance Tests, in: IOP Conference Series: Materials Science and Engineering, IOP Publishing, 2017, pp. 012104.

[35] R. Bhattacharya, H. Vaghela, B. Sarkar, P. Patel, J. Das, M. Srinivasa, T. Isono, K. Kawano, Experimental Results of ITER Cold Circulators Towards the Performance Demonstration, in: IOP Conference Series: Materials Science and Engineering, IOP Publishing, 2017, pp. 012058.

[36] B. Gravil, B. Jager, Experience with a Large Scale He II Refrigeration System at Tore Supra, in: Advances in cryogenic engineering, Springer, 1998, pp. 571-579.

[37] A. Bézaguet, P. Lebrun, L. Tavian, Performance Assessment of Industrial Prototype Cryogenic Helium Compressors for the Large Hadron Collider, (1998).

[38] S. Claudet, F. Millet, B. Jäger, L. Tavian, P. Gayet, U. Wagner, P. Roussel, Specification of Eight 2400 W @ 1.8 K Refrigeration Units for the LHC, 2000.

[39] B.t. Hilbert, G.M. Gistau-Baguer, A. Caillaud, Air Liquide 1.8 K Refrigeration Units for CERN LHC Project, in: AIP Conference Proceedings, American Institute of Physics, 2002, pp. 225-231.

[40] M. White, A. Martinez, R. Bossert, A. Dalesandro, M. Geynisman, B. Hansen, A. Klebaner, J. Makara, L. Pei, D. Richardson, Cryogenic System for the Cryomodule Test Facility at Fermilab, in: AIP Conference Proceedings, American Institute of Physics, 2014, pp. 179-186.

[41] W. Chronis, D. Arenius, D. Kashy, M. Keesee, C. Rode, The CEBAF Cryogenic System, in: Proceedings of the 1989 IEEE Particle Accelerator Conference,.'Accelerator Science and Technology, IEEE, 1989, pp. 592-594.

[42] D. Arenius, W. Chronis, M. Keesee, C. Rode, Commissioning, Operation of the CEBAF 2K Refrigeration System, in: Conference: Paper compiled for Cryogenic Engineering Conference, United States, 1991, pp. Medium: ED; Size: page(s) 410.

[43] V. Ganni, D. Arenius, B. Bevins, W. Chronis, J. Creel, J. Wilson Jr, Design, Fabrication, Commissioning, and Testing of a 250 g/s, 2-K Helium Cold Compressor System, in: AIP Conference Proceedings, American Institute of Physics, 2002, pp. 288-304.

[44] D. Hatfield, F. Casagrande, I. Campisi, P. Gurd, M. Howell, D. Stout, H. Strong, D. Arenius, J. Creel, K. Dixon, V. Ganni, P. Knudsen, SNS Cryogenic Systems Commissioning, in: AIP Conference Proceedings, American Institute of Physics, 2006, pp. 1436-1443.

[45] P. Knudsen, V. Ganni, F. Casagrande, A. Fila, N. Hasan, M. Wright, G. Vargas, N. Joseph, Design, Fabrication, Commissioning and Testing of FRIB 2 K Cold Compressor System, in: IOP Conference Series: Materials Science and Engineering, IOP Publishing, 2020, pp. 012092.

[46] B. Mastracci, S. Yang, J. Creel, K. Dixon, R. Norton, S. Thompson, J. Wieliczko, T. Wijeratne, Commissioning of a Replacement Subatmospheric Cold Box for Jefferson Lab's Central Helium Liquefier, in: IOP Conference Series: Materials Science and Engineering, IOP Publishing, 2022, pp. 012069.

[47] V. Ravindranath, LCLS-II Linear Accelerator Cool-down and Pump-down, in: Cryogenic Engineering Conference, 2023.

[48] H. Quack, Cold Compression of Helium for Refrigeration Below 4 K, in: Advances in Cryogenic Engineering, Springer, 1988, pp. 647-653.

[49] H. Kameno, A. Kubo, R. Takahata, H. Ueyama, Application of Active Magnetic Bearings for Helium-Cold Compressor, KOYO Engi—neering Journal, 158 (2000) 16-20.

CHAPTER 3 : DEVELOPMENT OF A MEAN-LINE MODEL FOR CENTRIFUGAL COMPRESSORS

This chapter was previously published as [1] at the 2023 ASME TurboExpo, and has been adapted and reformatted to meet the requirements of this dissertation.

3.1 Introduction

Centrifugal compressors are commonly employed in industrial processes due to their reliable performance capabilities over a wide range of process conditions. Controlling these compressors to maximize efficiency while ensuring adequate stability margin requires performance characteristics to be known at various process conditions. Centrifugal compressors are generally procured from compressor manufacturers (*vendors*), and performance characteristics produced by the manufacturers are typically limited to specified process conditions provided by the customer.

It is necessary to characterize the compressor performance over a wide range of off-design steady-state conditions to prediction compressor behavior during transient operation. Since limited off-design performance characteristics are provided through the manufacturer, predictive algorithms have been developed which enable estimation of centrifugal compressor performance under various process conditions. Different methods for performance prediction vary in complexity, ranging from simplified mean-line algorithms to those implementing full three-dimensional computational fluid dynamic (*CFD*) analysis. Although CFD has become prominent over the last several decades, three-dimensional impeller geometries are not consistently available, and solutions require significant computational time. Therefore, mean-line methods are still proven to be valuable for the prediction of compressor characteristics with minimal required geometrical information and low computational cost.

Introduction to mean-line modelling techniques can be found in numerous centrifugal compressor references, such as Whitfield and Baines [2], Japikse [3], Aungier [4], Dixon and Hall [5], and Casey and Robinson [6]. These references describe the fluid mechanics and thermodynamics associated with

centrifugal compressors, and derive the necessary equations and relationships required for mean-line performance evaluation.

In conjunction with fundamental equations, mean-line algorithms commonly adopt empirical correlations to estimate individual losses, allowing overall compressor performance to be estimated. Numerous loss correlations are available in open literature for each individual loss parameter, described in chapter 2, and proper selection of loss correlations is critical for accurate performance prediction. Mean-line analysis models implementing these loss parameters require basic dimensions and geometry of the impeller and diffuser systems. Although the geometry requirements are significantly less substantial than those for CFD, supplementary geometrical predictive correlations may be required to account for missing parameters or dimensions needed for the analysis.

Previous investigations have been published to identify loss correlation sets which can accurately predict pressure ratio and isentropic efficiency at off-design conditions. A historically known optimized set of loss correlations are those published by Oh *et al.* [7]. Over the past decade, several other correlation sets have been proposed [8-13], each selecting a unique set of loss correlations. Although loss correlation sets are proposed, there is often an absence of information regarding the mean-line methodology and how the correlations are implemented. Repeatability of the results found in these studies can become challenging when the mean-line analysis doesn't follow the specific methodology of the original author.

The objective of this chapter is to examine the loss correlations available in open literature and recommend a set of loss correlations which provide accurate prediction of centrifugal compressor performance. Additionally, a secondary objective is to provide an accurate and robust methodology for predicting centrifugal compressor performance over a wide range of operation. Mean-line analysis and loss correlation evaluation was conducted using an in-house *MATLAB* code developed by the authors. Prediction of pressure ratio and isentropic efficiency were validated against open literature experimental data, and evaluation of the individual losses were used to suggest a set of loss correlations that accurately predicts single-stage centrifugal compressor performance.

3.2 Model Development

3.2.1 Geometry Definitions

The mean-line analysis model for centrifugal compressors calculates parameters based on station locations along the fluid flow path through the compressor. As described in *Figure 3.1*, there are three individual stations considered for the initial (validation) analysis. The first station is located at the inlet impeller leading blade edge, the second station at the outlet impeller blade trailing edge, and the third station at the outlet of the diffuser section. These stations are solved in sequential order, meaning that a converged solution of the previous stage must be completed before initiating the next stage calculation.

Calculations at each station utilizes velocity triangle relationships between the fluid velocity, blade velocity, and corresponding relative velocity. The definitions for the velocity triangles at the inlet and outlet are presented in *Figure 3.2* and *Figure 3.3*. As shown in the figures, the angles are considered to be measured from the tangential reference line for the present analysis. This definition should be strictly followed, as the derivation of many equations used in the analysis are dependent on the angle definition implemented.

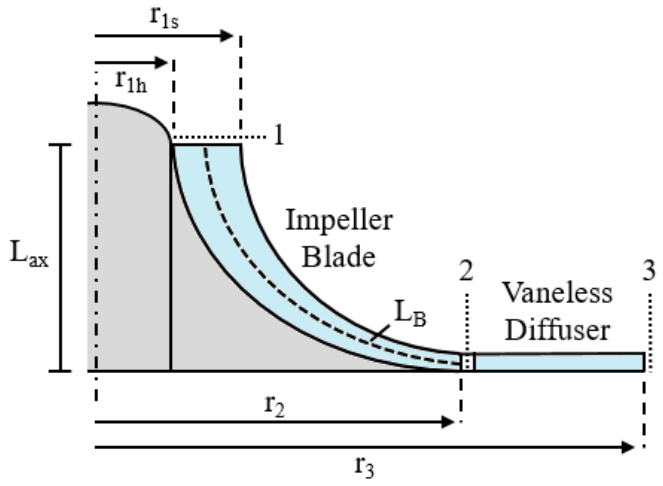

Figure 3.1: *Model geometry description and station number location*

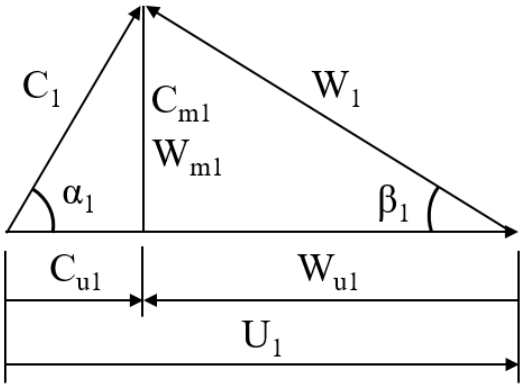

Figure 3.2: *Inlet velocity triangle definition*

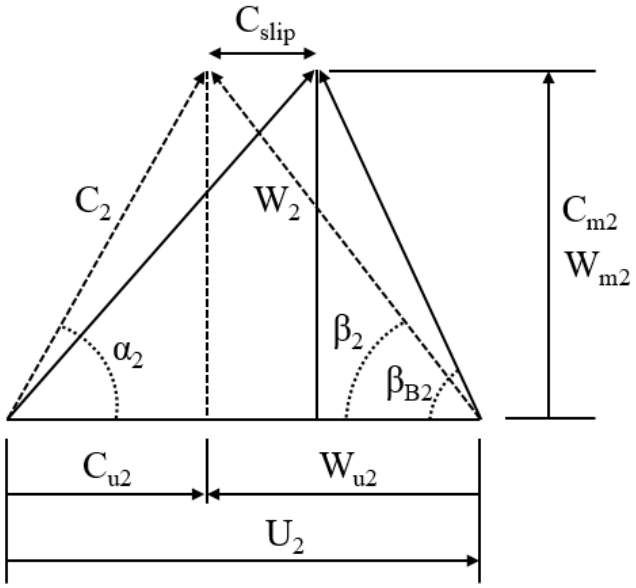

Figure 3.3: *Outlet velocity triangle definition*

3.2.2 Impeller Flow Area

To calculate the reduced inlet area of the impeller resulting from the blade blockage, a root-mean-square (*RMS*) blade angle is required. Given the blade angle at the hub and shroud of the impeller inlet, evaluating an RMS angle by interpolating between these angles was found to over-predict the actual angle. This was corrected by using velocity triangle relations to solve for the RMS angle based on the RMS radius, shroud (tip) blade angle, and the inlet pre-swirl angle at design process conditions.

Derivation of the RMS blade angle begins with the relationship between the shroud and RMS relative flow velocities, as described shown in equation (3.1) –

$$W_{m1} = tan(\beta_{B1})W_{u1} = tan(\beta_{B1s})W_{u1s} \tag{3.1}$$

Rearranging to solve for the RMS blade angle, equation (3.2) can be solved to estimate the RMS blade angle.

$$\beta_{B1} = tan^{-1}\left(\frac{tan(\beta_{B1s})W_{u1s}}{W_{u1}}\right) \tag{3.2}$$

Employing velocity triangle relationships, as described in equations (3.3) through (3.5), can simplify equation (3.2) to depend only upon the RMS radius, shroud (tip) blade angle, and the inlet pre-swirl angle.

$$C_{m1} = tan(\alpha_1)C_{u1} \tag{3.3}$$

$$U_{1s} = W_{u1s} + C_{u1} \tag{3.4}$$

$$C_{u1} = \frac{tan(\beta_{B1s})U_{1s}}{tan(\alpha_1) + tan(\beta_{B1s})} \tag{3.5}$$

Combining the developed relationships, and supplemental velocity triangle relations, the final derivation for the inlet RMS blade angle is defined through equation (3.6).

$$\beta_{B1} = tan^{-1}\left(\frac{tan(\beta_{B1s})(\omega r_{1s} - C_{u1})}{\omega r_1 - C_{u1}}\right) \tag{3.6}$$

This equation has been found to provide higher accuracy estimations for the RMS blade angle when compared to taking the RMS average of the hub and shroud blade angles. An example of the proposed correction is provided in *Figure 3.4****Error! Reference source not found.***.

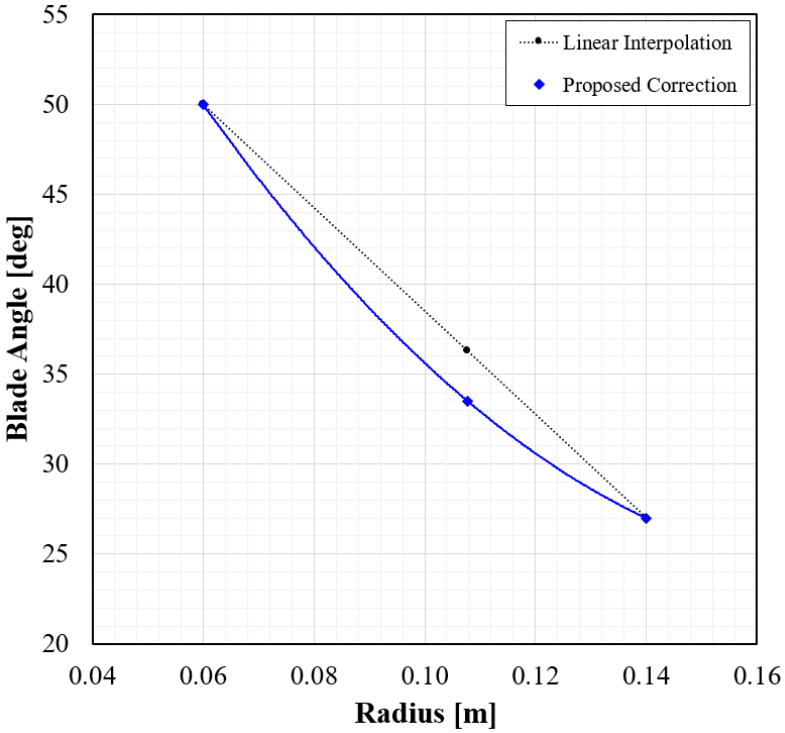

Figure 3.4: *Example application of inlet blade angle distribution across the blade height*

At the outlet of the impeller, the tip blade angle is assumed to be uniform along the height of the blade. Therefore, the tip blade angle can be used as the outlet RMS blade angle, and no further derivation or estimation is required.

In conjunction with the RMS blade angles, blade thickness at the inlet and outlet of the impeller impacts the performance prediction through the mean-line analysis. If the blade thickness is not provided with the geometry information of the impeller, a geometrical correlation may be implemented to get a reasonable estimation. Xu and Amano [14] provide data (surveyed from numerous industrial centrifugal compressors) on the relationship between blade height and blade RMS thickness. This data was used to create RMS thickness correlations for the impeller inlet and outlet, as provided in *Figure 3.5* and *Figure 3.6.* The linear curve-fit correlations created are based on the blade height in millimeters, and likewise output the RMS thickness in millimeters.

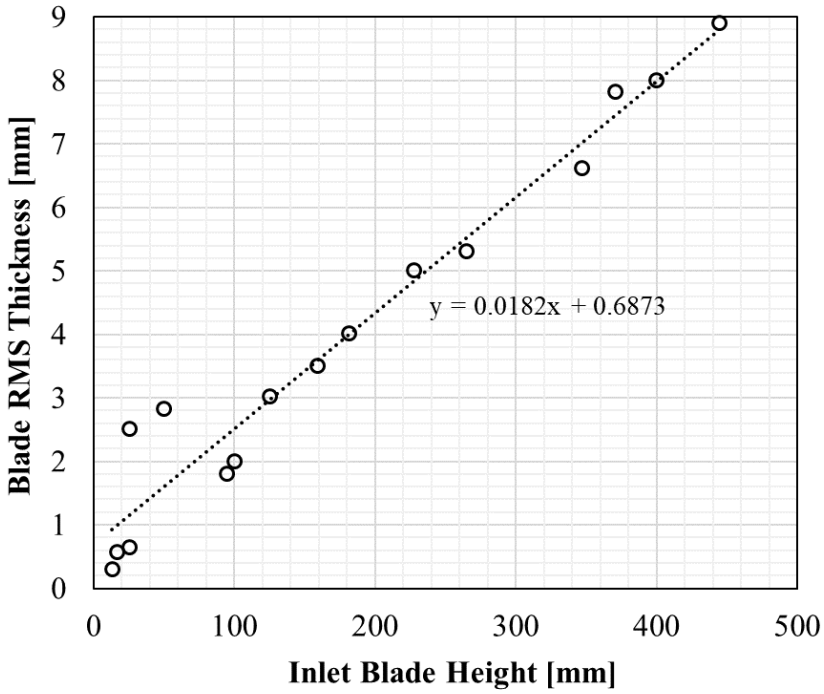

Figure 3.5: *Correlation for inlet RMS blade thickness estimation*

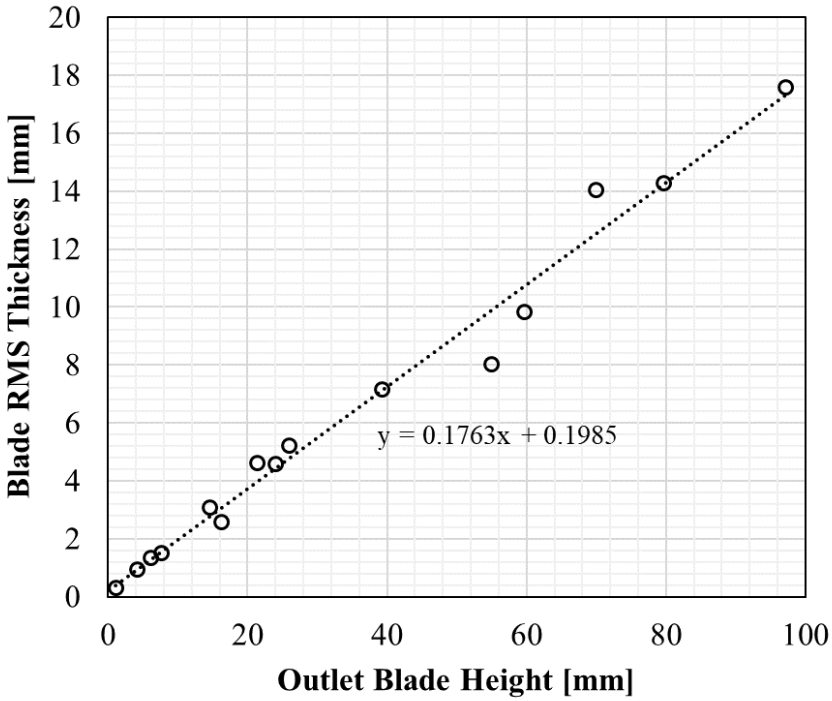

Figure 3.6: *Correlation for outlet RMS blade thickness estimation*

Variance in the impeller inlet and outlet areas can also be caused by aerodynamic blockage, namely through boundary layer growth and flow recirculation. These factors are considered when calculating the impeller inlet and outlet areas, with the blockage characterized through available correlations.

Developed by Qui et al. [15] and modified by Harley et al. [16], equation (3.7) describes the correlation used to estimate inlet flow area blockage –

$$B_1 = 1 - \frac{\dot{m}}{\rho_1 A_1 (U_1 - C_{u1})} \sqrt{\left(\frac{AR_{crit}}{sin(\beta_{B1})}\right)^2 - 1} \tag{3.7}$$

Where the critical area ratio is calculated using equation (3.8) and equation (3.9), *i.e.*

$$AR_{crit} = 160\varphi_{01}^2 - 25\varphi_{01} + 2.2 \tag{3.8}$$

$$\varphi_{01} = \frac{\dot{m}}{\rho_{01} U_2 (2r_2)^2} \tag{3.9}$$

When the value of blockage is negative, it is assumed to be equal to a value of zero. This allows for the inlet blockage to be variant based on the non-dimensional flow coefficient.

Similarly, Oh [17] provides a correlation to solve for the impeller exit aerodynamic blockage, as described in equation (3.10). This equation is a function of the area and diffusion ratio, as defined in equations (3.11) and (3.12), and the ratio of the impeller tip clearance to the outlet blade height.

$$B_2 = 0.02AR + 0.03DR^3 + \frac{c_2}{b_2} \tag{3.10}$$

$$AR = \frac{2\pi r_2 b_2 - Z b_2 t_2 / sin(\beta_{B2})}{b_1 (2\pi r_1 sin(\beta_{B2}) - (Z - S) t_1)} \tag{3.11}$$

$$DR = \frac{W_1}{W_2} \tag{3.12}$$

For each process condition considered, the blockage should be implemented in the iteration process such that the blockage will vary as the mass flow rate and rotational speed are changed. The effect of the blockage becomes increasingly prominent when approaching the surge limit of the compressor stable operational envelope.

Throat area estimation is critical in proper prediction of compressor choking conditions. Initially, the throat area was calculated using a simplified equation provided by Harley [18], as shown in equation (3.13) –

$$A_{th} = \pi\left(r_{1s}^2 - r_{1h}^2\right)sin(\beta_{1b}) - t_1(Z - S)(r_{1s} - r_{1h}) \tag{3.13}$$

It was found that this method tended to under-estimate the throat area, and therefore gave inaccurate prediction for the choking mass flow rate limit. A sub-divided area calculation approach was then adopted to account for the blade angle distribution at the throat area, as described by Hosseinpour [19]. The angle distribution was estimated using a polynomial fit calculated from the blade angles at the hub, shroud, and RMS radial locations. Using the polynomial, the throat area was then calculated by sub-dividing the area into '*n*' regions, as shown in equations (3.14) through (3.16) –

$$\Delta r = \frac{r_{1s} - r_{1h}}{n} \tag{3.14}$$

$$\Delta A_{th}(i) = \left(\frac{2\pi r_1(i)}{(Z - S)} - t_1\right) \cdot sin\beta_{1b}(i) \cdot \Delta r \tag{3.15}$$

$$A_{th} = (Z - S)\sum_{i=1}^{n} \Delta A_{th}(i) \tag{3.16}$$

3.2.3 Impeller Length Estimation

The axial length of an impeller may need to be estimated based on geometrical information available for the specific impeller of interest. There are several correlations available in open-literature that are commonly utilized to estimate the impeller axial length. A correlation developed by Birdi [20] is provided in equation (3.17), which is a function of the inlet relative Mach number and impeller radii.

$$L_{ax} = 2r_2\sqrt{0.28(M_{w1s} + 0.8)(1 - r_1/r_2)\left(\frac{r_{1s} - r_{1h}}{r_2}\right)} \tag{3.17}$$

A similar correlation is proposed by Aungier [16], as described in equation (3.18) –

$$L_{ax} = 2r_2\left(0.014 + 0.023\frac{r_2}{r_{1h}} + 1.58\frac{\dot{m}}{U_2(2r_2)^2}\right) \tag{3.18}$$

Each correlation gives reasonable estimations for the axial length of a centrifugal compressor impeller.

Along with the axial length of the impeller, a standard geometrical parameter that is often required for analysis is the mean-line blade length. This parameter can be estimated through equation (3.19), based on the suggested correlation developed by Jansen [21].

$$L_B = \frac{\pi}{4}\frac{(2r_2 - (r_{1s} + r_{1h}) - b_2 + 2L_{ax})}{\left(sin(\beta_{B1}) + sin(\beta_{B2})\right)} \tag{3.19}$$

An important aspect of these equations is that they should be implemented at a single process condition. These parameters should not be variant when performing a mass flow sweep to produce an impeller performance curve, as they are constant geometrical characteristics of the impeller. It is suggested that these correlations be implemented at the compressor design condition, and are subsequently held constant throughout the calculations for performance prediciton analysis.

3.2.4 Performance Analysis Methodology

Performance analysis developed for the present study follows the flow diagram shown in *Figure 3.7*. Inputting the geometrical and design paramters, flow area and impeller lengths are calculated. Specifying the rotational speed, and therefore the blade speed, an estimation for the surge limit mass flow rate is calculated. Mean parameter values are calculated at the impeller inlet, impeller outlet, and vaneless diffuser outlet as the mass flow rate is swept towards the choking limit. Once the choke limit is reached, a new rotational speed is selected and the process continues until all rotational speeds of interest are imposed. The results are tabulated within MATLAB, and subsequently plotted and exported once the analysis is complete.

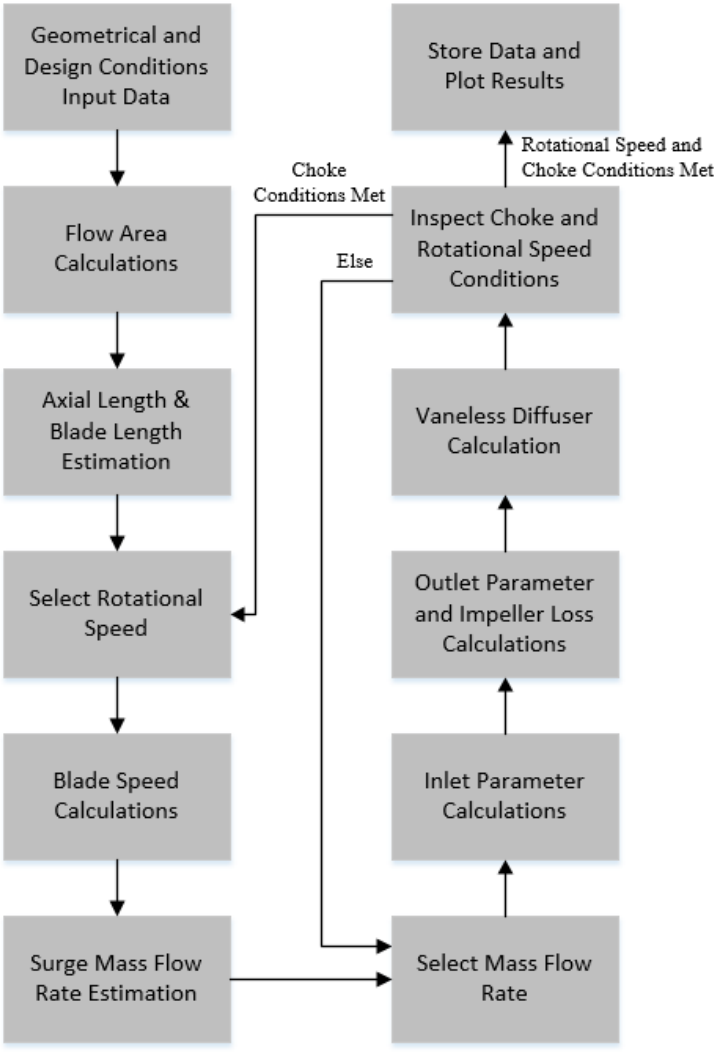

Figure 3.7: *Flow diagram for centrifugal compressor performance analysis*

Estimation of the surge limit mass flow rate follows the suggestion from Aungier [22] that the surge criteria is a function of the relative flow velocity at the inlet tip and the throat. Taking the ratio of these two parameters, the surge criteria is estimated through manipulation of the constant within equation (3.20).

$$\frac{W_{1s}}{W_{th}} = constant = c \tag{3.20}$$

Implementing velocity triangle relationships, *i.e.* equations (3.21) and (3.22), a second order polynomial is derived which can be solved iteratively to determine the corresponding surge limit mass flow rate. The final form, equation (3.23), is numerically solved using a MATLAB root finding function.

$$W_{1s} = \sqrt{(U_{1s} - C_{u1})^2 + C_{m1}^2} \tag{3.21}$$

$$W_{th} = tan(\beta_{B1}) \frac{\dot{m}}{\rho_1 A_{th}} \tag{3.22}$$

$$a_1 \dot{m}^2 + a_2 \dot{m} + a_3 = 0 \tag{3.23}$$

Where parameters a_1, a_2, and a_3 are defined as equations (3.24) through (3.26) –

$$a_1 = \left(\frac{ctan(\beta_{B1})}{\rho_1 A_{th}}\right)^2 - \left(\frac{1}{\rho_1 A_1}\right)^2 - \left(\frac{1}{\rho_1 A_1 tan(\alpha_1)}\right)^2 \tag{3.24}$$

$$a_2 = \frac{2\omega r_{1s}}{\rho_1 A_1 tan(\alpha_1)} \tag{3.25}$$

$$a_3 = -(\omega r_{1s})^2 \tag{3.26}$$

An estimation for the choked mass flow rate is calculated using the relationship provided by Dixon and Hall [5]. Equation (3.27) describes the relationship used to solve for a maximum mass flow rate,

showing that the choked mass flow is a function of the throat area and the rotational speed (*i.e.* inlet blade speed) –

$$\dot{m}_{ch} = A_{th}\rho_{01}a_{01}\left(\frac{2+(\gamma-1)\,U_1^2/a_{01}^2}{\gamma+1}\right)^{(\gamma+1)/2(\gamma-1)} \tag{3.27}$$

As noted by Harley et al. [18], this estimation for the choking mass flow rate tends to over-predict at lower rotational speeds. The calculated efficiency can be utilized at lower speeds to calculate choking mass flow rates more accurately.

Inlet and outlet parameter calculations were derived using fundamental governing equations and thermodynamic relations. Inlet calculations were based on a density iterative method, which was initialized through an assumption that the static density was eqivalent to the stagnation density. Equations (3.28) through (3.33) were then iteratively solved until the deviation in calculated static density fell below a specified tolerance value.

$$C_{m1} = \dot{m}/(\rho_1 A_1) \tag{3.28}$$

$$C_{u1} = C_{m1}/tan(\alpha_1) \tag{3.29}$$

$$C_1 = \sqrt{C_{m1}^2 + C_{u1}^2} \tag{3.30}$$

$$T_1 = T_{01} - C_1^2/(2C_p) \tag{3.31}$$

$$P_1 = P_{01}(T_1/T_{01})^{\frac{\gamma}{\gamma-1}} \tag{3.32}$$

$$\rho_1 = P_1/(RT_1) \tag{3.33}$$

Once the impeller inlet parameters converged and additional inlet parameters of interest were calculated using velocity triangle relationships, the outlet parameters can be calculated. Outlet calculations employed a similar method as the inlet, namely an overall density iteration, with some additional required equations to enable a closed form solution. Initialization for the outlet static density involved the design pressure ratio and associated isentropic outlet stagnation density, setting the initial static density equal to the estimated stagnation density. Equations (3.34) through (3.47) are iteratively solved until converging upon a final static density. A loss correlation script is employed within the static density iterative loop, where the internal and external enthalpy losses are calculated and updated. Loss correlations included in equations (3.41) and (3.42) will be discussed and are provided in ***Error! Reference source not found.***. As the calculated static density converges to a solution, the loss correlations also converge for estimation of the enthalpy losses.

$$C_{m2} = \dot{m}/(\rho_2 A_2) \tag{3.34}$$

$$C_{u2} = \sigma U_2 - \frac{C_{m2}}{tan(\beta_{B2})} \tag{3.35}$$

$$C_2 = \sqrt{C_{m2}^2 + C_{u2}^2} \tag{3.36}$$

$$W_{m2} = C_{m2} \tag{3.37}$$

$$W_{u2} = U_2 - C_{u2} \tag{3.38}$$

$$W_2 = \sqrt{W_{m2}^2 + W_{u2}^2} \tag{3.39}$$

$$\Delta h_{eul} = U_2 C_{u2} - U_1 C_{u1} \tag{3.40}$$

$$\Delta h_{int} = \Delta h_{BL} + \Delta h_{CH} + \Delta h_{CL} + \Delta h_{INC} + \Delta h_{MIX} + \Delta h_{SF} \tag{3.41}$$

$$h_{ext} = \Delta h_{DF} + \Delta h_{LK} + \Delta h_{RE} \tag{3.42}$$

$$P_{02} = P_{01}\left(\frac{\Delta h_{eul} - \Delta h_{int}}{C_p T_{01}} + 1\right)^{\gamma/(\gamma-1)} \tag{3.43}$$

$$T_{02} = T_{01} + \frac{\Delta h_{eul} + h_{ext}}{C_p} \tag{3.44}$$

$$T_2 = T_{02} - \frac{C_2^2}{2C_p} \tag{3.45}$$

$$P_2 = P_{02}\left(\frac{T_2}{T_{02}}\right)^{\gamma/(\gamma-1)} \tag{3.46}$$

$$\rho_2 = P_2/(RT_2) \tag{3.47}$$

Solving the outlet calculations requires the use of a slip factor parameter estimation. Qui et al. [23] proposed an accurate correlation for the slip factor based on radial rotational effects, blade turning, and passage width variation. Although this has become a readily accepted model, for instance by Dixon and Hall [5], this model requires extensive knowledge of the impeller geometry. To limit the geometrical information required when estimating the slip factor, several alternative slip factor correlations were considered [24-29]. Due its overall simplicity, the Wiesner [22] slip factor was initially adopted, as defined in equation (3.48) –

$$\sigma = 1 - \frac{\sqrt{sin(\beta_{B2})}}{Z^{0.7}} \tag{3.48}$$

The Wiesner slip factor tends to vary from experimental results for compressors as a function of the impeller tip speed. As explained by Harrison [28], it can be shown using the Euler turbomachinery equation that small errors in the outlet tangential flow velocity caused by slip factor inaccuracies are compounded due to multiplication of the impeller exit tip speed. Therefore, to minimize this error, the slip factor proposed by Harrison [28, 29] was implemented for the present study. This slip factor, equation (3.49), is based on an estimation for the total temperature ratio, as defined by Harrison, and the outlet flow coefficient.

$$\sigma = \frac{TTR}{(\gamma - 1)M_{u2}^2} + \frac{\phi_2}{tan(\beta_{2b})} \tag{3.49}$$

Total temperature ratio through the impeller is estimated through the correlation provided in equation (3.50), where parameters '*A'* and '*B'* are constants that depend on compressor characteristics. This correlation is a function of the Mach tip speed, *perfectly-guided* head coefficient, and *perfectly-guided* specific speed. Definitions for these parameters are provided as equations (3.50) through (3.53) –

$$TTR = A\psi_{PGF}M_{u2}^2\left(M_{u2}^2 N_{s,PFG}\right)^B \tag{3.50}$$

$$M_{u2} = \frac{U_2}{\sqrt{\gamma R T_{01}}} \tag{3.51}$$

$$\psi_{PGF} = \frac{U_2 C_{u2,PGF} - U_1 C_{u1}}{U_2^2} \tag{3.52}$$

$$N_{s,PFG} = \frac{\phi_1^{0.5}}{\psi_{PGF}^{0.75}} \tag{3.53}$$

Vaneless diffuser calculations were developed through manipulation of the model proposed by Stanitz [30], supplemented with insight obtained from Japikse, Baines, and Dubitsky [3, 31, 32]. Using the momentum conservation and continuity equations, along with the first law of thermodynamics and ideal gas equation of state, a set of equations were developed to solve for vaneless diffuser outlet parameters. The original equations proposed by Stanitz [30] are shown in equations (3.54) through (3.56) –

$$C_m \frac{dC_m}{dr} - \frac{C_u^2}{r} + f\frac{C^2 sin(\alpha)}{bsin(\phi)} + \frac{1}{\rho}\frac{dP}{dr} = 0 \tag{3.54}$$

$$C_m \frac{dC_u}{dr} + \frac{C_m C_u}{r} + f\frac{C^2 cos(\alpha)}{bsin(\phi)} = 0 \tag{3.55}$$

$$\frac{1}{\rho}\frac{d\rho}{dr} + \frac{1}{C_m}\frac{dC_m}{dr} + \frac{1}{b}\frac{db}{dr} + \frac{1}{r} = 0 \tag{3.56}$$

Noting that the differential of diffuser height in the radial direction is a geometrical function that is known or assumed, the unknowns in the set of equations are the differentials of meridional and tangential velocity components, pressure and the density. Applying the conservation of energy and ideal gas equation of state, *i.e.* equations (3.57) and (3.58), an unknown can be eliminated to create a system of three equations and three unknowns.

$$T_0 = T + \frac{C^2}{2C_p} \tag{3.57}$$

$$P = \rho RT \tag{3.58}$$

Equations (3.59) and (3.60) show the differentiation of these equations,

$$\frac{dT}{dr} = -\frac{1}{C_p}\left(C_m \frac{dC_m}{dr} + C_\theta \frac{dC_u}{dr}\right) \tag{3.59}$$

$$\frac{dP}{dr} = R\left(T\frac{d\rho}{dr} + \rho\frac{dT}{dr}\right) \tag{3.60}$$

Substituting equation (3.59) into (3.60), and subsequently substituting the resulting equation into (3.54), the simplified results takes the form of the following system of equations. This system of equations has been formatted such that all unknown gradients are on the left hand side.

$$\frac{C_m}{\gamma}\frac{dC_m}{dr} - \frac{R}{C_p}C_u\frac{dC_u}{dr} + \frac{RT}{\rho}\frac{d\rho}{dr} = \frac{C_u^2}{r} - f\frac{C^2 sin(\alpha)}{bsin(\phi)} \tag{3.61}$$

$$C_m\frac{dC_u}{dr} = -\frac{C_m C_u}{r} - f\frac{C^2 cos(\alpha)}{bsin(\phi)} \tag{3.62}$$

$$\frac{1}{\rho}\frac{d\rho}{dr} + \frac{1}{C_m}\frac{dC_m}{dr} = -\frac{1}{b}\frac{db}{dr} - \frac{1}{r} \tag{3.63}$$

This system of equations now has three unknowns, and can be solved using traditional numerical integration methods. A 4th order Runge-Kutta method was implemented to integrate through the diffuser along the radial direction, solving the system of equations at discretized points along the diffuser mean line.

Frictional loss effects are included in the system of equations through the use of a friction factor term in the two momentum equations. A correlation for this term is described in equation (3.64), as provided by Japikse [3]. This correlation includes the Reynolds number based on the hydraulic diameter and diffuser flow velocity, and an empirical constant, '*k'*, that varies based on compressor geometries and applications.

$$f = k\left(\frac{1.8\times10^5}{Re}\right)^{0.2} \tag{3.64}$$

Open-literature loss correlations that are considered for the present study coincide with those discussed in chapter 2 and are provided in *Table 3.1*. Loss correlations considered were implemented into an enthalpy loss script, where each individual correlation could be easily selected in the performance prediction mean-line script.

Table 3.1: *Loss correlations available in open-literature*

Loss Mechanism	***Loss Enthalpy***	***Loss Author***
a. Blade Loading	Δh_{BL}	*Aungier [22]* *Coppage et al. [33]*
b. Choking	Δh_{CH}	*Aungier [22]*
c. Clearance	Δh_{CL}	*Aungier [22]* *Jansen [21]* *Krylov & Spunde [34]* *Rodgers [35]*
d. Disk Friction	Δh_{DF}	*Aungier [22]* *Boyce [36]* *Daily & Nece [37]* *Shepherd [38]*
e. Incidence	Δh_{INC}	*Aungier [22]* *Conrad et al. [39]* *Galvas [40]* *Gravdahl & Egeland [41]* *Stanitz [42]*
f. Leakage	Δh_{LK}	*Aungier [22]* *Jansen [21]*
g. Mixing	Δh_{MIX}	*Aungier [22]* *Johnston & Dean [43]*
h. Recirculation	Δh_{REC}	*Aungier [22]* *Coppage et al. [33]* *Jansen [21]* *Oh et al. [7]*
i. Skin Friction	Δh_{SF}	*Aungier [22]* *Coppage et al. [33]* *Galvas [40]* *Jansen [21]*

Energy dissipation due to the loss mechanisms fall into two distinct categories, internal and external losses. The internal losses reduce total pressure gains due to entropy generation during the compression

process, while the external losses are parasitic losses that consume shaft work prior to being available for fluid total pressure gains. Each loss mechanism considered is categorized and described in chapter 2.

Internal losses associated with the vaneless diffuser were calculated in conjunction with solving the vaneless diffuser system of equations. For the present study, only the skin friction loss within the vaneless diffuser was considered. Specific loss correlations were not employed to solve the diffuser internal loss, and the method utilized to quantify losses is presented in equations (3.65) and (3.66). As described, the isentropic temperature was calculated using the actual outlet pressure. The difference between the actual temperature and isentropic temperature were then used to calculate the enthalpy loss in the diffuser.

$$T_{3s} = T_2 \left(\frac{P_3}{P_2}\right)^{\frac{\gamma-1}{\gamma}} \tag{3.65}$$

$$\Delta h_{VD} = C_p(T_3 - T_{3s}) \tag{3.66}$$

Centrifugal compressor performance is commonly evaluated using pressure ratio and isentropic efficiency. Pressure ratio for the present study is defined as the *total-to-total* pressure ratio, *i.e.* ratio between the stagnation pressure at the diffuser outlet and impeller inlet, as described in equation (3.67) –

$$P_R = \frac{P_{03}}{P_{01}} \tag{3.67}$$

The definition for isentropic efficiency follows the suggestion of Oh *et al.* [7]. This definition considers the internal enthalpy losses, including the quantified vaneless diffuser losses, and the external losses. Equation (3.68) shows the proposed definition below –

$$\eta_s = \frac{\Delta h - \Delta h_{int} - \Delta h_{VD}}{\Delta h + \Delta h_{ext}} \tag{3.68}$$

Other non-dimensional terms that are important in performance evaluation is the flow coefficient and the loading coefficient. The inlet flow coefficient is a form of non-dimensionalized mass flow rate and is defined in the present study as equation (3.69). The loading coefficient is the non-dimensionalized fluid enthalpy change, as defined in equation (3.70).

$$\phi = \frac{\dot{m}}{\rho_{01} D_2^2 U_2} \tag{3.69}$$

$$\psi = \frac{\Delta h}{U_2^2} \tag{3.70}$$

3.3 Model Validation and Discussion

Methodology developed in the present study was validated against open-literature experimental data. A common source of experimental data used for centrifugal compressor validation comes from measurements published by Eckardt [44-46]. For optimization of the loss correlations employed in this investigation, Eckardt's '*Impeller A*' was considered, and geometry details for the impeller are provided in *Table 3.2*.

Establishing an optimized set of loss models utilized the experimental data for both the pressure ratio and isentropic efficiency. A MATLAB script was written to calculate the percentage of deviation at several points along the mass flow rate range of each compressor speed line, and a set was chosen which minimized the average error across the data set. The recommended set of loss correlations is provided in *Table 3.3*.

The optimized set of loss correlations were further tested through performance prediction of other test impellers with available open-literature experimental data. These impellers included Eckardt impellers '*O'* and '*B'* [44-46], and two high pressure ratio impellers developed by Krain & Hoffman [47] and Came & Herbert [48]. The two high pressure ratio compressors also contained splitter blades, which are not present in the Eckardt impellers. Geometries and compressor design conditions for the additional open-literature compressors considered are also provided in *Table 3.2*.

Table 3.2: *Compressor characteristics for open-literature experimental data sets*

Parameter	***Eckardt A***	***Eckardt O***	***Eckardt B***	***Krain & Hoffmann***	***Came & Herbert***	***Unit***
Fluid	Air	Air	Air	Air	Air	[--]
PR_d	1.863	2.502	1.694	6.1	7.864	[--]
$\dot{m}_d$	5.314	6.062	4.531	2.55	1.847	[kg/s]
N_d	14000	14000	14000	50000	40000	[RPM]
Z	20	20	20	26	34	[--]
S	0	0	0	13	17	[--]
L_{ax}	0.130	0.130	0.084	-	-	[m]
r_{1h}	0.060	0.045	0.096	0.030	0.030	[m]
r_{1s}	0.140	0.140	0.140	0.078	0.067	[m]
r_2	0.200	0.200	0.200	0.112	0.137	[m]
r_3	0.400	0.400	0.400	0.212	0.260	[m]
b_2	0.026	0.026	0.026	0.010	0.006	[m]
b_3	0.013	0.013	0.013	0.010	0.005	[m]
α_1	90	90	90	90	90	[deg]
β_{B1h}	58	50	45	50	58.6	[deg]
β_{B1s}	27	27	30	26.5	36.2	[deg]
β_{B2}	60	90	60	52	60	[deg]

While most parameters within the correlations were previously calculated in the model methodology, there are several additional parameters that require separate calculation. The correlation for blade loading proposed by Coppage *et al.* [33] involves a diffusion factor, 'Δ', which is defined as equation (3.71). To solve for the diffusion factor, the non-dimensional theoretical enthalpy gain must be calculated. This parameter is described in equation (3.72), and is a form of the Euler turbomachinery equation non-dimensionalized by the impeller tip speed.

Table 3.3: *Recommended selection of loss correlations*

Loss Mechanism	***Correlation***	***Literature Source***
Blade Loading	$\Delta h_{BL} = 0.05\Delta^2 U_2^2$	Coppage et al. [31]
Choking	$\Delta h_{CH} = \begin{cases} W_1^2 \dfrac{(0.05x + x^7)}{2} & x > 0 \\ 0 & x \leq 0 \end{cases}$	Aungier [18]
Clearance	$\Delta h_{CL} = 0.6 \dfrac{\varepsilon}{b_2} C_2 \sqrt{4 C_{u2} C_1 \dfrac{(\pi/b_2)}{Z} \dfrac{(r_s - r_h)/(r_2 - r_s)}{1 + \rho_2/\rho_1}}$	Jansen [17]
Disk Friction	$\Delta h_{DF} = \dfrac{\bar{\rho} U_2^3 r_2^2 C_f}{4\dot{m}}$	Daily & Nece [35]
Incidence	$\Delta h_{INC} = \dfrac{W_L^2}{2}$	Galvas [38]
Leakage	$\Delta h_{LK} = \dfrac{\dot{m}_{cl} U_{cl} U_2}{2\dot{m}}$	Aungier [18]
Mixing	$\Delta h_{MIX} = \dfrac{C_2^2}{2\left(1 + tan^2(90 - \alpha_2)\right)} \left(\dfrac{1 - \epsilon_{wake} - b^*}{1 - \epsilon_{wake}}\right)^2$	Johnston & Dean [41]
Recirculation	$\Delta h_{REC} = 8 \times 10^{-5} sinh(3.5(90 - \alpha_2)^3) \Delta^2 U_2^2$	Oh et al. [4]
Skin Friction	$\Delta h_{SF} = \dfrac{2 C_f \bar{W}^2 L_B}{d_H}$	Aungier [18]

$$\Delta = 1 - \frac{W_2}{W_1} + \frac{0.75 q_{TH}}{W_1/\mu_2 \left[\frac{Z}{\pi}\left(1 - \frac{d_1}{D}\right) + 2\frac{d_1}{D}\right]} \tag{3.71}$$

$$q_{TH} = H_{TH}/U_2^2 = (U_2 C_{u2} - U_1 C_{u1})/U_2^2 \tag{3.72}$$

Aungier [22] developed a choking loss equation which is a function of the inlet relative flow velocity and a non-dimensional parameter '*x*'. The parameter '*x*', as shown in equation (3.73), is a function of the critical throat area, *i.e.* the area at which the specified mass flow rate would be choked, the actual throat area and a throat contraction ratio. The throat contraction ratio is defined as equation (3.74) and is bounded by equation (3.75).

$$x = 10\left(1.1 - \frac{A_{th}^*}{C_r A_{th}}\right) \tag{3.73}$$

$$C_r = \sqrt{A_1 \frac{sin(\beta_1)}{A_{th}}} \tag{3.74}$$

$$C_r \leq 1 - \left(A_1 \frac{sin(\beta_1)}{A_{th}} - 1\right)^2 \tag{3.75}$$

The disk friction loss correlation developed by Daily and Nece [37] is proposed as a function of average density, impeller tip speed, impeller tip radius, friction coefficient and the mass flow rate. The average density is simply the arithmetic mean of the inlet and outlet densities, *i.e.* equation (3.76). Daily and Nece [37] provide an empirical correlation for the friction coefficient, equation (3.77), which is split into two distinct flow regimes. The friction coefficient is a function of the Reynolds number, equation (3.78), and the ratio of impeller clearance to tip radius.

$$\bar{\rho} = \frac{\rho_1 + \rho_2}{2} \tag{3.76}$$

$$C_f = \begin{cases} 3.7(\varepsilon/r_2)^{0.1} Re^{-0.5}; & Re < 3E5 \\ 0.0102(\varepsilon/r_2)^{0.1} Re^{-0.2}; & Re > 3E5 \end{cases} \tag{3.77}$$

$$Re = \frac{U_2 r_2}{\nu_2} \tag{3.78}$$

Galvas [40] uses the optimal and actual relative flow angles to derive an equation for the lost relative velocity, described with equation (3.79). To find the optimal relative flow angle at the inlet, a relationship proposed by Rusch and Casey [49] was incorporated as shown in equation (3.80) –

$$W_L = W_1 sin(|\beta_{opt} - \beta_1|) \tag{3.79}$$

$$\beta_{opt} = sin^{-1}\left(\frac{\sqrt{\gamma M_{w1}^2 + 2M_{w1} + 3} - \sqrt{\gamma M_{w1}^2 - 2M_{w1} + 3}}{2M_{w1}}\right) \tag{3.80}$$

Supplementary equations that are required to adopt Aungier's [22] leakage loss correlation include the velocity of the flow through the leakage gap and the leakage mass flow rate. The velocity of the leakage flow, equation (3.81), utilizes the average pressure difference across the leakage gap, found using equations (3.82) through (3.84). Leakage mass flow is solved using the velocity of the leakage flow combined with other known parameters, defined in equation (3.85).

$$U_{cl} = 0.816\sqrt{2\,\Delta P_{cl}/\rho_2} \tag{3.81}$$

$$\Delta P_{cl} = \frac{\dot{m}[r_2 C_{u2} - (r_1 C_{u1})_m]}{Z\bar{r}\bar{b}L_B} \tag{3.82}$$

$$\bar{r} = \frac{r_1 + r_2}{2} \tag{3.83}$$

$$\bar{b} = \frac{b_1 + b_2}{2} \tag{3.84}$$

$$\dot{m}_{cl} = \rho_2 Z \varepsilon L_B U_{cl} \tag{3.85}$$

The mixing loss correlation given by Johnston & Dean [43] involves the wake area fraction. This fraction is defined as the area of the wake flow present at the impeller outlet over the total impeller exit area. Evaluation of the wake area fraction involves the implementation of a two-zone model, which was outside the scope of the present study. Therefore, a correlation developed by Stuart *et al.* [50] was implemented.

According to Stuart *et al.* [50], an assumption of constant wake area is not appropriate for various impeller geometries and operating conditions. The correlation developed, provided in equation (3.86), is a function of the wake mass flow rate, 'χ', and subsequently the outlet flow coefficient including the aerodynamic blockage. These two parameters are calculated using equation (3.87) and (3.88). The final required parameter is the ratio of diffuser inlet and outlet heights, equation (3.89). With these parameters known, the overall mixing loss correlation can then be solved.

$$\varepsilon = \frac{0.78 \frac{\chi}{\varphi_{2,AF}}}{0.88 + \frac{\chi}{\varphi_{2,AF}}} \tag{3.86}$$

$$\chi = 3.05\varphi_{2,AF}^2 - 2.65\varphi_{2,AF} + 0.778 \tag{3.87}$$

$$\varphi_{2,AF} = \frac{\dot{m}}{\rho_2 A_2 (1 - B_2) U_2} \tag{3.88}$$

$$b^* = \frac{b_3}{b_2} \tag{3.89}$$

The recirculation loss correlation proposed by Oh *et al.* [7] uses an identical definition for the diffusion factor as proposed by Coppage *et al.* [33]. Therefore, equation (3.71) was applied to the correlation to evaluate the recirculation loss.

Aungier's [22] proposed correlation for skin friction involves the mean relative velocity, blade length, friction coefficient, and hydraulic diameter. The mean relative velocity is between the inlet and outlet, equation (3.90), and is bounded by equation (3.91) which substitutes the throat relative velocity for the inlet relative velocity. The hydraulic diameter was calculated using equation (3.92), which is a formulation proposed by Jansen [21]. The friction coefficient was calculated using an implicit formula, equation (3.93), which was proposed by Casey [51] specifically for radial turbomachines.

$$\bar{W}^2 = \frac{W_1^2 + W_2^2}{2} \tag{3.90}$$

$$\bar{W}^2 \geq \frac{W_{th}^2 + W_2^2}{2} \tag{3.91}$$

$$d_H = \frac{d_2 sin(\beta_2)}{\left[\frac{Z}{\pi} + \frac{d_2 sin(\beta_2)}{b_2}\right]} + \frac{\frac{1}{2}(d_{1s} + d_{1h})\left(\frac{sin(\beta_{1s}) + sin(\beta_{1h})}{2}\right)}{\frac{Z}{\pi} + \left(\frac{d_{1s} + d_{1h}}{d_{1s} - d_{1h}}\right)\left(\frac{sin(\beta_{1s}) + sin(\beta_{1h})}{2}\right)} \tag{3.92}$$

$$\frac{1}{\sqrt{4C_f}} = 1.74 - 2log_{10}\left(\frac{2k_s}{d_{hyd}} + \frac{18.7}{Re\sqrt{4C_f}}\right) \tag{3.93}$$

Using the determined correlation set, the mean-line model was used to determine the performance of the Eckardt '*Impeller A*' geometry. Resulting plots from the model are provided in *Figure 3.8* and *Figure 3.9*, where the points are experimental data measurements and the solid lines are performance model results. Speed line labels are provided on the plots in units of rotations per minute (*RPM*).

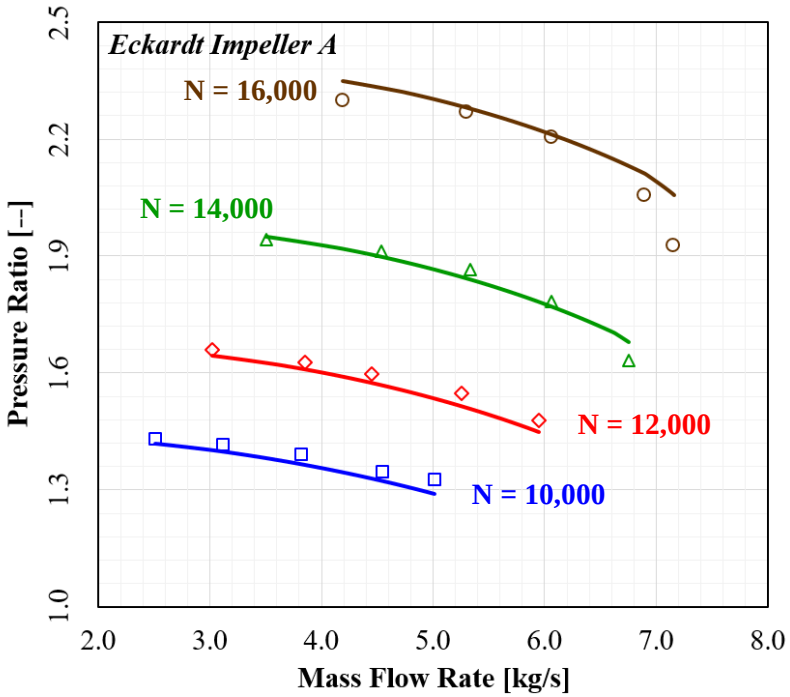

Figure 3.8: *Comparison between model pressure ratio estimation (solid lines) and experimental measurements (symbols) for Eckardt Impeller A*

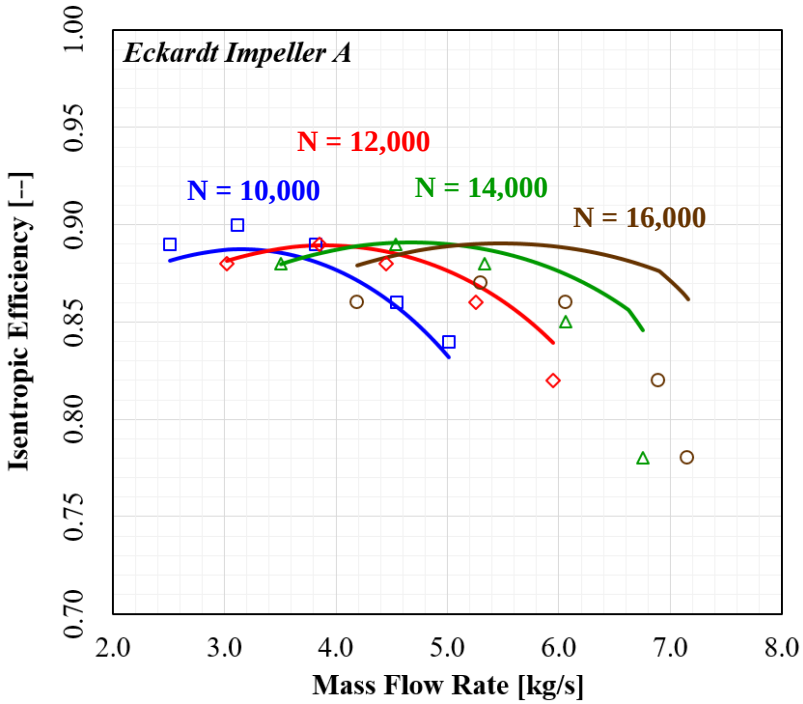

Figure 3.9: *Comparison between model isentropic efficiency estimation (solid lines) and experimental measurements (symbols) for Eckardt Impeller A*

The error for the pressure ratio ranges from a minimum of 0.3% to a maximum of 6.65%, and the isentropic efficiency error ranges from a minumum of 0.04% to a maximum of 10.49%. As evident from the figures, at low to moderate impeller rotational speeds the model has excellent agreement with the experimental data. At the high rotational speed, both the pressure ratio and efficiency estimations exhibit increased error.

Behavior during the loss set selection is captured in *Figure 3.10*, where the mean error is evaluated for every possible set of loss correlations. The error is established for both pressure ratio and isentropic efficiency, and an averaged error is calculated to get an overall ranking for each loss correlation set.

The loss correlation set ranking described in *Figure 3.10* was created by averaging the error over the 20 experimental points considered for Eckardt '*Impeller A*'. For the present analysis, all points were weighted equally. Since the set ranking is seperately evaulated for pressure ratio, efficiency, and mean average, the highest ranked loss set for each curve does not correspond to the same set of loss correlations. The chosen set of correlations was based on the ranked set which produced the minimum weighted average.

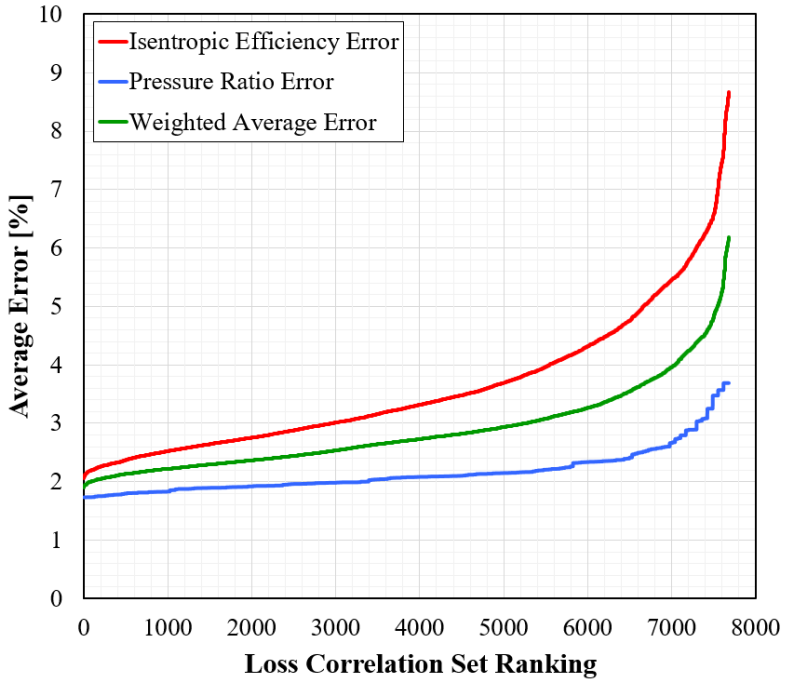

Figure 3.10: *Loss correlation set ranking for Eckardt Impeller A*

In conjunction with the pressure ratio and efficiency curves, an overall breakdown of each individual loss correlation was captured. *Figure 3.11* through *Figure 3.14* provide the breakdown of the individual losses for the each rotation speed considered. To properly compare the loss trends over different rotational speeds, the enthalpy losses were non-dimensionalized using the loading coefficient. The mass flow rate was also non-dimensionalized to show the span between surge and choking mass flow rates using equation (3.94) –

$$\dot{m}_{span} = \frac{\dot{m} - \dot{m}_{surge}}{\dot{m}_{choke} - \dot{m}_{surge}} \tag{3.94}$$

These losses follow general trends described in literature, and are similar to results published by Harrison [28]. As the speed increases, there is an increase in the blade loading and recirculation losses. Inversly, there is a decrease in the skin friction as the speed is increased. The other losses remain approximately constant when evaluated using the loading coefficient.

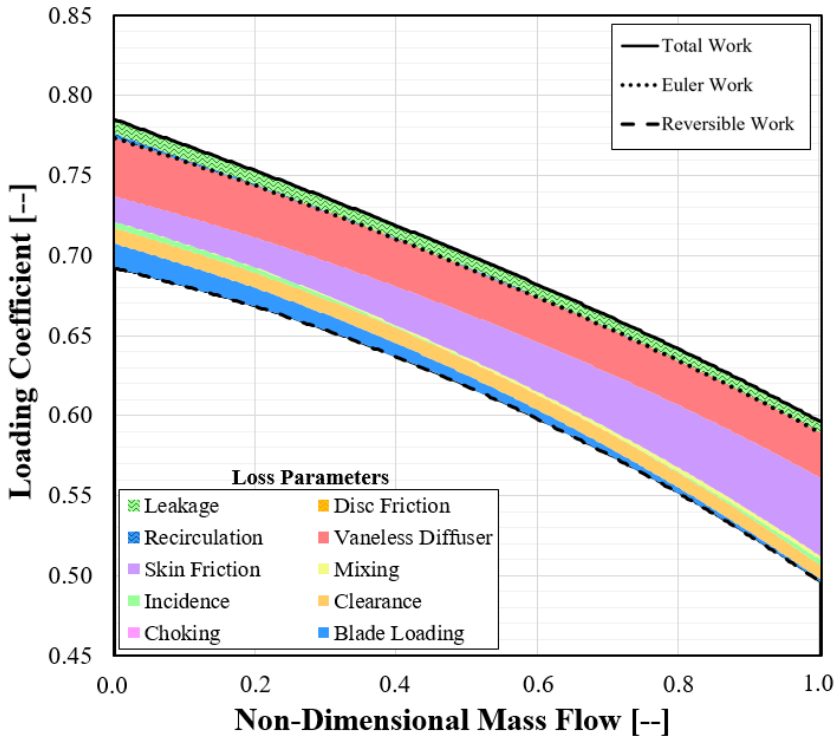

Figure 3.11: *Eckardt Impeller A loss breakdown over mass flow span at 10000 RPM*

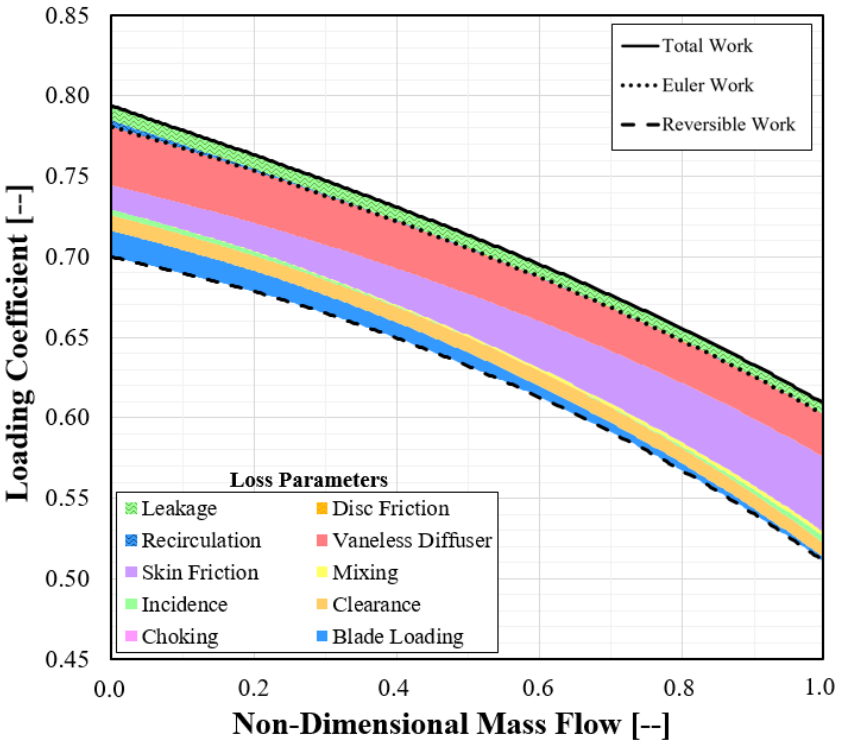

Figure 3.12: *Eckardt Impeller A loss breakdown over mass flow span at 12000 RPM*

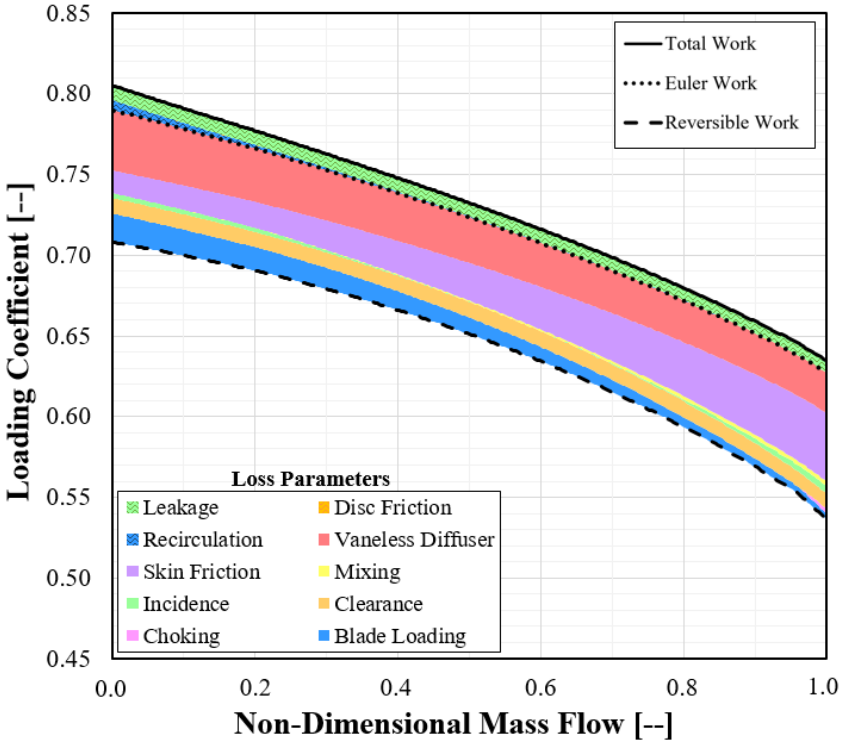

Figure 3.13: *Eckardt Impeller A loss breakdown over mass flow span at 14000 RPM*

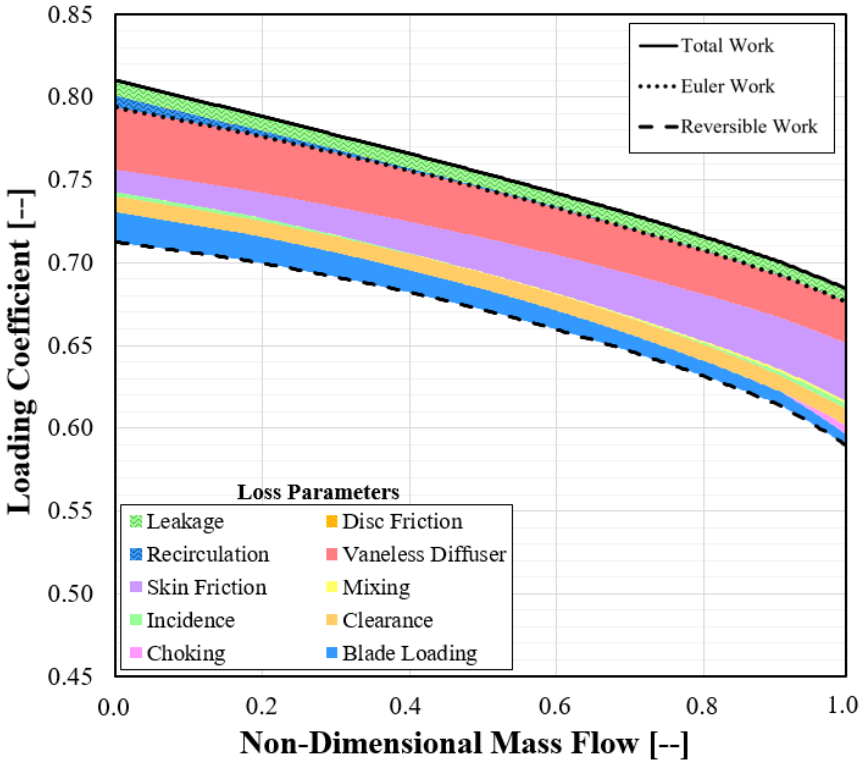

Figure 3.14: *Eckardt Impeller A loss breakdown over mass flow span at 16000 RPM*

To ensure the validity of the methodology when modelling other family types of centrifugal compressors, the performance prediction model and loss correlation set were used to evaluate additional experimentally measured data sets. All test impeller geometries described in *Table 3.2* were evaluated and the resulting performance estimations are provided in *Figure 3.15* through *Figure 3.22*.

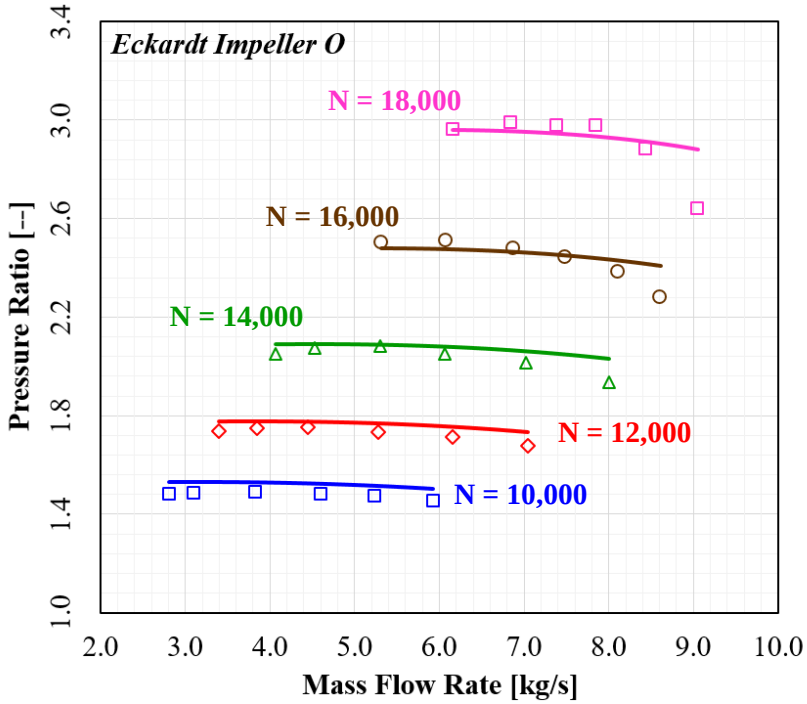

Figure 3.15: *Comparison between model pressure ratio estimation (solid lines) and experimental measurements (symbols) for Eckardt Impeller O*

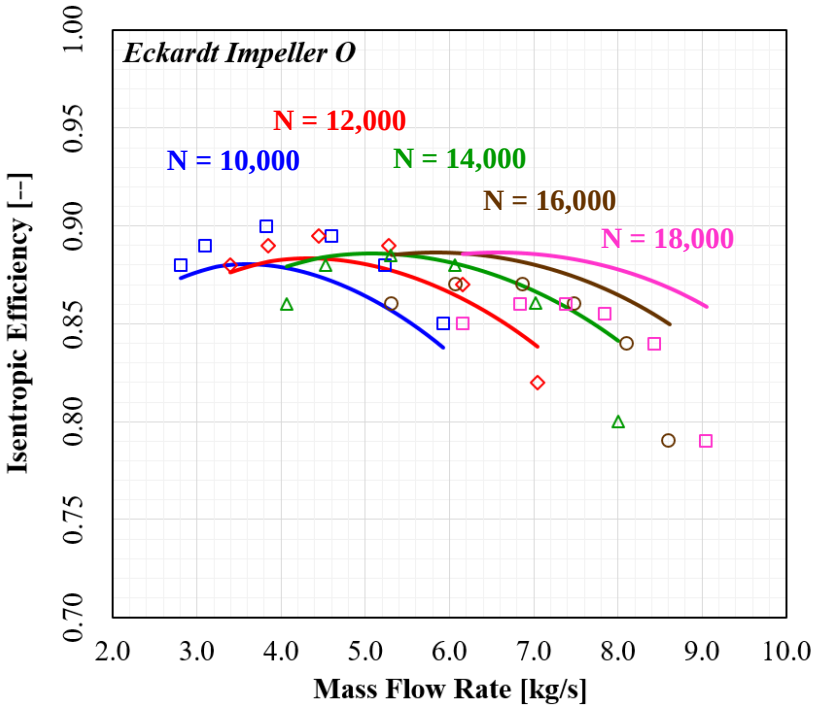

Figure 3.16: *Comparison between model isentropic efficiency estimation (solid lines) and experimental measurements (symbols) for Eckardt Impeller O*

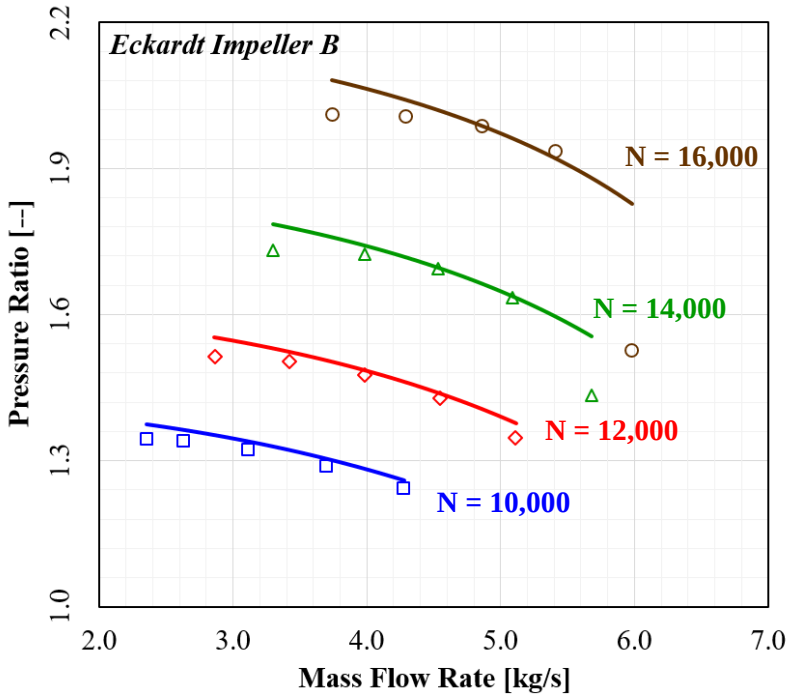

Figure 3.17: *Comparison between model pressure ratio estimation (solid lines) and experimental measurements (symbols) for Eckardt Impeller B*

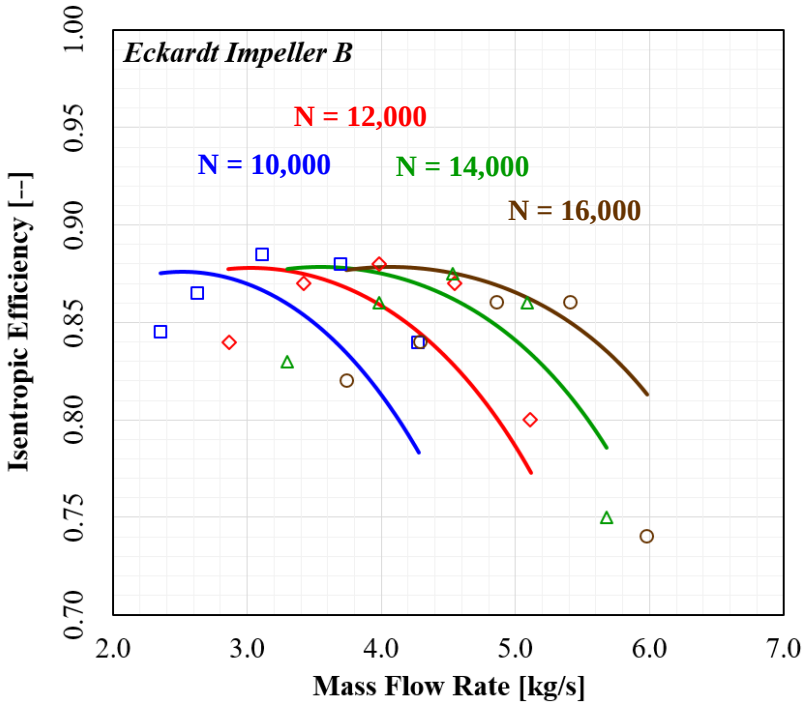

Figure 3.18: *Comparison between model isentropic efficiency estimation (solid lines) and experimental measurements (symbols) for Eckardt Impeller B*

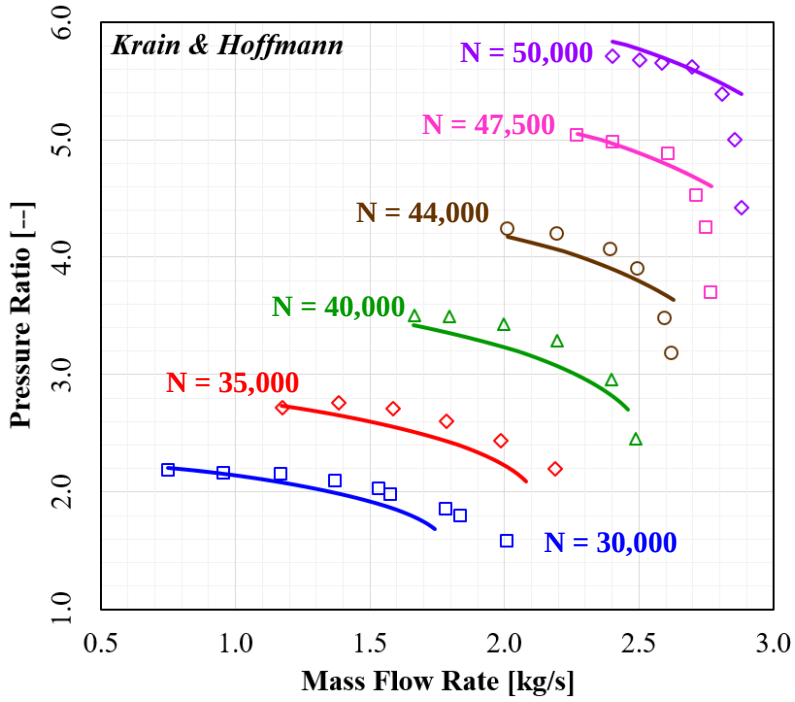

Figure 3.19: *Comparison between model pressure ratio estimation (solid lines) and experimental measurements (symbols) for Krain and Hoffmann impeller*

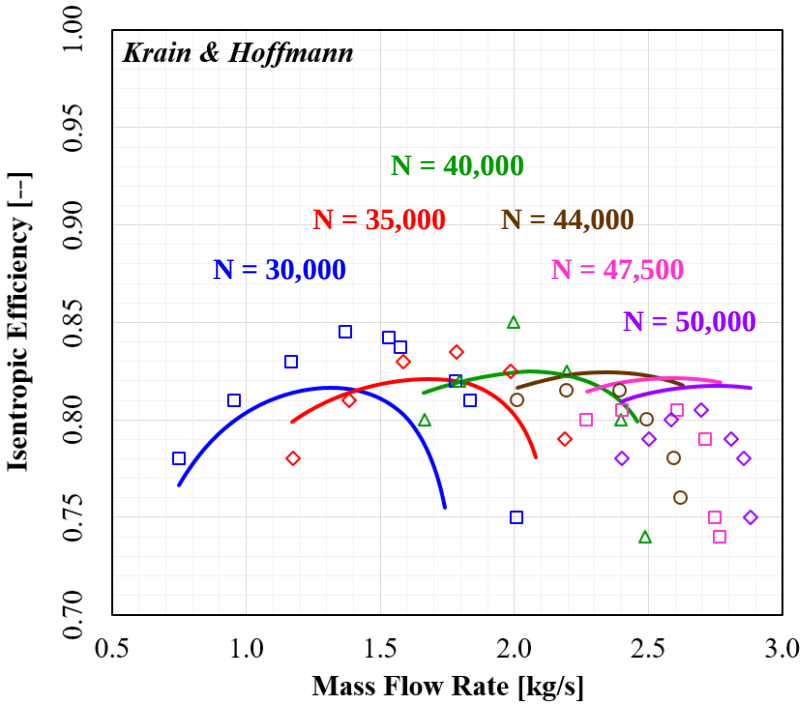

Figure 3.20: *Comparison between model isentropic efficiency estimation (solid lines) and experimental measurements (symbols) for Krain and Hoffmann impeller*

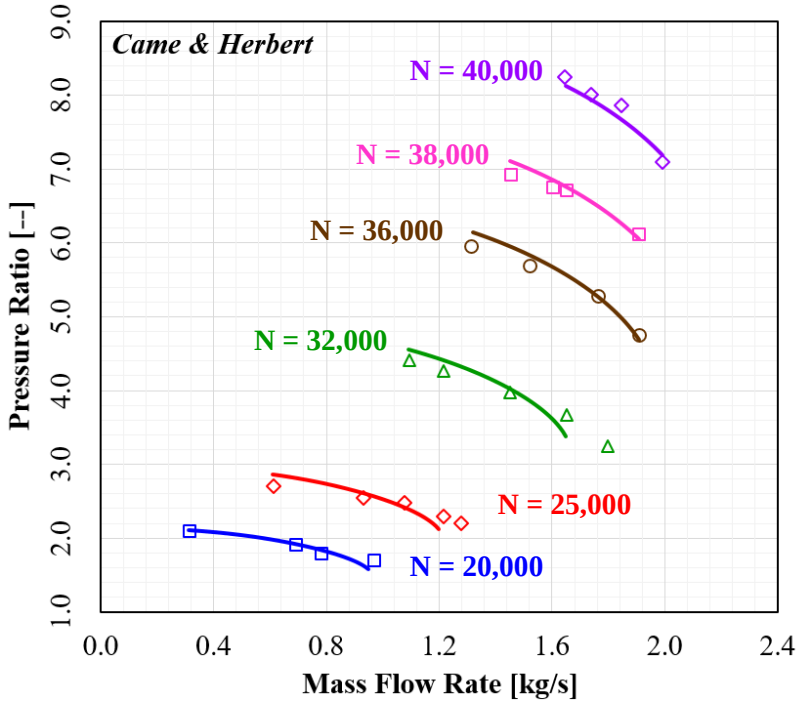

Figure 3.21: *Comparison between model pressure ratio estimation (solid lines) and experimental measurements (symbols) for Came and Herbert impeller*

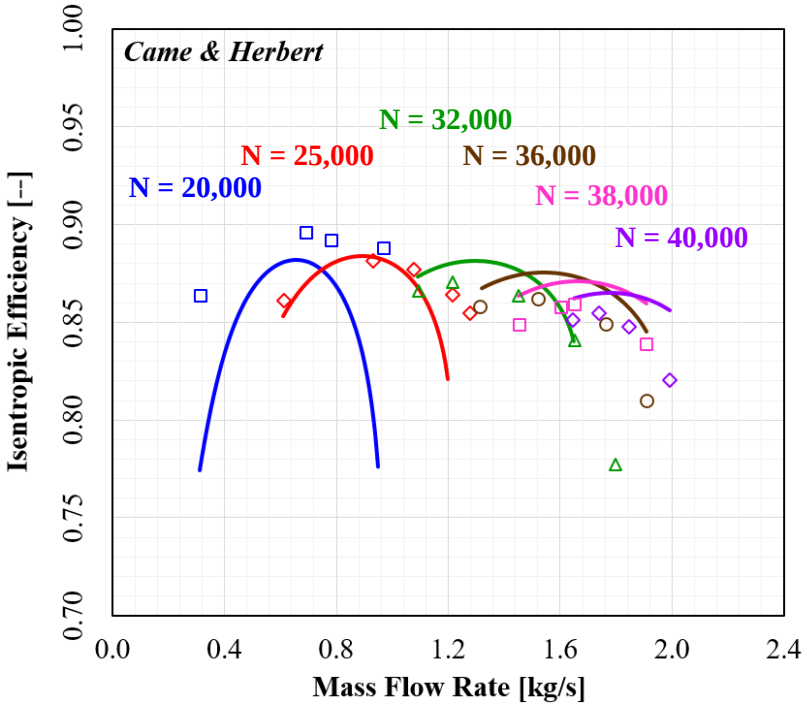

Figure 3.22: *Comparison between model isentropic efficiency estimation (solid lines) and experimental measurements (symbols) for Came and Herbert impeller*

Although the scope of the present work is focused on centrifugal compressors with a pressure ratio of approximately two or three, higher pressure ratio machines were also considered. This provides evidence for the developed models applicability to centrifugal compressors outside the range of the specific impeller used to optimize the set of loss correlations.

There were several trends that were observed in the performance prediction of each test impeller:

- The developed mean-line model has difficulty accounting for increased losses when approaching the choking condition. This is evident in both the pressure ratio and efficiency plots, as the tail of each speed line fails to properly fall off.
- The linear decrease in peak efficiency that is observed in the experimental data for each impeller is not fully captured by the model. The model only appears to capture this trend when evaluating the Came & Herbert impeller.
- Discrepencies of Eckardt '*Impeller B*' is anticipated to be due to the presence of forward blade sweep at the impeller inlet. This geometrical feature is not yet accounted for in the mean-line model.
- Lastly, there are discrepencies in the lower speed lines of the high pressure ratio machines (*i.e.* Krain & Hoffmann and Came & Herbert), which may be due to over-prediction of individual losses at significantly reduced mass flow rates.

3.4 Summary

This chapter recommends a methodology and set of loss correlations to accurately predict the pressure ratio and isentropic efficiency of centrifugal air compressors operating over a wide range of off-design conditions. The recommended loss correlation set and model methodology provides reasonable agreement over the tested range of each of the experimental impeller data sets surveyed. Further investigation is required to resolve the observed efficiency over-prediction present at higher RPMs and discrepancies near surge and choking conditions.

REFERENCES

[1] J. Howard, P. Knudsen, A. Engeda, Empirical Loss Model Optimization for the Prediction of Centrifugal Compressor Off-Design Performance, in: ASME Turbo Expo 2023: Turbomachinery Technical Conference and Exposition, 2023.

[2] A. Whitfield, N.C. Baines, Design of Radial Turbomachines, (1990).

[3] D. Japikse, Centrifugal Compressor Design and Performance, 1996.

[4] R.H. Aungier, Centrifugal Compressors: A Strategy for Aerodynamic Design and Analysis, in, Asme Press New York, 2000.

[5] S.L. Dixon, C. Hall, Fluid Mechanics and Thermodynamics of Turbomachinery, Butterworth-Heinemann, 2013.

[6] M. Casey, C. Robinson, Radial Flow Turbocompressors, Cambridge University Press, 2021.

[7] H.W. Oh, E.S. Yoon, M. Chung, An Optimum Set of Loss Models for Performance Prediction of Centrifugal Compressors, Proceedings of the Institution of Mechanical Engineers, Part A: Journal of Power and Energy, 211(4) (1997) 331-338.

[8] P.-Y. Li, C.-W. Gu, Y. Song, A New Optimization Method for Centrifugal Compressors Based on 1D Calculations and Analyses, Energies, 8(5) (2015) 4317-4334.

[9] E.I.G. Velásquez, Determination of a Suitable Set of Loss Models for Centrifugal Compressor Performance Prediction, Chinese Journal of Aeronautics, 30(5) (2017) 1644-1650.

[10] C. Zhang, X. Dong, X. Liu, Z. Sun, S. Wu, Q. Gao, C. Tan, A Method to Select Loss Correlations for Centrifugal Compressor Performance Prediction, Aerospace Science and Technology, 93 (2019) 105335.

[11] L. Bourabia, C.B. Abed, M. Cerdoun, S. Khalfallah, M. Deligant, S. Khelladi, T. Chettibi, Aerodynamic Preliminary Design Optimization of a Centrifugal Compressor Turbocharger Based on One-dimensional Mean-line Model, Engineering Computations, 38(9) (2021) 3438-3469.

[12] P. Kovář, A. Tater, P. Mačák, T. Vampola, Searching for the Most Suitable Loss Model Set for Subsonic Centrifugal Compressors Using an Improved Method for Off-design Performance Prediction, Energies, 14(24) (2021) 8545.

[13] X. Yang, Y. Liu, G. Zhao, Modification and Validation of 1D Loss Models for the Off-Design Performance Prediction of Centrifugal Compressors with Splitter Blades, Machines, 11(1) (2023) 118.

[14] C. Xu, R.S. Amano, Empirical Design Considerations for Industrial Centrifugal Compressors, International Journal of Rotating Machinery, 2012 (2012).

[15] X. Qiu, D. Japikse, M. Anderson, A Meanline Model for Impeller Flow Recirculation, in: Turbo Expo: Power for Land, Sea, and Air, 2008, pp. 1687-1694.

[16] P. Harley, S. Spence, D. Filsinger, M. Dietrich, J. Early, Meanline Modeling of Inlet Recirculation in Automotive Turbocharger Centrifugal Compressors, Journal of Turbomachinery, 137(1) (2015) 011007.

[17] J. Oh, K. Oh, Numerical Modeling of Some Parameters for Performance Prediction of Centrifugal Impellers, in: ASME Turbo Expo 2000: Power for Land, Sea, and Air, 2000.

[18] P. Harley, S. Spence, J. Early, D. Filsinger, M. Dietrich, An Evaluation of 1D Loss Model Collections for the Off-design Performance Prediction of Automotive Turbocharger Compressors, IOP Conference Series: Materials Science and Engineering, 52(4) (2013) 042011.

[19] J. Hosseinpour, Development and Investigation of A Centrifugal Compressor for 10 MWe Brayton Cycles Using Supercritical CO2, Michigan State University, 2023.

[20] K. Birdi, Mixed Flow Compressors, 1992.

[21] W. Jansen, A Method for Calculating the Flow in a Centrifugal Impeller when Entropy Gradients are Present, Inst. Mech. Eng. Internal Aerodynamics, (1970).

[22] R.H. Aungier, Mean Streamline Aerodynamic Performance Analysis of Centrifugal Compressors, (1995).

[23] X. Qiu, D. Japikse, J. Zhao, M.R. Anderson, Analysis and Validation of a Unified Slip Factor Model for Impellers at Design and Off-design Conditions, (2011).

[24] F. Wiesner, A Review of Slip Factors for Centrifugal Impellers, (1967).

[25] J. Stanitz, Some Theoretical Aerodynamic Investigations of Impellers in Radial- and Mixed-flow Centrifugal Compressors, Transactions of the American Society of Mechanical Engineers, 74(4) (1952) 473-497.

[26] T.W. von Backström, A Unified Correlation for Slip Factor in Centrifugal Impellers, (2006).

[27] K. Paeng, M.K. Chung, A New Slip Factor for Centrifugal Impellers, Proceedings of the Institution of Mechanical Engineers, Part A: Journal of Power and Energy, 215(5) (2001) 645-649.

[28] H.M. Harrison, III, Development and Validation of a New Method to Model Slip and Work Input for Centrifugal Compressors, Ph.D., Purdue University, United States -- Indiana, 2020.

[29] H.M. Harrison, N.L. Key, A New Approach to Modeling Slip and Work Input for Centrifugal Compressors, Journal of Engineering for Gas Turbines and Power, 143(2) (2021) 021013.

[30] J.D. Stanitz, One-dimensional Compressible Flow in Vaneless Diffusers of Radial- and Mixed-flow Centrifugal Compressors, Including Effects of Friction, Heat Transfer and Area Change, 1952.

[31] D. Japikse, N.C. Baines, Diffuser Design Technology, Concepts ETI, 1998.

[32] O. Dubitsky, D. Japikse, Vaneless Diffuser Advanced Model, Journal of Turbomachinery, 130(1) (2008).

[33] J. Coppage, F. Dallenbach, H. Eichenberger, G. Hlavaka, E. Knoernschild, N. Van Lee, Study of Supersonic Radial Compressors for Refrigeration and Pressurization Systems, Wright Air Development Center, 1956.

[34] E. Krylov, Y.A. Spunde, About the Influence of the Clearance Between the Working Blades and Housing of a Radial Turbine on its Exponent, Physics, Engineering, 9 (1967).

[35] C. Rodgers, A Cycle Analysis Technique for Small Gas Turbines, in: Proceedings of the Institution of Mechanical Engineers, Conference Proceedings, SAGE Publications Sage UK: London, England, 1968, pp. 37-49.

[36] M.P. Boyce, New Developments in Compressor Aerodynamics, in: Proceedings of the 1st Turbomachinery Symposium, Texas A&M University. Gas Turbine Laboratories, 1972.

[37] J.W. Daily, R.E. Nece, Chamber Dimension Effects on Induced Flow and Frictional Resistance of Enclosed Rotating Disks, (1960).

[38] D.G. Shepherd, Principles of Turbomachinery, Macmillan, 1956.

[39] O. Conrad, K. Raif, M. Wessels, The Calculation of Performance Maps for Centrifugal Compressors with Vane-island Diffusers, Performance prediction of centrifugal pumps and compressors, (1979) 135-147.

[40] M.R. Galvas, Fortran Program for Predicting Off-design Performance of Centrifugal Compressors, 1973.

[41] J.T. Gravdahl, O. Egeland, Centrifugal Compressor Surge and Speed Control, IEEE Transactions on control systems technology, 7(5) (1999) 567-579.

[42] J.D. Stanitz, Effect of Blade-thickness Taper on Axial-velocity Distribution at the Leading Edge of an Entrance Rotor-blade Row with Axial Inlet, and the Influence of this Distribution on Alignment of the Rotor Blade for Zero Angle of Attack, 1953.

[43] J. Johnston, R. Dean Jr, Losses in Vaneless Diffusers of Centrifugal Compressors and Pumps: Analysis, Experiment, and Design, (1966).

[44] D. Eckardt, Detailed Flow Investigations Within a High-Speed Centrifugal Compressor Impeller, Journal of Fluids Engineering, 98(3) (1976) 390-399.

[45] D. Eckardt, Flow Field Analysis of Radial and Backswept Centrifugal Compressor Impellers. I - Flow Measurements Using a Laser Velocimeter, in: Performance Prediction of Centrifugal Pumps and Compressors, 1979, pp. 77-86.

[46] D. Japikse, A Critical Evaluation of Three Centrifugal Compressors With Pedigree Data Sets: Part 5—Studies in Component Performance, Journal of Turbomachinery, 109(1) (1987) 1-9.

[47] H.H. Krain, B., Flow Physics in High Pressure Ratio Centrifugal Compressors, in: ASME Fluids Engineering Division Summer Meeting, 1998.

[48] P.M.H. Came, M. V., Design and Experimental Performance of Some High Pressure Ratio Centrifugal Compressors, in: AGARD Centrifugal Compressors, Flow Phenomena and Performance, 1980.

[49] D. Rusch, M. Casey, The Design Space Boundaries for High Flow Capacity Centrifugal Compressors, Journal of Turbomachinery, 135(3) (2013).

[50] C. Stuart, S. Spence, D. Filsinger, A. Starke, S.I. Kim, A Three-Zone Modeling Approach for Centrifugal Compressor Slip Factor Prediction, Journal of Turbomachinery, 141(3) (2019).

[51] M.V. Casey, The Effects of Reynolds Number on the Efficiency of Centrifugal Compressor Stages, Journal of Engineering for Gas Turbines and Power, 107(2) (1985) 541-548.

CHAPTER 4 : CHARACTERIZATION OF FRIB CRYOGENIC CENTRIFUGAL COMPRESSOR TRAIN FOR STEADY-STATE OPERATION

4.1 Introduction

At the Facility for Rare Isotope Beams (FRIB), superconducting radio frequency (SRF) cavities are operated within the linear accelerator (LINAC) segments to create high-energy isotope beams. These SRF cavities are submersed in cryogenic liquid helium to obtain the superconducting material properties necessary for operation. Cryogenic helium is provided at approximately 4.5 K by the FRIB helium refrigeration system, which supports each of the three LINAC segments (designated *LS1*, *LS2*, and *LS3*). Interactions between the LINAC segments and the FRIB cryogenic system is shown in *Figure 4.1*.

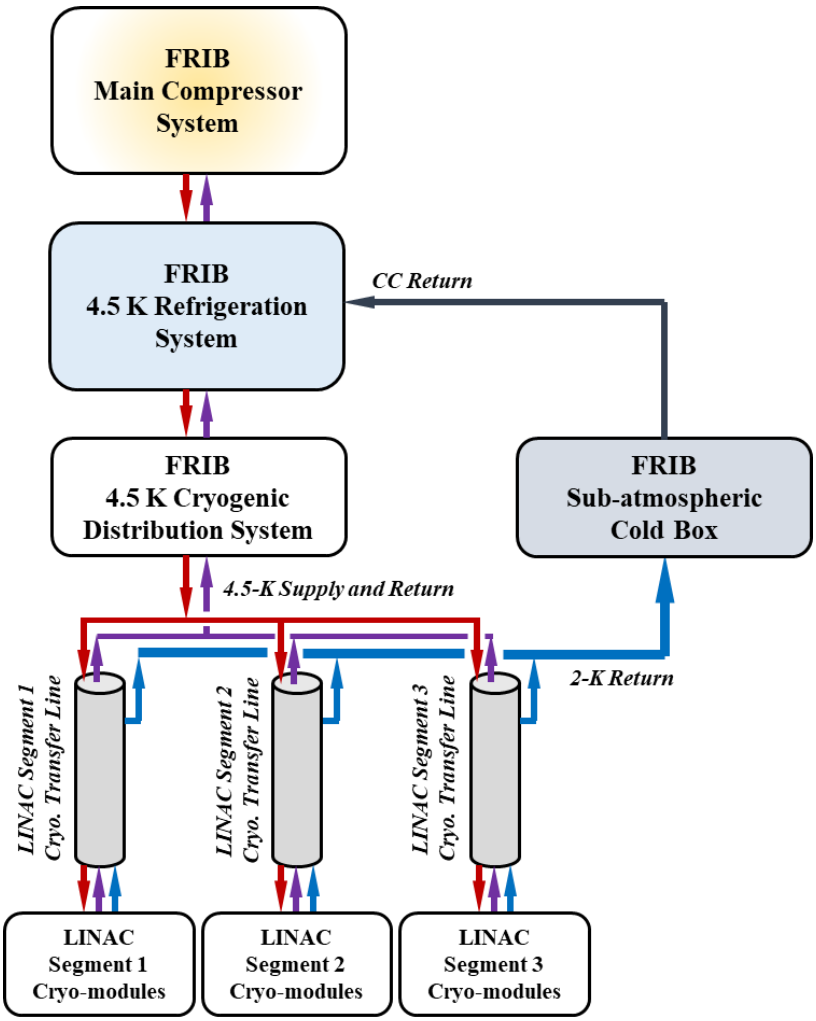

Figure 4.1: *Simplified diagram of FRIB cryogenic system coupling with linear accelerator segments*

To improve accelerator stability (*i.e. tuning*) and limit SRF losses, the cryogenic helium provided to the SRF cavities is cooled below the lambda point of helium (2.177 K and 50.42 mbar). Below the lambda point, helium exhibits superfluid properties which eliminates acoustic disturbances to the SRF cavity submerged in the liquid bath caused by boiling. Reduction in the helium temperature (from the NBP) is accomplished through lowering the saturation pressure of the liquid bath, and subsequently reducing the saturation temperature. A reduction in the saturation pressure to approximately 50 mbar or below will cross over the lambda point. At FRIB, the cryogenic process operates at sub-atmospheric pressures near 30 mbar, which corresponds to a saturation temperature ~ 2.0 K. The cryogenic system employed to reach sub-atmospheric pressure consists of five cryogenic centrifugal compressors, or '*cold-compressors*', operating in series. This compressor string is housed within a vacuum insulated vessel (*sub-atmospheric cold box*) and re-compresses the helium from around 28.5 mbar at compressor suction to above atmospheric conditions (a pressure ratio of around 40) before injection of the flow back into the main helium refrigerator. A simplified schematic of the FRIB cryogenic system is provided in *Figure 4.2*.

Stable operation of multistage centrifugal compressor systems depends strongly on compressor characteristics and overall system design considerations, such as flow straightening and transient decoupling between the compressor stages [1]. The five-stage *cold-compressor* system has been designed and fabricated at FRIB taking into account the operational experience and lessons learned over the last three decades. Details on system selection, design, and commissioning of the FRIB sub-atmospheric refrigeration system can be found in chapter 2 and [2].

Each centrifugal compressor assembly, or '*compressor cartridge*', is installed within the sub-atmospheric cold box. The sub-atmospheric cold box provides the necessary coupling between the LINAC return transfer lines, the centrifugal compressor train, and the main cold box injection transfer line. *Figure 4.3* shows the sub-atmospheric cold box installed at FRIB, including all cryogenic couplings and compressor cartridge assemblies.

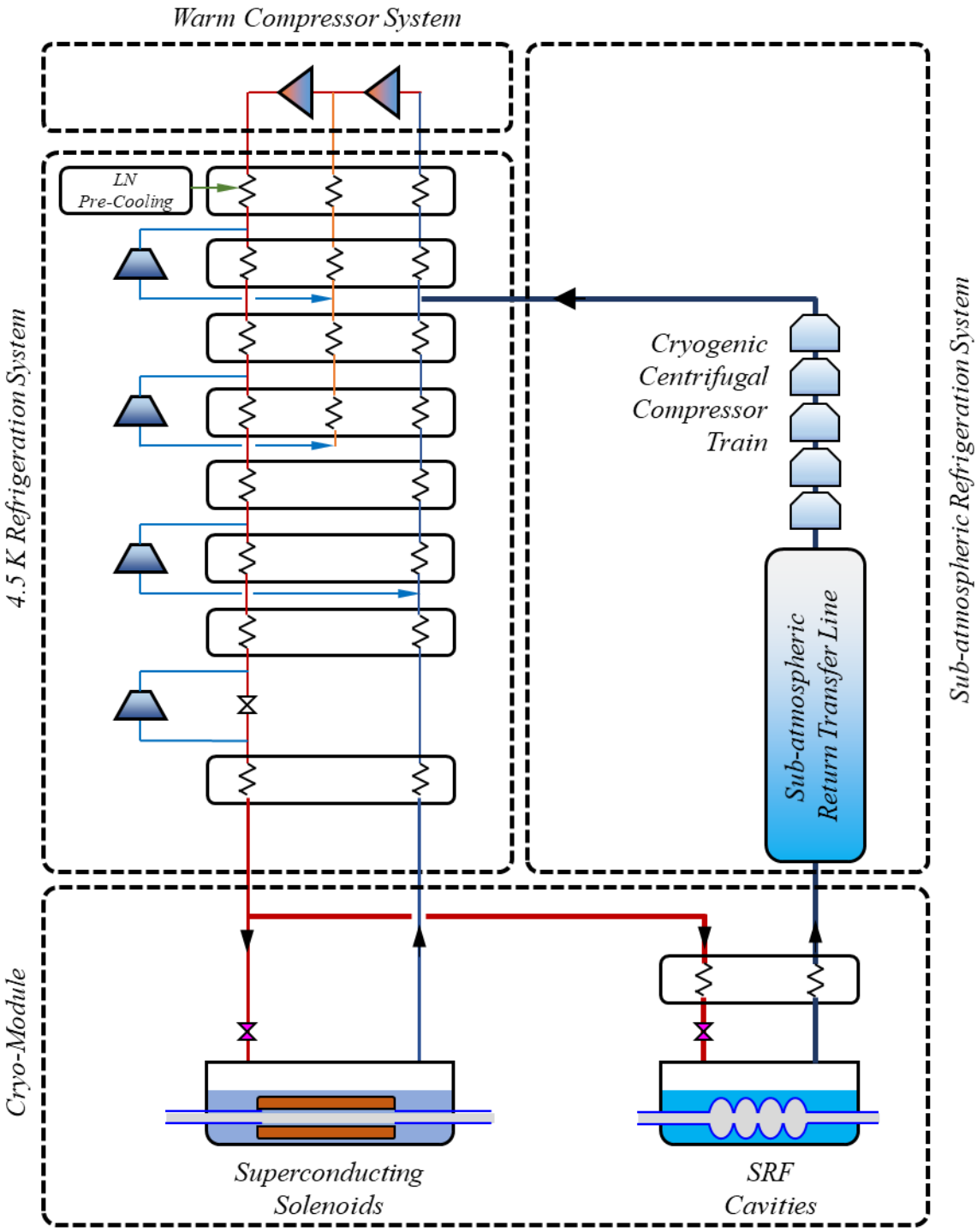

Figure 4.2: *FRIB cryogenic system block diagram*

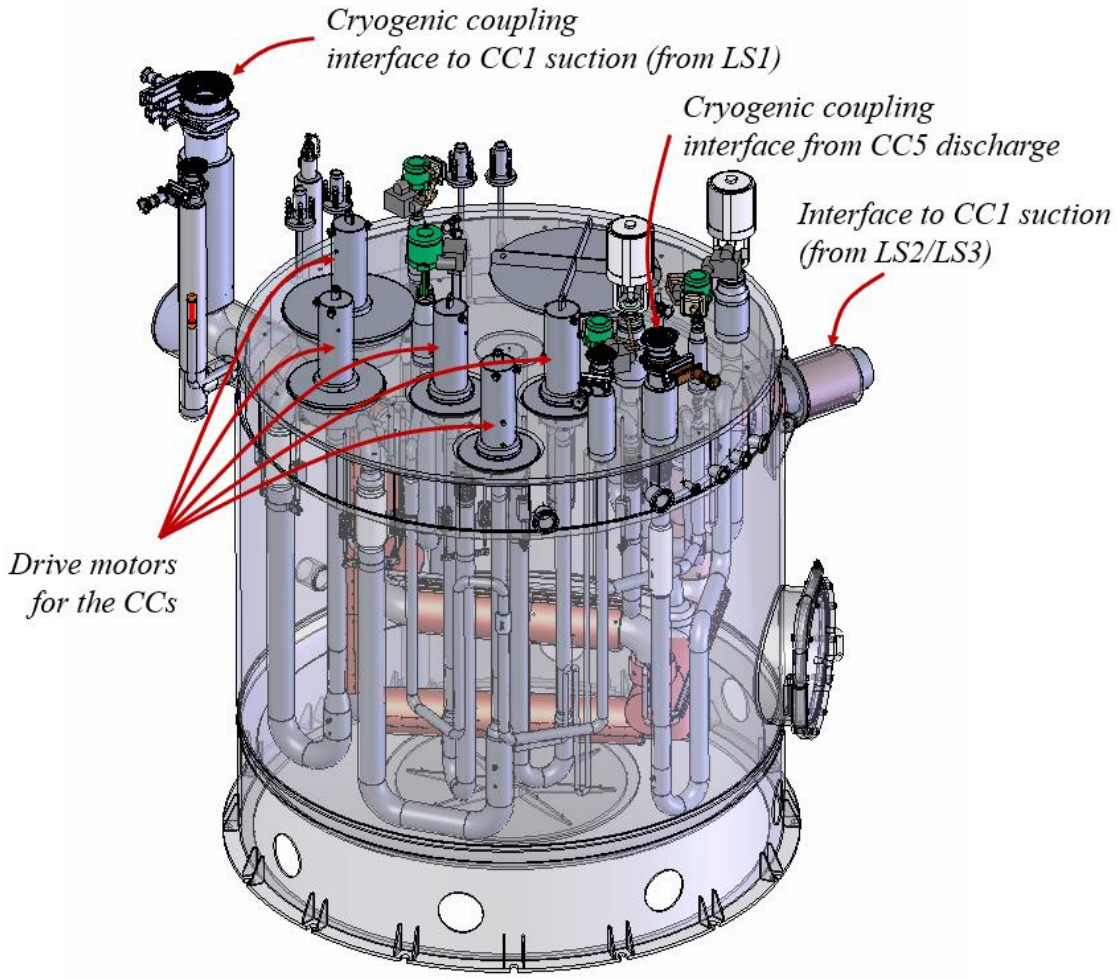

Figure 4.3: *FRIB sub-atmospheric cold box*

The centrifugal compressors vary in overall size and operational speeds, with wheel tip diameters ranging from 200 mm to 85 mm and maximum rotational speeds ranging from 300 to 800 Hz [2]. The compressors operate using 5-axis active magnetic bearings (AMB) and have emergency touch-down mechanical bearings to protect the compressor in the event of sudden signal or power loss. *Figure 4.4* provides a simplified schematic for the compressor assembly, which varies only in component size for each of the five compressors. The centrifugal compressor assembly includes both the housing sub-assembly (*i.e.* diffusers, and volute) and the drive sub-assembly (*i.e.* the compressor impeller mounted to the AMB and drive motor shaft).

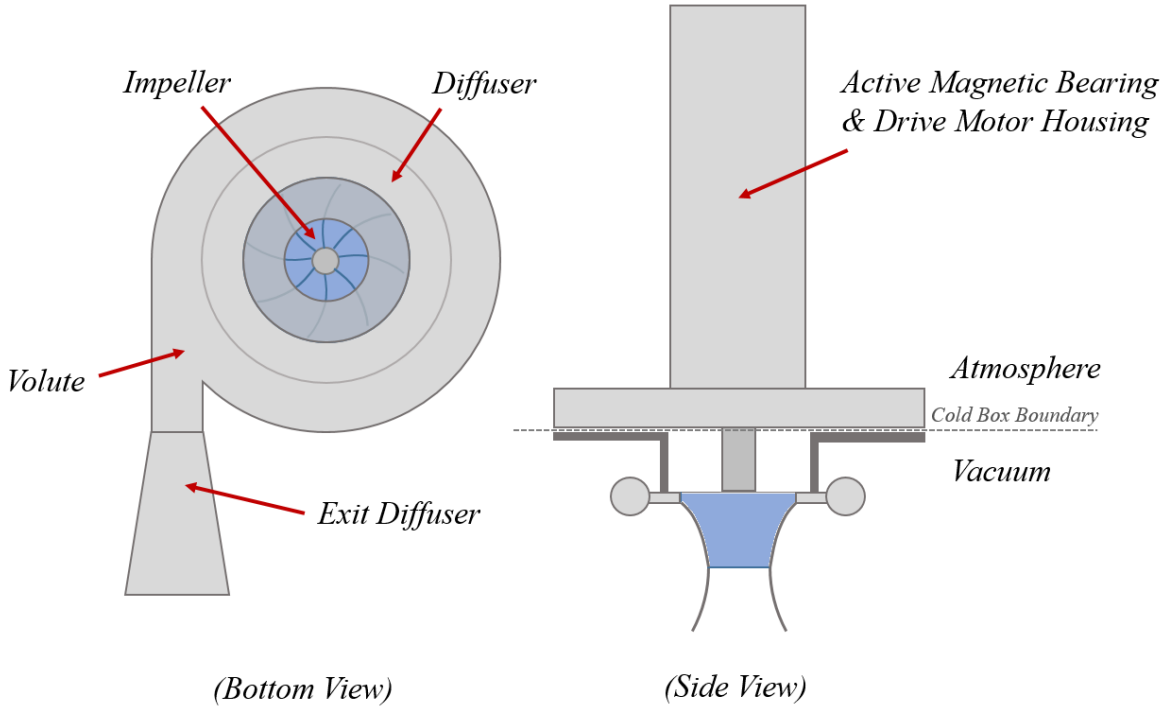

Figure 4.4: *Centrifugal compressor sub-system simplified schematic.*

Centrifugal compressor control at FRIB is presently based on compressor characteristics found through experimentation, and the compressor relative rotational speeds are electronically coupled to each other through experimentally established speed ratios. Reliance on experimentation requires actively exploring new operational regions of interest to expand the flexibility of the 2 K cryogenic system stable operational envelop. Despite the implementation of cryogenic centrifugal compressors in existing large-scale helium cryogenic systems, there is insufficient information available in open-literature to generally characterize the stable performance of these compressors at specified operational conditions.

Accurate prediction of cryogenic centrifugal compressor performance will allow for high-efficiency and reliable wide-range operation of the 2 K helium cryogenic system. A mean-line steady-state model to predict the performance of centrifugal compressors has been previously developed for air applications, as presented in chapter 3 and [3]. This chapter focuses on modifications required to enable the model to estimate the performance of cryogenic centrifugal compressors with helium as the operating fluid. Results from the modified mean-line model are directly compared to design basis performance plots

provided by the centrifugal compressor vendor. Further validation of the model is conducted using experimental test data measurements from the FRIB system that cover a wide range of centrifugal compressor train operation.

4.2 Model Development

Numerical modelling of the cryogenic compressor impeller and diffuser closely followed the procedure outlined in chapter 3. The compressor assembly contains additional components that were not present in chapter 3, *i.e.* the volute and the exit diffuser, which were added to the performance model. Furthermore, while an adiabatic assumption can be reasonably accurate for air compressors operating near ambient conditions, this assumption is no longer valid for cryogenic centrifugal compressors and therefore a heat input term was required to properly account for static heat in-leak. Values for the heat input were based on the predicted design basis static heat in-leak. A brief overview of each compressor section and methodology employed will be provided, with further details found in chapter 3 and [3], as well as other relevant centrifugal compressor literature sources.

Figure 4.5 provides the station locations considered for the centrifugal compressor performance analysis. The station numbers are located where the main calculations of the numerical procedure are conducted. Locations (0) and (6) are the generalized locations for the static pressure and temperature measurements, and at these locations stagnation conditions are calculated from static conditions or vice versa. The centrifugal compressor assembly geometry is split into four distinct regions: the impeller (1-2), the diffuser (2-3), the volute (3-4), and the exit diffuser (4-5). Calculations at station 1, 2 and 5 involve an iterative calculation process, where 3 and 4 are calculated directly or by marching methods moving along the flow mean-line through the component.

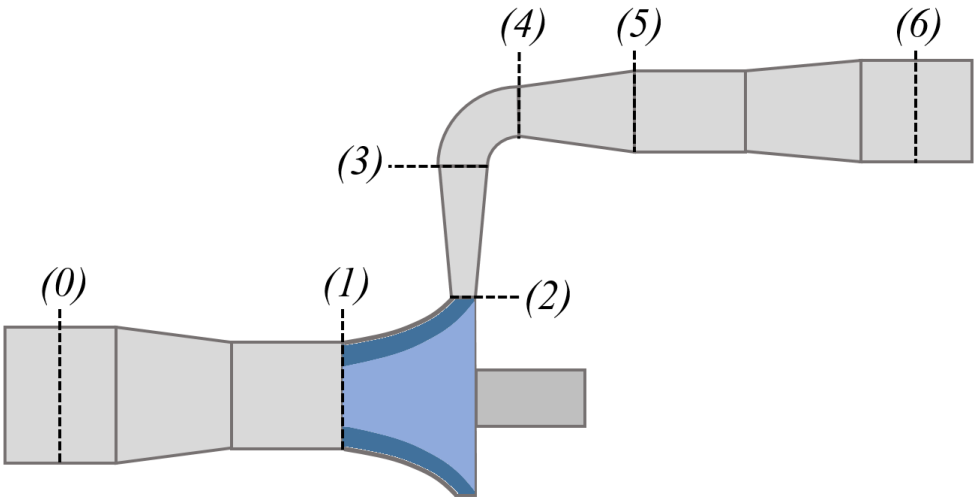

Figure 4.5: *Compressor performance model station locations*

Model input parameters include the compressor geometrical information, rotational speed, and inlet conditions (mass flow rate, temperature, and pressure). The inlet parameters were modified to accept static parameter inputs rather than stagnation. Traditionally, the inlet conditions are provided as stagnation parameters, and an iterative process is executed to solve for the corresponding static conditions and velocities. Experimental data obtained from the FRIB cryogenic system measures pressure and temperature in static form, and therefore the code was modified for input of these static inlet measurements. Using the compressor inlet piping NPS size and the measured mass flow rate, the static conditions were then translated into stagnation conditions required for impeller inlet calculations. Remaining inlet terms are solved using an iterative process, which is manipulating the static density within the inlet region. Iterative density calculations are coupled to the inlet velocity, and since velocity is dependent on the flow area blockage, the inlet static density converges to a condition which satisfies convergence of the flow area and therefore aerodynamic blockage. Estimation for the inlet flow area blockage follows the equations developed by Qui *et al.* [4] and modified by Harley *et al.* [5].

Outlet conditions at the impeller exit were calculated using the same methodology described in chapter 3. One modification that was required was the considered slip factor correlation. The previous correlation utilized in chapter 3 was developed for air compressors and was unable to reasonably predict

results with helium as the working fluid. Further investigation into the applicability of the previous correlation in helium compressors may lead to better results, but due to simplicity and reasonable accuracy the slip factor correlation developed by Wiesner [6] was substituted for slip estimation. Calculation of the outlet thermodynamic properties involves an iterative procedure based on the outlet static density. Using the conservation of energy and momentum along with an initial estimated isentropic efficiency, the impeller outlet pressure, temperature, and density can be calculated. A new isentropic efficiency estimation is then calculated using enthalpy loss correlations, and the outlet parameters are recalculated. This process continues until the impeller outlet density converges to within a set tolerance. The definition of the impeller isentropic efficiency is provided in equations (4.1) through (4.3). It is important to recognize that this is the isentropic efficiency through the impeller, *i.e.* stations (1) to (2), not the isentropic efficiency across the entire compressor assembly.

$$\eta_{s,imp} = \frac{\Delta h_0 - \Delta h_{int}}{\Delta h_0} \tag{4.1}$$

$$\Delta h_0 = C_p(T_{02} - T_{01}) \tag{4.2}$$

$$\Delta h_{int} = \Delta h_{BL} + \Delta h_{CH} + \Delta h_{CL} + \Delta h_{INC} + \Delta h_{MIX} + \Delta h_{SF} \tag{4.3}$$

A solution for the change in thermodynamic properties and flow velocities through the diffuser was obtained using the system of equations provided in chapter 3. Implementing a 4th order Runge-Kutta method, the diffuser was discretized and sequentially marched along the flow mean-line to calculate the parameters at the outlet of the diffuser. In conjunction with this calculation, the diffuser exit was the location selected for the injection of the heat input. For this calculation, the pressure is held constant, and the temperature is calculated based on the conservation of energy. Using the pressure and temperature, an updated value of static density was calculated. Lastly, mass conservation, exit flow area and density were then combined to determine the meridional velocity.

Volute calculations followed the methodology developed by Japikse [7]. This method is based on two parameters, the area ratio between the volute exit and entrance, $AR = A_o/A_i$, and the inlet swirl parameter, $\lambda = (C_u/C_m)_i$. The parameters can then be used to calculate the pressure recovery coefficient and the loss coefficient associated with the volute geometry and inlet flow conditions. Equations (4.4) through (4.8) show the application of these parameters in calculating the outlet pressure –

$$P_R = \frac{P_o - P_i}{P_{0,i} - P_i} \tag{4.4}$$

$$P_R = \frac{2\left(\lambda - {}^{1}/_{AR}\right)}{AR(1+\lambda^2)} \quad for \;\; \lambda AR > 1 \tag{4.5}$$

$$P_R = \frac{\lambda^2 - {}^{1}/_{AR^2}}{1+\lambda^2} \quad for \;\; \lambda AR \leq 1 \tag{4.6}$$

$$K = \frac{P_{0,i} - P_{0,o}}{P_{0,i} - P_i} \tag{4.7}$$

$$K = \frac{1}{1+\lambda^2} \tag{4.8}$$

Finally, the outlet conditions leaving the exit diffuser are calculated using a simplified model based on constant stagnation properties (*i.e.* no losses). Using the area ratio of the exit diffuser, the static density and pressure at the outlet can be estimated using a density iterative procedure that is coupled with the velocity through the diffuser. The approximation described was compared to a more complicated approach utilizing a coupled system of equations accounting for frictional losses and was found to give reasonably accurate predictions for the outlet pressure and temperature while greatly reducing the computational cost of the calculation.

Loss correlation selection has a significant effect on the accuracy of the centrifugal compressor performance prediction. Descriptions of the loss mechanisms and the available open-literature correlations are presented in chapter 2. The loss correlations considered for the mean-line performance model are equivalent to those provided in chapter 3, as shown in *Table 4.1*.

Table 4.1: *Loss correlations for available open-literature sources*

Loss Mechanism	***Loss Enthalpy***	***Loss Identifier***	***Loss Author***
a. Blade Loading	Δh_{BL}	1	*Aungier [8]*
		2	*Coppage et al. [9]*
b. Choking	Δh_{CH}	1	*Aungier [8]*
c. Clearance	Δh_{CL}	1	*Aungier [8]*
		2	*Jansen [10]*
		3	*Krylov & Spunde [11]*
		4	*Rodgers [12]*
d. Disk Friction	Δh_{DF}	1	*Aungier [8]*
		2	*Boyce [13]*
		3	*Daily & Nece [14]*
		4	*Shepherd [15]*
e. Incidence	Δh_{INC}	1	*Aungier [8]*
		2	*Conrad et al. [16]*
		3	*Galvas [17]*
		4	*Gravdahl & Egeland [18]*
		5	*Stanitz [19]*
f. Leakage	Δh_{LK}	1	*Aungier [8]*
		2	*Jansen [10]*
g. Mixing	Δh_{MIX}	1	*Aungier [8]*
		2	*Johnston & Dean [20]*
h. Recirculation	Δh_{REC}	1	*Aungier [8]*
		2	*Coppage et al. [9]*
		3	*Jansen [10]*
		4	*Oh et al. [21]*
i. Skin Friction	Δh_{SF}	1	*Aungier [8]*
		2	*Coppage et al. [9]*
		3	*Galvas [17]*
		4	*Jansen [10]*

An *optimum* set of loss correlation was selected in chapter 3 to fit the experimental data for air compressor applications. A similar optimization to fit measured data obtained from the FRIB helium

cryogenic centrifugal compressors was also performed. The data set consisted of 71 individual points ranging over a large portion of the present FRIB sub-atmospheric system operational range. *Figure 4.6* provides the human machine interface (*HMI*) for the FRIB sub-atmospheric system, showing the various types of measurements and their locations.

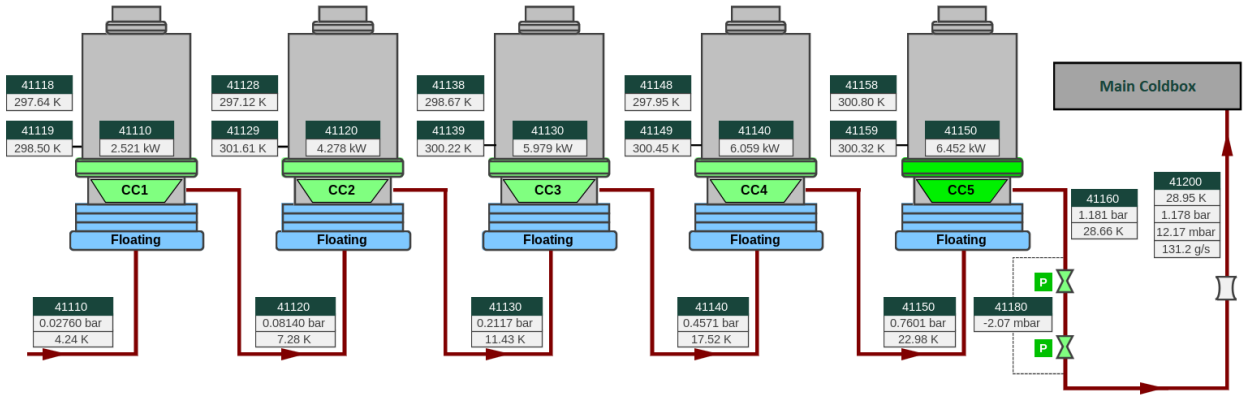

Figure 4.6: *Screenshot of FRIB sub-atmospheric human machine interface (HMI)*

In conjunction with *Figure 4.6*, *Table 4.2* provides supplementary information on the measurement devices employed at FRIB.

Table 4.2: *Characteristics of installed FRIB measurement devices*

Parameter	***Type***	***Vendor***	***Performance***
Temperature	Silicone Diode	Lake Shore Cryotronics	$\pm 12\ mK$
Pressure	Absolute / Differential	Rosemount	$\pm 0.10\%\ of\ span$
Venturi	ASME	Primary Flow Signal	$\beta = 0.45$ $Pipe\ ID = 4.26\ in$

For each of the centrifugal compressors, an average RMS error between the performance model prediction and the experimentally measured data was captured for every possible loss correlation combination. These loss correlation sets were then ranked from minimum to maximum average RMS error, and the resulting set rankings are shown in *Figure 4.7*.

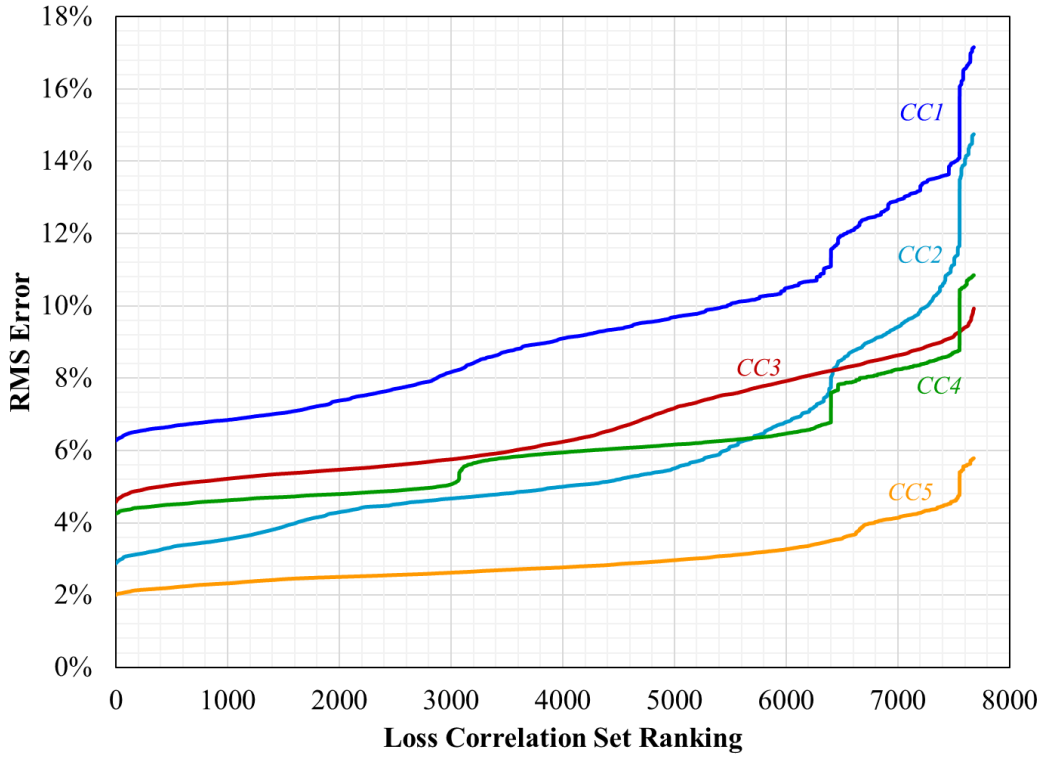

Figure 4.7: *Loss correlation set ranking for each individual compressor*

While there is an *optimal* loss correlation set for each of the centrifugal compressors, the highest ranking loss correlation set are not equivalent for every compressor. A comparison between the loss correlation selection for an air compressor and each of the FRIB compressors can be found in *Table 4.3*.

Table 4.3: *Loss correlation selection comparison between air compressors and FRIB compressors*

Loss Mechanism	***Air***	***CC1***	***CC2***	***CC3***	***CC4***	***CC5***
Blade Loading	2	1	2	2	2	2
Choking	1	1	1	1	1	1
Clearance	2	1	1	3	1	1
Disk Friction	3	4	1	1	1	1
Incidence	3	2	4	4	2	2
Leakage	1	1	1	1	1	1
Mixing	2	1	1	2	1	1
Recirculation	4	3	3	3	3	3
Skin Friction	1	1	3	3	1	3

During the loss correlation selection process, only the average RMS error was considered for the overall ranking. Another aspect of the performance model that is important to accuracy and general applicability is the maximum and minimum RMS error across the experimental data. *Table 4.4* shows that the variance in RMS error for each compressor reduces when moving through the compressor train.

Table 4.4: *Meanline model data set error using individual loss correlation sets*

RMS Error	***CC1***	***CC2***	***CC3***	***CC4***	***CC5***
Minimum [%]	3.6	0.9	3.9	3.0	1.1
Average [%]	6.3	2.9	4.6	4.3	2.0
Maximum [%]	9.8	7.3	7.0	6.4	3.3

Lastly, investigation was made into the use of CC5's loss correlation set across all five individual compressors. During the design and commissioning process of a cryogenic centrifugal compressor system, it is unlikely that there is sufficient experimental data to select a new set of optimal loss correlations for specific compressor geometries or operational conditions. Therefore, the RMS error was calculated for each compressor when solely using the loss correlation set optimized for CC5. Results from this calculation are provided in *Table 4.5*. Although there is a slight increase in both the average and variance of the RMS error, results from the performance model are reasonably accurate and can provide beneficial insight into compressor train performance prior to experimental testing.

Table 4.5: *Meanline model data set error using CC5 loss correlation set*

RMS Error	***CC1***	***CC2***	***CC3***	***CC4***	***CC5***
Minimum [%]	3.6	1.5	4.0	2.9	1.1
Average [%]	6.5	3.2	7.6	4.3	2.0
Maximum [%]	9.4	8.8	11.6	6.4	3.3

4.3 Model Validation

Validation of the helium centrifugal compressor performance model initially involved direct comparison between model results and design basis performance prediction. Performance maps developed during the design phase of the centrifugal compressors were provided to FRIB through the compressor vendor, and these maps conveyed the operational region or envelope of the compressor. Individual performance maps corresponding to each compressor were available, and the maps included the estimation of surge and choke margin lines and anticipated pressure ratio values along constant impeller rotational speed lines. While extensive experimental data was captured during operation of FRIB system, these data points are insufficient in fully capturing the performance characteristics over the entire range presented in the design basis performance maps.

Surge and choke conditions are critically important to centrifugal compressor operation, as these regions must be avoided due to flow instability within the impeller (caused by exceeding minimum or maximum mass flow limitations) resulting in decline of compressor isentropic efficiency and increased probability of compressor failure or component structural damage. Safety measures are implemented into the control system for compressor operation to ensure that system shutdown will occur before reaching these regions, but a clear understanding of the margin between operational points and surge or choke conditions is important to ensure reliable steady-state operation. The performance model predicts the surge and choke lines using the methodology described in chapter 3, namely using a diffusion ratio through the impeller to quantify surge conditions and a rapid decrease in isentropic efficiency to quantify choke conditions. Specific criteria used presently for helium centrifugal compressor are given in equations (4.9) and (4.10) below. Due to the lower gradient in isentropic efficiency at lower pressure ratios, additional criteria of a minimum isentropic value of 40 percent is also imposed, below which the compressor is considered to be choked. Equivalent criteria (*i.e.* no modification) was used across all of the compressors. Caution should be taken when applying the criteria for choking conditions, as equation (4.10) corresponds to a mass flow step change of 1 gram per second.

$$D_R = \frac{W_{1s}}{W_2} > 1.65 \tag{4.9}$$

$$\Delta\eta > 2\% \tag{4.10}$$

Results obtained from the mean-line performance model are compared to the design basis curves including both surge and choke in *Figure 4.8*. The plotted surge and choke lines are calculated with the mean-line model using nominal design inlet conditions for each of the individual compressors. Model predicted surge and choke curves follow nearly identical paths as the design basis performance map curves, with a slight discrepancy in the predicted choke line.

Along with direct comparison to design basis estimations, experimentally measured data obtained at FRIB was plotted along with the predicted operational region to observe how the surge and choke lines relate to actual measurements. Predicted operational regions from the model and design basis capture the experimental data completely for *CC2* through *CC5*, with some discrepancy for *CC1*. Maximum design flow at FRIB requires *CC1* to operate at a significantly higher pressure ratios than observed during the nominal flow conditions, and the design basis choke line does not accurately capture this operating region. The mean-line model is capable of predicting this region of interest, and captures all experimental data within the predicted operating range.

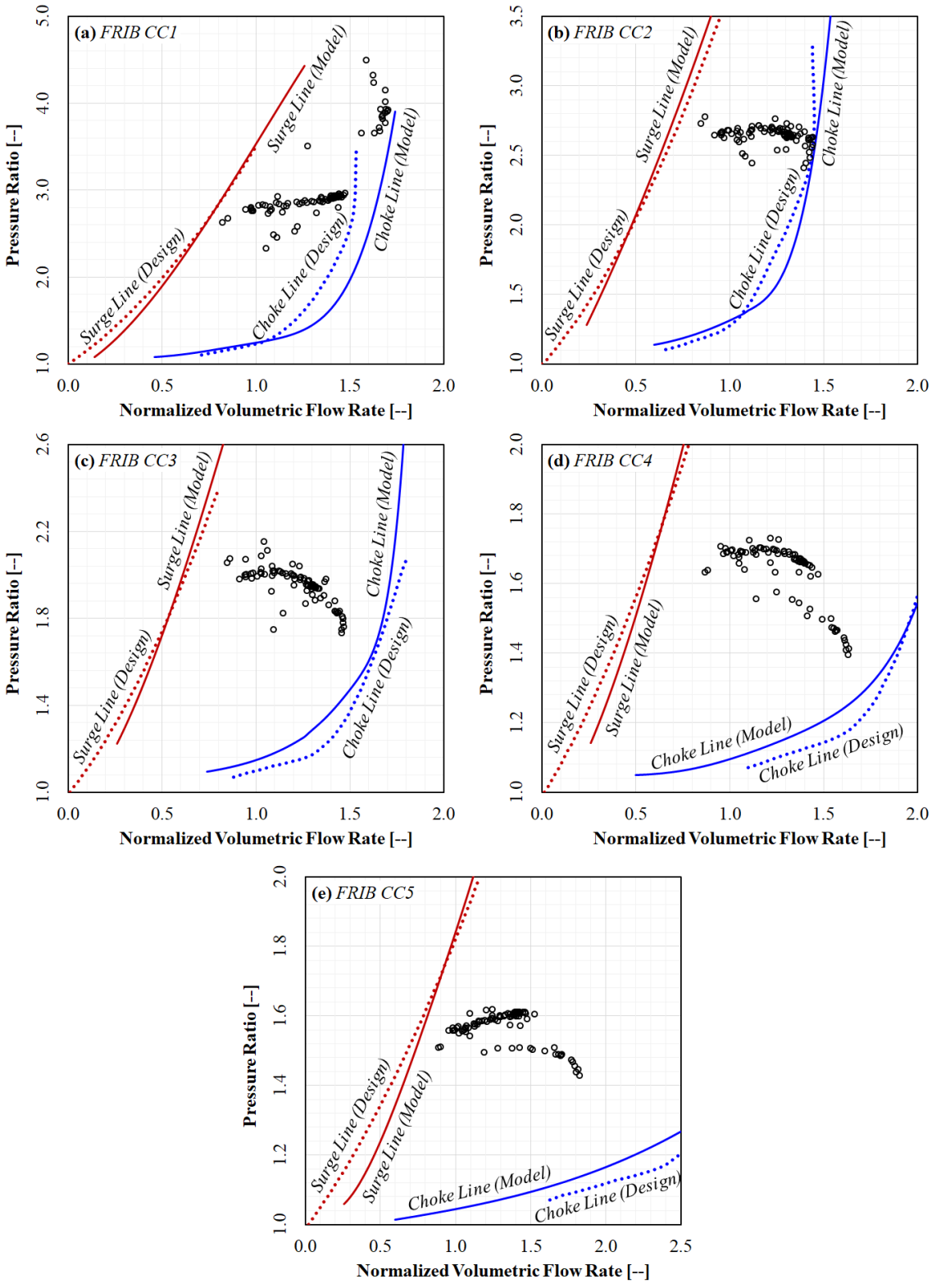

Figure 4.8: *Comparison of estimated (mean line model) and design surge and choke lines for FRIB cryogenic centrifugal compressors on their respective performance maps.*

Estimated performance of the cryogenic centrifugal compressors along constant rotational speed lines were also provided through the design basis performance maps. The speed lines cover nearly the full operational range for each compressor, and specified non-dimensional rotational speeds ($\overline{N}$) are given for each of the speed lines. The rotational speeds are non-dimensionalized by using the design speed at a reference condition. Therefore, this enabled an insightful comparison between mean-line and design basis performance predictions over a large operational range. Using known rotational speeds, and assuming inlet conditions corresponding to the nominal design condition, speed lines were developed using the mean-line model for each compressor geometry.

Comparison between the mean-line model results and the design basis can be seen in *Figure 4.9*. Similar trends are observed between the mean-line model and the design basis estimation, but there is a distinct shift between the results. The downward shift in the mean-line model prediction may be due to several contributing factors discussed below.

As described previously, inlet conditions and non-dimensional speed line values were assumed to correspond to nominal design conditions provided through the design basis documentation. Ambiguity in the actual conditions that were utilized for these calculations result in an assumption which may be incorrect. Adjustments in the inlet conditions and rotational speeds of the compressors were found to have a significant impact on the performance and trends of the speed lines, and thus any changes in these values can cause appreciable offset in the estimated performance values.

Within the mean-line model itself, the application of the slip factor correlation and selected loss correlations can have a large influence on the performance prediction. The slip factor correlation employed remains constant across different operating conditions and was developed for air compressors. Viscosity of helium is an order of magnitude less than that of air during normal operation, and therefore the flow through the helium compressor should behave closer to a potential flow. Likewise, all loss correlations were developed for air compressors and may provide inaccurate loss estimates for helium applications.

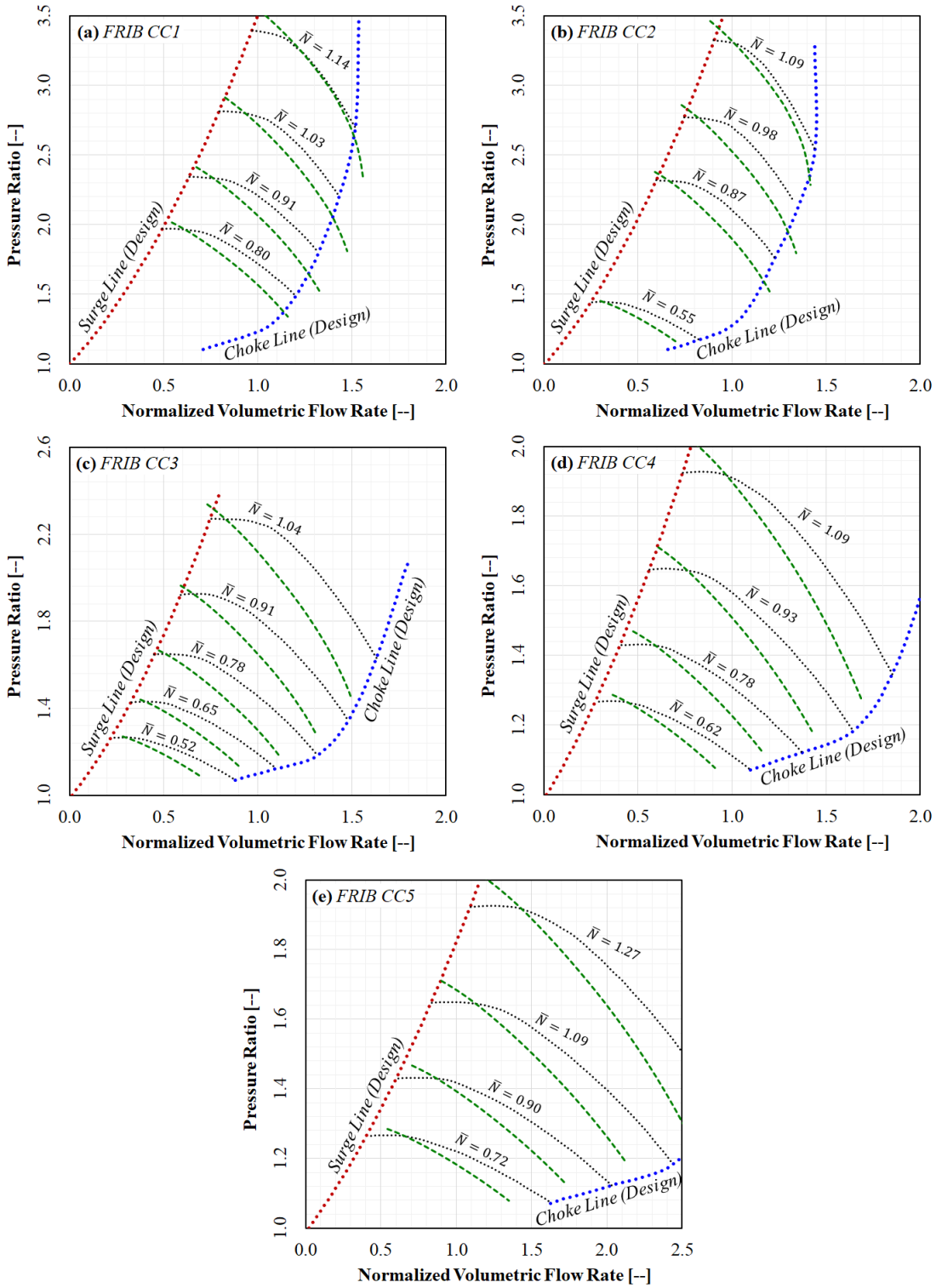

Figure 4.9: *Comparison of estimated (mean-line model) and design iso-speed lines for FRIB cryogenic centrifugal compressors on their respective performance maps (black dotted lines – design, green dashed lines – model).*

Supplementary validation of the mean-line model was conducted through comparison against measured performance data obtained from the FRIB cryogenic system. For conciseness, the pressure ratio, temperature, and efficiency were compared to four individual data sets, which are described in *Table 4.6*. The modes referred as '*design*' corresponds to the actual (measured) operating points near the design conditions, and the '*operation*' mode corresponds to the present (*CY2023*) steady-state operating point at FRIB.

Table 4.6: *Measured data points at various operating modes*

Operating Mode	$\dot{\mathbf{m}}$ [g/s]	$\mathbf{P_i}$ [bar]	$\mathbf{T_i}$ [K]	$\bar{N}_1$ [--]	$\bar{N}_2$ [--]	$\bar{N}_3$ [--]	$\bar{N}_4$ [--]	$\bar{N}_5$ [--]
Minimum (Design)	104.5	0.029	4.12	1.013	1.018	1.020	0.976	0.977
Nominal (Operation)	128.3	0.029	4.21	1.053	1.000	1.026	0.995	0.995
Nominal (Design)	151.0	0.029	4.10	1.031	1.024	1.032	1.036	1.037
Maximum (Design)	180.4	0.029	4.02	1.127	1.072	1.069	1.046	1.047

The mean-line calculations were directly compared to the four operating mode measurements associated with each of the cold compressors. The model initially used measured data as the inlet for each cold compressor individually, meaning that the cold compressors were not coupled together. *Figure 4.10* shows the pressure ratio, temperature ratio, and isentropic efficiency model estimations as compared to the measured results for each of the operating modes. Overall, there is reasonable agreement between pressure ratio and temperature ratio, but discrepancies are observed between the predicted efficiency and the efficiency calculated from measurement values.

As with the comparison to the design basis estimations, these discrepancies likely stem from the development of the employed slip and loss correlations. Furthermore, error due to calibration of the pressure and temperature measurements can produce inaccuracy in the experimental data measurements, which will not be captured in the mean-line model.

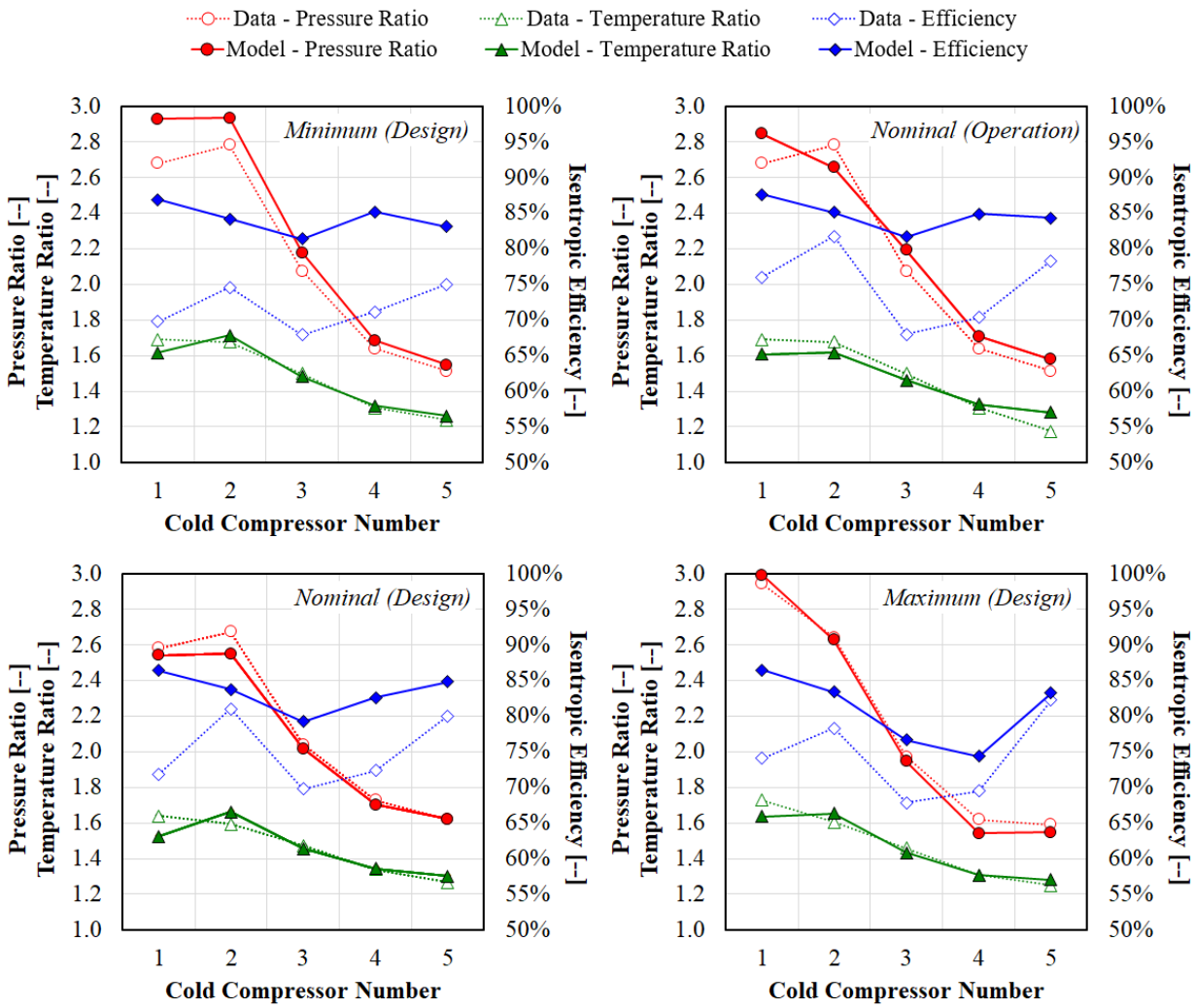

Figure 4.10: *Individual cold compressor pressure ratio and isentropic efficiency estimation.*

After individual compressor analysis, a complete train prediction was enabled within the mean-line model by selecting the estimated outlet pressure and temperature of each cold compressor as the inlet condition for the subsequent compressor. When using this method, only the inlet pressure and temperature into *CC1* and speed ratios for *CC1* through *CC5* were required. Adjustment of the rotational speed of *CC5* was made to match the measured compressor train outlet pressure, establishing the pressure ratio, temperature ratio and isentropic efficiencies for the entire compressor train. *Figure 4.11* provides a comparison between the mean-line model results and measured data for pressure ratio, temperature ratio,

and isentropic efficiencies for each operating mode. Larger discrepancies are again observed in the isentropic efficiency.

Under-prediction of the pressure ratio for *CC1* and *CC2* is directly related to the speed ratio coupling to *CC5*. With higher predicted isentropic efficiency than observed in operation, the helium density in later stages of the compressor train is substantially larger due to lower predicted temperatures. Density error propagates through the compressor train, and therefore this error has minor effects on *CC1* and *CC2*. *CC3* through *CC5* observe increased pressure ratio and requires the entire compressor train to lower speed to match the compressor train outlet pressure, but this effectively lowers the pressure ratio of *CC1* and *CC2*.

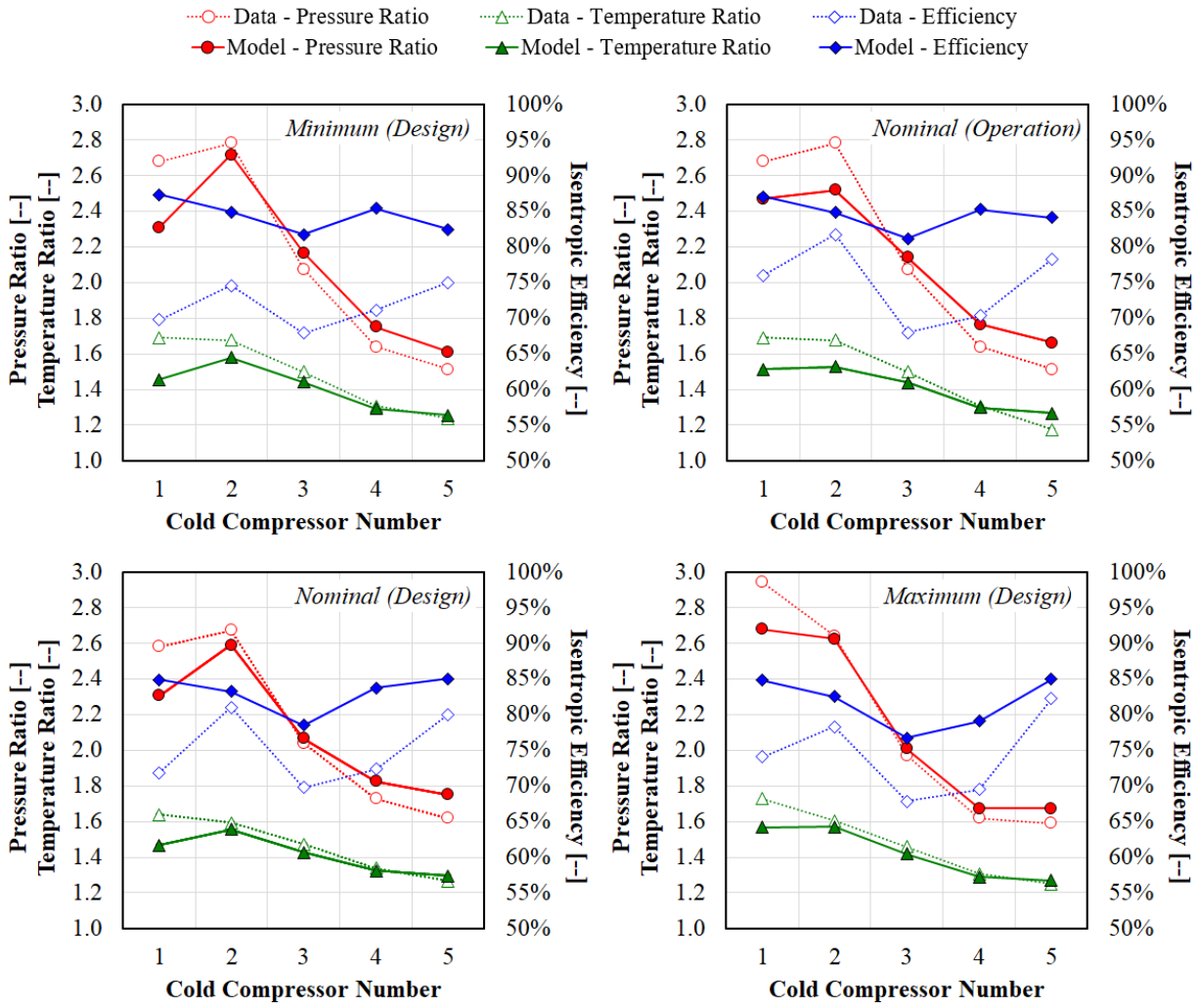

Figure 4.11: *Cold compressor train pressure ratio and isentropic efficiency estimation.*

4.4 Selection of Optimum Steady-State Operating Parameters

The main objective of the mean-line performance prediction model is the estimation of appropriate speed ratios at steady-state operation conditions. After validation of the mean-line model, the model was utilized in the selection of speed ratios that will provide *optimal* stability at operational conditions of interest. In conjunction with the mean-line model, the design basis performance maps were digitized to enable speed ratio prediction using numerical interpolation methods.

Determination of the operational points which provide sufficient stability margin involved the surge line prediction, as described earlier in this chapter. Normalized performance plots with the estimated surge line were used to calculate volumetric flow surge margins for each individual compressor. It has been observed during FRIB operation that the surge margin for the larger wheels (*i.e. CC1 – CC3*) has a greater impact on overall stability than the smaller wheels (*CC4* and *CC5*). Therefore, weights were chosen for the surge margin calculation such that the margin for the larger wheels had more influence on the optimal operational point selection. A weighting factor of three was chosen for *CC1* and *CC2*, two for *CC3*, and one for *CC4* and *CC5*. The product of these weighting factors and the volumetric flow margin between the operational point and the surge line were calculated for all compressors individually, and the summation of the margins was maximized using an excel solver solution. Solving this also requires the input of estimated isentropic efficiencies for each compressor, which was obtained from calculating an average value from measured FRIB data. *Figure 4.12* provides the location of the optimized steady-state operational points for each compressor.

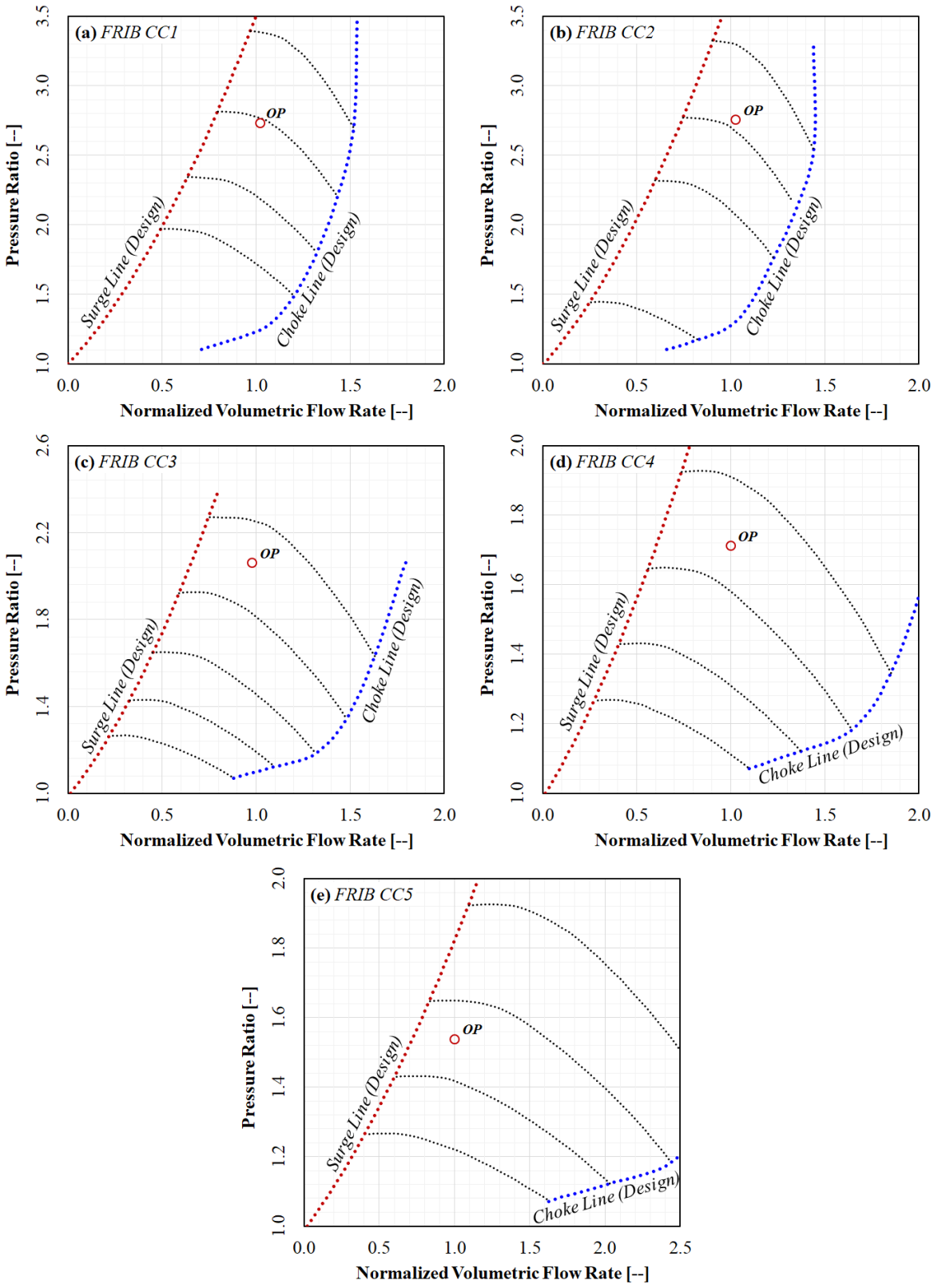

Figure 4.12: *Steady-state operational point of interest*

Due to the coupling between the compressors, the *optimal* operational point corresponding to a maximum weighted volumetric surge margin may be somewhat unintuitive. While each compressor can decrease the pressure ratio value for a corresponding normalized volumetric flow rate to increase surge margin, the overall train pressure ratio would then be insufficient. The reduction in pressure ratio would then require recuperation from the remaining compressors, moving these compressors towards their respective surge limits. Additionally, the volumetric flow rate for each compressor is directly coupled to the pressure ratio and isentropic efficiency of the previous compressor. Variance in the pressure ratio of an upstream compressor can have significant impact on the volumetric flow rate of downstream compressors.

Speed ratio calculations for the *optimal* operational points were completed using both the mean-line performance model and interpolation of the design basis performance map. *Table 4.7* provides both the normalized wheel speed and speed ratio for each of the compressors, and the variance between the design basis and mean-line model calculations. The wheel speed was normalized using the nominal design point wheel speed, as established in the design of the compressor system. Variance between the design basis and mean-line model is below 4% for all compressors, showing good agreement between the two calculation methods. The application of these speed ratios, and the ability for calculation of speed ratios at other operational points of interest, will improve stability of steady-state operation of the FRIB sub-atmospheric system. Due to the higher assumed accuracy of the vendor provided performance maps and the ease of model use (within excel), the performance model which utilizes the vendor provided performance maps was implemented for subsequent cryogenic centrifugal compressor analysis pertaining to the FRIB system.

Table 4.7: *Speed ratio estimation at the optimal operational point*

	Normalized Wheel Speed			**Speed Ratio**		
Cold Compressor Number	*Design Performance Map*	*Mean-line Model Estimation*	*Variance*	*Design Performance Map*	*Mean-line Model Estimation*	*Variance*
	[--]	[--]	[%]	[--]	[--]	[%]
1	1.032	1.051	1.89	0.304	0.312	2.62
2	1.022	1.033	1.08	0.604	0.615	1.80
3	0.979	1.008	3.03	0.823	0.854	3.76
4	0.991	1.004	1.33	1.000	1.020	2.05
5	0.991	0.984	-0.71	--	--	--

4.5 Conclusions

An accurate prediction of cold-compressor performance will enable more robust and efficient control and operation of the sub-atmospheric cryogenic system at FRIB at various operational requirements. Through the modification of a previously developed centrifugal compressor performance prediction methodology, a mean-line steady-state numerical model for helium cryogenic centrifugal compressors was developed. Loss model correlations for centrifugal compressors with helium as the operating fluid were selected by minimizing RMS error between model prediction and extensive FRIB measured data. Using design basis performance maps and measured FRIB system data, the mean-line model was validated and showed reasonable accuracy over large operational regions. Initial estimation of the performances of individual cryogenic centrifugal compressors as well as the entire string of compressors at FRIB were compared to measurements acquired during FRIB cryogenic system commissioning and performance testing. Research which could further benefit the mean-line model includes investigation into the observed discrepancies in isentropic efficiency prediction, *i.e.* loss correlation development for helium compressors and the application of more accurate slip correlations to properly capture impeller performance.

REFERENCES

[1] V. Ganni, D. Arenius, B. Bevins, W. Chronis, J. Creel, J. Wilson Jr, Design, Fabrication, Commissioning, and Testing of a 250 g/s, 2-K Helium Cold Compressor System, in: AIP Conference Proceedings, American Institute of Physics, 2002, pp. 288-304.

[2] P. Knudsen, V. Ganni, F. Casagrande, A. Fila, N. Hasan, M. Wright, G. Vargas, N. Joseph, Design, Fabrication, Commissioning and Testing of FRIB 2 K Cold Compressor System, in: IOP Conference Series: Materials Science and Engineering, IOP Publishing, 2020, pp. 012092.

[3] J. Howard, P. Knudsen, A. Engeda, Empirical Loss Model Optimization for the Prediction of Centrifugal Compressor Off-Design Performance, in: ASME Turbo Expo 2023: Turbomachinery Technical Conference and Exposition, 2023.

[4] X. Qiu, D. Japikse, M. Anderson, A Meanline Model for Impeller Flow Recirculation, in: Turbo Expo: Power for Land, Sea, and Air, 2008, pp. 1687-1694.

[5] P. Harley, S. Spence, D. Filsinger, M. Dietrich, J. Early, Meanline Modeling of Inlet Recirculation in Automotive Turbocharger Centrifugal Compressors, Journal of Turbomachinery, 137(1) (2015) 011007.

[6] F. Wiesner, A Review of Slip Factors for Centrifugal Impellers, (1967).

[7] D. Japikse, Centrifugal Compressor Design and Performance, 1996.

[8] R.H. Aungier, Mean Streamline Aerodynamic Performance Analysis of Centrifugal Compressors, (1995).

[9] J. Coppage, F. Dallenbach, H. Eichenberger, G. Hlavaka, E. Knoernschild, N. Van Lee, Study of Supersonic Radial Compressors for Refrigeration and Pressurization Systems, Wright Air Development Center, 1956.

[10] W. Jansen, A Method for Calculating the Flow in a Centrifugal Impeller when Entropy Gradients are Present, Inst. Mech. Eng. Internal Aerodynamics, (1970).

[11] E. Krylov, Y.A. Spunde, About the Influence of the Clearance Between the Working Blades and Housing of a Radial Turbine on its Exponent, Physics, Engineering, 9 (1967).

[12] C. Rodgers, A Cycle Analysis Technique for Small Gas Turbines, in: Proceedings of the Institution of Mechanical Engineers, Conference Proceedings, SAGE Publications Sage UK: London, England, 1968, pp. 37-49.

[13] M.P. Boyce, New Developments in Compressor Aerodynamics, in: Proceedings of the 1st Turbomachinery Symposium, Texas A&M University. Gas Turbine Laboratories, 1972.

[14] J.W. Daily, R.E. Nece, Chamber Dimension Effects on Induced Flow and Frictional Resistance of Enclosed Rotating Disks, (1960).

[15] D.G. Shepherd, Principles of Turbomachinery, Macmillan, 1956.

[16] O. Conrad, K. Raif, M. Wessels, The Calculation of Performance Maps for Centrifugal Compressors with Vane-island Diffusers, Performance prediction of centrifugal pumps and compressors, (1979) 135-147.

[17] M.R. Galvas, Fortran Program for Predicting Off-design Performance of Centrifugal Compressors, 1973.

[18] J.T. Gravdahl, O. Egeland, Centrifugal Compressor Surge and Speed Control, IEEE Transactions on control systems technology, 7(5) (1999) 567-579.

[19] J.D. Stanitz, Effect of Blade-thickness Taper on Axial-velocity Distribution at the Leading Edge of an Entrance Rotor-blade Row with Axial Inlet, and the Influence of this Distribution on Alignment of the Rotor Blade for Zero Angle of Attack, 1953.

[20] J. Johnston, R. Dean Jr, Losses in Vaneless Diffusers of Centrifugal Compressors and Pumps: Analysis, Experiment, and Design, (1966).

[21] H.W. Oh, E.S. Yoon, M. Chung, An Optimum Set of Loss Models for Performance Prediction of Centrifugal Compressors, Proceedings of the Institution of Mechanical Engineers, Part A: Journal of Power and Energy, 211(4) (1997) 331-338.

CHAPTER 5 : DEVELOPMENT AND CHARACTERIZATION OF OPTIMUM 'PUMP-DOWN' PATH FOR FRIB SUB-ATMOSPHERIC REFRIGERATION SYSTEM

5.1 Introduction

The operation of centrifugal '*cold*' compressors in cryogenic systems can be very challenging. The operational challenges are mainly relating to the stability and control of the compressor train – in both steady and transient operating states. A multi-stage centrifugal compressor train for sub-atmospheric helium cryogenic system was first deployed for the Tore Supra tokamak in the mid-1980s [1], but this system used partial compression (from 13 to 80 mbar) with two centrifugal compressor stages and relatively low capacity (15 – 20 g/s). The centrifugal compressor train commissioned at the Continuous Electron beam Accelerator Facility (CEBAF) in 1994 was the first full '*cold-compression*' helium cryogenic system. This system was innovative and was on the cutting edge of sub-atmospheric technology at the time, and there were significant obstacles to overcome for the design, implementation and reliable operation of these devices. It used four centrifugal compressor stages in series to obtain the full '*cold-compression*' (30 mbar to 1.15 bar), with a significantly larger capacity (up to 230 g/s) than its predecessor. A historical perspective of the problems encountered at CEBAF and the efforts to reliably operate this system is discussed in [2]. Additional insight on this systems design, installation, and control methodologies can be found in [3]. Since the early 1990s, control philosophy for the stable and reliable operation of these systems have been relying heavily on experimentation (trial and error basis) and thereby limiting the operational envelop. Moreover, unlike their non-cryogenic counter parts, these systems are required to be operated through a relatively prolonged transient operating phase to reach the steady-state operation. Such a mode of operation is known as '*pump-down*', where the cryogenic loads (cryo-module liquid helium bath) and the vapor return (cryogenic) transfer lines are evacuated from approximately 1.1 bar to the operating pressure (approximately 30 mbar).

Optimization of the required '*pump-down*' time while maintaining the stability and reliability of the system depends on several parameters, such as speeds of the individual compressors and transient

variation of the mass flow rate (‘*pump-down*’ flow) within the constraints of the cryogenic centrifugal compressors and the supporting 4.5 K refrigerator system. The system pressure and the required ‘*pump-down*’ time is directly coupled to the pumped mass flow rate. The stability of the centrifugal compressor depends on the pumped mass flow rate and system pressure at a given rotational speed (and the pressure ratios across the compressors). To minimize the required ‘*pump-down*’ time, the mass flow rate during this process needs to be maximized while satisfying the choke margin of the cold compressor train as well as the capacity of the 4.5 K refrigeration system. On the other hand, selecting a very low mass flow rate will result in long ‘*pump-down*’ time and might also fall beyond the surge line of the compressor train. Hence, a transient mass flow ramp is required that varies from maximum allowable flow within 4.5 K refrigerator limits at the beginning (due to low volume flow rate at high suction pressure) to the operating mass flow at the end. There are several other system parameters that affect the optimization of this process, such as pumped-out system volume (including the return transfer line, cryostat ullage spaces) and heating of the fluid during this process (isothermal and non-isothermal). However, these parameters are fixed for a given system and are not considered as variables.

Historically, one of the cryogenic centrifugal compressors (typically the final stage in the compressor train with the smallest wheel diameter) was assigned as the leading compressor and the speed was actively controlled to maintain a prescribed mass flow rate. The rest of the centrifugal compressors (*CCs*) served as secondary compressors with their speeds individually controlled via assigned electronic speed ratios with respect to the lead compressor (*i.e.* CC5 for FRIB system). In most cases [3], the vendor provided steady-state performance maps couldn’t be validated prior to the ‘*pump-down*’ process and a trial and error solution was adopted. For the FRIB cryogenic centrifugal compressors, both the mass flow rate ramp and the required speed ratios for each of the compressors were obtained using a trial and error basis. An example of the mass flow ramp and compressor speed ratios used during a successful ‘*pump-down*’ sequence at FRIB is provided in *Figure 5.1*. It is observed that a variable speed ratio for each compressor in the cryogenic centrifugal compressor train was used and that the mass flow ramp was also discrete.

The numerous successful '*pump-down*'s achieved (through trial and error basis) previously in several sub-atmospheric systems using cryogenic centrifugal compressors are an important part of the overall understanding of these systems. However, a theoretical basis for this process to explain the observed trends as well as formulate the process path for present and future systems was absent. This chapter focuses on the transient '*pump-down*' process and the development of a theoretical basis for it. The following sections cover both the development of the theoretical models, the implementation of the model prediction in system operation, and the results between theoretical predictions and measured test data.

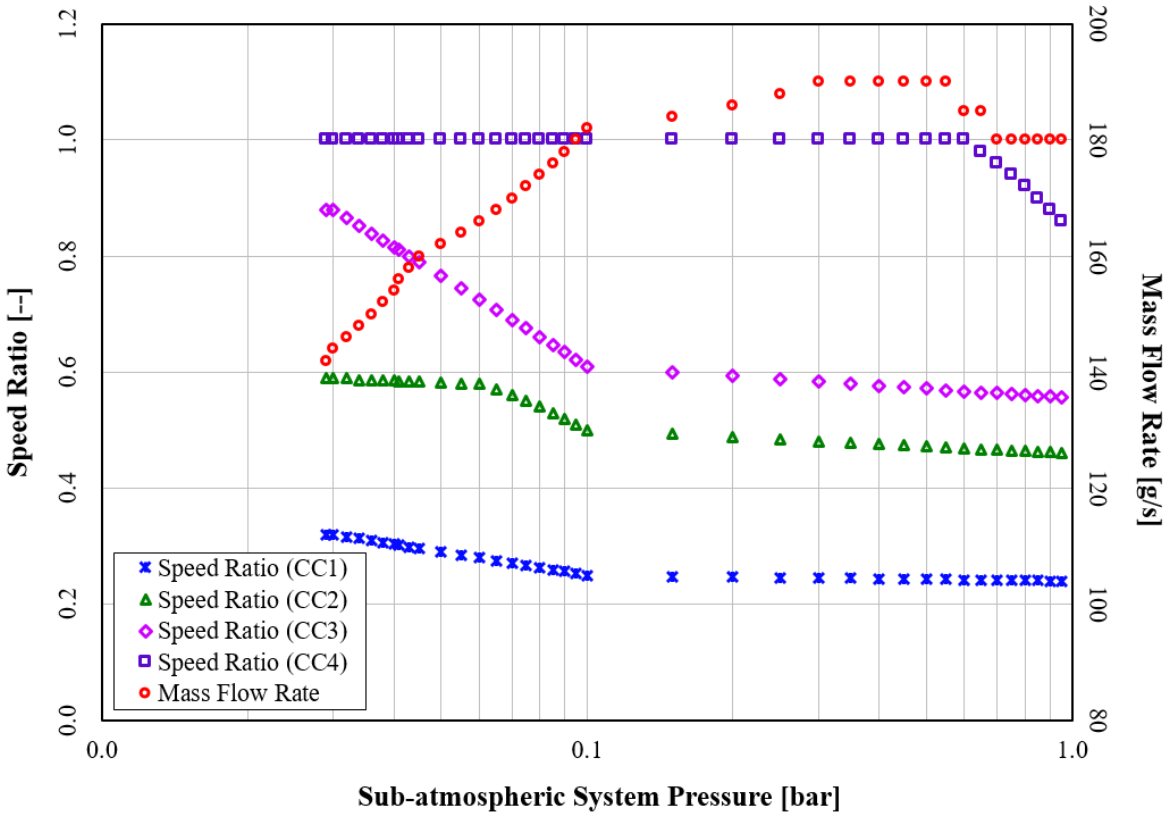

Figure 5.1: *Mass flow rate and secondary centrifugal compressor (CC1-CC4) speed ratios traditionally used (up to CY2022) for FRIB sub-atmospheric system 'pump-down'.*

5.2 Model Development

5.2.1 Theoretical Model for the FRIB 2K Sub-atmospheric System

A theoretical model for the FRIB sub-atmospheric system is developed based on the work proposed by Dinger [4], and Bottura and Rosso [5]. A schematic of this system is presented in *Figure 5.2*. The sub-atmospheric system is divided into four segments; the cryostat saturated liquid helium bath and the heat exchanger (shown in *Figure 5.2* as control volumes CV-1 and CV-2), the helium vapor return transfer line (shown in *Figure 5.2* as control volume CV-3) and the cryogenic centrifugal compressor train. The theoretical model presented in this section is developed using control volumes CV-1, CV-2 and CV-3.

For a given fluid volume (stored liquid, ullage space in the cryostats, and the vapor return transfer lines), and heat input to the control volumes, the transient response of the pressure following a specified compressor mass flow rate ($\dot{m}_{CC}$) is modeled. For the sake of simplicity, pressure drop across the saturated liquid helium bath, heat exchanger return stream and the vapor return transfer line is ignored and the uniform return stream pressure across the three control volumes CV-1, CV-2 and CV-3 is denoted by p_i. The heat input to control volume CV-1 (cryostat) is considered isothermal. It is sub-divided into two parts, the persistent parasitic heat in-leak, $\dot{q}_{static}$, and the applied heat (either due to losses from the SRF cavity or due to electric heating for capacity modulation), $\dot{q}_{dynamic}$. The heat input to control volume CV-3 (vapor return transfer lines) is non-isothermal and is denoted by $\dot{q}_{RTL}$. No accumulation of mass is considered in the heat exchanger and for the control volume, CV-1, conservation of mass and energy can be written as –

$$\dot{m}_s - \dot{m}_g = \dot{m}_l + \dot{m}_v \tag{5.1}$$

$$\frac{dU}{dt} = \dot{m}_s h_{s,1} - \dot{m}_g h_{g,1} + \dot{q}_{CV-1} \tag{5.2}$$

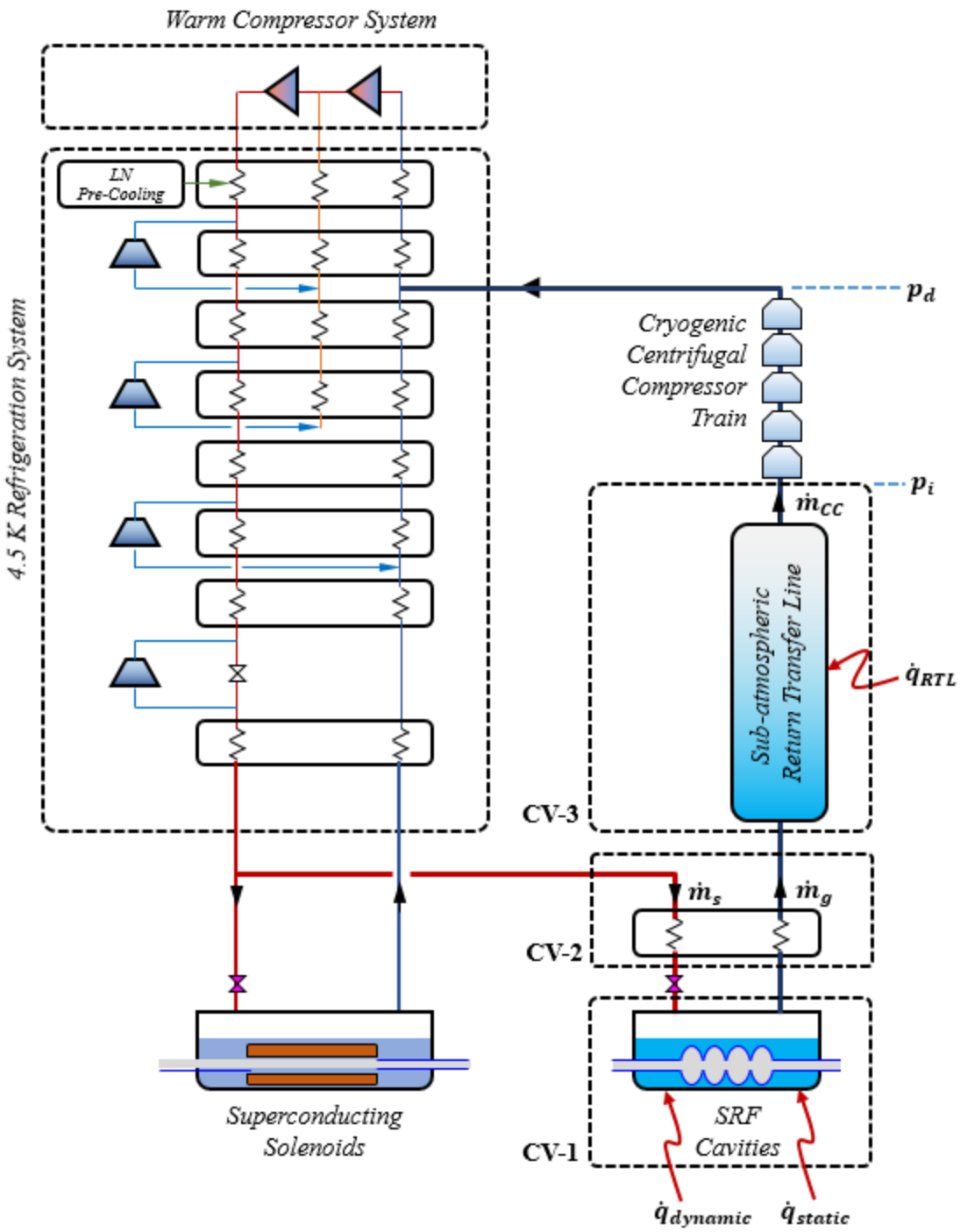

Figure 5.2: *Simplified schematic diagram of the FRIB sub-atmospheric system*

Here, $\dot{m}_s$ and $\dot{m}_g$ are the supply and return mass flow rates from the control volume CV-1 (cryo-module SRF cavity), respectively, and $h_{s,1}$ and $h_{g,1}$ are the corresponding enthalpies. The terms $\dot{m}_l$ and $\dot{m}_v$ denote the (time) rate of change of liquid and vapor mass within the control volume. U represents the overall internal energy of the control volume and $\dot{q}_{CV-1}$ is the heat input to the control volume, as defined through the following equation –

$$\dot{q}_{CV-1} = \dot{q}_{static} + \dot{q}_{dynamic} \tag{5.3}$$

Assuming that all fluid within the cryostat is under saturated conditions at pressure, p_i, enthalpy of the gas leaving the cryostat, $h_{g,1}$, can be considered as that of the saturated vapor (h_v). For the specific heat exchanger under design conditions, the temperature differential at the cold end can be assumed constant (*i.e.* ΔT_{CE} = 0.2 K) and the enthalpy of the supplied fluid to the cryostat ($h_{s,1}$) can be found. Considering isenthalpic expansion across the supply valve, the supplied fluid enthalpy ($h_{s,1}$) can be expressed in terms of the saturated liquid (h_l) and vapor (h_v) enthalpies and the vapor quality (x) –

$$h_{g,1} = h_v \tag{5.4}$$

$$h_{s,1} = (1 - x)h_l + xh_v \tag{5.5}$$

Substituting (5.1), (5.3), (5.4) and (5.5) into (5.2) –

$$\frac{dU}{dt} = \left(\dot{m}_g + \dot{m}_l + \dot{m}_v\right)[xh_v + (1 - x)h_l] - \dot{m}_g h_v + \dot{q}_{static} + \dot{q}_{dynamic} \tag{5.6}$$

The left side of equation (5.6) represents the rate of change of internal energy (U) within the control volume (CV-1) and can be expanded using the following equations –

$$U = mu \tag{5.7}$$

$$\frac{dU}{dt} = m_l \dot{u}_l + \dot{m}_l u_l + m_v \dot{u}_v + \dot{m}_v u_v \tag{5.8}$$

Here, u is the specific internal energy of the fluid and the subscripts l and v represent the saturated liquid and vapor states, respectively. Implementing the differential chain rule and assuming the cryogenic fluid within the cryostat remains at saturation conditions, the time rate change of the specific internal energy terms can be expanded to reach the form of equation (5.9). Substituting this back into equation (5.8), the change of total internal energy with respect to time is modified to take the form of equation (5.10).

$$\dot{u} = \dot{p}_i \left(\frac{du}{dp_i}\right)_{sat} \tag{5.9}$$

$$\frac{dU}{dt} = \dot{p}_i \left[m_l \left(\frac{du_l}{dp_i}\right)_{sat} + m_v \left(\frac{du_v}{dp_i}\right)_{sat} \right] + \dot{m}_l u_l + \dot{m}_v u_v \tag{5.10}$$

Here, $\dot{p}_i$ denotes the time rate of change of the return stream (cryostat and vapor return line) pressure.

From (5.6) and (5.10) –

$$\begin{aligned} &\dot{p}_i \left[m_l \left(\frac{du_l}{dp_i}\right)_{sat} + m_v \left(\frac{du_v}{dp_i}\right)_{sat} \right] + \dot{m}_l u_l + \dot{m}_v u_v \\ &\qquad = \left(\dot{m}_g + \dot{m}_l + \dot{m}_v\right)[x h_v + (1-x) h_l] - \dot{m}_g h_v + \dot{q}_{static} + \dot{q}_{dynamic} \end{aligned} \tag{5.11}$$

The left side terms within the square bracket of the above equation requires additional manipulation to develop a form which can easily be evaluated. Considering the total derivative of specific internal energy, $u \equiv u(T, v)$ with respect to temperature (T) and specific volume (v), equation (5.12) is derived and further modified by taking the derivative of the return stream pressure (p_i) to form equation (5.13). Each term in this equation can then be derived to include only evaluable thermodynamic properties.

$$du = \left(\frac{\partial u}{\partial T}\right)_v dT + \left(\frac{\partial u}{\partial v}\right)_T dv \tag{5.12}$$

$$\left(\frac{du}{dp_i}\right)_{sat} = \frac{\left(\frac{\partial u}{\partial T}\right)_v}{\left(\frac{dp_i}{dT}\right)_{sat}} + \left(\frac{\partial u}{\partial v}\right)_T \left(\frac{dv}{dp_i}\right)_{sat} \tag{5.13}$$

From the definition of the specific heat capacity at constant volume –

$$C_v = \left(\frac{\partial u}{\partial T}\right)_v \tag{5.14}$$

The second and third terms on the right side of (5.13) require further adjustment to form evaluable thermodynamic properties. Using the first '*T-ds*' equation ($Tds = du + pdv$) –

$$\left(\frac{\partial u}{\partial v}\right)_T = T\left(\frac{\partial s}{\partial v}\right)_T - p_i \tag{5.15}$$

Through the Helmholtz thermodynamic potential and the corresponding Maxwell relation, equation (5.16), and applying the triple product rule, equation (5.17), equation (5.15) can be further modified –

$$\left(\frac{\partial s}{\partial v}\right)_T = \left(\frac{\partial p_i}{\partial T}\right)_v \tag{5.16}$$

$$\left(\frac{\partial p_i}{\partial T}\right)_v \left(\frac{\partial v}{\partial p_i}\right)_T \left(\frac{\partial T}{\partial v}\right)_{p_i} = -1 \tag{5.17}$$

$$\left(\frac{\partial u}{\partial v}\right)_T = \frac{T\beta}{\kappa} - p_i \tag{5.18}$$

Here, the volume expansivity (β) and isothermal compressibility factor (κ) are defined with equations (5.19) and (5.20), respectively.

$$\beta = \frac{1}{v}\left(\frac{\partial v}{\partial T}\right)_{p_i} \tag{5.19}$$

$$\kappa = -\frac{1}{v}\left(\frac{\partial v}{\partial p_i}\right)_{T} \tag{5.20}$$

Modification of the third term follows a similar strategy to the second term. The total derivative of the specific volume, $v \equiv v(p_i, T)$ in terms of pressure and temperature is derived, as shown in equation (5.21). Dividing by the pressure differential, the equation takes the form of equation (5.22), which can be modified by multiplying and dividing the right side by the specific volume. Through this modification the volume expansivity and isothermal compressibility terms arise, simplifying the expression to equation (5.23).

$$dv = \left(\frac{\partial v}{\partial p_i}\right)_{T} dp_i + \left(\frac{\partial v}{\partial T}\right)_{p_i} dT \tag{5.21}$$

$$\left(\frac{dv}{dp_i}\right)_{sat} = \left(\frac{\partial v}{\partial p_i}\right)_{T} + \frac{\left(\frac{\partial v}{\partial T}\right)_{p_i}}{\left(\frac{dp_i}{dT}\right)_{sat}} \tag{5.22}$$

$$\left(\frac{dv}{dp_i}\right)_{sat} = v\left[\frac{\beta}{\left(\frac{dp_i}{dT}\right)_{sat}} - \kappa\right] \tag{5.23}$$

Collecting all the terms, the derivative of specific internal energy with respect to pressure takes the final form of equation (5.24).

$$\left(\frac{du}{dp_i}\right)_{sat} = \frac{C_v}{\left(\frac{dp_i}{dT}\right)_{sat}} + v\left(\frac{T\beta}{\kappa} - p_i\right)\left[\frac{\beta}{\left(\frac{dp_i}{dT}\right)_{sat}} - \kappa\right] \tag{5.24}$$

Although the overall volume (V) within the cryostat (control volume, CV-1) remains constant, the specific volume of the vapor and liquid are transient during the '*pump-down*' process. The total fluid volume in the cryostat is a combination of both the liquid (V_l) and the vapor (V_v) volumes –

$$V = V_l + V_v = constant \tag{5.25}$$

Assuming the total liquid (and the vapor) volume within the cryostat remains constant during the '*pump-down*' process –

$$\frac{d}{dt}(V) = \frac{d}{dt}(V_l) = \frac{d}{dt}(V_v) = 0 \tag{5.26}$$

$$\dot{V}_l = m_l\dot{v}_l + \dot{m}_l v_l = 0 \tag{5.27}$$

$$\dot{V}_v = m_v\dot{v}_v + \dot{m}_v v_v = 0 \tag{5.28}$$

Considering the chain rule of the specific volume term, the following can be written –

$$\dot{v}_l = \dot{p}_l\left(\frac{dv_l}{dp_i}\right)_{sat},\ \dot{v}_v = \dot{p}_l\left(\frac{dv_v}{dp_i}\right)_{sat} \tag{5.29}$$

And the (time) rate of change of liquid and vapor masses ($\dot{m}_l$ and $\dot{m}_v$) can be expressed in terms of the (time) rate of change of pressure –

$$\dot{m}_l = -\dot{p}_l\left(\frac{m_l}{v_l}\right)\left(\frac{dv_l}{dp_i}\right)_{sat}, \dot{m}_v = -\dot{p}_l\left(\frac{m_v}{v_v}\right)\left(\frac{dv_v}{dp_i}\right)_{sat} \tag{5.30}$$

Substituting equations (5.24) and (5.30) into (5.11) yields equation (5.31) with $\dot{p}_i$, $\dot{m}_g$ and x as the unknown. All rest of the terms of this equation are either known or evaluable thermodynamically.

$$\dot{p}_l[m_l A + m_v B] - \dot{p}_l\left(\frac{m_l}{v_l}\right)\left(\frac{dv_l}{dp_i}\right)_{sat} u_l - \dot{p}_l\left(\frac{m_v}{v_v}\right)\left(\frac{dv_v}{dp_i}\right)_{sat} u_v$$
$$= \left[\dot{m}_g - \dot{p}_l\left(\frac{m_l}{v_l}\right)\left(\frac{dv_l}{dp_i}\right)_{sat} - \dot{p}_l\left(\frac{m_v}{v_v}\right)\left(\frac{dv_v}{dp_i}\right)_{sat}\right][xh_v + (1-x)h_l] - \dot{m}_g h_v \quad (5.31)$$
$$+ \dot{q}_{static} + \dot{q}_{dynamic}$$

Here, A and B are thermodynamically evaluable parameters $\left(\frac{du_l}{dp_i}\right)_{sat}$ and $\left(\frac{du_v}{dp_i}\right)_{sat}$ as given by equation (5.24). Considering energy conservation across the heat exchanger control volume CV-2 –

$$\dot{m}_s(h_s - h_{s,1}) = \dot{m}_g(h_g - h_{g,1}) \quad (5.32)$$

Here, h_s is the enthalpy of the fluid supplied to the heat exchanger inlet (supply stream) and is known. Additionally, h_g is the enthalpy of the fluid leaving the heat exchanger outlet (return stream). Using equations (5.1), (5.4), (5.5) and (5.30), the equation (5.32) can be re-written as –

$$\left[\dot{m}_g - \dot{p}_l\left(\frac{m_l}{v_l}\right)\left(\frac{dv_l}{dp_i}\right)_{sat} - \dot{p}_l\left(\frac{m_v}{v_v}\right)\left(\frac{dv_v}{dp_i}\right)_{sat}\right][h_s - xh_v - (1-x)h_l] = \dot{m}_g(h_g - h_v) \quad (5.33)$$

Combining equations (5.31) and (5.33) –

$$\dot{p}_l[m_l A + m_v B] - \dot{p}_l\left(\frac{m_l}{v_l}\right)\left(\frac{dv_l}{dp_i}\right)_{sat} u_l - \dot{p}_l\left(\frac{m_v}{v_v}\right)\left(\frac{dv_v}{dp_i}\right)_{sat} u_v$$
$$= h_s\left[\dot{m}_g - \dot{p}_l\left(\frac{m_l}{v_l}\right)\left(\frac{dv_l}{dp_i}\right)_{sat} - \dot{p}_l\left(\frac{m_v}{v_v}\right)\left(\frac{dv_v}{dp_i}\right)_{sat}\right] - \dot{m}_g h_g + \dot{q}_{static} \quad (5.34)$$
$$+ \dot{q}_{dynamic}$$

The above equation has three unknowns, *i.e.* $\dot{p}_i$, $\dot{m}_g$ and h_g. Using the control volume analysis for CV-3, two additional equations can be formulated with $\dot{p}_i$, $\dot{m}_g$ and h_g.

Considering a constant volume, V, for the sub-atmospheric vapor return transfer line control volume (CV-3), the mass and energy balance equations can take the form of equations (5.35) and (5.36).

$$V\frac{\partial \rho}{\partial t} = \dot{m}_g - \dot{m}_{cc} \tag{5.35}$$

$$V\frac{\partial (\rho u)}{\partial t} = \dot{m}_g h_g - \dot{m}_{cc} h_{cc} + \dot{q}_{RTL} \tag{5.36}$$

Here, u is the specific internal energy and h_{cc} is the specific enthalpy at the centrifugal compressor train suction. Incorperation of pressure and temperature terms to replace the density involves the selection of an equation of state. The ideal gas equation of state modified by the compressibility factor, equation (5.37), is considered due to its simplicity and accuracy within the pressure and temperature range observed in the return transfer line during the pump-down process.

$$\rho = \frac{p_i}{ZRT} \tag{5.37}$$

For this analysis, T is the (uniform) temperature of the sub-atmospheric vapor return transfer line. Although the temperature of the sub-atmospheric vapor return transfer line varies along the length of the pipeline (due to parasitic heat in-leak), this variation is insignificant to have any impact on the calculated transient response of the pressure. From the measurements, it is observed that the vapor return transfer line temperature quickly converges to a steady value after starting the '*pump-down*' process. It remains approximately constant over the subsequent duration of the '*pump-down*' process. Hence, for the sake of simplicity, the vapor return transfer line temperature is assumed constant. Substituting equation (5.37) for

the density term and differentiating using the product rule, the derivative of the density in the mass and energy balance equations can be modified using equation (5.38) and (5.39).

$$\frac{\partial \rho}{\partial t} = \frac{\partial}{\partial t}(p_i/ZRT) = \frac{\dot{p}_i}{ZRT} \tag{5.38}$$

$$\frac{\partial (\rho u)}{\partial t} = \rho \frac{\partial u}{\partial t} + u \frac{\partial \rho}{\partial t} = u\left(\frac{\dot{p}_i}{ZRT}\right) \tag{5.39}$$

Applying these derivates, the mass and energy balance equations take the form of equations (5.40) and (5.41) –

$$V\left[\frac{\dot{p}_i}{ZRT}\right] = \dot{m}_g - \dot{m}_{cc} \tag{5.40}$$

$$V\left[u\frac{\dot{p}_i}{ZRT}\right] = \dot{m}_g h_g - \dot{m}_{cc} h_{cc} + \dot{q}_{RTL} \tag{5.41}$$

Equations (5.34), (5.40) and (5.41) are combined and solved to obtain $\dot{p}_i$, $\dot{m}_g$ and h_g. The remaining parameters in these equations are either known or can be evaluated explicitly. The term $\dot{p}_i$ is integrated in time to evaluate the transient response of the sub-atmospheric system pressure during the '*pump-down*' process.

The model discussed above required validation against measurements during '*pump-down*' process of the FRIB sub-atmospheric system. Variation of the centrifugal compressor train mass flow rate ($\dot{m}_{cc}$) and the electric heat ($\dot{q}_{dynamic}$) are provided to the model as functions of time. The rest of the model parameters are considered as constants during the '*pump-down*' process. Values of these process parameters are provided in *Table 5.1*.

Table 5.1: FRIB process parameter values for 'pump-down' model

Primary Supply		
Pressure	3	[bar]
Temperature	4.5	[K]
Cryo-module (LS2 & LS3)		
Liquid Helium Volume	7.046	[m^3]
Ullage Volume	2.310	[m^3]
Static Heat In-leak	248	[W]
Return Transfer Line (LS2 & LS3)		
Volume	16.511	[m^3]
Temperature	4.5	[K]
Static Heat In-leak	800	[W]

Figure 5.3 presents the transient variation of the FRIB sub-atmospheric system pressure during a '*pump-down*' process. Both the estimated (using the developed model discussed in this section) and the measured pressure variation for the given centrifugal compressor train mass flow rate ($\dot{m}_{cc}$) are shown. Before the onset of the '*pump-down*' process, there is negligible flow through the vapor return transfer line and the vapor (gas) in the transfer line exists as a thermally stratified column. Assuming the vapor return transfer line exists with a uniform temperature distribution prior to '*pump-down*' results in incorrect (*i.e.* greater) prediction of the overall transfer line vapor mass and hence a longer '*pump-down*' time. This is corrected explicitly using measured temperatures and initializing the system pressure based on calculated total mass contained within the vapor return transfer line (*i.e.* density within the constant volume).

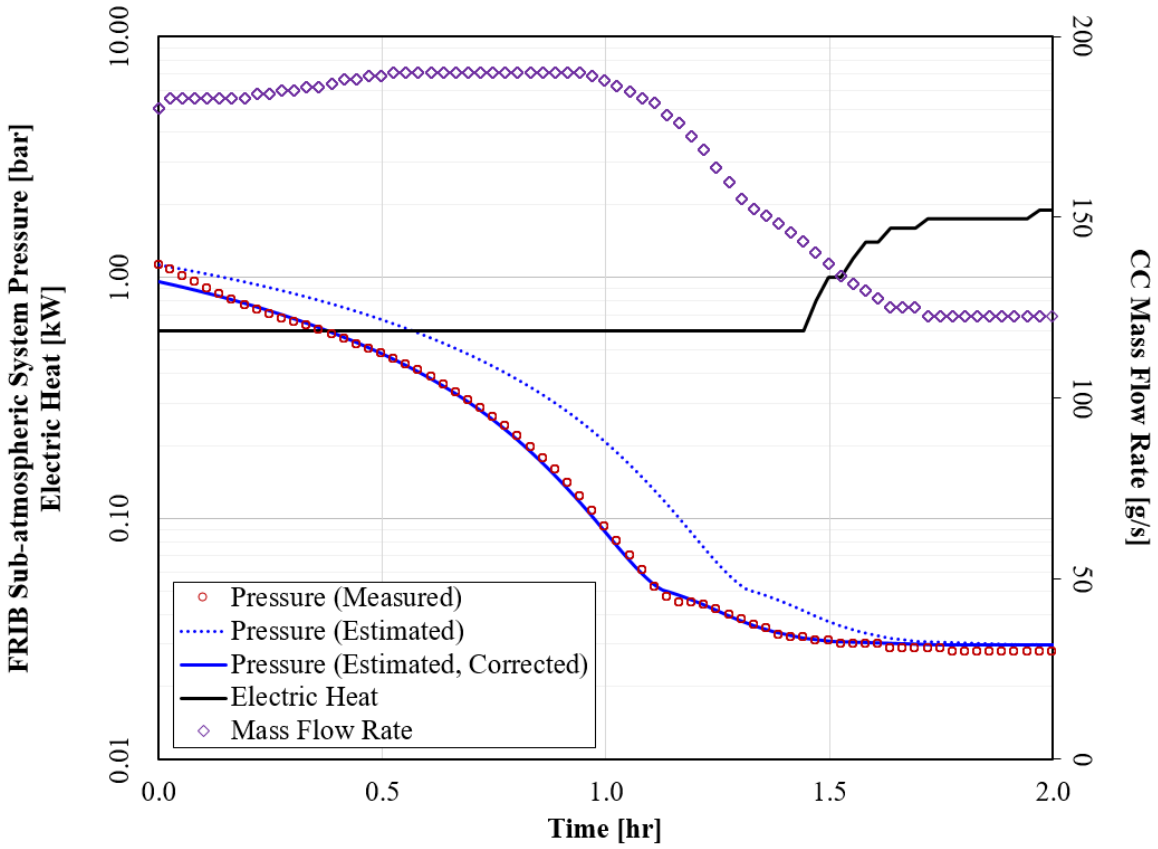

Figure 5.3: *Variation of FRIB sub-atmospheric system pressure (estimated and measured) during a 'pump-down' process.*

5.2.2 Estimation of Speed Ratio and Mass Flow Profile

The model described in Sec. 5.2.1 calculates the transient pressure variation in the sub-atmospheric system given the centrifugal compressor mass flow rate ($\dot{m}_{cc}$). Further investigation needs to be carried out evaluating the effects of different mass flow rate transient profiles, *i.e.* $\dot{m}_{cc}(p_i)$, and compressor speed ratios on the performance of the centrifugal compressors (individual and overall train), and the impact on the rest of the system (*e.g.* 4.5 K refrigerator, warm compressors). For a successful '*pump-down*' process, theoretically the maximum centrifugal compressor flow ($\dot{m}_{cc}$) must be greater than the steady-state boil-off flow due to the static heat in-leak ($\dot{q}_{static}$) and the load dynamic heat ($\dot{q}_{dynamic}$). However, it is often significantly above the steady-state operating flow to minimize the '*pump-down*' time. An optimum '*pump-down*' flow profile, *i.e.* $\dot{m}_{cc}(p_i)$, is required as the input to the control system while maintaining the

operational stability of the cryogenic centrifugal compressor train and the supporting 4.5 K refrigeration system. This optimum flow profile can vary depending on the selected speed ratios of each centrifugal compressor (stage) and hence it is useful to represent the '*pump-down*' path on the individual compressor (stage) performance maps. *Figure 5.4* shows a typical centrifugal compressor performance map (pressure ratio vs. normalized volumetric flow) with the '*pump-down*' starting point (*SP*) and the steady-state operating point (*OP*). Three different types of generic *paths* (*A*, *B* and *C*) can be considered to '*pump-down*' from state SP to state OP. These paths are based on the second derivative of the pressure ratio (p_R) with respect to the normalized volumetric flow rate ($\dot{V}_n$), as described in (5.42) –

$$\text{Path A:} \quad \frac{d^2 p_R}{d\dot{V}_n^2} > 0$$

$$\text{Path B:} \quad \frac{d^2 p_R}{d\dot{V}_n^2} = 0 \qquad (5.42)$$

$$\text{Path C:} \quad \frac{d^2 p_R}{d\dot{V}_n^2} < 0$$

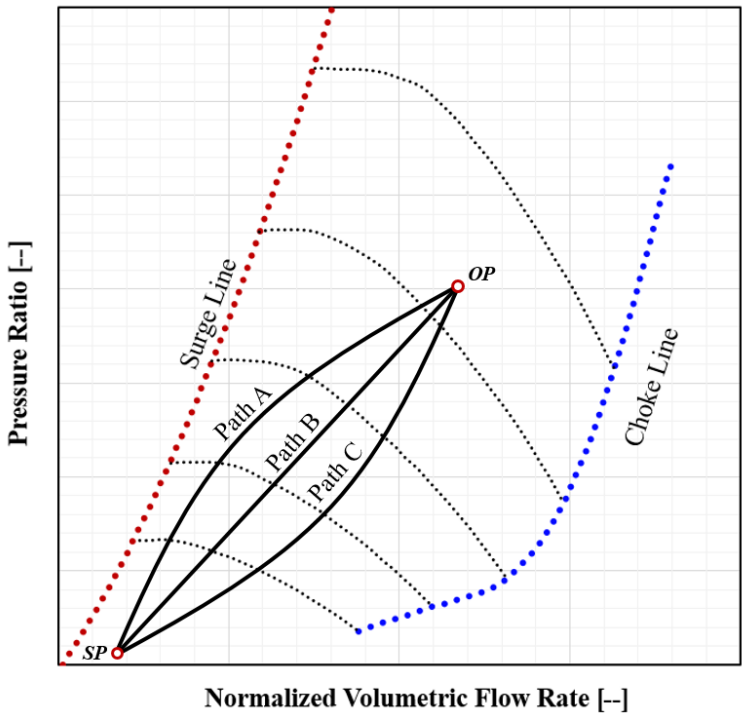

Figure 5.4: *Generic 'pump-down' process paths on a centrifugal compressor performance map.*

By observation (*Figure 5.4*), it can be deduced that path A requires minimal flow but can be limited by the surge line. On the other hand, path C requires higher flow and can be limited by the choke line or the 4.5 K refrigerator system. For systems where the operating point (OP) is relatively near the surge line (*e.g.* FRIB), selecting path A may result in flow instabilities and surge of the centrifugal compressor train during the '*pump-down*' process. However, the higher flow requirement for path C during the '*pump-down*' process may not be compatible to the characteristics of the 4.5 K refrigerator (warm compressor low pressure stage capacity). Hence, an optimum '*pump-down*' process path needs to be found which satisfies the constraints outlined above. The '*pump-down*' process path for each of the cryogenic centrifugal compressors (*CC1-CC5*) previously used at FRIB (through *CY2022*) are shown in *Figure 5.5*. As mentioned earlier, this process path utilizes variable speed ratios for each of the centrifugal compressors (*CC1-CC4*, see *Figure 5.1*) with a compressor mass flow rate (see *Figure 5.3*) that is established empirically. Although this path is clearly outside the steady-state surge line for some of the centrifugal compressor stages, it is observed that the system can continue to function without surge if the compressor train is not allowed to decelerate during this transient process (accomplished through the control scheme). Moreover, the process path doesn't provide a monotonous (and smooth) variation of the stage pressure ratio ($p_{R,x}$) with respect to the normalized volumetric flow rate ($\dot{V}_{n,x}$), which would enable a simpler control scheme.

Considering a linear '*pump-down*' profile for each centrifugal compressor (stage), *i.e.* similar to path B – with $p_{R,x} = a_x \dot{V}_{n,x} + c_x$, the required *CC* mass flow can be calculated. Assuming the electronic speed ratio (S_R), and the mean operating isentropic efficiency ($\eta_{s,x}$) for each centrifugal compressor stage (x = 1 to 5) at the steady-state operating point (OP) are known (see Sec. 4.4 for details on obtaining the optimum steady-state operating point for the cryogenic centrifugal compressor train), the coefficients a_x and c_x can be calculated for each compressor. The total pressure ratio, $p_{R,total}$, across the cryogenic centrifugal compressor train is also known for a given sub-atmospheric system pressure, p_i (the centrifugal compressor train discharge pressure, p_d, is maintained at a constant value). Hence, the following objective

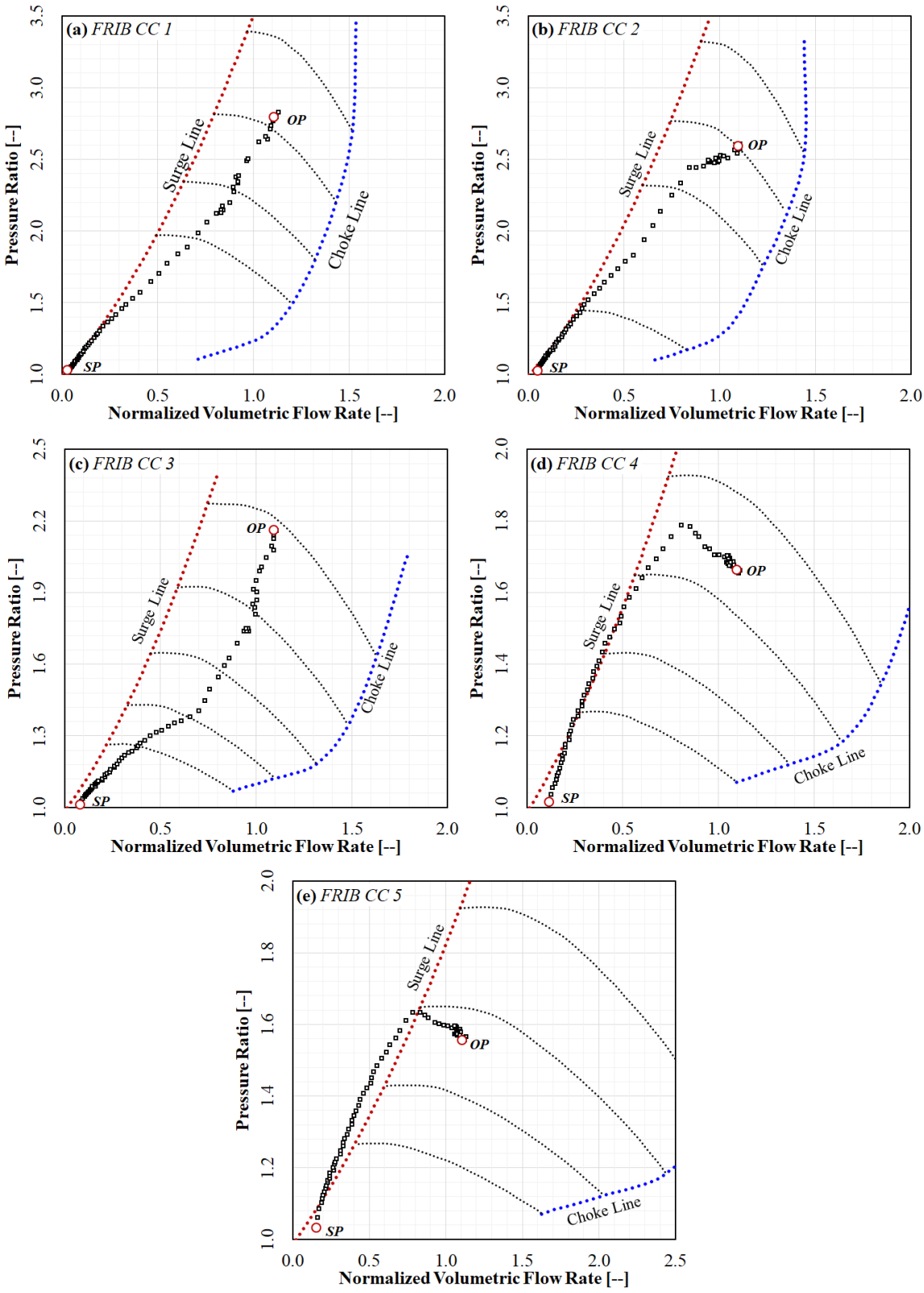

Figure 5.5: *'Pump-down' process paths for each of the cryogenic centrifugal compressors (CC1-CC5) traditionally used (up to CY2022) at FRIB.*

function, equation (5.43), can be solved for any given sub-atmospheric system pressure, p_i, with the constraint equations $p_{R,x} = a_x \dot{V}_{n,x} + c_x$ (where x = 1 to 5).

$$\prod_{x=1}^{x=5} p_{R,x} = p_{R,total} \tag{5.43}$$

The CC mass flow rate, $\dot{m}_{cc}$, is solved using the objective function with the constraint equations of form $p_{R,x} = a_x \dot{V}_{n,x} + c_x$. The normalized volumetric flows for each stage are calculated from the compressor performance map, $\dot{V}_{n,x+1} = f(p_{R,x}, \eta_x)$. A Generalized Reduced Gradient (GRG) method [6] for solving non-linear equations under imposed constraint equations is used for the solution. The overall calculation algorithm is implemented in Microsoft Excel.

The resulting *CC* mass flow rate (path B) and the corresponding 4.5 K refrigeration load (equivalent, using an equal exergy basis) are compared with measurements obtained from the traditionally used '*pump-down*' profile and are presented in *Figure 5.6*. Equivalent 4.5 K refrigeration loading is calculated using the supply conditions provided in *Table 5.1*. The steady-state operating points (OP) for each compressor stage are considered the same as used traditionally at FRIB (up to *CY2022*) for the sake of this comparison. It is observed that the linear profile (path B) yields a significantly higher peak CC mass flow and peak 4.5 K refrigeration (equivalent) load. The time averaged 4.5 K refrigeration (equivalent) load is approximately 14% greater with a linear profile than the traditional FRIB '*pump-down*' profile. As a result, path B and path C (which will require even greater *CC* mass flow and 4.5 K refrigeration (equivalent) loading) were no longer considered viable '*pump-down*' process paths for the FRIB sub-atmospheric system.

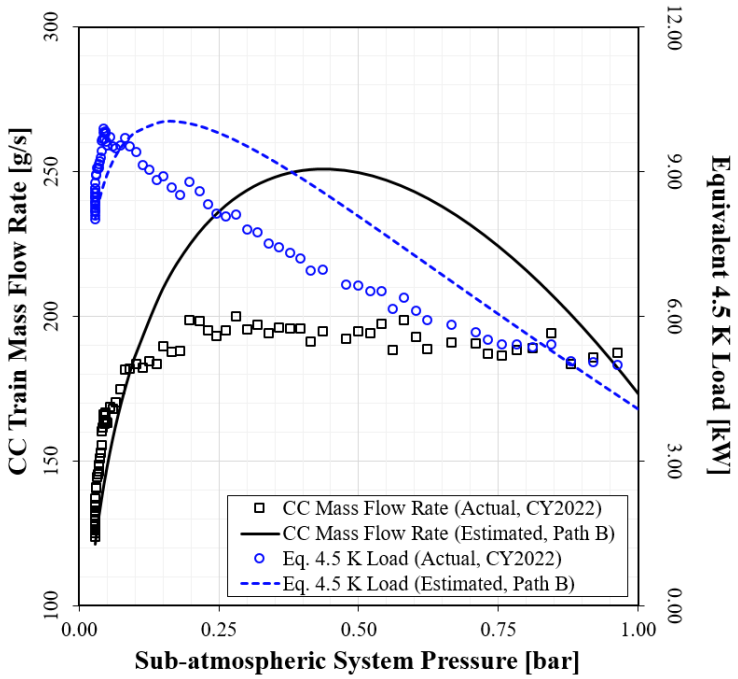

Figure 5.6: *Comparison of the CC mass flow and equivalent 4.5 K refrigeration load using a linear 'pump-down' profile (path B) and the traditionally used (up to CY2022) profile at FRIB*

Considering a concave down '*pump-down*' profile for each centrifugal compressor (stage), *i.e.* similar to path A, the required *CC* mass flow can be also be calculated. As a first approximation, a second order polynomial path, $p_{R,x} = f(\dot{V}_{n,x})$, as provided in equation (5.44), is assumed for each of the compressor stages.

$$p_{R,x} = a_x \dot{V}_{n,x}^2 + b_x \dot{V}_{n,x} + c_x \tag{5.44}$$

A polynomial function for the '*pump-down*' process path should yield a smooth variation of the process parameters (*e.g.* centrifugal compressor mass flow and speed) and provide a smoother transient path for the compressor train. Similar to the calculation procedure for path B, the starting points (SP) and the steady-state operating points (OP) for each cryogenic centrifugal compressor stages are known. Moreover, the pressure ratio corresponding to the surge line (limit), $p_{R,x,s}(\dot{V}_{n,x})$, are also known. Assuming the following constraint, the coefficients (a_x, b_x and c_x) can be calculated for each of the centrifugal compressors.

$$p_{R,x} < p_{R,x,s} \tag{5.45}$$

The *CC* mass flow rate, $\dot{m}_{cc}$ is then solved using the objective function (equation (5.44)) with the constraints from equation (5.45) and not allowing the slope of the polynomial to become negative. The normalized volumetric flows for each stage are calculated from the compressor performance map, $\dot{V}_{n,x+1} = f(p_{R,x}, \eta_x)$. The resulting *CC* mass flow rate (path A) and the corresponding 4.5 K refrigeration load (equivalent, using an equal exergy basis) are compared with those using the traditionally used '*pump-down*' profile and are presented in *Figure 5.7*. Similar to the comparison for path B, the steady-state operating points (OP) for each compressor stage are considered the same as used traditionally at FRIB (up to *CY2022*). In this case (path A), the peak *CC* mass flow is approximately 5% greater, while the time averaged 4.5 K refrigeration (equivalent) load is around 6% less with a concave down profile (path A) than the traditional FRIB '*pump-down*' profile. The corresponding '*pump-down*' process paths (conforming to path A) on the respective centrifugal compressor steady-state performance maps are shown in *Figure 5.8.*

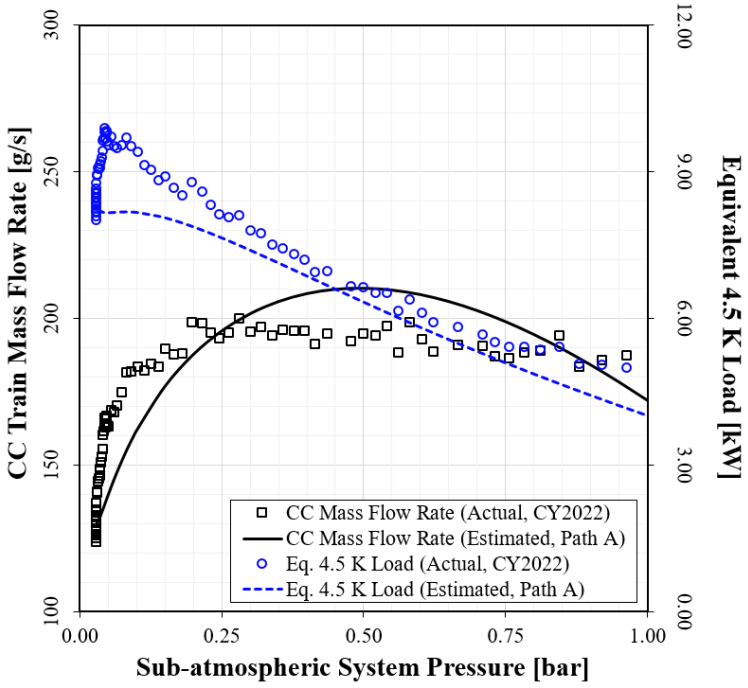

Figure 5.7: *Comparison of the CC mass flow and equivalent 4.5 K refrigeration load using a concave down 'pump-down' profile (path A) and the traditionally used (up to CY2022) profile at FRIB*

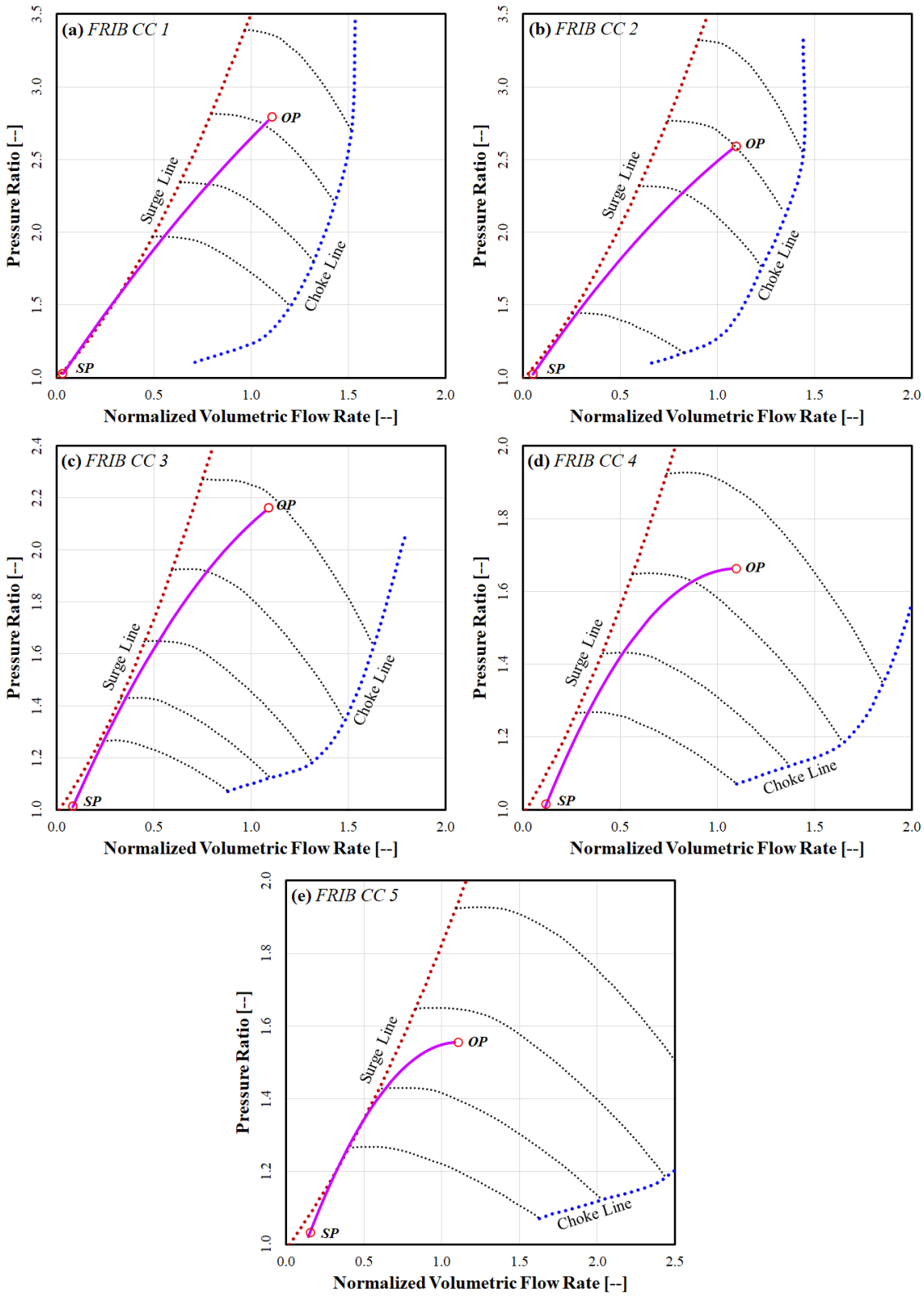

Figure 5.8: *Estimated 'pump-down' process paths for each of the cryogenic centrifugal compressors (CC1-CC5) with path A.*

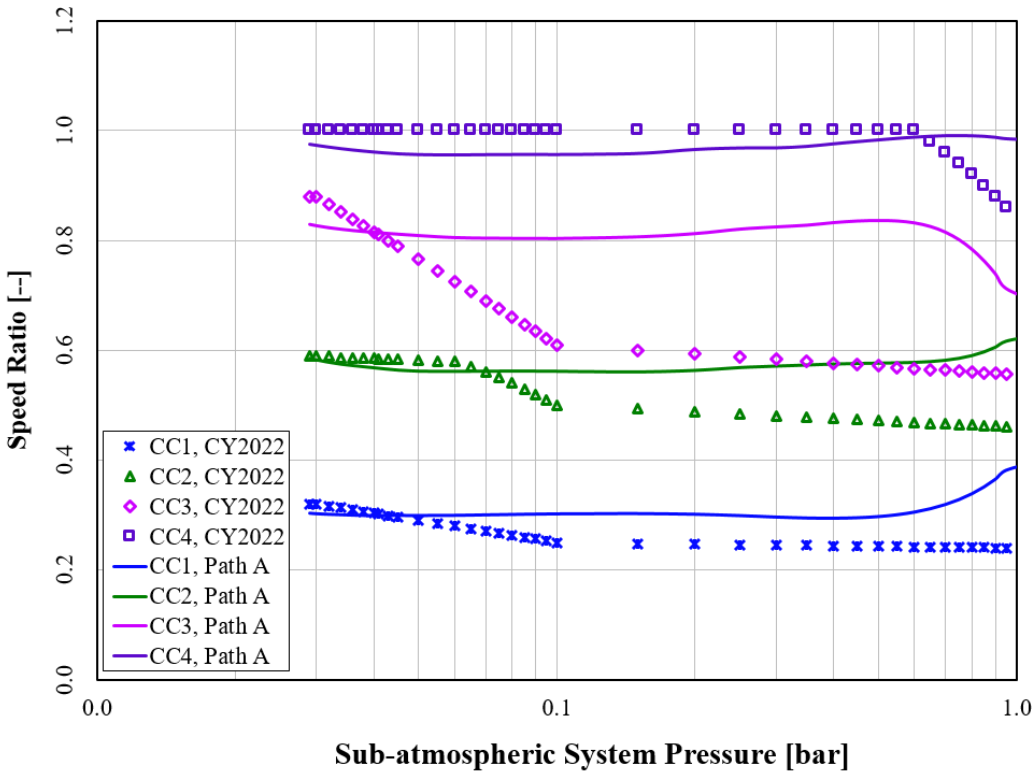

Figure 5.9: *Comparison of estimated secondary centrifugal compressor (CC1-CC4) speed ratios using a concave down 'pump-down' profile (path A) and traditionally used (up to CY2022) for FRIB sub-atmospheric system 'pump-down'.*

The corresponding rotational speeds (N_x) for each cryogenic centrifugal compressor stages are estimated from their respective steady-state performance maps, $N_x = f(p_{R,x}, \dot{V}_{n,x})$. The required electronic speed ratios ($S_{R,x}$) for each of the secondary compressors ($x = 1$ to 4) following process path A are calculated and shown as a function of the sub-atmospheric system pressure (p_i) in *Figure 5.9*. It is observed that the estimated speed ratios ($S_{R,x}$) for the secondary compressor stages ($x = 1$ to 4) maintains a fairly constant value over the entire '*pump-down*' process. It should be noted that due to the imposed methodology the accuracy of the compressor performance maps increases as pressure ratios become higher, which explains the larger variation of speed ratios ($S_{R,x}$) at system pressures above 0.6 bar. Maintaining constant speed ratios throughout the entire '*pump-down*' process for all the compressor stages significantly simplifies the control scheme. This constant speed ratio '*pump-down*' path from the start to the final steady-

state operational pressure greatly reduces the complexity of this process and maintains the constrains of the *cold-compressors* and the supporting 4.5 K refrigeration system, resulting in an easily repeatable operational choice. Details on estimation of the optimal steady-state speed ratio for the secondary compressor stages are discussed in Sec. 4.4.

5.2.3 Alternate Method for Estimation of CC Train Mass Flow Profile

The described method of estimating the *CC* train mass flow profile in Sec. 5.2.2 is entirely theoretical and requires accurate information regarding the compressor performance maps across the entire range of operation during the '*pump-down*' process (*i.e.* from SP to OP). Any deviation of the actual compressor performance characteristics from the estimated values may lead to reduced (or zero) stability margins during '*pump-down*' operation. As the '*pump-down*' profile (path A) constraint is imposed in this method, it is also not feasible to maintain a strictly constant speed ratio to the secondary compressors (x =1 to 4). Hence, an explicit method of estimating the *CC* train mass flow profile is described in this section. The following assumptions are considered for the estimation of the *CC* train mass flow as a function of the sub-atmospheric system pressure –

a) Temperature at the inlet to the cryogenic centrifugal compressor train is invariant during the entire '*pump-down*' process.
b) The secondary compressor (x = 1 to 4) speed ratios are known and are maintained constant during the '*pump-down*' process.
c) Since the centrifugal compressor stages are coupled with a fixed speed ratio, the entire compressor train is considered as one single compressor with the total pressure ratio ($p_{R,total}$) as a function of the volumetric flow ($\dot{V}$) at compressor stage 1 (CC1) inlet or vice versa. For simplicity, the total pressure ratio across the CC train is given by p_R in this section.
d) The '*pump-down*' process is governed by the vapor mass (*i.e.* return transfer line) within the sub-atmospheric system and the gas (vapor) in the sub-atmospheric system follows the ideal gas law.

With these assumptions, the volumetric flow ($\dot{V}$) in the general centrifugal compressor performance map coordinate system (*i.e.* p_R vs. $\dot{V}$) can be represented as a generic polynomial function of the pressure ratio as provided in equation (5.46). This form should produce a '*pump-down*' process path similar to path A from Sec. 5.2.2.

$$\dot{V} = ap_R^m + bp_R^n \tag{5.46}$$

Here, a, b, m and n are constants. Since the temperature remains invariant (assumption a), the total pressure ratio across the *CC* train at any given point during the '*pump-down*' process is inversely proportional to the specific volume ratio within the sub-atmospheric system (vapor) space. The volumetric flow across the *CC* train at any point can then be calculated using the following –

$$p_R = \frac{p_o}{p};\ p_R \propto \frac{v}{v_o} \tag{5.47}$$

$$\dot{V} = \tilde{a}\left(\frac{v}{v_o}\right)^m + \tilde{b}\left(\frac{v}{v_o}\right)^n \tag{5.48}$$

Here, p_o refers to the sub-atmospheric system pressure at the initiation of the '*pump-down*' process, and v_o is the corresponding specific volume of the fluid in the system. Selection of the constants m and n are based on a trade-off between the compressor train stability and 4.5 K refrigeration (equivalent) load. Here,a value of $m = 2$ and $n = 1$ are chosen. Greater values of m and n may yield instability of the compressor train, while smaller values may yield a path similar to path B with higher 4.5 K refrigeration (equivalent) load.

$$\dot{V} = \tilde{a}\left(\frac{v}{v_o}\right)^2 + \tilde{b}\left(\frac{v}{v_o}\right) \tag{5.49}$$

The above equation can be simplified further, and expressed as the following –

$$\dot{V} = cv^2 + dv \tag{5.50}$$

For the '*pump-down*' process to follow a path similar to path A (Sec. 5.2.2), *i.e.* a concave down process path on the general centrifugal compressor performance map coordinate system (*i.e.* p_R vs. $\dot{V}$), the following constraint must be met (*i.e.* both c and d must be positive) –

$$\frac{d^2\dot{V}}{dp_R^2} > 0 \tag{5.51}$$

$$\frac{d^2\dot{V}}{dv^2} > 0 \tag{5.52}$$

Although the volumetric flow ($\dot{V}$) is considered as the dependent variable in equation (5.50), *CC* train mass flow rate ($\dot{m}_{cc}$) is the parameter of interest from a compressor train control scheme perspective. Using equation (5.50), the following can be found –

$$\dot{m}_{cc}(p) = \frac{\dot{V}}{v} = cv + d \tag{5.53}$$

Here, v is the specific volume of the gas (vapor) in the sub-atmospheric system and is a function of the system pressure p. There are two unknowns in the above equation that can be solved using the following boundary conditions –

$$\dot{m}_o = cv_o + d \tag{5.54}$$

$$\dot{m}_f = cv_f + d \tag{5.55}$$

Here, $\dot{m}_o$ and $\dot{m}_f$ are the initial and final *CC* train mass flow rates, respectively, while v_o and v_f are the corresponding specific volumes (in the sub-atmospheric system). The above equations can be solved simultaneously and the value of the coefficients c and d can be determined –

$$c = \frac{(\dot{m}_o - \dot{m}_f)}{(v_o - v_f)} \tag{5.56}$$

$$d = \dot{m}_f - \frac{(\dot{m}_o - \dot{m}_f)}{(v_o - v_f)} v_f \tag{5.57}$$

Collecting like coefficients and simplifying, the final form of equation (5.53) becomes –

$$\dot{m}_{cc}(p) = \frac{(\dot{m}_o - \dot{m}_f)}{(v_o - v_f)} v + \dot{m}_f - \frac{(\dot{m}_o - \dot{m}_f)}{(v_o - v_f)} v_f \tag{5.58}$$

$$\dot{m}_{cc}(p) = \frac{(v - v_f)}{(v_o - v_f)} (\dot{m}_o - \dot{m}_f) + \dot{m}_f \tag{5.59}$$

The *CC* train mass flow profile as given by equation (5.59) is dependent on three parameters only, the required *CC* mass flow rate at the end of the '*pump-down*' process, $\dot{m}_f$ (*i.e.* the steady-state operating flow), the *CC* mass flow rate at the beginning of the '*pump-down*' process, $\dot{m}_o$ (*i.e.* at time $t = 0$), and the target operation (final) pressure and corresponding specific volume. *Figure 5.10* represents the variation of the *CC* train mass flow rate with the sub-atmospheric system pressure, as calculated using equation (5.59) with $\dot{m}_f = 120$ g/s and $\dot{m}_o = 190$ g/s. The variation of the specfic volume in the system is also provided. The inverse relationship between the specific volume and the *CC* train mass flow rate is evident, which is expected from the proposed equation.

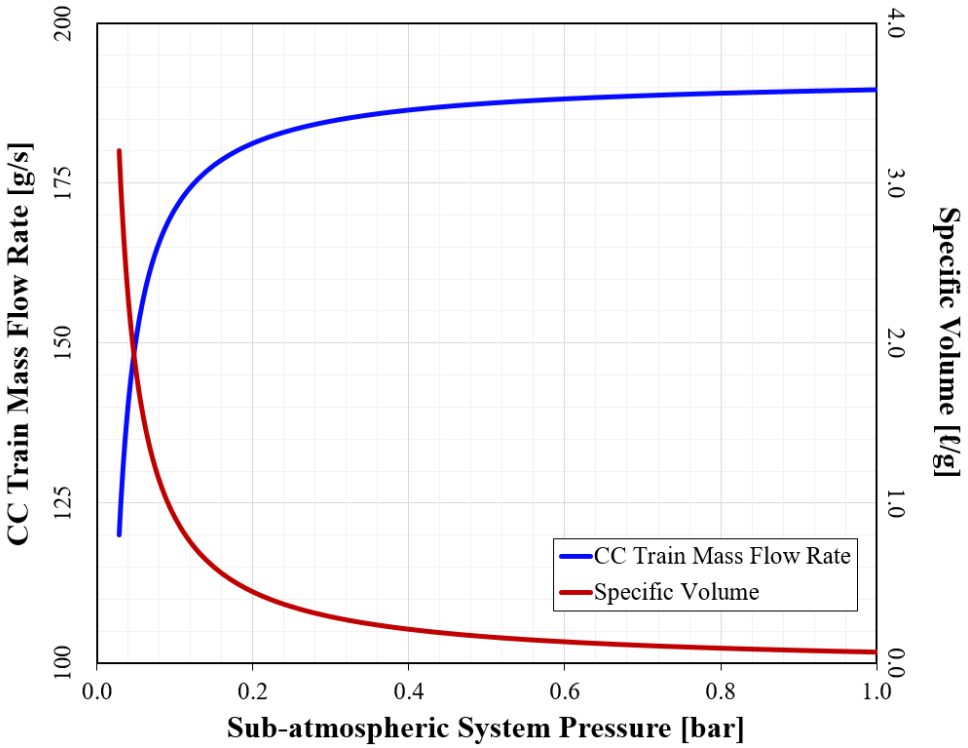

Figure 5.10: *Variation of the CC train mass flow rate and specific volume with the sub-atmospheric system pressure, calculated following equation (5.59) with* $\dot{m}_f = 120$ *g/s and* $\dot{m}_o = 190$ *g/s*

It should be noted that the stability criteria of the cryogenic centrifugal compressor train during the '*pump-down*' process is not explicitly imposed on the *CC* mass flow profile calculated using equation (5.59). In this case, the process path stability is dependent on the initial *CC* mass flow rate, $\dot{m}_o$. Once the *CC* train mass flow rate, $\dot{m}_{cc}(p)$, is calculated, the validity of such a profile can be determined either by tracing the process path on each of the compressor performance maps (if accurate performance maps are available), or experimentally by implementing the calculated *CC* mass flow rate to the '*pump-down*' compressor control scheme.

To demonstrate the applicability of the concept presented in this section, five different *CC* mass flow profiles are selected for analysis. These profiles (as listed by cases 1 – 5) are presented in *Figure 5.11*. Out of these five, the first three profiles (cases 1 – 3) are developed explicitly using equation (5.59), with $\dot{m}_o =$ 180 g/s, 190 g/s, and 200 g/s respectively. Case 4 is calculated considering a hybrid approach, where

equation (5.59) is followed below 0.2 bar, and a mass flow profile is followed elsewhere (above 0.2 bar) that supports compressor acceleration and minimizes 4.5 K refrigerator loading by starting with a lower flow and increasing the mass flow rate during the '*pump-down*' process to approach maximum flow (similar to previously utilized empirical '*pump-down*' process paths). Case 5 is a modification of case 4, where a reduced peak *CC* train mass flow rate is considered. In all these cases, fixed (*i.e.* constant) speed ratios for the secondary compressor stages are assumed. The final (steady-state) *CC* train mass flow rate for all these cases is selected as 120 g/s.

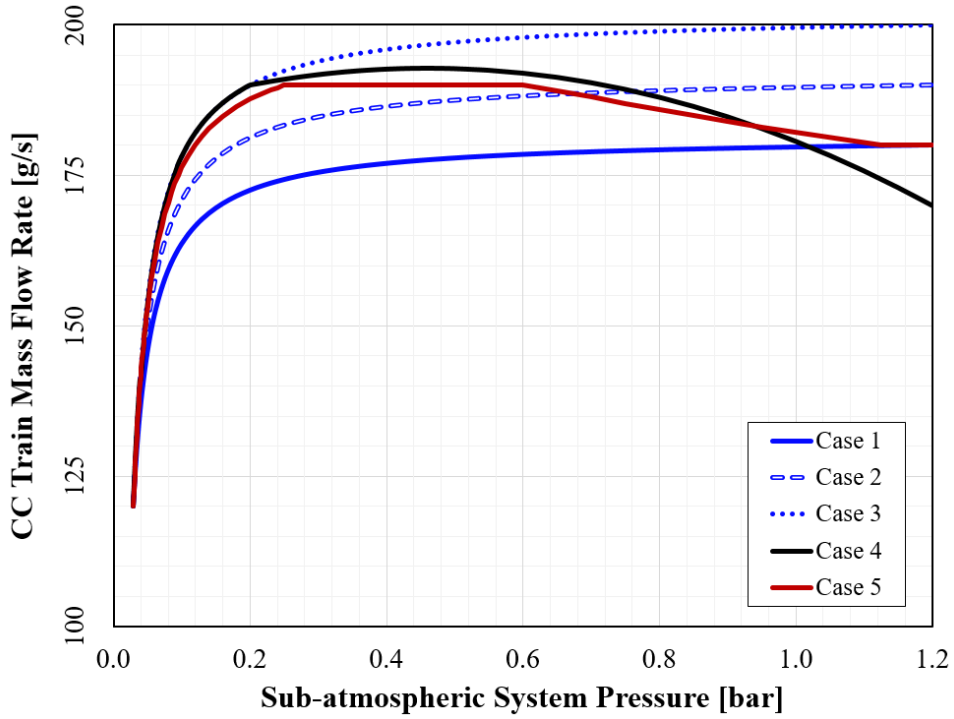

Figure 5.11: *Different CC mass flow rate profiles considered for FRIB sub-atmospheric system 'pump-down' process.*

5.3 Results and Discussion

Testing of the sub-atmospheric system at FRIB was completed during a maintenance period when the accelerator was not in operation, *i.e.* the LINAC was offline. This allowed for flexibility in cryogenic testing where the system could go through various transient operations without effecting user experimental testing. The main objectives of this testing were threefold; (1) verify that a constant speed ratio '*pump-down*' was

achievable, (2) characterize the effects of mass flow profile selection on the '*pump-down*' path, and (3) selection of a standard '*pump-down*' path for FRIB operations.

Testing plans included executing a '*pump-down*' sequence for each of the mass flow profile cases provided in *Figure 5.11*. Although the '*pump-down*' sequence was planned for each of the proposed mass flow profiles of interest, only cases 2, 4 and 5 were successfully completed due to stability complications and 4.5 K refrigeration system limitations. After each '*pump-down*' attempt, data was archived and exported to excel for analysis. Exported parameters included the pressure and temperature at the inlet and outlet of each *cold-compressor*, the mass flow rate, and the rotational speeds of the individual compressors. The transient sub-atmospheric system pressures and total '*pump-down*' time were estimated using the model developed and described in Sec. 5.2.1. Mass flow rate set points, estimated pressure profiles and compressor performance were compared to measured data for each attempted '*pump-down*', and are provided in *Figure 5.12* through *Figure 5.21*.

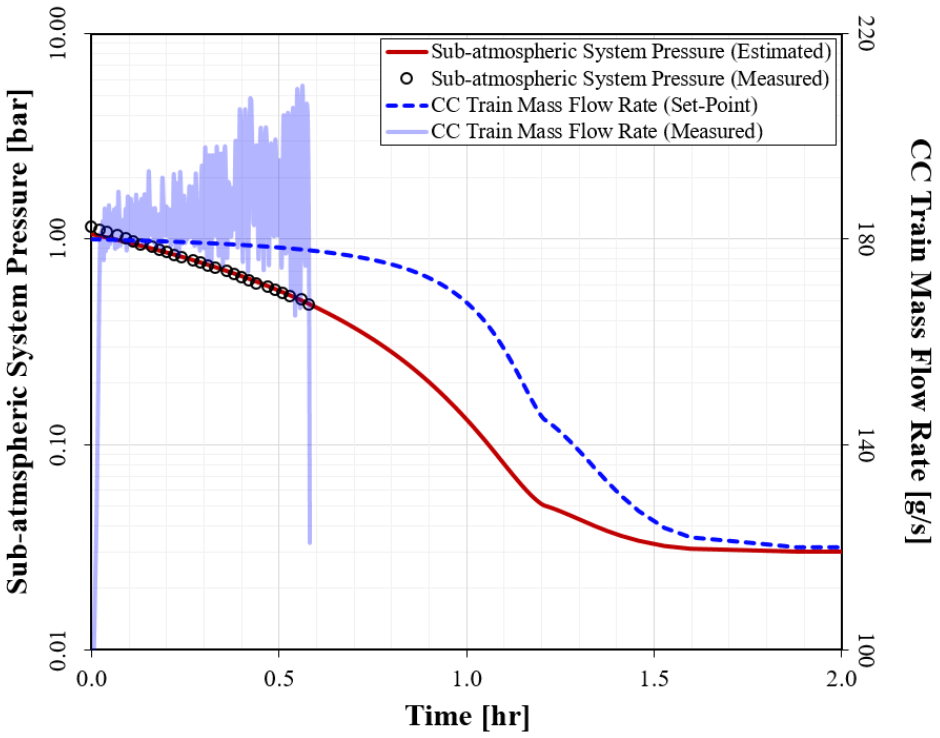

Figure 5.12: *FRIB sub-atmospheric system measurements for Case 1*

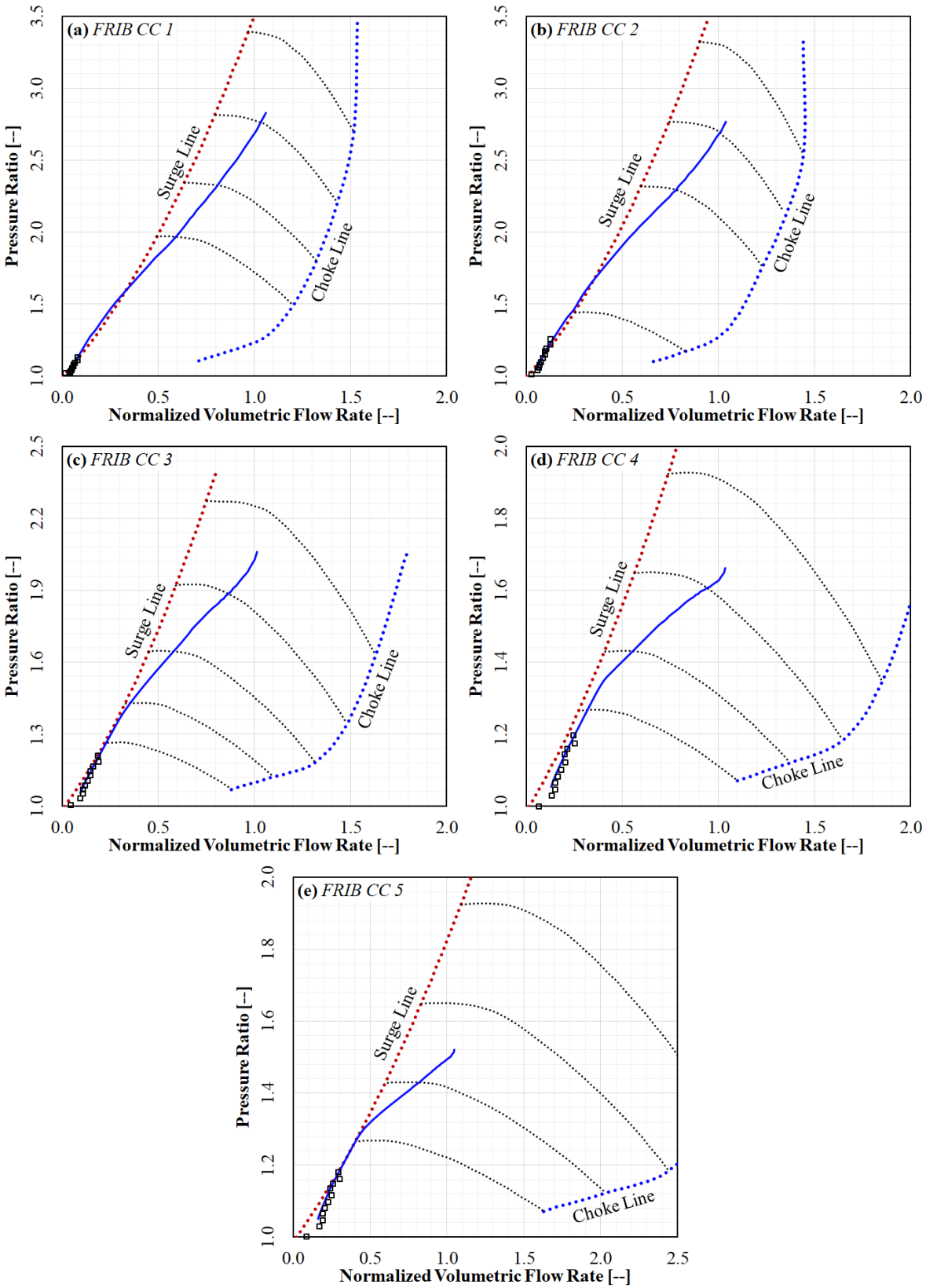

Figure 5.13: *Compressor performance maps for Case 1 (estimated – solid line, measured – symbols)*

Case 1 experienced compressor shutdown, or a "*trip*", during the '*pump-down*' sequence. This was caused by instabilities of cryogenic centrifugal compressor train operation under the imposed lower mass flow rate. Instabilities arise from two main sources due to the reduced mass flow; temperature and pressure fluctuations due to non-uniform static heat in-leak within the return transfer lines, and the performance path moving towards the compressor surge limit. These instabilities can be visually observed through the large oscillations in the measured mass flow rate data, with oscillations reaching nearly 50 g/s swings prior to *cold-compressor* shut-down.

Case 2 produced a successful '*pump-down'* and the measured data from the FRIB system closely followed the estimated sub-atmospheric system pressure and *CC* performance paths. When compared to case 1, the estimated performance curves for *CC1* are noticeably shifted away from the surge region of the performance map. Slight variation between the estimation and measured data for *CC4* and *CC5* performance are anticipated to be linked to the assumptions of the upstream *CC's* isentropic efficiencies.

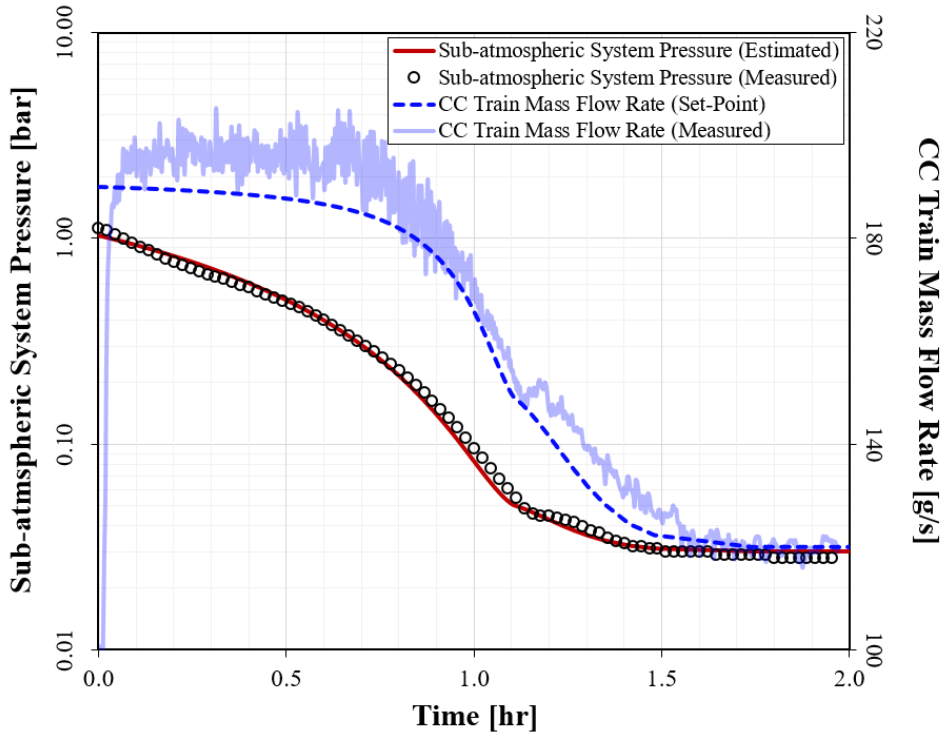

Figure 5.14: *Comparison between estimated pump-down characteristics and measured pump-down data from the FRIB sub-atmospheric system for Case 2*

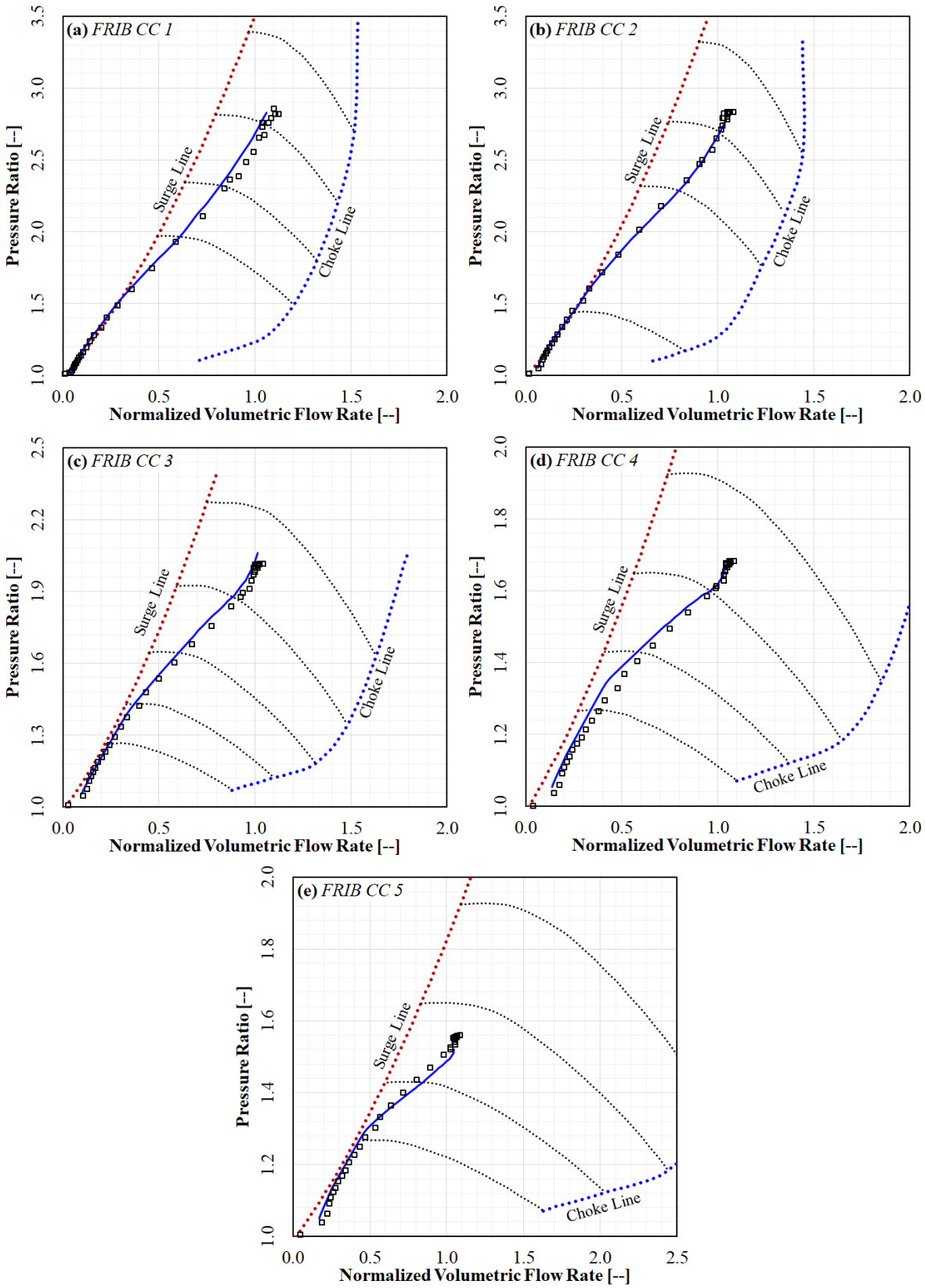

Figure 5.15: *Compressor performance maps for Case 2 (estimated – solid line, measured – symbols)*

Case 3 was not attempted due to the upper flow limits of the FRIB cryogenic system low stage warm compressors. Although the higher mass flow will produce a stable path from a *cold-compressor* operation standpoint, some limits of the 4.5 K main cryogenic refrigeration system were nearly reached (*i.e.* approached minimum limit of main compressor bypass flow) when attempting case 2 and were anticipated to be exceeded for case 3. While this case was not attempted, inherent stability margin gains from increased cryogenic centrifugal compressor train mass flow rates should allow for successful '*pump-down*' using the case 3 '*pump-down*' path.

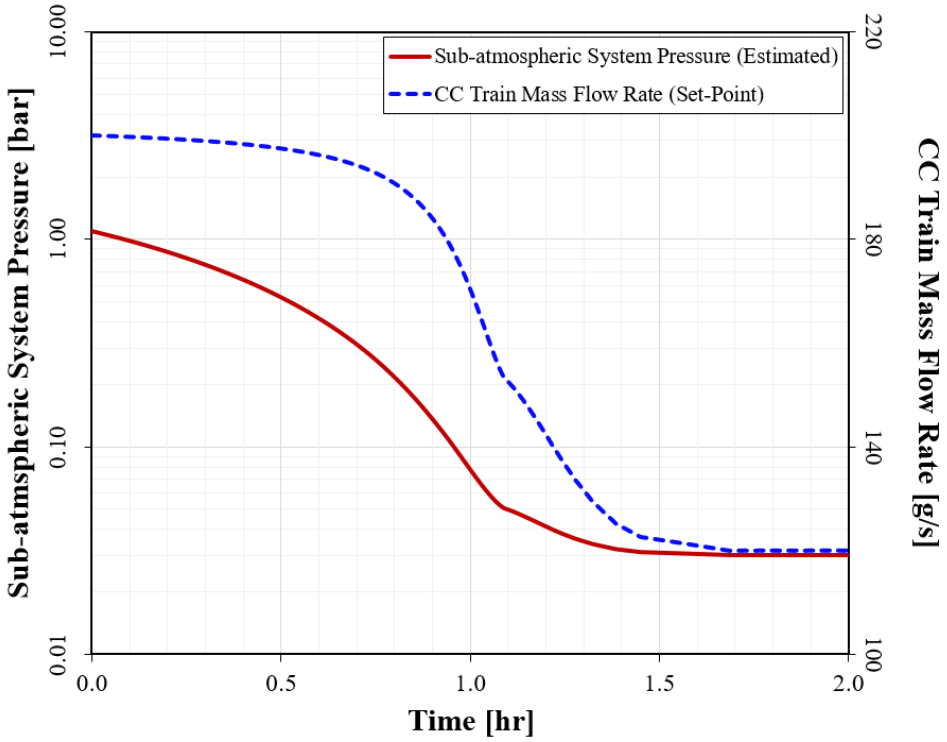

Figure 5.16: *Estimated pump-down characteristics for Case 3*

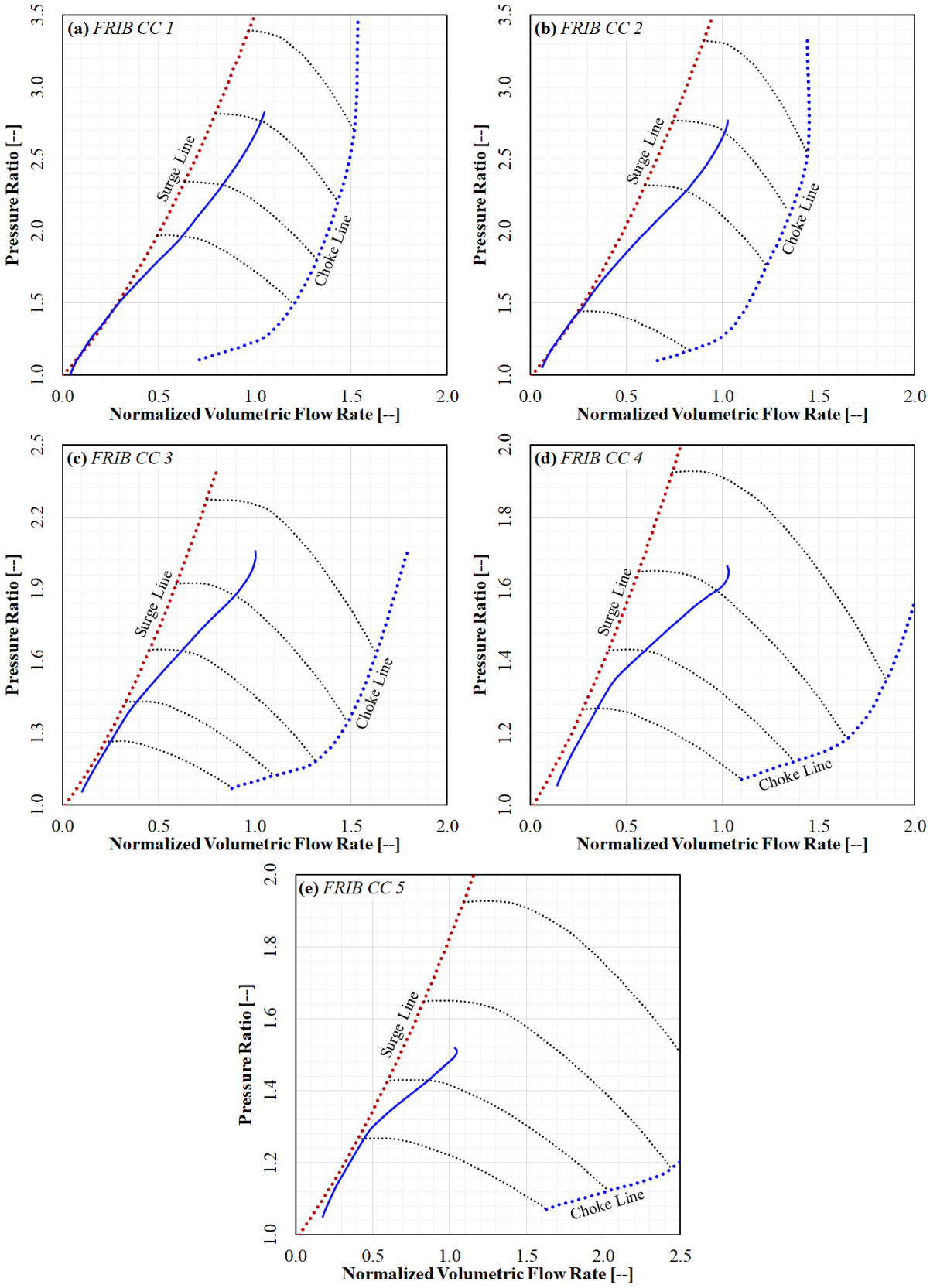

Figure 5.17: *Estimated compressor performance maps for Case 3*

Case 4 produced a successful '*pump-down'*, but the sub-atmospheric system pressure shifted slightly from the estimated system pressure. This is due to a temperature pulse (and subsequent choked flow) through the sub-atmospheric return transfer line. The choked flow is evident in the measured *CC* train mass flow rate, as there is a significant dip in the mass flow at approximately 0.7 hours into the '*pump-down*' process (around 0.3 bar – where the specific volume of the fluid begins significantly increasing, as shown in *Figure 5.10*, setting up secondary flows in the return transfer line). The cryogenic centrifugal compressor train continued to operate during this brief unanticipated transient condition and was able to recover the mass flow. While the '*pump-down*' sequence continued, the transient heat pulse shifted the sub-atmospheric system pressure away from the anticipated pressure curve and was offset for the remainder of the '*pump-down*' sequence.

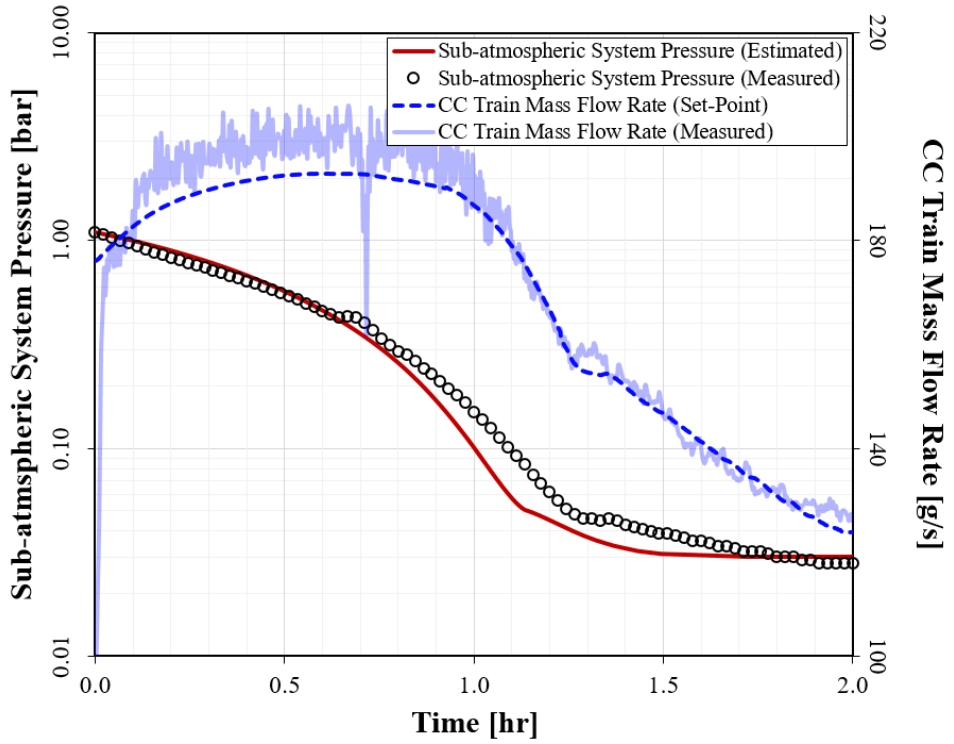

Figure 5.18: *Comparison between estimated pump-down characteristics and measured pump-down data from the FRIB sub-atmospheric system for Case 4*

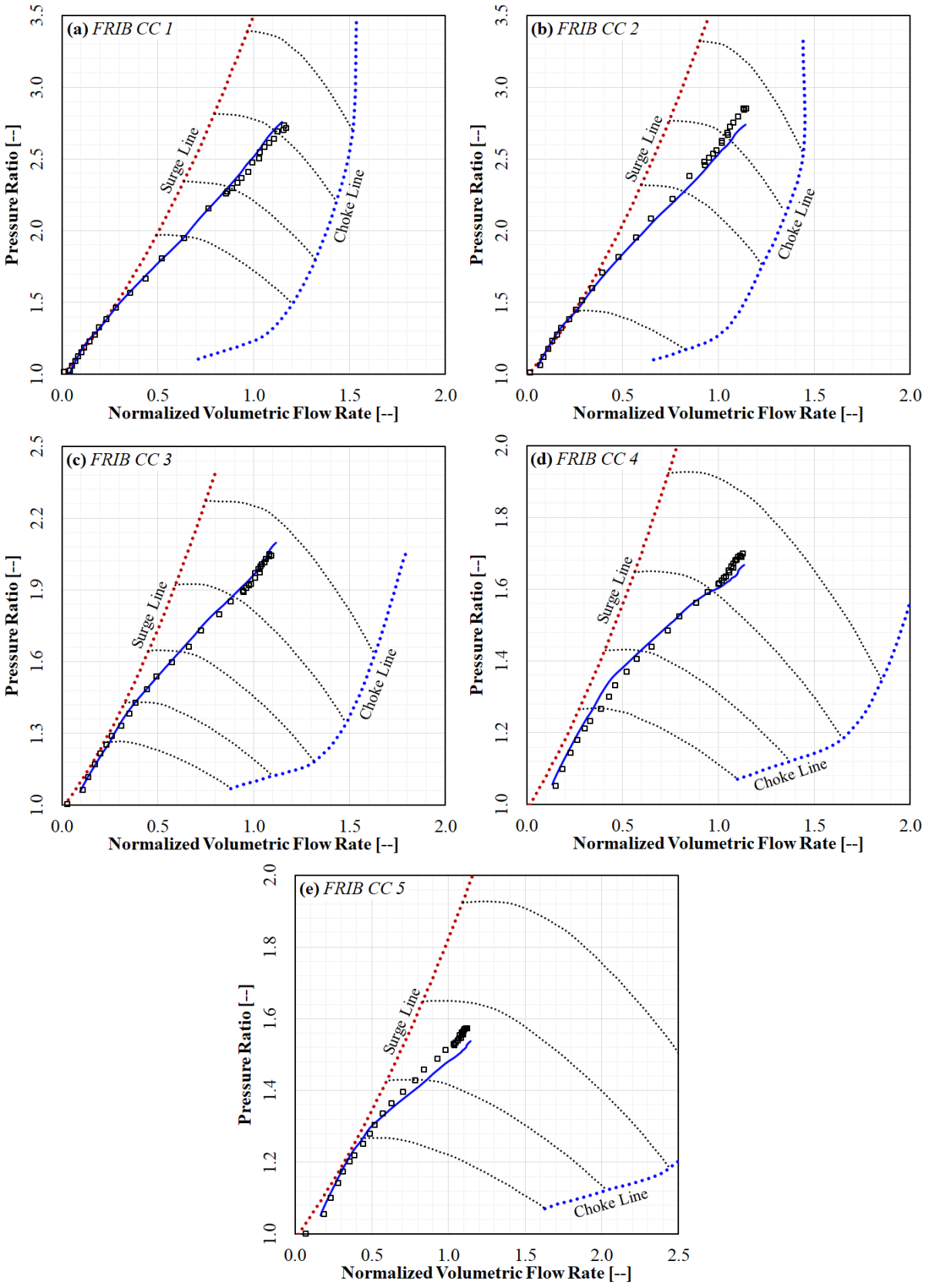

Figure 5.19: *Compressor performance maps for Case 4 (estimated – solid line, measured – symbols)*

Unlike the previous cases, case 5 was applied to a system performing a cold '*pump-down*', *i.e.* a '*pump-down*' where the liquid within the cryostat is sub-cooled due to prior operation under sub-atmospheric conditions. While the '*pump-down*' curves on the individual *CC* performance maps follow the estimated paths, the sub-atmospheric system pressure model does not presently have the capabilities of distinguishing the sub-cooling effect on the liquid helium baths. Therefore, there is deviation observed between the estimated and measured sub-atmospheric system pressure.

Case 5 showcases the stability of the cryogenic centrifugal compressor train during the accelerated '*pump-down*' sequence due to the presence of sub-cooled liquid. When the sub-atmospheric system '*trips*', *i.e.* goes offline, the objective of the operator is to re-establish sub-atmospheric steady-state conditions in a reliable and quick manner. The case 5 '*pump-down*' verifies that steady-state conditions at positive pressures are not required to initiate the '*pump-down*' sequence, and a stable and reliable '*pump-down*' can be achieved with sub-cooled liquid helium present within the cryostat.

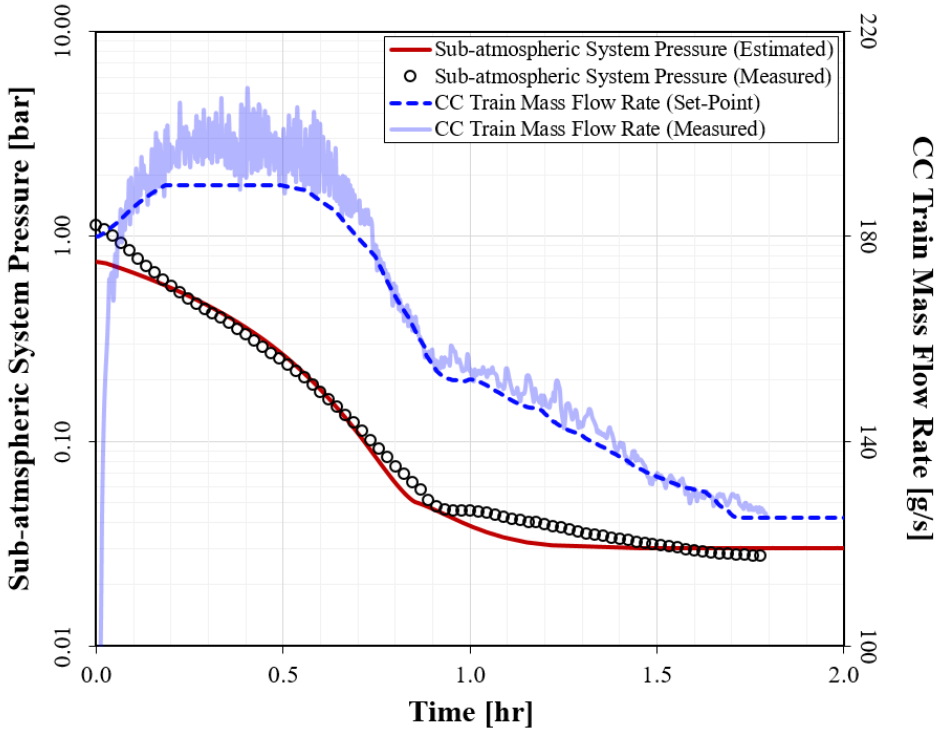

Figure 5.20: *Comparison between estimated pump-down characteristics and measured pump-down data from the FRIB sub-atmospheric system for Case 5*

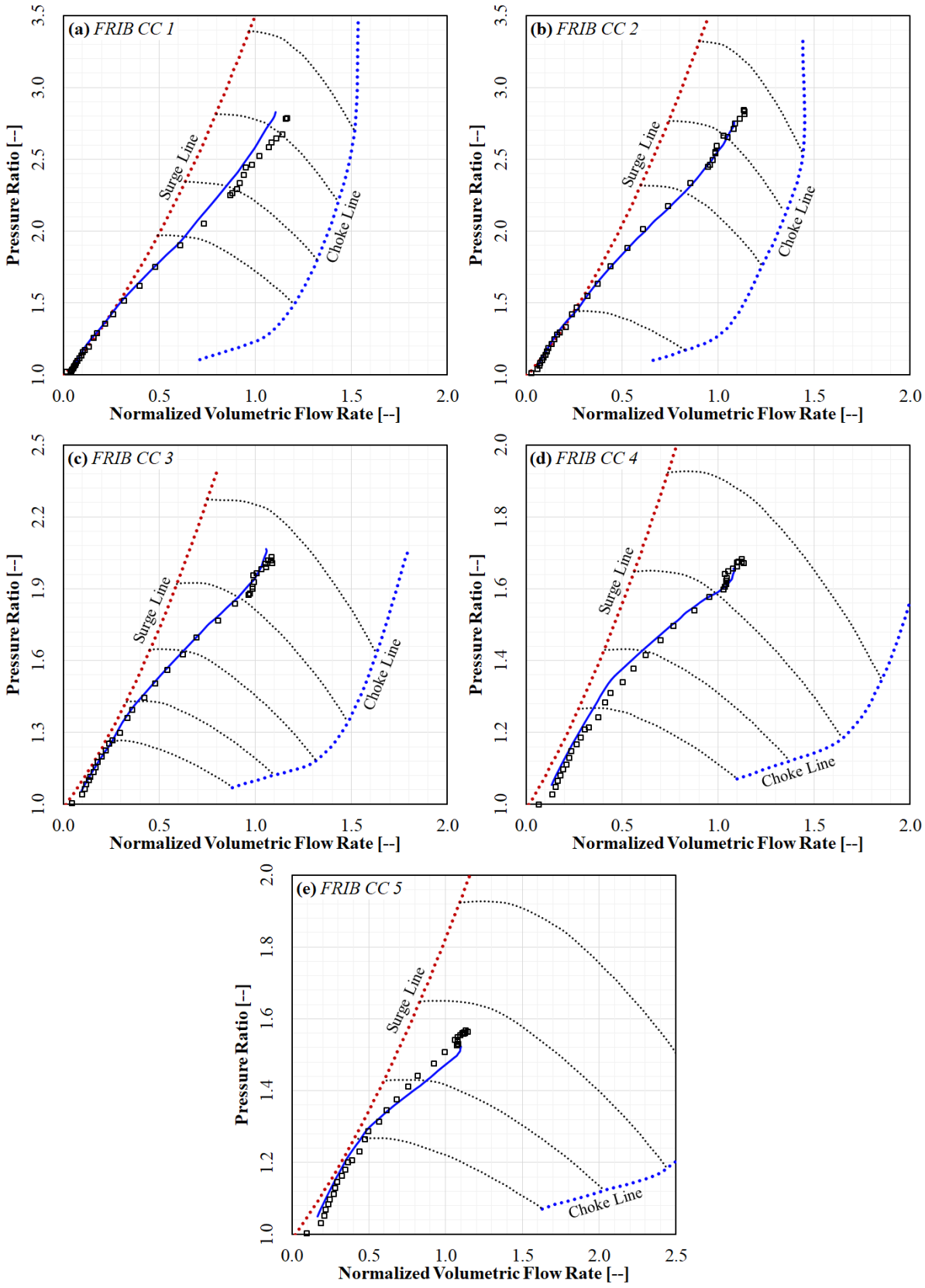

Figure 5.21: *Compressor performance maps for Case 5 (estimated – solid line, measured – symbols)*

The predicted complete '*pump-down*' times vary from 1.5 to 1.8 hours between the five cases, with case 3 being estimated to be the quickest to reach final operational conditions. It is observed that even with the significant reduction of mass flow at the onset of pump-down for case 5, this profile shows little reduction in total pump-down time when compared to case 3. Additionally, if the '*pump-down*' sequence is initiated when there is sub-cooled liquid present in the cryostat, this will result in a different '*pump-down*' time than calculation (estimated).

Performance curves for each mass flow profile was estimated using a cardinal spline interpolation [7] in conjunction with the normalized performance maps provided from the vendor. Using constant speed ratios, an inflection point is encountered along the pump-down path. This inflection was found to be located at the lambda point, and is present for all '*pump-down*' mass flow profiles considered. The second-order polynomial curve assumption for the performance profile is followed until this inflection point, after which the super-fluid properties of the helium cause the curve to diverge from the second-order profile. As anticipated, the mass flow profiles with higher average rates move the curves further into the stable operating region. Case 3 achieves the most stable *cold-compressor* operation, while case 1 trends closest to the surge limit.

Cases 2, 4 and 5 significantly dampened the oscillatory behavior that was observed in case 1, and each of these cases produced a stable and complete '*pump-down*'. A heat pulse was encountered during the '*pump-down*' for case 5, but the *CC* train reacted promptly and was able to continue the sequence. The offset between the actual mass flow and the set point early during the '*pump-down*' process is due to the control philosophy of the *cold-compressor* system, and the exponential relationship between the suction pressure and the required rotational speeds of the compressors. As the suction pressure drops below 0.2 bar, the exponential behavior of the compressor rotational speed increases the sensitivity of the speed adjustment. Therefore, there is greater controllability (*i.e.* increased amount of step changes required) to reach the mass flow rate set point, and the mass flow does not over-correct as easily.

The method for performance estimation proved to accurately predict the characteristics of the *cold-compressors* over the range encountered during the '*pump-down*' path. Minor discrepancies between the estimation and measured data likely derive from the assumption of the *cold-compressor* efficiencies. There is variation in the isentropic efficiency for each *cold-compressor* during the '*pump-down*' sequence, and efficiencies inputted into the model were estimated through curve fitting of previous '*pump-down*' data. Additionally, error bands for temperature and pressure measurements can account for a significant (5 – 10 percent) change in the calculated isentropic efficiency. As predicted, an inflection point in the '*pump-down*' curve was observed for each of the successful cases, and this inflection corresponds to the lambda point transition from normal fluid to super-fluid helium. This is due to the change in thermodynamic property behavior when moving across the lambda line.

5.4 Conclusions

Predictive models based on theoretical principles were developed to attempt to eliminate reliance on empirical and statistical methods currently employed for the operation of sub-atmospheric helium systems. Specifically, developing models for the transient process of reducing the pressure from atmospheric conditions to low pressure operating conditions of approximately 30 mbar, *i.e.* "*pump-down*". Main areas of model development with respect to the pump-down process included:

- Sub-atmospheric system pressure profile and total '*pump-down*' time
- Mass flow rate profile selection
- *Cold-compressor* speed and control

The pressure profile was modeled through the expansion and coupling of depressurization and flow models developed by Dinger [4] and Bottura and Rosso [5]. This model included the total '*pump-down*' time and was validated using measured '*pump-down*' data. It was proven to be reliable in accurately predicting the sub-atmospheric system pressure profile, including the transition through the lambda line and the effects of the dynamic heating within the cryo-module.

Development of the alternative mass flow rate profile relied on the assumption that the volumetric flow rate can be correlated to the total pressure ratio through a second order polynomial. Using the initial and final operational points of the '*pump-down*' sequence and the relationship between the mass flow rate and volumetric flow rate, it was found that the mass flow rate profile can be defined as a function of the specific volume. Therefore, the mass flow rate profile can be directly calculated with respect to compressor suction pressure (*i.e.* specific volume at a constant temperature) if the starting and final points of the '*pump-down*' are established.

Finally, vendor provided compressor performance maps were used in the prediction of compressor stability and speed ratio selection. Through this analysis, it was proven that a '*pump-down*' which used constant speed ratios was achievable for stable operation. An optimized selection of the speed ratios at final operation conditions was calculated in chapter 4, and these speed ratios were chosen for the '*pump-down*' sequence to remove any speed ratio manipulation required during and at the conclusion of the '*pump-down*'.

Overall, appreciable progress was made in understanding the physical characteristics of the multi-stage centrifugal *cold-compressor* sub-atmospheric system at FRIB during transient and steady-state operation. The methodology developed for the FRIB sub-atmospheric system can be applied to other large-scale sub-atmospheric cryogenic facilities utilizing *cold-compression* with the appropriate modifications for system and *cold-compressor* configurations. The present analysis has also provided useful insight into other potential areas of interest and model improvements for future studies of large scale sub-atmospheric cryogenic systems.

REFERENCES

[1] B. Gravil, B. Jager, Experience with a Large Scale He II Refrigeration System at Tore Supra, in: Advances in cryogenic engineering, Springer, 1998, pp. 571-579.

[2] C. Westfall, Engineering the Big Chill: The Story of JLab's Central Helium Liquefier, Physics in Perspective, 16(1) (2014) 37-68.

[3] V. Ganni, D. Arenius, B. Bevins, W. Chronis, J. Creel, J. Wilson Jr, Design, Fabrication, Commissioning, and Testing of a 250 g/s, 2-K Helium Cold Compressor System, in: AIP Conference Proceedings, American Institute of Physics, 2002, pp. 288-304.

[4] K.A. Dinger, modeling of Cold Compressor Pump Down Process, Grand Valley State University, 2018.

[5] L. Bottura, C. Rosso, Flower, A Model for the Analysis of Hydraulic Networks and Processes, Cryogenics, 43(3) (2003) 215-223.

[6] L.S. Lasdon, Design and Testing of a Generalized Reduced Gradient Code for Nonlinear Optimization, in, 1975.

[7] I.J. Schoenberg, Cardinal Spline Interpolation, SIAM, 1973.

CHAPTER 6 : SUMMARY AND CONCLUSIONS

6.1 Overall Summary

Research goals for this dissertation are centered on characterization of the FRIB cryogenic centrifugal compressors during steady-state and transient operation. Compressor characterization required the development of a mean-line centrifugal compressor performance prediction model, which was validated against experimentally measured data sets. Applying the model to the FRIB cryogenic centrifugal compressors, the model will enable the prediction of compressor performance and operational envelopes at a given operating point, *i.e.* estimate the range between surge and choking conditions. Estimations of the cryogenic centrifugal performance will then provide insight to establish a dependable '*pump-down*' path for the transient process when reducing the LINAC helium bath pressure from above atmospheric conditions to steady-state operation near 30 mbar. The objectives from this research are anticipated to benefit any large scale sub-atmospheric helium cryogenic system, and be invaluable for cryogenic centrifugal compressor operation and control.

Model development for the prediction of centrifugal compressor performance began with modeling of air compressors. Open-literature information on centrifugal air compressors is widely available, including strategies for modeling and numerous experimental data sets. Therefore, validation of the developed model with air as the operating fluid took advantage of previous open-literature research and data. Due to the general understanding that known geometrical information of the FRIB compressors will be insufficient for more complicated two or three-dimensional modeling techniques, the main avenue chosen was an accurate mean-line model which minimized required geometrical input.

Development of the air compressor mean-line model involved two major components, the compressor impeller (wheel) and vaneless diffuser. Experimental data available through open-literature commonly measure pressure and temperature values at the inlet of the impeller and the exit of the diffuser, which promotes focusing the initial model on these components. Prediction of property variation through the components of interest rely on derivations centered on conservation equations, *i.e.* conservation of mass,

energy and momentum. Solving the derived equations required specified assumptions, including ideal gas fluid properties, adiabatic compressor housing, and compressor losses (and thus isentropic efficiency) being defined through adopted loss correlation equations.

Integrating loss correlations to predict isentropic efficiencies and overall compressor performance, the developed model was validated against available open-literature experimental data sets for air compressors. Unique compressor geometries for individual data sets were incorporated into the model, and resulting performance estimation, *i.e.* pressure ratio and isentropic efficiency, were directly compared to experimentally measured data. Compressor experimental data sets encompassed both radial and backswept impeller blade geometries, and moderate to high pressure ratio performance characteristics.

Adoption of the developed mean-line compressor modeling to predict helium centrifugal compressor performance involved the incorporation of several new components. As installed, the FRIB compressor assembly includes the compressor impeller (and housing/shroud), diffuser, volute, and exit diffuser. Process piping reducers and expanders present at the compressor system inlet and outlet, respectively, must also be accounted for during model development due to installed measurement locations for the temperature and pressure sensors. All components corresponding to those installed between measurement locations within the compressor system were implemented into the performance model. Along with component modification, fluid properties (ideal gas constant, specific heat ratio, viscosity, *etc.*) were adjusted to account for the shift from air to helium as the operating fluid.

Validation of the mean-line performance model utilized design basis information provided through the compressor vendor and experimental compressor performance data measured at FRIB. Estimated operational regions, *i.e.* the stable region between the surge and choke limits, were calculated for each individual compressor and compared directly to both design basis and experimental data. In conjunction, constant rotational speed performance lines were estimated through the stable region and compared to those provided through the design basis information. Lastly, four operational points of interest (minimum

operation, nominal actual operation, nominal design operation, and maximum operation) were estimated and compared to measured results obtained during FRIB operation.

Once the mean-line performance model was validated, it was used to calculate compressor train speed ratios during steady-state operation. This steady-state point was selected based on compressor performance optimization, *i.e.* maximum weighted surge margin, of the complete compressor train under specified operational conditions. Results from the mean-line model were compared to those found using the design basis performance maps, which were digitized and subsequently interpolated to estimate speed ratios at the optimized steady-state condition.

After using the developed mean-line model to estimate steady-state operation, research focus shifted towards transient operation of the centrifugal compressor train during LINAC depressurization, or '*pump-down'*. Research and development for this transient mode were defined as two coupled interactions, operation of the centrifugal compressor train during '*pump-down*' (*i.e.* selection of the '*pump-down*' path) and thermodynamic trends within the cryo-module and return transfer line volumes during the '*pump-down*' process.

Characterization of the helium thermodynamic trends during the '*pump-down*' process involved mass and energy conservation, and their coupling between the cryo-module volumes and the return transfer line volume. Since the helium within the cryo-modules is two-phase and therefore non-ideal, real fluid properties were required to accurately capture the helium property variance within the vessel. The '*pump-down*' model requires the input of the mass flow rate profile and dynamic electric heat profile, both as functions of the compressor suction pressure. Additional input requirements include the initial conditions, geometrical composition of the cryo-modules and the return transfer lines, and the target liquid level maintained within the cryo-module vessels during '*pump-down*'. Output from the model is the process pressure as a function of time, which can be used to determine how much total time is required for the '*pump-down*' process, or the time required to reach important '*pump-down*' regions, such as the lambda line region.

Centrifugal compressor characteristics during '*pump-down*' are estimated through the use of the mean-line model and design basis performance maps. Stability of the compressor train is strongly coupled to the mass flow profile and the distributed pressure ratios, both provided as function of the compressor suction pressure, and the speed ratios of the individual compressors. The maximum mass flow rate is governed by the main 4.5 K cryogenic refrigerator characteristics, while the minimum is governed by the surge line characteristics of the individual centrifugal compressors. Mass flow profiles were selected to satisfy both of these requirements, remaining below maximum flow limitations while maintaining stable compressor operation without surge (*i.e.* minimum flow limitations). Speed ratios were selected based on performance map surge margin limitations and the objective to maintain smooth compressor '*pump-down*' paths during the transient process.

Different '*pump-down*' profiles were selected and experimentally tested using the FRIB sub-atmospheric cryogenic system. Prior to testing, the '*pump-down*' path and total '*pump-down*' time were estimated using the mean-line centrifugal compressor performance model and the '*pump-down*' model. Results from these estimations were compared to measured data captured during FRIB testing.

6.2 Specific Conclusions and Impact of Findings

6.2.1 Development of a Mean-line Model for Centrifugal Compressors

The developed mean-line centrifugal compressor model for applications with air as the operating fluid was validated as a performance prediction model. Validation was performed on five centrifugal compressors with different geometries and target pressure ratios, yielding satisfactory results for all compressor geometries considered. Main contributions towards improved accuracy of the model included proper selection of the slip factor model and the selection of optimal individual loss correlations.

Literature review of various slip factor correlations and their applications in centrifugal compressor performance predictions revealed the requirement for an adaptive slip correlation, *i.e.* a correlation that is a function of important non-dimensional compressor parameters such as Mach tip speed, flow coefficient, and work coefficient. Constant slip factor correlations, such as the proposed correlation of Wiesner [1], are

based solely on compressor geometry and do not sufficiently react to variance in compressor speed or flow conditions. This can become problematic with higher pressure ratio centrifugal compressors, as these constant slip factor correlations tend to over-predict the slip factor and therefore estimate greater pressure ratios than observed through experimental measurement. Harrison [2, 3] developed a slip factor correlation which is variable and based on non-dimensional compressor parameters such as those discussed previously. This slip factor includes constants which are required to be tuned for specific compressor geometries, but Harrison [2, 3] also provides generalized constant values that can be applied to all air compressor geometries to obtain sufficient accuracy. Significant improvement in predicted slip factor for air compressors can be gained through the implementation of this correlation, even when simply using the generalized constants.

There are numerous loss mechanisms that require consideration when accurately modelling centrifugal compressor performance. Due to the nature of mean-line modeling, an isentropic efficiency is required to calculate the outlet conditions of the compressor. The isentropic efficiency can either be assumed as a constant value, estimated through previous experience or intuition, or estimated using loss correlations. These loss correlations are available in open-literature and have been developed for individual loss mechanisms, with many loss mechanisms having multiple available loss correlations. Therefore, an optimization technique was integrated into the model to select an *optimal* set of loss correlations which produce the least amount of RMS error between model estimation and experimental measurements. The RMS error for all experimental data points was calculated for all possible combinations of loss correlations, and the loss correlation set corresponding to the lowest average RMS error for pressure ratio and isentropic efficiency prediction was selected. This loss correlation set enables a variable yet precise prediction of isentropic efficiency, rather than reliance on constant efficiencies based on experimental data, previous experience, or general intuition.

Appropriate selection of the slip factor correlation and individual loss correlations enabled the compressor performance model to be robust and capable of accurate performance prediction over a wide range of compressor geometries and operating conditions. This model was sufficiently validated, and

provided ample evidence that mean-line modeling can produce reasonably accurate results with minimal required geometrical inputs (*i.e.* when extensive three-dimensional impeller geometry information is unavailable).

6.2.2 Steady-state Characterization of FRIB Cryogenic Centrifugal Compressor Train

Adaptation of the developed mean-line compressor model for usage in helium compressor applications required the addition of several components, including the volute, exit diffuser and process piping reducers and expanders. Development for the volute modeling was available in open literature, while the other components were developed in-house. Minimal amounts of compressor irreversibility occur in the process piping reducers/expanders and exit diffuser, and therefore simplistic models were imposed for each of these components. As previously recognized during air compressor performance prediction, the slip factor correlation and loss correlation selection was critically important in accurate prediction of helium compressor performance.

The slip factor correlation developed by Harrison [2, 3] was unable to predict the slip factor for helium compressors using the generalized constants provided. Using the generalized constants, slip factor values were significantly under-predicted, and caused erroneous results within the model due to inaccurate slip estimation. Due to the lack of experimental slip measurements for centrifugal compressors with helium as the operating fluid, new constants for the Harrison [2, 3] slip factor correlation were unable to be determined. Therefore, the Wiesner [1] slip factor correlation needed to be applied for the helium compressor model. Although, as previously mentioned, this can cause error at higher pressure ratios, the pressure ratio range of the FRIB cryogenic centrifugal compressors are low enough where this error is somewhat negated.

Loss correlation selection employed a similar technique as the air compressor optimization, namely RMS error minimization. For this optimization, 71 experimental measurements taken from FRIB's cryogenic system were used to minimize pressure ratio RMS error. An *optimal* loss correlation set was then

selected using this technique for each of the individual cryogenic centrifugal compressors, with slight variation in loss selection between the various compressor geometries.

Validation of the helium cryogenic centrifugal compressor mean-line model was completed using both FRIB experimentally measured data and design basis performance maps provided through the compressor vendor. Operational regions between the surge and choke lines were predicted by the mean-line model with excellent accuracy, fully encapsulating the entire FRIB data set within the bounds. The mean-line model reasonably matched estimations provided through the design basis performance maps but had higher accuracy than the design basis estimation for the first stage (*CC1*) cryogenic centrifugal compressor. Additional validation of the model was established by comparing mean-line model results with four selected operational points of interest. The mean-line model provided reasonable results, with slight variation between the measured and estimated values due to over-prediction of the isentropic efficiency.

Once the model was validated, it was utilized in the estimation of speed ratios at steady-state operation. This operational point was selected based on surge margin throughout the compressor train. Applying the mean-line model, speed ratios were calculated and compared to speed ratios found through the interpolation of the design basis performance maps. Overall, there was excellent agreement between the two methods for both impeller rotational speeds and speed ratios.

Evidence was provided through these results that mean-line centrifugal compressor modeling can be applied to helium cryogenic centrifugal compressors and yield sufficiently accurate results. Testing of cryogenic centrifugal compressor trains operated in large sub-atmospheric cryogenic systems can be difficult due to complexity of the systems, capital cost of the equipment, and lack of available testing time. Development of this mean-line model allows for significant planning prior to available testing periods and gives insight into operational conditions and performance map regions of interest.

6.2.3 Characterization and Optimization of FRIB Sub-atmospheric Refrigeration System during Transient Operation

Transient operation of the cryogenic centrifugal compressor train is inherently more complicated than steady-state operation. Traditionally, there has been a reliance on previous operational experience and intuition for the control philosophy imposed during transient '*pump-down*' operation. Application of the mean-line performance model and design basis performance maps, and the development of a '*pump-down*' pressure estimation model, were aimed at increasing fundamental understand of trends observed during '*pump-down*'.

Comparing mean-line model predictions and the estimations provided through the design basis performance maps, it was observed that the mean-line model produces results that agree closely with the design basis performance maps. The mean-line model was found to slightly over-prediction compressor isentropic efficiency, while interpolation methods using the design basis performance maps could estimate compressor performance with higher accuracy by manually reducing the isentropic efficiency. Due to the simplicity of the design basis interpolation method (*i.e.* reduction in computational cost), calculations for the transient cryogenic centrifugal compressor behavior were completed using this method in conjunction with estimated efficiencies obtained through experimental measurements. It should be noted that this evaluation strategy is only valid if design basis performance maps are available (and accurate), combined with experimental measurements to estimate isentropic efficiency for each compressor.

Thermodynamic analysis and coupling between the cryomodule and return transfer line volumes allowed for a predictive '*pump-down*' pressure model which enabled the estimation of total '*pump-down*' time and pressure curve characteristics. Mass flow rate and dynamic heat are required inputs for the model, both provided as functions of compressor suction pressure. Results from this model were compared to previously measured FRIB '*pump-down*' sequences, and the model characterized the pressure profile accurately while producing slightly erroneous results in '*pump-down*' time. Variability between the model '*pump-down*' time and experimental measurements is due to the assumption that the return transfer line

(*RTL*) remains at a constant temperature. At the onset of the '*pump-down*' process, the temperature within the RTL quickly (~ 5% of total '*pump-down*' time) transitions from an elevated temperature to a nearly constant temperature of approximately 4.5 K. Reduction in the '*pump-down*' starting pressure, *i.e.* correction in the total return transfer line helium mass storage, to account for the elevated temperature completely eliminates the erroneous results for '*pump-down*' time. With adjustments in starting '*pump-down*' conditions, the total '*pump-down*' time and LINAC pressure can be accurately estimated.

'*Pump-down*' paths along the centrifugal compressor performance maps are strongly influenced by the selection of the mass flow rate profile and the speed ratios within the compressor train. Beginning with a generic '*pump-down*' path profile, adjustment of the mass flow rate profile along the transient sequenced enabled the discovery of a '*pump-down*' path which contained nearly constant speed ratios over the full duration of the '*pump-down*' sequence. Selection of constant speed ratios significantly reduces the complexity for the '*pump-down*' process by removing variability during the transient mode. Further simplification can be made by selecting the speed ratios at the target steady-state conditions, which eliminates the requirement for speed ratio manipulation at the conclusion of the '*pump-down*' sequence.

The mass flow profile for the '*pump-down*' is formed as a function of the compressor suction pressure. Through experimental observations and the nature of volumetric flow type machines, it was discovered that the mass flow profile which satisfies compressor stability and system limitations reassembles the inverse of the specific volume curve as function of the suction pressure. Therefore, mass flow profiles of interest were selected based on the interaction between the RTL specific volume and the suction pressure. Selecting the maximum and minimum mass flow rates based on main cryogenic refrigerator limitations and target stead-state operational conditions, the entire profile was generated with interpolation methods along the specific volume curve. Following the specific volume curve was found to be most critical below suction pressure of ~ 0.2 bar, allowing for modifications to the mass flow profile above this pressure to minimize loading on the main 4.5 K refrigerator.

'*Pump-down*' process characteristics were estimated for transient operation using constant speed ratios and generated mass flow profiles. This characterization included the '*pump-down*' paths along the centrifugal compressor performance maps for the individual compressors, and the total '*pump-down*' time required. Experimental '*pump-down*' measurements provided validation for the modeling of the '*pump-down*' process, with strong agreement between the predicted path and the measured path.

Prediction of the '*pump-down*' path and associated mass flow profiles and speed ratios produced '*pump-downs*' that were continuous and stable throughout the '*pump-down*' process. Previously, fundamental understanding of the sub-atmospheric cryogenic system during transient operation was insufficient in allowing reasonable prediction of the '*pump-down*' process. Advancement in theoretical understanding allows for further optimization of the '*pump-down*' process (*i.e.* reduction in total '*pump-down*' time) while retaining system stability during the '*pump-down*' process. Sub-atmospheric system shutdown limits the ability for physics research to continue through operation of the LINAC. Efficient and stable '*pump-down*' sequences are critical in re-establishing sub-atmospheric conditions required for LINAC operation, and the models developed enable '*pump-down*' paths to be explored in greater detail and provide overall improvement for the transient operation.

6.3 Future Work and Recommendations

Although significant progress was made in fundamental characterization and understanding of these cryogenic systems, there are still many challenges that require additional investigation. During model development and experimental testing, numerous questions and avenues of interest arose which expanded well beyond the research objectives of this dissertation. This section provides a brief discussion on recommendations of future research work.

6.3.1 Investigation of Parameter Correlations for Mean Line Model of Centrifugal Compressor

When using the developed mean-line centrifugal performance model, it has been clear that the selection of appropriate slip factor correlations and loss correlations have significant impact on the estimated performance accuracy. Centrifugal compressors with air as the operating fluid are extremely common in

industry, and therefore correlations are generally developed specifically for air compressor applications. This dissertation was focused on the development of a mean-line centrifugal compressor model that utilized existing correlations from literature, which may deviate in accuracy when applied to systems with a different operating fluid.

Correlation accuracy for slip factor and specific loss mechanisms may improve for applications in helium centrifugal compressors from further investigation. Although full geometrical detail of the present cryogenic centrifugal compressors operated at FRIB are unavailable, compressor wheels can be designed or purchased where these parameters are known. This would allow for further analysis into slip factor and loss correlations through experimental testing and computational fluid dynamic studies. Meaningful improvement may be made to the mean-line model if correlations can be developed specifically for helium cryogenic applications.

6.3.2 Advanced Model for FRIB Sub-atmospheric Refrigeration System

Solution of the '*pump-down*' model required the assumption of constant return transfer line (*RTL*) temperatures. This assumption was primarily set to remove the non-linear components within the system of equations. Real fluid properties were calculated using an excel VBA code, and development of a non-linear system of equations solver within the excel platform was outside of the present research objectives. Development of a VBA code which can solve a non-linear system of equations will allow for the removal of the constant RTL temperature constraint, and present modifications to account for this assumption can be removed from the model.

Pressure drop along the process piping through the RTL was also removed to simplify the solution process. This produces a minor deviation between estimated and measured LINAC pressure. Incorporating the pressure reduction between the cryo-modules and the compressor suction will provide further insight into the relationship between dynamic heat loading, centrifugal compressor mass flow rate, and pressure variation along the process piping.

Dynamic heat loads produced in the cryo-module helium baths are critical to steady-state operation of the sub-atmospheric system. Propagation of the pressure produced from the dynamic heat load is not instantaneous, and is affected by time constants associated with the cryo-modules and RTL volumes. Investigation into dynamic heat loading, and the implications of the volume ratio between cryo-module and the RTL, can provide insight into system stability during and immediately following the '*pump-down*' process.

6.3.3 Further Testing for Process Optimization

Loading on the entire helium cryogenic system is strongly coupled to the mass flow rate through the sub-atmospheric system, *i.e.* cryogenic centrifugal compressor mass flow rate. Minor reduction in this mass flow rate can have significant energy savings for the cryogenic process. Minimization of the cryogenic centrifugal compressor flow is therefore desirable to maximize energy cost savings. Due to the nature of the centrifugal compressor train, stability becomes the main deterrent from operating at reduced mass flow rates. Flow minimization studies and subsequent experimental testing may discover higher stability regions of operation at lower mass flow rates.

At the start of the '*pump-down*' sequence, the volume flow through the compressor train is at a minimum, requiring excessive mass flow rates that can be limited by the 4.5 K refrigerator characteristics or the choking limits of the *cold-compressors*. It was observed that the '*pump-down*' with lower flow rates near the surge line or sometimes within the surge region were successful with continuous acceleration of the compressor wheels. It will be of interest to evaluate the influence of continuous acceleration of the *cold-compressor* system with low flow '*pump-down*' process options to alleviate the limitations imposed by the 4.5 K refrigeration system.

6.3.4 Modification of the Mean Line Model for Design Applications

The mean-line centrifugal compressor model was developed for the performance prediction of compressors with specified geometrical parameters. Modifications to the mean-line model could enable the model to become a design model, giving optimal geometrical parameters for particular performance criteria of

interest, *i.e.* pressure ratio, operational range, maximum efficiency, *etc*. Design basis geometries for the cryogenic centrifugal compressors operated in FRIB's sub-atmospheric system were found to follow scaling factors along the compressor train. Application of the mean-line model in the compressor design phase of the sub-atmospheric system may allow for improvements in cryogenic centrifugal compressor train performance, operational range, and reliability.

REFERENCES

[1] F. Wiesner, A Review of Slip Factors for Centrifugal Impellers, (1967).

[2] H.M. Harrison, III, Development and Validation of a New Method to Model Slip and Work Input for Centrifugal Compressors, Ph.D., Purdue University, United States -- Indiana, 2020.

[3] H.M. Harrison, N.L. Key, A New Approach to Modeling Slip and Work Input for Centrifugal Compressors, Journal of Engineering for Gas Turbines and Power, 143(2) (2021) 021013.